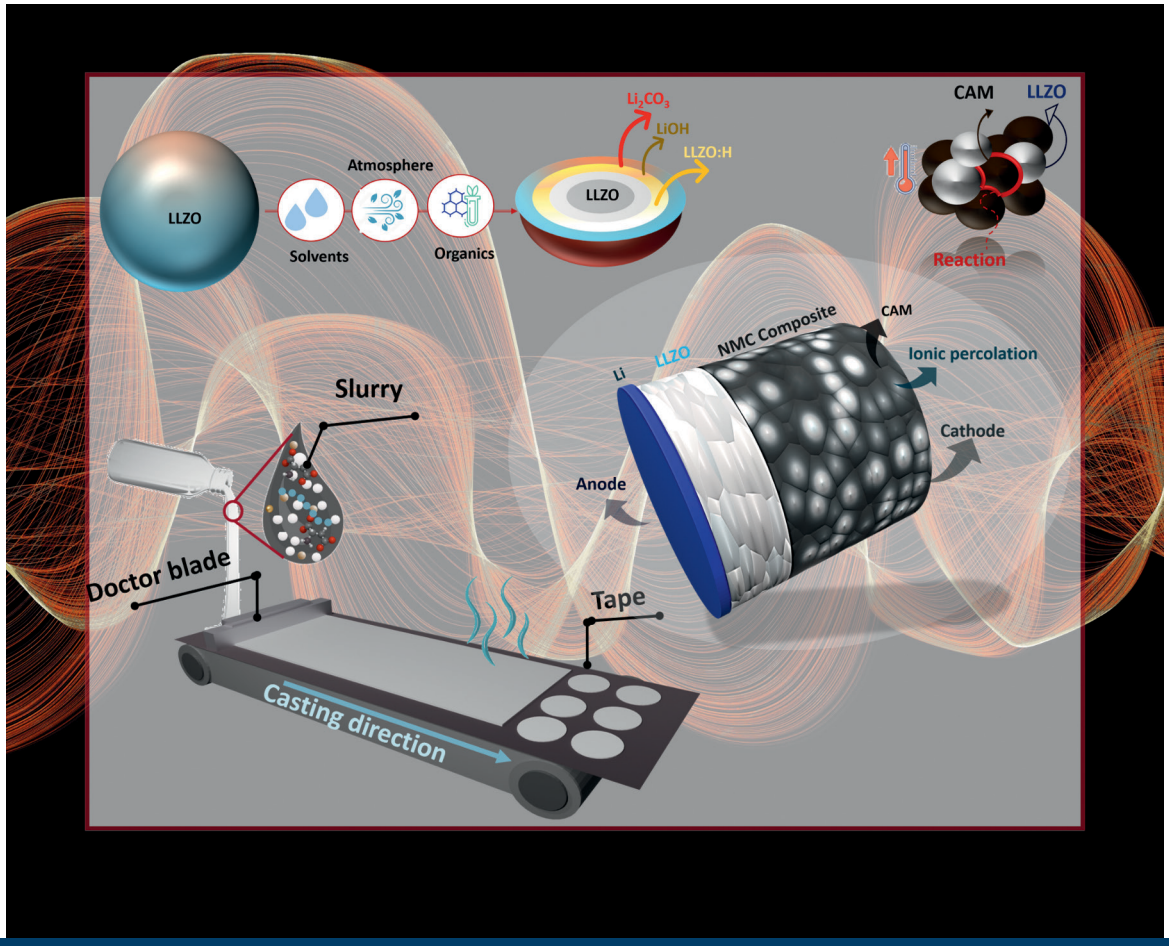


Comprehensive Understanding and Optimization of the Tape Casting Process for the Fabrication of LLZO-Based Solid-State Battery Components

Kaouther Nahr El Khouloud Touidjine

Energie & Umwelt / Energy & Environment
Band / Volume 741
ISBN 978-3-69367-017-0

Mitglied der Helmholtz-Gemeinschaft

JÜLICH
Forschungszentrum

Schriften des Forschungszentrums Jülich
Reihe Energie & Umwelt / Energy & Environment Band / Volume 741

Forschungszentrum Jülich GmbH
Institute of Energy Materials and Devices (IMD)
Werkstoffsynthese und Herstellungsverfahren (IMD-2)

Comprehensive Understanding and Optimization of the Tape Casting Process for the Fabrication of LLZO-Based Solid-State Battery Components

Kaouther Nahr El Khouloud Touidjine

Schriften des Forschungszentrums Jülich
Reihe Energie & Umwelt / Energy & Environment Band / Volume 741

ISSN 1866-1793 ISBN 978-3-69367-017-0

Bibliografische Information der Deutschen Nationalbibliothek.
Die Deutsche Nationalbibliothek verzeichnet diese Publikation in der
Deutschen Nationalbibliografie; detaillierte Bibliografische Daten
sind im Internet über http://dnb.d-nb.de abrufbar.

Herausgeber und Vertrieb:	Forschungszentrum Jülich GmbH Zentralbibliothek, Verlag 52425 Jülich Tel.: +49 2461 61-5368 Fax: +49 2461 61-6103 zb-publikation@fz-juelich.de www.fz-juelich.de/zb
Umschlaggestaltung:	Grafische Medien, Forschungszentrum Jülich GmbH
Druck:	Grafische Medien, Forschungszentrum Jülich GmbH
Copyright:	Forschungszentrum Jülich 2026

Schriften des Forschungszentrums Jülich
Reihe Energie & Umwelt / Energy & Environment, Band / Volume 741

D 464 (Diss. Duisburg-Essen, Univ., 2026)

ISSN 1866-1793
ISBN 978-3-69367-016-3 (Print)
ISBN 978-3-69367-017-0 (E-Book)

Vollständig frei verfügbar über das Publikationsportal des Forschungszentrums Jülich (JuSER)
unter www.fz-juelich.de/zb/openaccess.



This is an Open Access publication distributed under the terms of the Creative Commons Attribution License 4.0, which permits unrestricted use, distribution, and reproduction in any medium, provided the original work is properly cited.

Abstract

Garnet $Li_7La_3Zr_2O_{12}$ (LLZO) is a ceramic material characterized by high lithium-ion conductivity and a broad electrochemical stability window, making it a promising solid-state electrolyte for next-generation solid-state batteries (SSBs). Ceramic membranes made of LLZO are promising separators for lithium-metal SSBs, as they are chemically stable toward lithium and can resist the growth of lithium dendrites. Combining such separators with ceramic composite cathodes containing high-energy cathode active materials (CAMs) and LLZO as the catholyte would enable the production of ceramic SSBs with high energy density and most importantly high inherent safety due to the non-flammability of the ceramic electrolyte. Numerous publications have already demonstrated the feasibility and potential of this battery concept. However, to leverage the advantageous properties of LLZO and enhance the industrial appeal of LLZO-based SSBs, various challenges must still be overcome on both the materials and processing sides.

One of the practical challenges is to manufacture LLZO components with optimized geometry, morphology, and performance using scalable production processes, which is essential for future commercialization. Among the various production options, tape casting stands out as an established technique for the large-scale production of thin ceramic components. In this process, large-area tapes are cast in a continuous process from a slurry containing ceramic powder and organic additives and then sintered at high temperatures to produce free-standing ceramic layers. Tape casting has proven to be a suitable technique for manufacturing LLZO separators; however, their quality, performance, and reproducibility are often compromised by the protonation of moisture-sensitive LLZO during processing and the irreversible loss of lithium during sintering. Therefore, for the production of high-performance LLZO separators, it is important to understand the degradation processes along the entire production chain and to find ways to minimize protonation and lithium loss.

In addition to separators, the scalable production of ceramic composite cathode layers, particularly the integration of Ni-rich $LiNi_xMn_YCoZO_2$ (NMC) cathode active material, is important for the realization of ceramic SSBs with competitive energy densities. However, tape casting of NMC/LLZO cathodes remains a technical challenge, as both LLZO and NMC are highly susceptible to processing-induced chemical and interfacial degradation. To overcome these limitations, this work focused on understanding the

relationships between process, structure, and performance, as well as on optimizing the parameters of the tape casting process for the fabrication of LLZO separators and NMC ceramic composite cathodes, to enable reproducible, economically viable production of battery components with improved performance.

In Chapter 3, we reviewed the degradation phenomena during the tape casting of LLZO separators, particularly LLZO protonation and lithium loss, which significantly impair their performance in cells. Although both phenomena are well documented in the literature, they have previously been studied outside the context of tape-casting manufacturing process. In tape casting of LLZO, however, protonation and lithium loss are inextricably linked and occur across multiple processing steps, including slurry preparation, milling, drying, and sintering. Their cumulative effect determines phase stability, densification behaviour, microstructure, and ultimately electrochemical performance. By investigating these degradation mechanisms throughout the entire process, we were able to demonstrate how processing-induced chemical changes in LLZO manifest as microstructural defects and performance fluctuations in the final separators.

A holistic understanding of process-induced LLZO degradation enabled us to identify critical processing steps responsible for irreversible lithium loss and to develop rational, process-compatible mitigation strategies. The systematic investigation of individual process steps in the production of tape-cast LLZO separators described in Chapter 4 revealed that LLZO undergoes significant protonation during wet ball-milling, which impairs processability and separator quality in subsequent steps. By adding excess Li_2CO_3 at selected processing steps as a lithium re-lithiation strategy, lithium loss could be effectively counterbalanced while maintaining a simplified and scalable fabrication route. This enabled the production of dense, flat LLZO separators with high ionic conductivity and stable lithium stripping/plating behaviour using significantly reduced excess lithium.

Building on these findings, we were able to take a step further and develop a tape-casting process for the fabrication of freestanding, Ni-rich NMC composite cathodes with high CAM loading for LLZO-based solid-state batteries as described in Chapter 5, thereby, representing the first reported fabrication of freestanding Ni-rich NMC/LLZO composite cathodes via tape casting. The integration of NMC with LLZO during ceramic processing is inherently difficult due to their limited thermal and chemical compatibility,

as this promotes interfacial reactions and the formation of resistive secondary phases during co-sintering. To counteract this, composite cathodes were processed at reduced temperatures using Li_3BO_3 as a sintering aid and systematically designed with and without LLZO to disentangle the functional role of the catholyte phase. By correlating cathode chemistry with electrochemical performance and explicitly separating the contributions of ionic and electronic transport, we were able to demonstrate that the performance of NMC cathodes fabricated via tape-casting is more strongly determined by the balance between ionic and electronic conductivity than by the incorporation of solid electrolytes alone.

This work establishes clear relationships between process, structure and performance for LLZO-based separators and Ni-rich NMC composite cathodes produced in a tape casting process and provides experimentally grounded guidelines for the development of thin layer components for oxide-based solid-state battery suitable for mass production.

Kurzfassung

Granat-$Li_7La_3Zr_2O_{12}$ (LLZO) ist ein keramisches Material, das sich durch eine hohe Lithiumionenleitfähigkeit und ein breites elektrochemisches Stabilitätsfenster auszeichnet und damit einen vielversprechenden Festkörperelektrolyten für Festkörperbatterien (SSBs) der nächsten Generation darstellt. Keramische Membranen aus LLZO sind vielversprechende Separatoren für Lithiummetall-SSBs, da sie chemisch stabil gegenüber Lithium sind und dem Wachstum von Lithiumdendriten widerstehen können. Die Kombination solcher Separatoren mit keramischen Verbundkathoden, die hochenergetische Kathodenaktivmaterialien (CAMs) und LLZO als Katholyt enthalten, würde die Herstellung keramischer SSBs mit hoher Energiedichte und vor allem hoher inhärenter Sicherheit aufgrund der Nicht-Entflammbarkeit des keramischen Elektrolyten ermöglichen. Zahlreiche Publikationen haben bereits die Machbarkeit und das Potenzial dieses Batteriekonzepts demonstriert. Um jedoch die vorteilhaften Eigenschaften von LLZO zu nutzen und die industrielle Attraktivität von LLZO-basierten SSBs zu steigern, müssen sowohl auf der Materialseite als auch auf der Prozessseite noch verschiedene Herausforderungen überwunden werden.

Eine der praktischen Herausforderungen besteht darin, LLZO-Komponenten mit optimierter Geometrie, Morphologie und Leistung mithilfe skalierbarer Produktionsprozesse herzustellen, was für die zukünftige Kommerzialisierung unerlässlich ist. Unter den verschiedenen Produktionsoptionen sticht die Foliengießtechnik als etabliertes Verfahren zur Großserienherstellung dünner keramischer Komponenten hervor. Bei diesem Verfahren werden großflächige Folien in einem kontinuierlichen Prozess aus einer Schlickermasse, die Keramikpulver und organische Additive enthält, gegossen und anschließend bei hohen Temperaturen gesintert, um freitragende keramische Schichten herzustellen. Die Foliengießtechnik hat sich als geeignetes Verfahren zur Herstellung von LLZO-Separatoren erwiesen; jedoch werden deren Qualität, Leistung und Reproduzierbarkeit häufig durch die Protonierung des feuchtigkeitsempfindlichen LLZOs während der Verarbeitung und den irreversiblen Lithiumverlust beim Sintern beeinträchtigt. Für die Herstellung leistungsstarker LLZO-Separatoren ist es daher wichtig, die Degradationsprozesse entlang der gesamten Produktionskette zu verstehen und Wege zur Minimierung von Protonierung und Lithiumverlust zu finden.

Neben Separatoren ist die skalierbare Herstellung keramischer Verbundkathodenschichten, insbesondere die Integration von Ni-reichem $LiNi_xMn_yCoz O_2$ (NMC) als CAM, für die Realisierung keramischer SSBs mit wettbewerbsfähigen Energiedichten von Bedeutung. Das Foliengießen von NMC/LLZO-Kathoden bleibt jedoch eine technische Herausforderung, da sowohl LLZO als auch NMC anfällig für prozessinduzierte chemische und interfaciale Degradation sind. Um diese Einschränkungen zu überwinden, konzentrierte sich diese Arbeit auf das Verständnis der Zusammenhänge zwischen Prozess, Struktur und Leistung sowie auf die Optimierung der Parameter des Foliengießprozesses für die Herstellung von LLZO-Separatoren und keramischen NMC-Verbundkathoden, um eine reproduzierbare und wirtschaftlich tragfähige Produktion von Batteriekomponenten mit verbesserter Leistung zu ermöglichen.

In Kapitel 3 wurden die Degradationsphänomene beim Foliengießen von LLZO-Separatoren untersucht, insbesondere die LLZO-Protonierung und der Lithiumverlust, die ihre Leistungsfähigkeit in Zellen erheblich beeinträchtigen. Obwohl beide Phänomene in der Literatur gut dokumentiert sind, wurden sie bisher außerhalb des Kontexts des Foliengießprozesses untersucht. Beim Foliengießen von LLZO sind Protonierung und Lithiumverlust jedoch untrennbar miteinander verbunden und treten in mehreren Prozessschritten auf, darunter Schlickervorbereitung, Mahlen, Trocknen und Sintern. Ihre kumulative Wirkung bestimmt die Phasenstabilität, das Verdichtungsverhalten, die Mikrostruktur und letztendlich die elektrochemische Leistung. Durch die Untersuchung dieser Degradationsmechanismen über den gesamten Prozess hinweg konnten wir zeigen, wie prozessinduzierte chemische Veränderungen in LLZO sich als mikrostrukturelle Defekte und Leistungsschwankungen in den fertigen Separatoren manifestieren.

Ein ganzheitliches Verständnis der prozessinduzierten LLZO-Degradation ermöglichte es uns, kritische Prozessschritte zu identifizieren, die für den irreversiblen Lithiumverlust verantwortlich sind, und rationale, prozesskompatible Gegenmaßnahmen zu entwickeln. Die systematische Untersuchung einzelner Prozessschritte bei der Herstellung von foliengegossenen LLZO-Separatoren, beschrieben in Kapitel 4, ergab, dass LLZO während des Nassmahl-Prozesses eine erhebliche Protonierung erfährt, die die Verarbeitbarkeit und Separatorqualität in den nachfolgenden Schritten beeinträchtigt. Durch die Zugabe von überschüssigem Li_2CO_3 an ausgewählten Prozessschritten als Relithiierungsstrategie konnte der Lithiumverlust effektiv ausgeglichen werden, während eine vereinfachte und skalierbare

Herstellungsroute beibehalten wurde. Dies ermöglichte die Herstellung dichter, flacher LLZO-Separatoren mit hoher Ionenleitfähigkeit und stabilem Lithium-Strippen/Plattieren-Verhalten unter Verwendung von deutlich reduziertem Lithiumüberschuss.

Aufbauend auf diesen Erkenntnissen konnten wir einen Schritt weitergehen und einen Foliengießprozess für die Herstellung freitragender, Ni-reicher NMC-Verbundkathoden mit hoher CAM-Beladung für LLZO-basierte Festkörperbatterien entwickeln, wie in Kapitel 5 beschrieben, und damit die erste berichtete Herstellung freitragender Ni-reicher NMC/LLZO-Verbundkathoden mittels Foliengießen darstellen. Die Integration von NMC mit LLZO während der keramischen Verarbeitung ist aufgrund ihrer begrenzten thermischen und chemischen Kompatibilität inhärent schwierig, da dies Grenzflächenreaktionen und die Bildung resistiver Sekundärphasen beim Co-Sintern fördert. Um dem entgegenzuwirken, wurden Verbundkathoden bei reduzierten Temperaturen unter Verwendung von Li_3BO_3 als Sinterhilfsmittel verarbeitet und systematisch mit und ohne LLZO ausgelegt, um die funktionale Rolle der Katholytphase zu entkoppeln.

Durch die Korrelation der Kathodenchemie mit der elektrochemischen Leistung und die explizite Trennung der Beiträge des Ionen- und Elektronentransports konnten wir zeigen, dass die Leistung von mittels Tape-Casting hergestellten NMC-Kathoden stärker vom Gleichgewicht zwischen Ionen- und Elektronenleitfähigkeit bestimmt wird als allein durch den Einbau von Festelektrolyten.

Diese Arbeit stellt klare Zusammenhänge zwischen Verfahren, Struktur und Leistung für LLZO-basierte Separatoren und Ni-reiche NMC-Verbundkathoden her, die im Tape-Casting-Verfahren hergestellt wurden, und liefert experimentell fundierte Leitlinien für die Entwicklung von Dünnschichtkomponenten für oxidbasierte Festkörperbatterien, die für die Massenproduktion geeignet sind.

À ma mère, ma première enseignante et celle de toute une vie, qui portait en elle le rêve de devenir docteure, mais à qui le destin a refusé ce chemin. Ce travail est le sien, la promesse tenue, et le témoignage de tout mon amour.

À toutes les femmes de ce monde qui, envers et contre toute circonstance, choisissent encore de se donner pour son progrès.

Et à tous les hommes qui ont cru en nous, et qui continuent, encore, de nous offrir leur amour.

La vie n'est pas juste pour tout le monde. Alors, à ceux qui gardent l'espoir malgré tout.

إِنْ أُرِيدُ إِلَّا ٱلْإِصْلَٰحَ مَا ٱسْتَطَعْتُ ۚ وَمَا تَوْفِيقِىٓ إِلَّا بِٱللَّهِ ۚ عَلَيْهِ تَوَكَّلْتُ وَإِلَيْهِ أُنِيبُ

« Je ne veux que la réforme, autant que je le puis. Et ma réussite ne dépend que d'Allah. En Lui je place ma confiance, et c'est vers Lui que je reviens repentant. »
Sourate Hûd, 11:88

List of abbreviations

AAM	Anode Active Material
ASSB	All-Solid-State Battery
BM	Ball Milling
BSE	Backscattered Electrons
CAM	Cathode Active Material
CBM	Conduction Band Maximum
CCD	Critical Current Density
CMC	Carboxymethyl Cellulose
CPE	Constant Phase Element
CV	Cyclic Voltammetry
CVD	Chemical Vapour Deposition
DEC	Diethyl Carbonate
DMC	Dimethyl Carbonate
DSC	Differential Scanning Calorimetry
EC	Ethylene Carbonate
EDS	Energy-Dispersive X-ray Spectroscopy
EIS	Electrochemical Impedance Spectroscopy
EMC	Ethyl Methyl Carbonate
ESW	Electrochemical Stability Window
EV	Electric Vehicle
FAST	Field-Assisted Sintering Technique

FID	Free Induction Decay
FT	Fourier Transformation
GCPL	Galvanostatic Cycling with Potential Limitation
GITT	Galvanostatic Intermittent Titration Technique
HP	Hot Pressing
IEA	International Energy Agency
LAGP	$Li_{1.5}Al_{0.5}Ge_{1.5}(PO_4)_3$
LATP	$Li_{1.3}Al_{0.3}Ti_{1.7}(PO_4)_3$
LBO	Li_3BO_3 (Lithium Borate)
LCO	$LiCoO_2$ (Lithium Cobalt Oxide)
LD	Laser Diffraction
LFP	$LiFePO_4$ (Lithium Iron Phosphate)
LIB	Lithium-Ion Battery
LiM-SSB	Lithium Metal Solid-State Battery
LIPON	Lithium Phosphorus Oxynitride
LLZO	$Li_7La_3Zr_2O_{12}$ (Lithium Lanthanum Zirconium oxide)
LLZTO	$Li_7La_3Zr_{2-x}Ta_xO_{12}$ (Ta-doped LLZO)
LMO	$LiMn_2O_4$ (Lithium Manganese Oxide)
LT-LLZO	Low-Temperature Cubic Phase of LLZO
MAS	Magic Angle Spinning
MCI	Mixed Conducting Interphase
NASICON	Sodium Superionic Conductor

NMC	$LiNi_xMn_yCozO_2$ (Lithium Nickel Manganese Cobalt Oxide)
NMC333	$LiNi_{0.33}Co_{0.33}Mn_{0.33}O_2$
NMC811	$LiNi_{0.8}Mn_{0.1}Co_{0.1}O_2$
NMP	N-Methyl-2-pyrrolidone
OCV	Open-Circuit Voltage
PAN	Polyacrylonitrile
PEG	Polyethylene Glycol
PEO	Polyethylene Oxide
PLD	Pulsed Laser Deposition
PSD	Particle Size Distribution
PVB	Polyvinyl Butyral
PVD	Physical Vapour Deposition
RC	Resistor-Capacitor
RF	Radiofrequency
SE	Secondary Electrons
SEI	Solid Electrolyte Interphase
SEM	Scanning Electron Microscopy
SPS	Spark Plasma Sintering
SS-NMR	Solid-State Nuclear Magnetic Resonance
SSB	Solid-State Battery
SSE	Solid-State Electrolyte
SSR	Solid-State Reaction

T_1	Spin-Lattice Relaxation Time Constant
T_2	Spin-Spin Relaxation Time Constant
TGA	Thermogravimetric Analysis
VBM	X-ray Diffraction

TABLE OF CONTENTS

Table of Contents ..... **XIII**

Motivation and objective **1**

1 Theoretical background of energy storage in batteries **5**

1.1 General principle of a battery 5

1.2 Battery Metrics and Battery Materials 7

1.3 Solid-state batteries 13

1.3.1 The concept of solid-state battery 13

1.3.2 Inorganic solid electrolytes 15

1.4 Solid-state batteries with LLZO electrolyte 18

1.4.1 LLZO solid ion conductor: crystalline structure 18

1.4.2 LLZO electrochemical stability 19

1.4.3 LLZO: chemical stability and protonation reactions 20

1.5 Fabrication of LLZO-based solid-state batteries 22

1.5.1 Architecture and design of LLZO-based SSBs 22

1.5.2 Selection of active electrode materials 24

1.5.3 Sintering of LLZO components 26

1.5.4 Processing methods for the fabrication of LLZO-based battery components 28

1.6 Tape casting of LLZO components: general introduction 32

2 Methodology and techniques **34**

2.1 Synthesis and fabrication methods 34

2.1.1 Solid-state reaction (SSR) 34

2.1.2 Powder pre-conditioning: Planetary ball milling 35

2.1.3 Tape casting 36

2.1.4 Sintering 37

2.2 Material Characterization 38

2.2.1 X-ray diffraction (XRD) analysis 38

2.2.2 Raman spectroscopy 39

2.2.3 Solid-state neutron magnetic resonance spectroscopy (SS-NMR) 40

2.2.4 Laser diffraction (LD) 43

2.2.5 Scanning electron microscopy (SEM) 44

2.2.6 Confocal white light microscopy 46
2.2.7 Thermo-analytical techniques 46
2.3 Electrochemical characterization techniques 48
2.3.1 Galvanostatic cycling with potential limitation (GCPL) 48
2.3.2 Critical current density (CCD) 49
2.3.3 Electrochemical impedance spectroscopy (EIS) 52
3 Tape Casting of LLZO Ceramic Separators: Overview of the Challenges and Optimization Strategies 57
3.1 Background and chapter scope 57
3.2 Manufacturing ceramic LLZO separators via tape casting 58
3.3 Main challenges during slurry fabrication 63
3.3.1 Treatment of LLZO powders for the fabrication of slurries 65
3.4 Main problems during the sintering step 67
3.4.1 Li loss at high temperature 67
3.4.2 Deformation of tapes during sintering and the influence of the sintering substrate 72
3.4.3 Integration of advanced sintering techniques 75
3.5 Post-Processing of Sintered Tapes 76
3.5.1 Optimization of the surface 76
3.5.2 Integration of tape-cast LLZO separators into the cells 79
3.6 Chapter summary 82
4 Minimising Lithium Loss in the Production of LLZO Separators via THE Tape-casting Process.....83
4.1 Background and chapter scope 83
4.2 Processing Route as a Determinant of LLZO Separator Quality 84
4.3 Optimization of Lithium Compensation Strategy via Li_2CO_3 Addition 88
4.3.1 Effect of Li_2CO_3 Addition Timing on LLZO Morphology and Phase Stability 88
4.3.2 Raman and NMR Investigation of Li_2CO_3-Mediated Protonation Suppression during Ball Milling .. 92
4.3.3 Process Refinement: Lowering Li_2CO_3 Addition during Ball Milling 95
4.4 Electrochemical Evaluation of Optimized LLZO Tape-Cast Separators 96
4.5 Chapter summary 98
5 Tape-Cast NMC-Based Composite Cathodes for Solid-State Batteries 100
5.1 Chapter background and scope 100
5.2 NMC composite cathode fabrication: 102

5.2.1 Tape casting process optimization 102
5.2.2 Sintering composite cathode 105
5.3 Structural analysis of composite cathode: 107
5.4 Electrochemical Evaluation of Composite Cathodes 111
5.5 Chapter summary 122
Conclusion and outlook 123
References 127
Appendix 153
Publications and presentations 164
Acknowledgement 167
Curriculum Vitae 169

MOTIVATION AND OBJECTIVE

Driven by the global ambition of achieving net-zero CO_2 emissions, batteries have become one of the key technologies enabling the clean-energy transition and complementing renewable generation from solar and wind power. While batteries do not generate electricity, they play a crucial role in storing, transporting, and redistributing energy. They stabilise power grids by storing excess renewable energy during periods of high generation and releasing it when production declines. In the transport sector, batteries power electric vehicles, ships, and potentially future aircraft, shifting away from combustion engines and eliminating of direct CO_2 emissions. According to the International Energy Agency (IEA)[1], batteries deployed in electric-vehicles (EV) and stationery-storage applications are directly responsible for nearly 20 % of the CO_2-emission reductions needed by 2030 and indirectly for another 40 % through the electrification of other sectors. Figure 0.1 shows the battery contribution in decreasing CO_2 emissions, which supports the transition toward a decarbonised energy system.

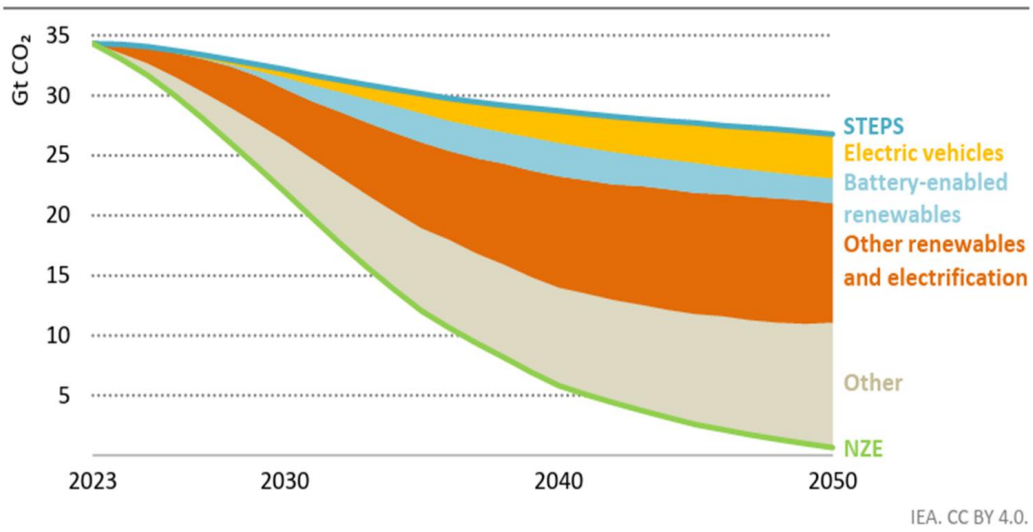


Figure 0.1|Avoided CO_2 combustion emissions linked to batteries and other technologies by scenario, 2023-2050. Reported from the International Energy Agency (IEA)[1]

As battery deployment scales rapidly to meet these climate and energy targets, the limitations of current lithium-ion battery technology become increasingly evident. Higher energy density, improved safety, faster charging capability, and long-term reliability are progressively required not only for extending driving range and reducing charging times, but also for enabling large-scale, dependable stationary energy storage. However, conventional LIBs based on liquid electrolytes are approaching their limitations in capacity and range (most electric vehicles provide ranges between 300 and 500 km per charge [4]), and safety limits [2,3], particularly with respect to thermal stability and electrode design. Consequently, further progress toward climate-neutral energy systems requires battery architectures that move beyond incremental improvements of existing technologies.

One of the serious limitations of conventional lithium-ion batteries is their reliance on flammable organic liquid electrolytes, which can trigger thermal runway, as evidenced by several incidents involving electric vehicles such as Tesla, Chevy Bolt, and other electric vehicles models[5]. On the other side, the implementation of lithium metal anodes, which offer a very high theoretical capacity (3860 mA h g^{-1})[6] and substantially higher energy density, is hindered in liquid electrolyte- based cells, since lithium metal tends to deposit unevenly during repetitive stripping/plating, forming filamentary or dendritic structures that can penetrate the separator and cause short circuits and fire. To address this problem, next-generation systems such as solid-state batteries (SSBs), in which the flammable liquid electrolyte is entirely or partially replaced by a solid component, have emerged as a promising alternative. The performance and reliability of SSBs are critically determined by the properties of the solid electrolyte. Among the various classes of solid electrolytes investigated to date, oxide-based electrolytes, particularly garnet $Li_7La_3Zr_2O_{12}$ (LLZO), have emerged as highly promising candidates. LLZO is a non-flammable solid oxide, has relatively high lithium-ion conductivity and high reduction stability against lithium metal[7]. However, favourable intrinsic properties alone are not sufficient to make LLZO based batteries competitive alternative. Unlike liquid electrolytes, which are directly injected into assembled cells, solid ceramic LLZO must be individually shaped, densified, and integrated as a structural separator component. On the cathode side, the rigid nature of LLZO prevents it from infiltrating the electrode; ionic connectivity must therefore be engineered directly into the cathode by co-sintering the cathode active material (CAM) and the solid electrolyte into a dense, three-dimensionally (3D) percolating ceramic composite layer. Accordingly, realising these components at scale demands fabrication methods that are technically capable and importantly industrially and economically viable.

Tape casting is a wet-coating process in which powders are dispersed into slurries and cast into thin, free-standing films is industrially established in lithium-ion battery manufacturing and adopted in thin ceramic component production for electronics and semiconductor application[8]. It has been recently adopted for producing LLZO solid electrolyte layers and composite cathodes[9–13], demonstrating its feasibility as a scalable processing route for oxide-based solid-state batteries.

However, the multi-stage workflow of ceramic tape casting including slurry preparation, casting, and sintering exposes LLZO to chemical and thermal environments that trigger degradation through interconnected mechanisms: protonation, in which Li^+ ions are exchanged for H^+ upon contact with moisture or protic solvents, and lithium volatilisation at elevated sintering temperatures. Both generate lithium-deficient, poorly conducting phases that compromise sinterability, ionic conductivity, and electrochemical performance[14–16]. On the cathode side, elevated sintering temperatures potentially drive chemical reactions between LLZO and the cathode active material, forming resistive secondary phases that further impair cell performance [15–17]. Although individual aspects of the LLZO challenges have been reported, their cumulative propagation across the full tape-casting production chain and their interdependencies had not been investigated prior to this work. Production of 3D composite cathodes for LLZO solid state batteries by tape casting and sintering have been reported to other relatively low-capacity cathodes like $LiCoO_2$ (LCO)[9,11] but not yet for Ni-rich $LiNi_xMn_yCoz_2$ (NMC) CAM.

The objective of this thesis is to advance the tape-casting fabrication of LLZO-based solid-state battery components by identifying systematic relationships between process, structure, and performance that enable reproducible and scalable production of high-quality separators and composite cathodes.

Specifically, this work pursues the following objectives:

- Systematic analysis of the degradation mechanisms of LLZO protonation and lithium loss that occur throughout the entire tape-casting process chain for LLZO separators, as well as determining how these mechanisms are interrelated and cumulatively affect separator quality and electrochemical performance
- Identification of the critical processing step responsible for LLZO protonation, as well as the development of a process-compatible mitigation strategy that enables the compensation of lithium loss and reproducible fabrication of dense, flat, free-standing LLZO separators with competitive electrochemical performance

- Integration of a tape-casting process for the fabrication of thick, free-standing Ni-rich NMC composite cathode for LLZO-based solid-state batteries by optimizing slurry formulation, sintering compatibility, and the microstructural challenges specific to this material system.
- Investigation of the electrochemical performance in tape-cast NMC composite cathodes as a function of their chemistry through systematic examination of the role of LLZO and decoupling of the contributions of ion and electron transport

1 THEORETICAL BACKGROUND OF ENERGY STORAGE IN BATTERIES

This chapter covers the theoretical background relevant to the scope of the thesis. It describes the basic operating principles of electrochemical battery cells and provides an overview of current lithium-ion batteries and solid-state batteries, with a particular focus on LLZO-based components, their design, and their fabrication.

1.1 General principle of a battery

A battery is a device composed of one or more electrochemical cells connected in series and/or in parallel, designed to convert chemical energy into electrical energy (and vice versa) through redox reactions. Each electrochemical cell contains two electrodes at which oxidation and reduction reactions take place, with the electrons involved in the reaction transferred via an external circuit. By convention, the electrode at which oxidation occurs and thereby releases electrons to the external circuit is called the anode (the negative electrode in a battery during discharge), and an electrode at which reduction occurs by accepting electrons from the external circuit is called the cathode (the positive electrode in a battery during discharge). The electrodes should be electrically separated from each other to prevent short circuits while simultaneously allowing ion conduction between them; this is ensured by a battery separator. In batteries with liquid electrolytes, the separator is a porous layer of insulating material (e.g., polymers or paper) infiltrated with the liquid electrolyte. In SSBs, separators may consist of a dense layer of solid electrolyte. The difference in electrochemical potential between the anode and the cathode generates a thermodynamic driving force that causes ions to migrate internally through the electrolyte and electrons to flow externally through the circuit, thereby generating an electric current.

Batteries are generally classified into primary batteries (non-rechargeable) and secondary batteries (rechargeable). In primary batteries, the electrochemical reactions are irreversible. Once the redox reactions at the electrodes are complete, the cell cannot be restored to its original chemical state. In contrast, in secondary batteries, the redox reactions at both electrodes can be reversed by reversing the polarity of the electrodes via an external electrical current, thereby enabling multiple charge-discharge cycles. Following Planté's invention of the lead-acid batteries[17], several secondary batteries, such as Ni-Cd, Ni-MH, Ni-Zn, and eventually Li-ion batteries, have been introduced[18]. The first rechargeable lithium battery was developed by M. Stanley Whittingham at Exxon in 1972. In this battery, the layered

titanium disulfide (TiS_2) was used as the cathode and metallic lithium as the anode[19]. However, the reactivity of metallic lithium caused dendrite formation and thermal runaway, leading to several safety incidents and the eventual withdrawal of these cells from the market[20]. This limitation redirected research toward inventing safer electrode materials that could reversibly insert lithium ions through intercalation mechanism instead of using metallic lithium. The discovery of intercalation-type (or insertion-type) electrode materials, such as layered $LiCoO_2$ cathode[21] and graphite anode, enabled the development of stable lithium-ion batteries commercialized by Sony in 1991[22], marking the beginning of the modern Li-ion battery (LIB) era. Intercalation-type materials adopt layered crystal structures in which strongly bonded atomic layers are stacked and held together by weak van der Waals forces. The resulting interlayer van der Waals gaps provide the structural space into which Li^+ ions can be reversibly inserted and extracted during charge and discharge, inducing only minor and reversible changes in the lattice parameters, leaving the host framework structurally intact ensuring high structural stability and long cycle life of the electrode materials during several hundred charge/discharge cycles [23]. Figure 1.1 illustrates a conventional Li-ion battery cell in discharge.

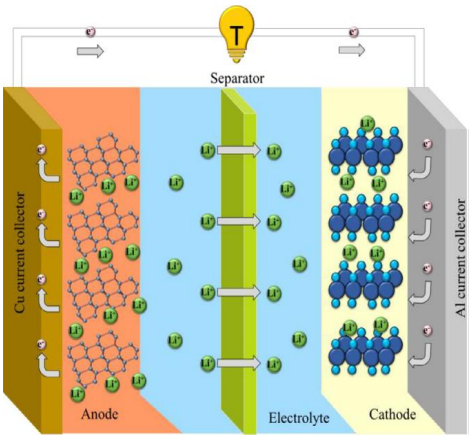


Figure 1.1|Schematic representation of a conventional Li-ion battery set-up and its working principle during discharge. Reprinted from ref[225]. Copyright Elsevier Ltd (2022).

During charging, Li^+ ions are deintercalated from the layered $LiCoO_2$ cathode and migrate through the electrolyte toward the graphite anode. To maintain charge neutrality in the cathode, the extraction of Li^+ is accompanied by the oxidation of Co^{3+} to Co^{4+} according to the following reactions:

Cathode reaction: $LiCoO_2 \rightleftharpoons Li_{1-x}CoO_2 + xLi^+ + xe^-$ Equation 1.1

Anode reaction: $C_6 + xLi+ + xe^- \rightleftharpoons Li_xC_6$ Equation 1.2

During discharge, the reverse reaction occurs spontaneously, in which Li^+ ions migrate from the anode back to the cathode through the liquid electrolyte, while electrons flow through the external circuit to release electrical energy.

1.2 Battery Metrics and Battery Materials

The overall performance of a battery is determined by fundamental electrochemical and physical parameters.

The cell voltage (E), measured in volts (V) is the difference of electrochemical potentials of the cathode and the anode, which drives the flow of electrons (electrical current) (Equation 1.3)[17]:

$$E_{cell} = E_{Cathode} - E_{Anode} \quad \text{Equation 1.2}$$

The electrochemical potential represents the Gibbs free energy per unit charge. The term “potential” is generally used for individual electrode materials, while “voltage” typically applies to a full cell. The equilibrium potential is the potential of the electrode reaction in equilibrium state (without net current flow). It is determined by the standard potential of the redox process (E^0), the activity (concentration) of the redox species , and the temperature according to the Nernst equation (Equation 1.4):

$$E = E^0 + \frac{RT}{zF} ln \frac{a_{Oxidized}}{a_{Reduced}} \quad \text{Equation 1.4}$$

where *R* is the universal gas constant, *T* is the absolute temperature, *z* is the number of electrons exchanged, *F* is Faraday’s constant, and *a* is *the* activity of the redox species involved. The standard potential E^0 is the potential measured under standard conditions (e.g., 25 °C, 1 atm, and unit activity of all electroactive species) and is thermodynamically related to the standard Gibbs free energy of the

respective redox reaction. The difference between the equilibrium potentials of the electrodes (or the voltage of a cell at equilibrium, e.g., no net current flowing) is referred to as open-circuit voltage (OCV).

The capacity (C) of a battery or an electrode material is the total amount of electrical charge that can be reversibly stored or released. Specific capacity is expressed per unit mass (gravimetric capacity, C_{Grav}) or per unit volume (volumetric capacity, C_{Vol}) and measured in ampere-hours per gram (Ah g^{-1}) or ampere-hours per litre (Ah L^{-1}), respectively. The theoretical gravimetric capacity can be calculated using Equation 1.5[17]:

$$C_{Grav} = \frac{zF}{M} \qquad \text{Equation 1.5}$$

where *z* is the number of electrons exchanged per formula unit, *F* is Faraday's constant, and *M* is the molar mass of the active material. The volumetric capacity C_{Vol} is then obtained by multiplying C_{Grav} by the material density (ρ).

The energy density ($E_{Density}$) of a battery or an electrode material is the total stored energy per unit mass, referred as gravimetric energy density, measured in watt-hour per kilogram, (Wh kg^{-1}) or per volume, referred as volumetric energy density, measured in watt-hours per litre, (Wh L^{-1}). It is determined by the product of the specific capacity (gravimetric or volumetric) and the cell voltage (for a battery) or the electrode potential (for an electrode material), as shown in Equation 1.6[24]

$$E_{Density} = C_{Grav}\, E \qquad \text{Equation 1.6}$$

Another important performance metric is power density, which indicates how quickly energy can be delivered or consumed. Power density is the product of the current (*I*) and the voltage (*E*) of the cell[17]; it therefore depends not only on thermodynamic properties but also on the kinetics of the processes. The specific power density (P_{grav}), measured in watts per kilogram (W kg^{-1}), is obtained by normalizing the power density to the total mass (m), as described by Equation 1.7, or the volume (v) to calculate volumetric power density (P_{vol}), which is measured in watts per litre (W L^{-1}):

$$P_{Grav} = \frac{I\,E}{m} \qquad \text{Equation 1.7}$$

Power density is influenced by intrinsic properties of materials, such as their electronic and ionic conductivities, by properties of various interfaces, such as contact resistance or resistance of interfacial charge transfer, as well as by design factors at cell level, including electrode thickness, porosity, and

interfacial contact area[25]. Electrode thickness, in particular, has a significant impact on battery performance. Thinner electrodes offer shorter charge transport paths and lower polarization losses, enabling higher power density; however, their lower loading of active material limits areal capacity and energy density. Conversely, thicker electrodes allow for higher capacity and energy density but suffer from sluggish ion diffusion and increased internal resistance[26]. Therefore, achieving optimal performance requires a balance between electrode thickness, electrode microstructure and interfacial design to ensure efficient ion transport and mechanical integrity across the entire cell architecture[27–29].

The energy and power densities can be estimated at the material level using only weight or volume of the active materials (cathode and anode), which are useful in academic studies to evaluate intrinsic properties. They can be calculated also at the cell or pack level; for that, the weight (or volume) of all components, including electrolyte, separator, current collectors, casing, and safety systems should be included into calculation[30,31].

In addition to power density, the performance of a battery is typically characterized by rate capability expressed by the C-rate, which defines the applied current relative to the nominal capacity of the cell[32]. It indicates the rate at which a maximum capacity of a battery can be charged or discharged and is mathematically expressed by Equation 1.8:

$$C_{rate} = \frac{I}{C_n} \qquad \text{Equation 1.8}$$

where I is the applied current (A) and C_n is the nominal capacity of the cell, typically expressed in ampere-hours (Ah). A rate of 1 C corresponds to a complete charge or discharge within one hour, while 0.5 C and 2 C represent operation at half and double the rate, respectively.

Among the existing battery technologies, Li-ion batteries offer the most favourable metrics (Figure 1.2), which explains their steadily growing market dominance in key application areas such as portable electronics and electric vehicle markets.

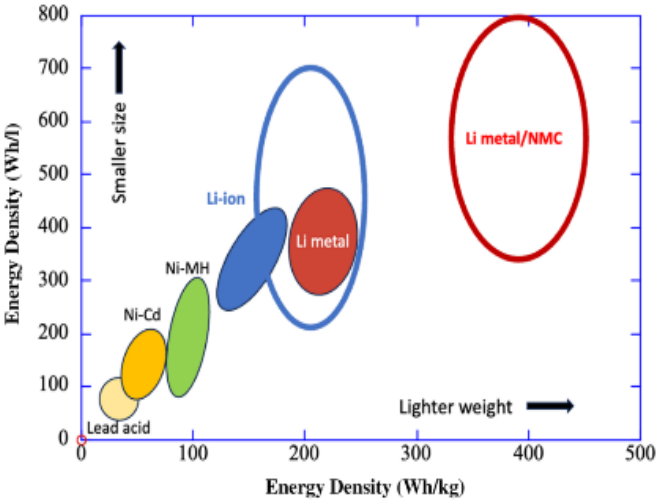


Figure 1.2| Comparison of energy density of different battery chemistry.[50]

State-of the-art LIBs mainly use graphite as anode active material (AAM) due to its low electrochemical potential (0.02 Vs Li/Li^+)[33], high reversibility, and mechanical stability during cycling[34]. Cathode active materials (CAMs) generally belong to three main families: (i) layered oxides such as $LiCoO_2$ (LCO) and $LiNi_xMn_yCoz O_2$ (NMC), (ii) spinel oxides (e.g., $LiMn_2O_2$), and (iii) olivine phosphates (e.g., $LiFePO_4$). Important performance metrics of cathode materials are summarized in Table 1.1[35–37]. These compounds contain redox-active transition-metal cations (M^{n+}) capable of undergoing rapid and reversible redox reactions with lithium at high potentials[35].

Table 1.1| Potential vs Li/Li^+ and specific capacity of most common CAMs for LIBs. Adopted from[35]

Material type	Composition	Potential vs Li/Li^+	Specific capacity ($mAh.g^{-1}$)
Layered	$LiCoO_2$ (LCO)	3.9	140
	$LiNi_{1-x}Co_xMn_yO_2$ (NMC)	4.3	160-200
	$LiNi_{0.8}Co_{0.15}Al_{0.05}O_2$ (NCA)	3.8	180-200
Spinel	$LiMn_2O_2$ (LMO)	4.1	100-120
Olivine	$LiFePO_4$ (LFP)	3.5	150-170

Typical electrolytes for LIBs contain lithium salt such as $LiPF_6$, $LiClO_4$, or $LiBF_4$ dissolved in a mixture of organic carbonate solvents such as ethylene carbonate (EC), dimethyl carbonate (DMC), diethyl carbonate (DEC) or ethyl methyl carbonate (EMC)[38]. These liquid electrolytes provide high ionic conductivity at room temperatures (~10^{-3}-10^{-2} S cm^{-1})[39], a relatively wide electrochemical stability window, and good wettability of electrode surfaces which facilitate efficient ion transport and allows straightforward integration into established battery manufacturing processes. However, the liquid electrolytes have several drawbacks that limit both safety and performance of current LIBs. Organic electrolytes begin to decompose at high positive potentials (e.g., those of high-voltage cathodes) and low negative potentials (such as the potential of lithium metal anodes)[33], thereby limiting the practical electrochemical window and the energy density[40]. At low anode potentials, the electrolyte undergoes reductive decomposition at the anode surface, producing a solid electrolyte interphase (SEI). On graphite anodes, a stable and electronically insulating SEI is essential for passivating the electrode surface and preventing continued electrolyte decomposition. However, its continuous reformation across cycles leads to the accumulation of resistive interface formation[41], which increases the ohmic resistance of lithium ions intercalation into the graphite anode, consequently promoting lithium plating on the electrode surface. The Li plating promotes the formation of Li filaments (known as Li dendrites) that can pierce the separator or form electrically isolated "dead lithium**"** that can shuttle between the electrodes, potentially causing short circuit and fire. This problem is further exacerbated in the case of lithium metal anode, where the SEI is inherently unstable due to the large volume changes leading to uneven Li dissolution and plating over multiple charge/discharge cycles. The electrolyte instability at low potentials prevents the practical use of lithium metal, despite its exceptionally high theoretical capacity. On the cathode side, charging to a high positive potential can trigger the oxidation of lattice oxide ions in the transition metal oxide structure, leading to oxygen release. This can initiate highly exothermic reactions

that may escalate into catastrophic cell failure through thermal runaway[42]. Furthermore, the decomposition of $LiPF_6$ salt can release acidic by-products (HF) that attack the CAM, dissolve transition metals, promote their migration to the anode, where they accelerate SEI degradation and electrolyte decomposition. These parasitic reactions progressively deteriorate cell performance and further destabilize the SEI, intensifying the degradation mechanisms described above and jeopardizing the safety[43]. The safety hazard is further intensified by the inherent flammability of organic electrolytes, which severely restricts the deployment of LIBs in demanding applications such as aerospace systems, high-power electric vehicles, and grid-scale energy storage in extreme climates. Possible failure mechanisms and fire risk in conventional LIBs are illustrated in Figure 1.3. Given these limitations, research efforts have increasingly shifted toward employing solid-state electrolytes (SSEs), which offer superior thermal stability, a wider electrochemical stability window, and, in many cases, compatibility with lithium metal anodes, thereby enabling higher energy densities and substantially improved safety.

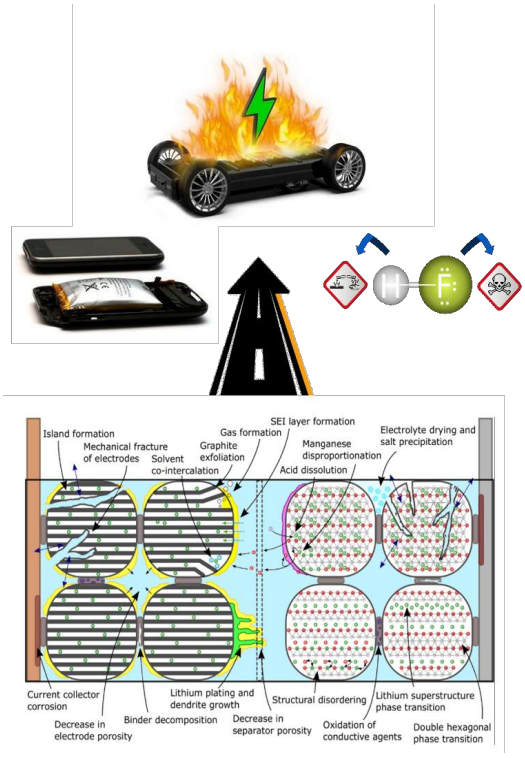


Figure 1.3|Scheme illustrating the different degradation scenario and their consequences. Adapted from[226] with permission. Copyright Elsevier (2016).

1.3 Solid-state batteries

1.3.1 The concept of solid-state battery

Solid-state batteries (SSBs) are electrochemical battery cells in which all components, including the electrolyte, anode, and cathode, are predominantly solid. The key difference from conventional Li-ion batteries is the replacement of the flammable liquid electrolyte with a solid electrolyte material, which must fulfil the same fundamental functions: simultaneously conducting charge carriers (Li^+ ions in lithium-based systems) while preventing electric contact between the anode and cathode. The transition to a solid electrolyte is expected to address many of the inherent limitations of liquid-based batteries, particularly with respect to safety, and operational temperature range, making SSBs more resilient under conditions where liquid electrolytes would decompose or evaporate. Beyond improved safety, solid electrolytes, particularly solid oxides, open up the possibility of using lithium metal as the anode, which is a significant step toward higher energy density. Lithium metal offers a very high theoretical capacity (3860 mAh g^{-1}) and low redox potential (−3.04 V vs. SHE)[44]. Its implementation in a solid-state cell architecture could raise energy density at the cell level to as high as 400 Wh kg^{-1} and 800 Wh l^{-1}, compared to about 260 Wh kg^{-1} and 770 Wh l^{-1} for state-of-the-art conventional LIBs[45] . As shown in Figure 1.4, replacing the graphite anode with lithium metal in lithium-metal solid-state batteries (LiM-SSBs) leads to a substantial increase in energy of approximately 40 % in gravimetric and 70 % in volumetric energy density.

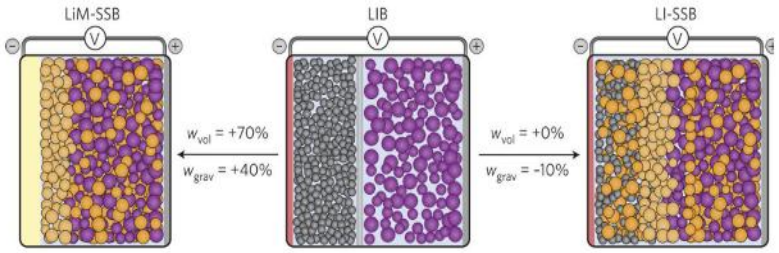


Figure 1.4| Schematic representations of lithium-ion (LIB), lithium-metal-solid-state (LIM-SSB), and lithium-ion-solid state batteries (LI-SSB). Reprinted from ref[45] with permission. Copyright Springer Nature (2016).

To replace liquid electrolytes effectively, a solid electrolyte must exhibit high ionic conductivity along with strict electronic insulation as well as good chemical and electrochemical stability with respect to both electrodes. Solid electrolytes can be classified into three main categories**:** organic, inorganic, and composite electrolytes, each of which presents specific advantages and challenges. Organic electrolytes, such as polyethylene oxide (PEO)[46], polyvinylidene fluoride (PVDF)[47], and polyacrylonitrile (PAN)[48], offer mechanical flexibility and ease of processing but exhibit low ionic conductivity at room temperature (10^{-9}-10^{-6} S cm^{-1}), strong temperature dependence of conductivity, and limited oxidation stability[46], making them unsuitable for use with high-voltage cathodes[25]. Inorganic solid electrolytes including oxides, sulfides, and halides generally have inherent mechanical rigidity; however, they offer higher conductivity at room temperature (10^{-4}-10^{-2} S cm^{-1})[28], and better thermal tolerance and stability. Composite electrolytes, which combine organic and inorganic phases, generally exhibit better mechanical flexibility than pure inorganic electrolytes and higher ionic conductivity than pure polymer electrolytes, but often face challenges related to interfacial incompatibility, phase separation, and long-term stability[49]. The key properties of representative solid electrolytes from each category are summarised in Figure 1.5. The work of this thesis is focussed on inorganic electrolytes class and, in particular, on oxide-based garnet $Li_7La_3Zr_2O_{12}$ (LLZO) electrolyte. Thus, the next section provides a more detailed overview of inorganic electrolytes properties and a detailed description of LLZO properties.

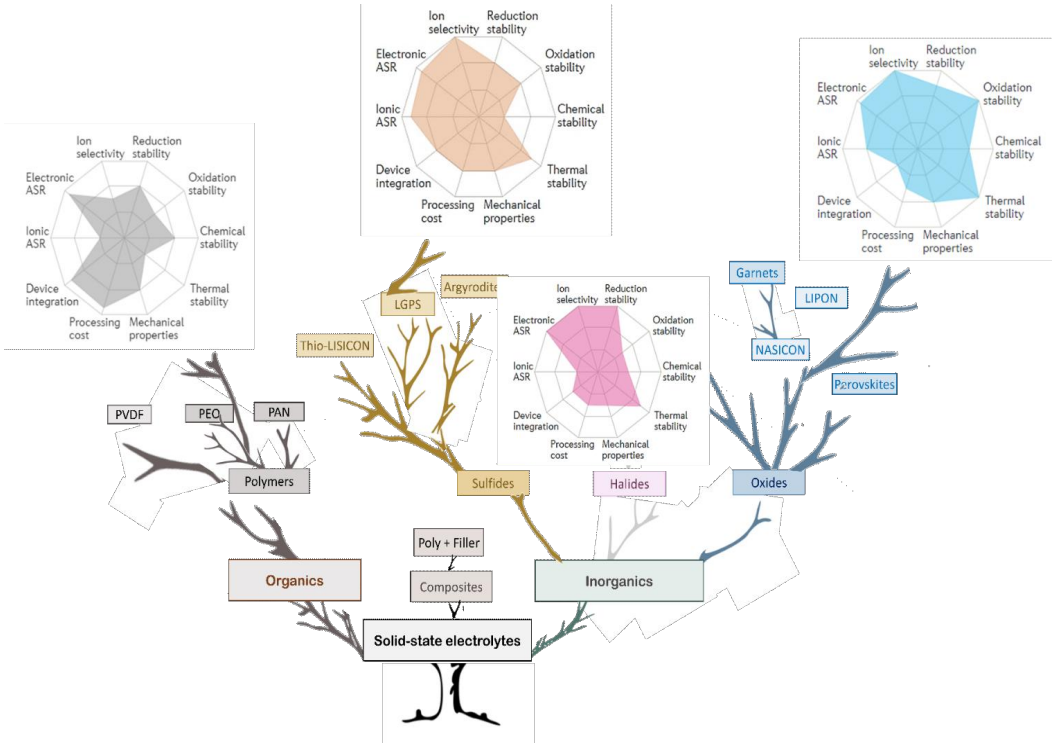


Figure 1.5| Family tree of solid-state electrolytes together with radar plots performance, which are adapted from ref[54] with permission. Copyright Springer Nature (2017).

1.3.2 Inorganic solid electrolytes

Inorganic solid electrolytes are crystalline solids or amorphous frameworks, where ion conduction occurs via a hopping mechanism[50]. In this process, Li^+ ions migrate through thermally activated hops between energetically favourable lattice sites, such as interstitial or vacant positions (Figure 1.6a). The ionic conductivity of a solid electrolyte follows Arrhenius behaviour[51] (Equation 1.9):

$$\sigma = \sigma_0 \exp\left(-\frac{E^a}{k_B T}\right) \qquad \text{Equation 1.9}$$

where σ is the ionic conductivity, σ_0 is the pre-exponential factor, E_a is the activation energy for ion migration, k is the Boltzmann constant, and T is the absolute temperature. Ion hopping occurs when Li^+ acquires sufficient thermal energy to overcome the migration barrier *(E_a),* enabling migration along

interconnected diffusion pathways within the crystal lattice (Figure 1.6b,c). The magnitude of E_a depends strongly on the crystal symmetry, bottleneck size (the radius of the diffusion channel), and the electrostatic interaction between mobile ions and the host lattice[51]. In polycrystalline inorganic solid electrolytes, the total ionic conductivity reflects contributions from both the bulk (grain interior) and grain boundaries. Grain boundaries typically exhibit higher activation energies and represent a significant source of ionic resistance that must be minimised by material densification[39,52].

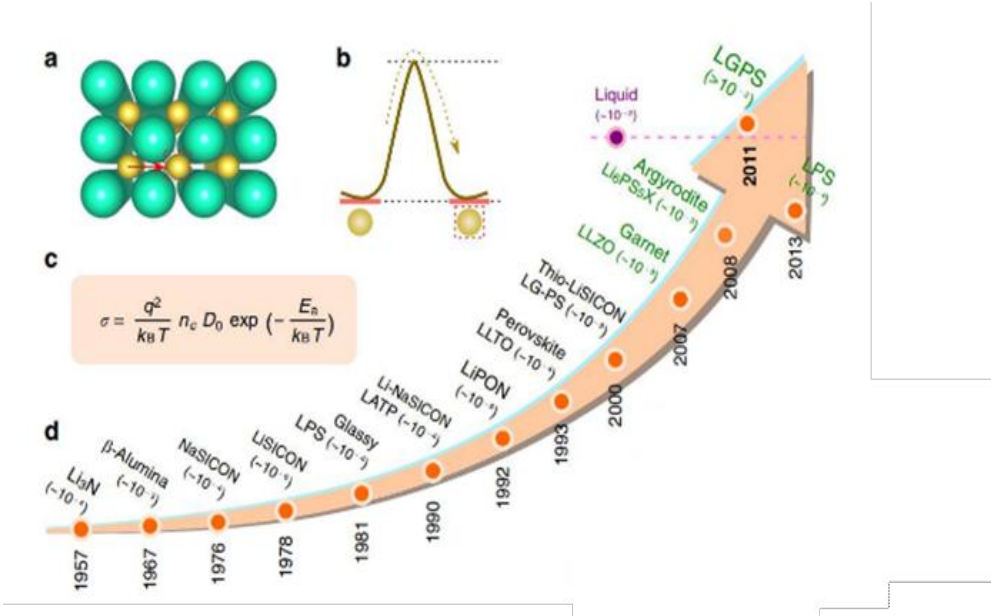


Figure 1.6| (a and b) ions hopping between adjacent sites in the crystal structure; (c) the equation of the ionic conductivity and example of most favourable migration path for ions; (d) the chronological evolution of the Li-ion conductivity in solids.[50].

Ion conduction in solids was first observed in 1914 in silver iodide (AgI) and later followed by the discovery of fast lithium-ion conductors such as Li_3N (1957) and β-alumina (1967)[50]. Figure 1.6d shows the chronological discoveries of inorganic Li-ion conductors.

For a long time, the main limitation of inorganic solid electrolytes was their lower ionic conductivity compared to liquid electrolytes. However, extensive research has led to the development of several families of inorganic solid electrolytes exhibiting competitive ionic conductivities. Among the most intensively studied are perovskites, garnets, Na-superionic conductors (NASICON), sulfides, argyrodites,

lithium phosphorus oxynitride (LIPON), and halides. Among these, sulfides such as $Li_{10}GeP_2S_{12}$ (LGPS) have demonstrated the highest ionic conductivities of ~10^{-2} S cm^{-1} [53] that approach and even exceed those of liquid electrolytes. However, sulfide-based electrolytes exhibit a very narrow thermodynamic stability window, poor chemical stability at electrode interfaces, and moisture sensitivity with the release of toxic H_2S gas upon air exposure[53]. This poses significant challenges for large-scale processing and raises serious safety concerns[54,55]. Compared to sulfides, the garnet-type $Li_7La_3Zr_2O_{12}$ (LLZO) exhibits high chemical stability, a broad electrochemical stability window (ESW), and, in particular, excellent reduction stability against lithium metal, combined with sufficiently high ionic conductivity of up to 2.10^{-3} S cm^{-1} at room temperature[56]. These properties collectively make LLZO one of the most promising candidates for the development of safe, high-energy-density SSBs employing lithium metal anodes and define the main motivation for its selection as the focus of this thesis. Figure 1.7a,b provides a comparative overview of the ionic conductivities and ESWs of the most studied inorganic solid electrolytes.

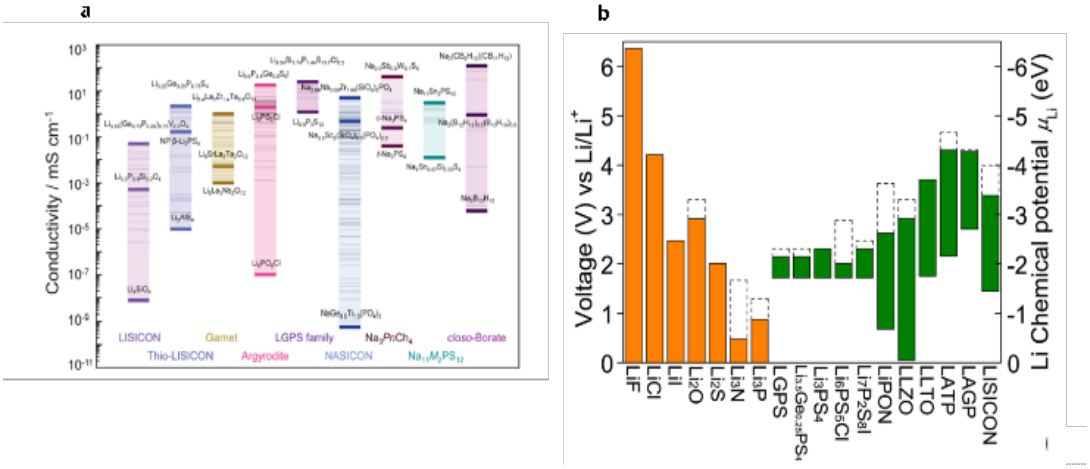


Figure 1.7| (a) Comparison of the indicative ionic conductivities of inorganic solid electrolytes. Reprinted from ref[28]. Copyright Publishing Ltd (2020); (b) theoretical electrochemical stability window of the available inorganic solid electrolytes. Reprinted From ref[227].Copyright American Chemical Society (2015).

1.4 Solid-state batteries with LLZO electrolyte

1.4.1 LLZO solid ion conductor: crystalline structure

$Li_7La_3Zr_2O_{12}$ (LLZO) belongs to the family of garnet oxides, which have the general formula $A_3B_2C_3O_{12}$, where A, B, and C are cations occupying dodecahedral (8-fold), octahedral (6-fold), and tetrahedral (4-fold) coordination sites, respectively. The garnet-type LLZO structure was first described in 2007 by Murugan et al. *with an ionic activity of* 10^{-4} S cm^{-1} [57]. Subsequent studies showed that LLZO exists in two crystallographic structures: the cubic and the tetragonal phases, with the tetragonal phase demonstrating two orders of magnitude lower conductivity (10^{-6} S cm^{-1})[58,59]. In cubic LLZO, lithium ions occupy partially 24d tetrahedral and 96h octahedral sites (with a total of 7 Li^+ per formula unit), forming a three-dimensionally interconnected disordered network that facilitates rapid Li^+ transport. In contrast, tetragonal LLZO, exhibits a more ordered arrangement of lithium ions and longer distances between adjacent Li^+ sites, which restricts ionic motion and accounts for its lower conductivity[58] (Figure 1.8).

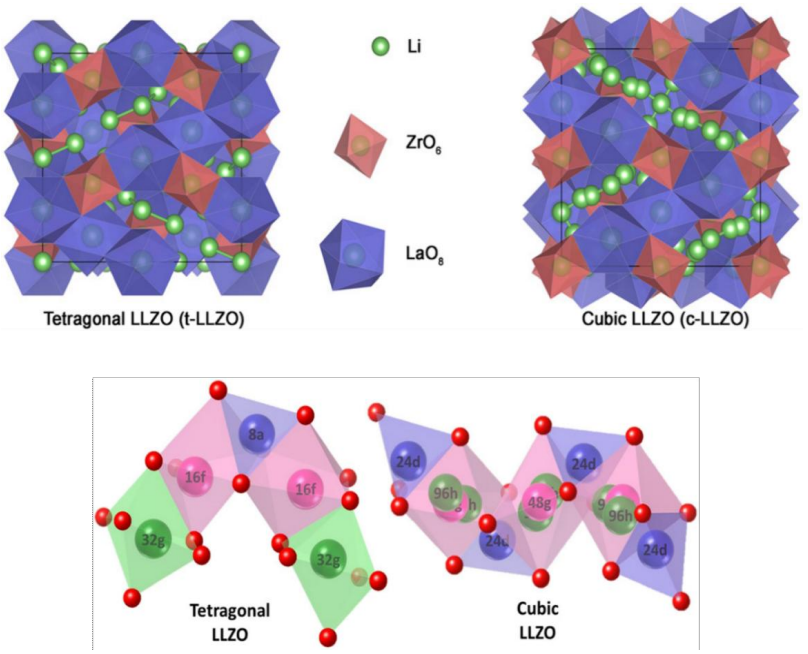


Figure 1.8|Structure of tetragonal and cubic LLZO along (100) plane, together with the Li position in both cases. Reprinted from ref[188].Copyright Royal Society of Chemistry (2024).

The cubic LLZO phase is thermodynamically unstable at room temperature and transforms to the tetragonal phase upon cooling, with the tetragonal-to-cubic transition occurring at 645 °C[58,60]. However, researchers have demonstrated that doping with aliovalent cations such as Al^{3+} [60] can stabilize the cubic phase at lower temperatures by introducing lithium vacancies that suppress the long-range Li^+/vacancy ordering responsible for the tetragonal distortion. Extensive efforts have been realised to optimise the cubic phase stability and ionic conductivity of LLZO through site-specific doping at Li, La, and Zr sites including Ga^{3+} and Al^{3+} at the Li site, and Ta^{5+} and Nb^{5+} at the Zr site[59,61,62]. Substitution at the Zr site with higher-valence cations (e.g., Ta^{5+}, Nb^{5+}) introduces lithium vacancies to maintain charge neutrality, increasing the concentration of available hopping sites and reducing the activation energy for Li^+ migration, thereby enhancing ionic conductivity. In this thesis, co-substitution of Al^{3+} at the Li site and Ta^{5+} at the Zr site is employed as a dual doping strategy for the used LLZO. This approach simultaneously stabilises the cubic phase at room temperature and enhances ionic conductivity.

1.4.2 LLZO electrochemical stability

The electrochemical stability window (ESW) of LLZO solid electrolyte defines the range of lithium chemical potentials (μLi) over which the electrolyte is thermodynamically stable without undergoing reduction or oxidation. If the electrochemical potential of lithium at the anode lies below the lower stability limit of the electrolyte, lithium is driven into the electrolyte, leading to its reduction and the formation of a lithium-rich interphase at the anode-electrolyte interface, accompanied by vacancy depletion and a positive space-charge region. Conversely, if the electrochemical potential of the cathode exceeds the upper stability limit of the electrolyte, oxidation occurs, producing a lithium-poor interphase at the cathode-electrolyte interface, with vacancy accumulation and a negative space-charge region (Figure 1.9a). Early experimental studies reported that LLZO remains kinetically stable within an apparent electrochemical window of up to 5-6 V vs. Li/Li^+[63,64]. However, first-principles calculation narrows this down to 2.91 V vs. Li/Li above which LLZO can decompose into secondary phases such as $La_2Zr_2O_7$, Li_2ZrO_3, and La_2O_3[65] (Figure 1.9b). This window stability can extend to approximately 3.6 V vs. Li/Li^+ when the kinetics of decomposition are considered[65]. On the anode side, the LLZO has a low reduction potential (~0.05 V vs Li/Li^+) and a high decomposition reaction energy (~49 kJ mol^{-1} at 0 V Li/Li^+)[66], which

kinetically inhibits electrolyte reduction and ensures that LLZO remains electrochemically stable when in direct contact with the lithium anode.

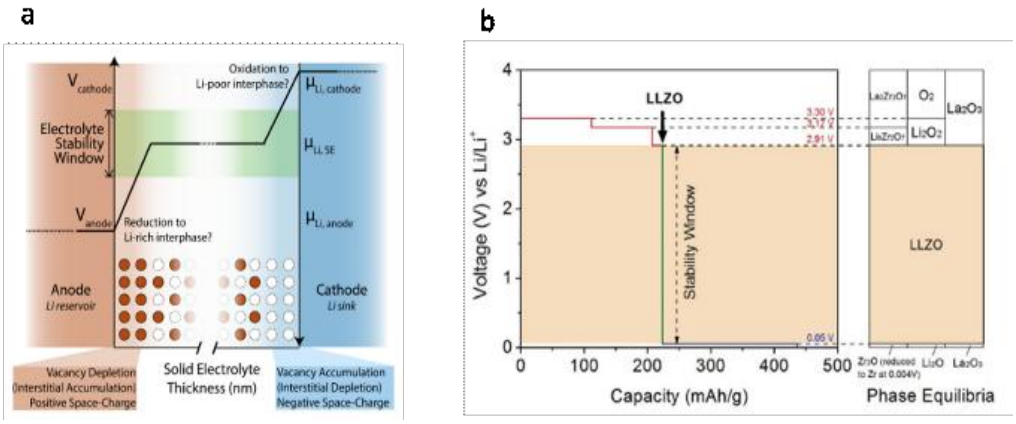


Figure 1.9| (a) Scheme of the evolution of the chemical potential across the solid electrolyte in contact with anode and cathode. Reprinted from ref[228]. Copyright Springer Nature (2019); (b) the first principal calculation results of the voltage profile of LLZO SE upon lithiation and delithiation. Reprinted from ref [65]. Copyright Wiley-VCH (2016).

1.4.3 LLZO: chemical stability and protonation reactions

As an oxide, LLZO exhibits good thermodynamic stability. However, its surface is sensitive to water[67] (including moisture[68–72]), carbon dioxide,[73] and protic solvents[3]. This sensitivity is attributable to lithium-proton exchange, also known as protonation. In the presence of CO_2, protonation leads to the formation of Li_2CO_3 in a two-step process, which is energetically favourable ($\Delta G < 0$) and thus proceeds spontaneously (Figure 1.10a). When exposed to humidity or protic solvents, an exchange of Li^+ ions for H^+ ions take place at the surface of LLZO, resulting in formation of LiOH, which subsequently reacts with CO_2 from the atmosphere to form Li_2CO_3 on the LLZO surface according to Equation 1.10 and 1.11 [68,72,74].

$$Li_7La_3Zr_2O_{12} + xH_2O \rightleftharpoons Li_{7-x}H_xLa_3Zr_2O_{12} + xLiOH \qquad \text{Equation 1.10}$$

$$LiOH + ½\ CO_2 \rightleftharpoons ½\ H_2O + ½\ Li_2CO_3 \qquad \text{Equation 1.11}$$

The protonation of LLZO was initially observed under aging conditions involving exposure to air and humidity during storage[35,40]. Later studies by Kun et al. and *Grissa et al.* extended these findings and demonstrated that a similar degradation occurs when LLZO interacts with polar and protic solvents,

including water and alcohols[75,76]. Furthermore, Nie et al. demonstrated that protonation can also occur with solvents such as N-Methyl-2-pyrrolidone (NMP)[77], which is commonly used in the preparation of slurries for electrode coating. In all cases, the degradation proceeds via the same mechanism, which is triggered by Li^+/H^+ exchange as illustrated in Figure 1.10.

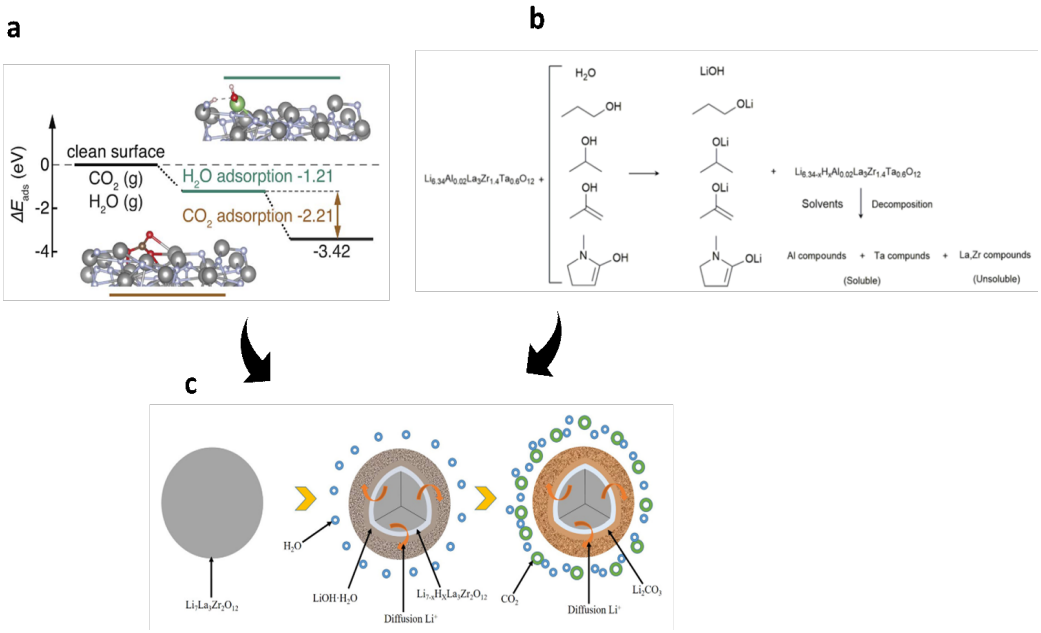


Figure 1.10|(a) An illustration of the LLZO surface decomposition and Li_2CO_3 formation via protonation: Absorption energy diagram of protonation steps with negative calculated absorption energies. Reproduced from[229] with permission. Copyright Royal Society of Chemistry (2022); (b) reaction mechanisms of LLZO protonation with different solvents. Reported from[77] with permission. Copyright American Chemical Society (2021); (c) a macroscopic illustrating the Li_2CO_3 formation on LLZO surface via protonation. Reproduced from[70] with permission. Copyright Wiley-VCH (2017)

The degree of reaction varies from solvent to solvent due to the different Brønsted acidity of the hydrogen atoms in these compounds (Figure 1.10b). The stronger the acidity of a solvent, the more intense the protonation. Water and alcohols react more vigorously due to their high acidity and protic nature, resulting in the formation of impurity layers, predominantly Li_2CO_3, on the LLZO surface and depletion of Li from the LLZO lattice (Figure 1.10c). The degree of protonation increases with increasing temperatures[78,79], humidity [70], and duration of exposure[78,79]. Deep protonation leads to an increase

in lattice parameters as the O-Li bond is replaced by the O-H bond. Consequently, the ionic conductivity of LLZO decreases due to the depletion of charge-carrying Li^+ ions from the lattice and the formation of less conductive phases such as hydrated LLZO (LLZO:H), LiOH, and Li_2CO_3[14–16,80]. Garnet protonation has been observed with various dopants (Al, Ta, Nb, Sn)[16,81–85]. To date, however, neither a clear correlation between the type of dopant and the protonation rate has been established, nor has any doping strategy successfully prevented this degradation pathway, including the Al^{3+} and Ta^{5+} co-substituted LLZO investigated in this thesis.

Structural studies have shown that proton exchange primarily involves lithium ions occupying the octahedral sites (48g and 96h) in the LLZO lattice[84] likely due to the higher mobility of Li ions in these sites, making them more susceptible to exchange with protons from the surrounding medium. This degradation pathway is particularly critical from a process engineering perspective. LLZO is initially handled in powder form and subsequently processed into solid electrolyte components; during these steps, it is inevitably exposed to solvents and ambient humidity conditions under which protonation readily occurs. Since protonation alters both the surface and bulk properties of LLZO, including wettability, sinterability, and ionic conductivity, it represents a critical processing challenge with direct consequences for the performance of LLZO-based solid-state cells. The implications of protonation for LLZO powder processing and the strategies employed to mitigate it are examined in detail in Chapter 3.

1.5 Fabrication of LLZO-based solid-state batteries

1.5.1 Architecture and design of LLZO-based SSBs

The overall configuration of a SSB must be carefully designed to ensure the highest possible performance. It is important to note that while the solid electrolyte is crucial for lithium-ion conduction, it does not contribute to cell capacity. Consequently, the electrolyte thickness must be minimized so as not to compromise the overall energy density. Since LLZO has a relatively high density of ~5.1 g cm^{-3}[57], the separator layer should be as thin as possible to minimise its weight. In addition, free-standing separator layers should be dense, flat and mechanically robust. Insufficiently densified LLZO layers with microstructural porosity do not exhibit sufficient tolerance for the penetration of Li dendrites[86]. Furthermore, surface impurities and secondary phases on the LLZO separator reduce its chemical compatibility with lithium metal, while cracks and defects create localised current density hotspots that

promote localized lithium deposition, thus dendrite growth.[87] To enable maximum performance, the LLZO separator must have a high relative density (>97%), a uniform microstructure, and good interfacial adhesion to lithium[86,88]. The densification of LLZO powders is achieved through a sintering process[89,90], which represents a crucial step in the manufacture of LLZO-based components, as further detailed in chapter 3.

Another important aspect is the microstructure of the cathode layer. Unlike liquid electrolytes, which can infiltrate the porous cathode to establish ionic contact, solid LLZO cannot penetrate the cathode layer. Therefore, the cathode must be engineered as a dense three-dimensional (3D) composite structure[9,91,92] that incorporates a solid-electrolyte phase (often referred to as the catholyte) with the cathode active material (CAM)[9,91,92]. To achieve efficient ion transport across the entire electrode thickness, a balanced ratio between the active material and the solid electrolyte is required[93,94]. Furthermore, good interfacial contact between the two phases is essential, which can be achieved by sintering powders at high temperatures; however, this can promote chemical interdiffusion and interfacial reactions between the LLZO and the CAM, which may degrade both ionic conductivity and electrochemical performance. The thickness and architecture of the 3D composite cathode are critical for the balance between the energy density and rate capability of the cell. If it is too thin, the limited CAM loading restricts the areal capacity; if it is too thick, longer lithium-ion diffusion pathways and increased resistance cause polarisation and kinetic losses[94]. A possible structure of an oxide-based SSB is illustrated schematically in Figure 1.11.

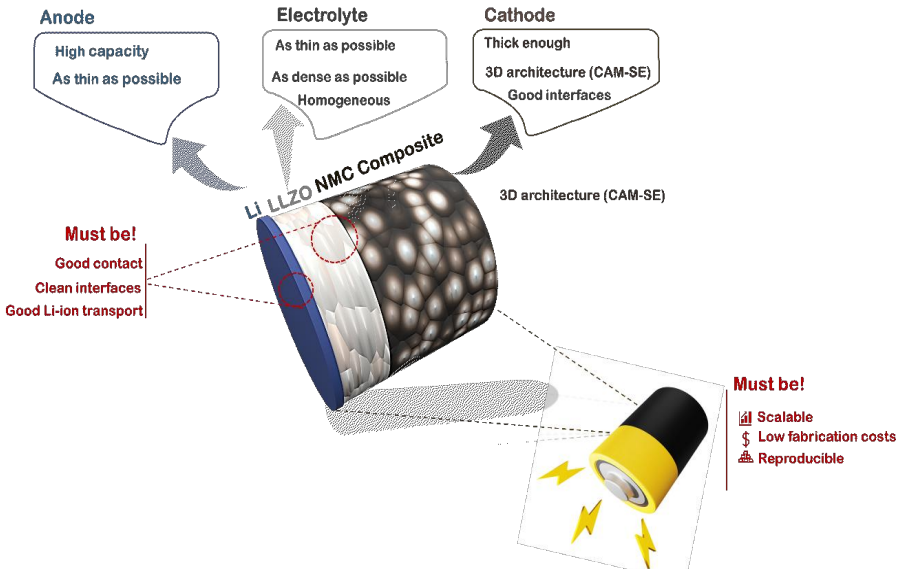


Figure 1.11 | Illustration of an optimal solid-state battery design and requirement

1.5.2 Selection of active electrode materials

As discussed above, an important advantage of LLZO is its high reduction stability, which enables the use of Li metal anodes[36]. Several studies have experimentally demonstrated that LLZO can form a stable interface with lithium metal in various solid-state cell configurations[9,24,95,96]. Despite thermodynamic compatibility, wetting of the LLZO surface with Li metal is often poor, leading to high resistance at the Li/LLZO interface[97]. This problem can be effectively addressed by cleaning the LLZO surface from Li_2CO_3 impurities through acid treatment or thermal annealing, or by employing interfacial engineering strategies, such as coating with thin lithium-aluminium alloy (Li-Al)[98] or ZnO[99] interlayers. These layers improve wetting, reduce interfacial impedance, and enhance the homogeneity of current density across the contact area. As a result, symmetric Li/LLZO/Li cells demonstrated stable cycling over hundreds of hours and achieved critical current densities (CCDs) of up to 1 mA cm^{-2} [100]. Through further optimisation of the LLZO separator morphology, symmetric Li/LLZO/Li cells have been cycled at CCDs of up to 100 mA cm^{-2}[10] , confirming the suitability of Li/LLZO solid electrolyte for next-generation high-energy density oxide-SSBs. Accordingly, lithium metal is used as the anode material in all cell configurations investigated in this thesis.

On the cathode side, most of the CAMs originally developed for liquid-electrolyte LIBs remain theoretically applicable for solid-state systems, provided they are compatible with LLZO and exhibit sufficient structural stability under the processing and operating conditions. To maximise energy density, high-voltage CAMs such as $LiNi_{0.8}Mn_{0.1}Co_{0.1}O_2$ (NMC811), which can achieve a practical capacity of 200 mAh g^{-1} [101], should be targeted. $Li[Ni_{1-x-y}Mn_xCo_y]O_2$ (NMC) has become the dominant cathode material in modern LIBs, offering significant advantages over $LiCoO_2$ (LCO). Structurally, both NMC and LCO crystallise in the layered α-$NaFeO_2$-type structure with $R\bar{3}m$ symmetry, where lithium ions occupy the octahedral 3a sites and transition metals (Ni, Co, Mn) reside in the 3b sites[101], as shown in Figure 1.12. This layered framework allows Li-ion diffusion in two dimensions within *ab-planes*, ensuring high ionic mobility and supporting efficient charge transfer during operation. In LCO, the reversible capacity is limited by structural instability arising when more than half of the lithium is extracted ($x > 0.5$ in $Li_{1-x}CoO_2$), which triggers a hexagonal-to-monoclinic phase transition, and promote oxygen release from the lattice at higher degrees of delithiation[37]. By substituting cobalt with nickel and manganese, NMC significantly expands the range of reversible lithium extraction. Nickel contributes significantly to redox activity through $Ni^{2+}/N^{3+}/Ni^{4+}$ redox pairs and enables higher theoretical capacities, while cobalt improves electronic conductivity and structural ordering. Although manganese is electrochemically inactive, it improves structural and thermal stability by reducing cation disorder and stabilising the layered arrangement during high-voltage operation[35,37]. Increasing the nickel content improves the specific capacity by allowing a larger fraction of lithium to participate in the redox process, thereby raising the practical capacities to over 200 mAh g^{-1}, compared to ~140 mAh g^{-1} for LCO[35]. However, Ni-rich NMC compositions, such as NMC811, exhibit poor thermal stability induced by oxygen release at temperatures as low as 150 °C. The released oxygen reacts exothermically with the solvent and trigger thermal runaway[35–37]. This hazard can be substantially mitigated when non-flammable oxide solid electrolytes such as LLZO are employed. The present work therefore investigates the integration of NMC811 as the cathode material in LLZO-based solid-state cells, targeting both the enhanced energy density afforded by high-capacity Ni-rich compositions and the improved thermal safety enabled by the non-flammable oxide solid electrolyte.

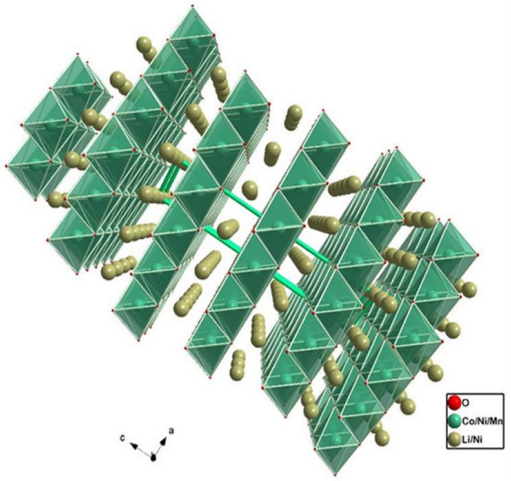


Figure 1.12 | Crystal structure of layered NMC, space group R-3m. Reprinted from[230].

1.5.3 Sintering of LLZO components

Sintering is a thermal consolidation process in which a powder compact is transformed into a dense, cohesive solid through thermally activated atomic transport, without full melting of the material. The driving force for sintering is the reduction of the total free energy of the systems. This promotes atomic diffusion along energy gradients, progressively eliminating porosity and consolidating the powder compact into a single dense solid body[102]. Important mechanisms of mass transport include surface diffusion, grain boundary diffusion, and lattice (bulk) diffusion, each of which contributes differently to neck formation and densification. While surface diffusion primarily promotes neck growth without significant densification, grain boundary diffusion and lattice diffusion enable pore reduction and overall densification of the ceramic network[103] (Figure 1.13). Sintering can be performed using different techniques including conventional (pressureless) sintering, which is typically performed in furnaces under controlled atmospheres, or fast advanced techniques such as field-assisted sintering techniques (FAST), which involve applying uniaxial pressure and pulsed current to accelerate densification, thereby producing high-density ceramics in shorter processing times[92,102,104,105].

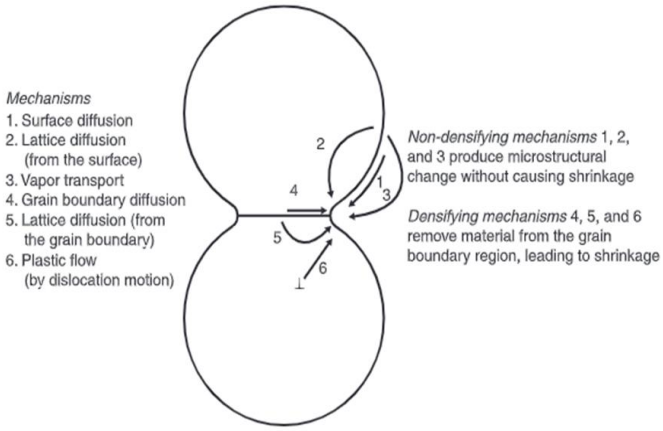


Figure 1.13|Schematic representation of the sintering mechanism. Reprinted from[231] with permission. Copyright Elsevier Inc (2003).

In the fabrication of LLZO-based SSBs, sintering is an essential step in the process. It enables the densification of the ceramic LLZO powder compact into a mechanically robust, pore-free solid electrolyte layer. For the 3D composite cathode, sintering establishes the intimate solid-solid contact between the CAM and the catholyte particles necessary to form a continuous, three-dimensionally interconnected ionic network throughout the electrode volume.

LLZO is typically sintered at temperatures above 1000 °C [106,107] at which undesirable processes such as the evaporation of lithium and the formation of secondary phases (e.g., $La_2Zr_2O_7$ or Li_2ZrO_3)[90,108–110] may also occur. These issues are generally mitigated by adding excess lithium precursors (e.g., Li_2CO_3, LiOH) to compensate for volatilisation during the sintering process[16,111,112]. Sintering becomes even more challenging in the production of composite cathodes, as it involves simultaneous densification of two chemically distinct phases, under conditions that must preserve the structural and electrochemical integrity of both. At the temperatures required for LLZO sintering, most CAMs undergo structural degradation in the presence of LLZO, leading to the formation of secondary phases[113–115]. The reaction at high temperature includes either elemental interdiffusion at the CAM/LLZO interface[113], driven by high cation mobility at elevated temperatures, or by the formation of new decomposition phases, typically at the interfaces [52,94]. In both cases, these reactions degrade the ionic and electronic transport properties of the composite cathode and impair electrochemical performance, as evidenced by

numerous published studies[24,113,115–117]. Ren et al. investigated the thermal stability of various CAMs relative to LLZO and reported that $LiFePO_4$ (LFP) exhibits the poorest thermal compatibility and reacts with LLZO at temperatures as low as 500 °C, whereas with $LiNi_{0.33}Co_{0.33}Mn_{0.33}O_2$ (NMC333), the formation of secondary phases begins at higher temperatures of around 700 °C. In contrast, $LiCoO_2$ (LCO) remains stable up to approximately 1050 °C [118], which explains why LCO remains the most commonly employed cathode with LLZO despite its moderate capacity and relatively lower operating voltage compared to Ni-rich NMC. A practical strategy to enable the co-sintering of two phases is to add a supplementary component (sintering aid) that lowers the sintering temperature and accelerates sintering via a liquid-phase sintering mechanism, or melts at relatively low temperatures, wetting both LLZO and NMC particles and promoting interfacial bonding. This strategy has already been demonstrated for thin NMC-LLZO composite cathode layers deposited on thick LLZO pellets[96,119]. However, the fabrication of freestanding NMC composite cathodes has so far been scarcely researched and documented in the literature, representing one of the central fabrication challenges addressed in this thesis.

1.5.4 Processing methods for the fabrication of LLZO-based battery components

Given the design requirements outlined above, the fabrication of LLZO-based SSBs must rely on processing methods capable of producing thin, dense electrolyte layers and composite cathode layers with precise thickness control[26]. The thick LLZO pellets (300 µm-1 mm) commonly used in laboratory research[64,91,113,116,119] are not a viable option, as they reduce energy density, introduce additional ohmic resistance, and are not scalable. Studies by Rupp et al.[120] demonstrated that achieving competitive energy and power densities in oxide-based SSBs can be achieved by the fabrication of thin LLZO layers with high ionic conductivity and uniform microstructure free of cracks and secondary phases. Current processing methods for manufacturing solid-state battery components cover a wide range of thicknesses, ranging from submicrometric vacuum-deposited layers (30 nm-1.8 µm) to wet-chemically deposited layers (50 nm-10 µm), and tape-cast layers (25-150 µm) to sintered pellets (300 µm-1 mm), as shown in Figure 1.14.

Physical vapour deposition (PVD) techniques such as magnetron sputtering, vacuum evaporation, and pulsed laser deposition (PLD) enable the production of very thin LLZO layers, but are limited by low deposition rates (typically a few nm to min), and by the high volatility of lithium during deposition, which can lead to the formation of lithium-poor or lithium-free phases (e.g., $La_2Zr_2O_7$, Li_2ZrO_3) with low ionic conductivity[121–123].

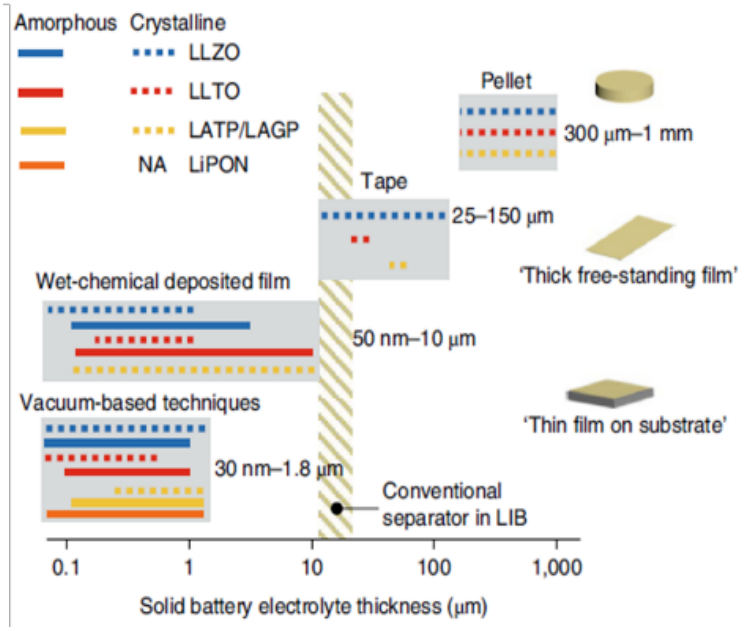


Figure 1.14| Illustration of solid-solid battery electrolyte thicknesses enabled by different fabrication techniques. Reprinted from[120] with permission. Copyright Nature Energy (2021).

Chemical vapor deposition (CVD) enables the conformal deposition of very thin layers with atomic-scale control, but is also limited by slow throughput, the challenging lithium precursor chemistry, and the need for high-temperature post annealing to achieve sufficient crystallinity[121,123]. Solution-based methods (spin-coating, sol-gel) are simpler and scalable but generally result in porous layers that require further densification at high temperatures[124,125]. The principal advantages and limitations of the thin-film deposition methods are summarised in Table 1.2[120]. While PVD and CVD processes are effective on a laboratory scale, they are constrained by low throughput, high capital cost, and restricted deposition areas, rendering them poorly evaluated using industrial manufacturing metrics. Nevertheless, these thin-film deposition methods are inherently limited to the deposition of single-phase layers which,

cannot incorporate the mixed ionic-electronic composite architecture required for 3D composite cathodes (e.g., a thin cathode layer of $LiCoO_2$)[126,127], making them unsuitable for the cathode configurations targeted in this thesis. Schnell and Tietz[26] identified wet coating processes such as tape casting as more realistic for the large-scale production of oxide-based SSBs and predicted that cell-level costs for garnet-based systems could fall below US$150 kWh^{-1}, provided that solid electrolytes cost decrease sufficiently. Against this backdrop, the high throughput and cost-efficiency of tape casting make this method a viable approach for the fabrication of LLZO solid electrolytes and composite cathodes with controlled thickness, homogeneity, and densification in line with the design requirements discussed earlier.

Table 1.2| Summary of advantages and disadvantages of thin film deposition for Li-oxide films. Form ref[120]

Thinn film deposition		Examples methods	Advantages	Disadvantages	Thicknesses	Materials deposited
Wet chemical methods		•Sol-gel •Spray pyrolysis •Spin coating	• Easy to adjust lithiation degrees • Ability to scale up for large-scale production • No vacuum chamber needed and low cost • Low temperature to form desired phases	• Difficult to control film roughness and thickness • Complicated chemistry and multiple parameters affect film deposition • Drying process needs to be carefully controlled to prevent film rupture • Time consuming to develop two- or multication synthesis routes	Up to 10 µm	• $Li_7La_3Zr_2O_{12}$ • $Li_xLa_{1-x}TiO_3$
Vacuum-based methods	PVD	•Sputtering •PLD	• Ability to deposit out-of-equilibrium phases • High control of film thickness and surface roughness • Wide range of pressure and temperature available for film growth • Relatively easy to deposit for two- or multication oxide films (compared with wet-chemical methods)	• Vacuum chamber required and high operational cost •Usually less conformal surface coating • Difficult to prevent lithium loss during deposition	Up to a few micrometres	•LiPON •$Li_7La_3Zr_2O_{12}$ • $Li_xLa_{1-x}TiO_3$
	CVD	•ALD	• Low kinetic energy of deposited particles: reduced surface and film degradation during growth • Versatility of deposition chemistry • Excellent conformal coating • Ability to deposit on structure with high three-dimensional aspect ratio • Low deposition temperature	• Slow growth rate • High dependence of processing window on precursor volatility •Difficult for multication deposition • Challenging to control atomic concentration (Stoichiometry)	Up to a few micrometres	•$Li_7La_3Zr_2O_{12}$ • LiPON

1.6 Tape casting of LLZO components: general introduction

Tape casting is an established industrial process for production of thin layers from powders and offers numerous advantages in the production of free-standing ceramic layers: it does not require complex infrastructure, is scalable, can be performed continuously, and is relatively inexpensive. In a typical tape casting process, ceramic powder is mechanically dispersed in a solvent with a dispersant to stabilise the particles. Binders and plasticisers are added to create a viscoelastic slurry that can be cast onto a stationary or moving substrate to form a cohesive green tape (Figure 1.15). After drying, the green tape can be removed, shaped, and sintered into mechanically stable thin ceramic components. Tape casting offers a high degree of flexibility in controlling the thickness, microstructure, and properties of the resulting layers, and is suitable for the production of complex multilayer component architectures with different microstructures[8].

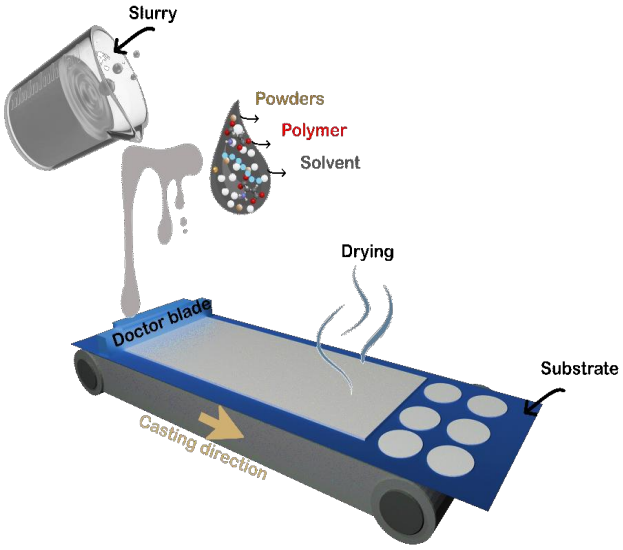


Figure 1.15| General illustration of film tape casting technique

Tape casting of LLZO-based battery components has gained increasing momentum since 2021, with several groups reporting slurry formulations and proof-of-concept cell demonstrations[12,16,128]. However, the reproducibility remains a central challenge because the tape cast workflow exposes LLZO to multiple sequential chemical and thermal environments, each altering the powder properties and influencing all subsequent stages, yet the cumulative impact on microstructure, phase composition and electrochemical performance has not been systematically addressed. On the cathode side, no tape-casting route had been demonstrated for thick, free-standing Ni-rich NMC-LLZO composite cathodes prior to this work, primarily due to the complexity of multi-component slurry formulation and the limited thermal compatibility between NMC and LLZO during co-sintering

This thesis addresses these gaps across three interconnected chapters. Chapter 3 provides a comprehensive process-chain analysis of LLZO tape casting, identifying the critical challenges at each stage and establishing the mechanistic framework required for reproducible separator fabrication. Chapter 4 focuses on the systematic investigation of protonation onset and progression throughout the process chain and introduces an in-situ Li_2CO_3 relithiation strategy that counterbalances protonation-induced lithium loss, enabling the reproducible fabrication of dense, flat, free-standing LLZO separators with competitive ionic conductivity and cycling stability in Li/LLZO/Li symmetric cells. Chapter 5 reports the first tape-casting a reproducible methodology for thick, high-loading, free-standing NMC composite cathodes, enabled by low-temperature co-sintering with Li_3BO_3 sintering aids, and establishes the design principles governing capacity and electrochemical performance in oxide-based composite cathodes.

2 METHODOLOGY AND TECHNIQUES

This chapter describes the experimental methods and characterization techniques used in this study, as well as the theoretical foundations required for their interpretation. Thermogravimetric analysis (TGA) was performed by Marie-Theres Gerhards (IMD-2), particle size distribution (PSD) measurements by Andrea Hilgers (IMD-2), and solid-state nuclear magnetic resonance (SS-NMR) by Dr. S. Swapna Ganapathy at Delft University of Technology. The LLZO synthesis was performed by Grit Häuschen and Tobias Lammert (IMD-2). All other experiments, data analysis, and interpretation were performed by the author.

2.1 Synthesis and fabrication methods

2.1.1 Solid-state reaction (SSR)

$Li_{6.45}Al_{0.05}La_3Zr_{1.6}Ta_{0.4}O_{12}$ (LLZO:Ta,Al) and Li_3BO_3 (LBO) powders were produced using solid-state reaction (SSR). This method involves high-temperature diffusion-driven reactions between solid precursors, typically oxides or carbonates, and is widely used for producing large batches of materials with high structural stability[129]. For LLZO powder production, stoichiometric amounts of $LiOH{\cdot}H_2O$ (Applichem, 99%), La_2O_3 (Merck, 99%) pre-dried at 900 °C for 10 h, ZrO_2 (Treibacher, 99.7%), Ta_2O_5 (Treibacher, 99.95%), and Al_2O_3 (Inframat, 99.82%) were used, with an additional 10 wt% LiOH to compensate for lithium volatilization during calcination. The precursors were homogenized using a planetary ball mill (PM 400, Retsch, Germany) and pressed into pellets, followed by second calcination at 850 °C for 20 h. The resulting material was crushed by a jaw crusher (BB 50, Retsch, Germany) and dry-milled in 250 ml tungsten carbide jars with 20 mm tungsten carbide milling balls at 200 rpm using a planetary ball mill (PM 400, Retsch, Germany) and subsequently sieved with a 50 µm mesh by using a vibratory sieving machine (Analysette 3, Fritsch, Germany). The obtained powder was pressed into pellets and calcined a second time at 1000 °C for 20 h. Afterwards, the pellets were crushed and dry-milled again. For Li_3BO_3, $LiOH{\cdot}H_2O$ (Applichem, 99%) and H_3BO_3 (Sigma Aldrich, >99.5%) were manually ground and homogenized in an agate mortar for 10 minutes. The resulting mixture was heated in an Al_2O_3 crucible in air to 650 °C with a heating rate of 5 K min^{-1} and a dwell time of 6 h.

2.1.2 Powder pre-conditioning: Planetary ball milling

The production of ceramic layers with controlled morphology using the tape casting process requires optimization of the particle size and particle size distribution (PSD). The particle size determines the stability of the slurry and the casting behaviour[130], furthermore, by influencing the compaction kinetics, it significantly affects the sintering process. Well-packed particles in the green tapes improve interparticle contact and shorten diffusion pathways during thermal treatment, thereby improving sinterability and increasing the relative density of the sintered tapes[103]. To achieve the desired particle size of the powder for slurry preparation, a high-energy planetary ball milling was employed. This technique uses jars that rotate around their own axes while simultaneously orbiting a central disk, generating strong centrifugal and Coriolis forces. These forces create repeated impact and shear forces between the milling balls and powder particles, leading to effective mechanical size reduction and mixing, as illustrated in Figure 2.1. The process also results in lattice strain and surface defects that can influence reactivity in subsequent steps[131].The efficiency of the milling process depends on milling speed, time, the materials of the balls and the jar, the medium (dry or wet), and the powder load. These variables determine the resulting particle size, morphology, and defect structure[131]. In our work, the milling parameters were selected based on experimental optimization. This work used three protocols: Dry milling of LLZO powder was performed using a Fritsch Pulverisette 7 at 500 rpm for 230 minutes in an 80 ml ZrO_2 jar with 3 mm ZrO_2 balls. Wet milling was carried out using the same parameters, using ethanol as the dispersion medium. The powder was then dried in air at 70 °C for at least 12 hours and annealed in an Al_2O_3 crucible at 750 °C for 2 hours (heating/cooling rate: 5 K min^{-1}) to remove organic components and restore crystallinity. For the NMC powder, milling was carried out in isopropanol using a 45 ml ZrO_2 jar and 3 mm balls at 750 rpm for 150 minutes. The powder was subsequently dried in air at 70 °C for at least 12 hours.

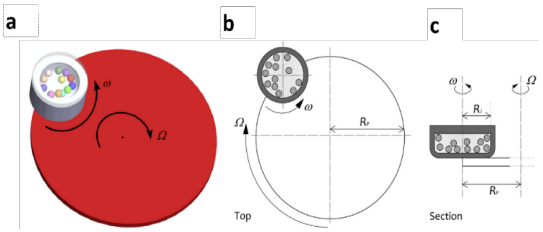


Figure 2.1|(a) Schematic representation of a planetary ball-mill; (b and c) three-dimensional view and definition of the jar radius Rj and the distance between axis of rotation (angular velocity ω) and revolution (angular velocity) Rp. Reprinted from ref[131]with permission. Copyright Elsevier (2016).

2.1.3 Tape casting

Tape casting is a wet processing technique for producing thin layers from a slurry containing powders, dispersants, binders, plasticizers and, if necessary, other additives dispersed in a suitable solvent. The slurry must be carefully optimized to achieve the required viscosity and ensure suitable rheological behaviour during casting. The slurry is applied using doctor blades with adjustable gaps to control the thickness of the deposited layers. In this study, two types of slurry formulations were developed: one for LLZO separators and another for the NMC composite cathodes (Table 2.1). Since prolonged exposure of the solvent to the powder surface can lead to protonation, the polymers (binder, dispersant and additives) were first dissolved in the solvent and homogenized at least for 12h to minimize the solvent's effect on LLZO and NMC.

To prepare the LLZO slurry, the LLZO powder was added to the pre-prepared polymer solution in a ratio of 1:0.6 and then homogenized using planetary mixer (ARE-250, Thinky, Japan) at 1500 rpm for 2 min. The resulting slurry was then cast on Mylar foil using a 450 µm doctor blade gap and allowed to dry for 2 to 3 hours. After drying, the green tapes were compacted and laminated at 80 °C for 2 minutes at 500 MPa, and then cut into discs with a diameter of 12 mm. For NMC-LLZO-LBO tapes, LLZO, NMC, and LBO powders were mixed in a weight ratio of 46:46:8. For NMC-LBO tapes, NMC and LBO were mixed in weight ratio of 92:8. The respective powder mixtures were then added to the polymer solution in a powder-to-solution ratio of 1.8:1 and homogenized using a planetary mixer (ARE-250, Thinky, Japan) at 1500 rpm for 2 min. The resulting slurries were cast onto Mylar foil using a doctor blade gap of 450 µm

and dried for at least 4 h at room temperature. The green tapes were laminated at 300 MPa and 60 °C for 2 min, after which 10-mm discs were punched out

Table 2.1| Slurry compositions of LLZO and NMC composite cathodes formulation.

	Powder (wt%)			**Binder solution (wt%)**					**(powder : binder solution) wt%**
Slurry System	LLZO (wt%)	NMC (wt%)	LBO (wt%)	Binder (type, wt%)	Solvent mixture (type, wt%)	Plasticizers (wt%) (type, wt%)		Dispersant (type, wt%)	
LLZO slurry	100	_	–	PVB (5.23)	EtOH:MEK (86.44)	PEG-400 (2.59)	TEG-EH (2.59)	BYK-180 (3.15)	1:0.65
NMC-LLZO-LBO slurry	46	46	8	CMC (7.07)	EtOH:MEK (84.74)	PEG-400 (3.76)	TEG-EH (3.76)	BYK-180 (0.7)	1.8:1
NMC-LBO slurry	_	92	8	CMC (7.07)	EtOH:MEK (84.74)	PEG-400 (3.76)	TEG-EH (3.76)	BYK-180 (0.7)	1.8:1

2.1.4 Sintering

Conventional sintering was used to densify LLZO separator tapes and free-standing NMC-based composite cathodes. The heat treatment serves to remove organic components and consolidate the ceramic particles through thermally activated densification, thereby establishing continuous particle-to-particle contact, which is necessary for efficient electrochemical operation. The sintering parameters were selected based on the thermal stability and phase behaviour of the respective material system. All heat treatments were carried out under unpressurized conditions in conventional furnaces with controlled heating and cooling rates. LLZO green tapes were sintered in Al_2O_3 crucibles. To minimize interfacial reactions and element transfer between the tapes and the crucible at high temperature, the samples were placed on an MgO plate and embedded in sacrificial mother powder of identical composition. The LLZO tapes were sintered at 1175 °C for 10 h in air, using heating and cooling rates of 5 °C min^{-1} to promote uniform grain growth and limit thermal stress. The NMC composite cathode green tapes were densified by liquid-phase sintering enabled by the presence of Li_3BO_3. Upon heating, LBO partially melts at temperatures well below the decomposition temperature of NMC, forming a transient

liquid phase that enhances mass transport, improves particle rearrangement, and promotes densification at reduced sintering temperatures. The cathode tapes were placed on a bed of starting powder on an MgO plate in an Al_2O_3 crucible and sintered for 45 min at 750 °C in pure oxygen, with intermediate dwell steps of 15 min at 200 °C and 600 °C, to ensure complete removal of organic components and controlled development of the microstructure.

2.2 Material Characterization

2.2.1 X-ray diffraction (XRD) analysis

X-ray diffraction (XRD) analysis is a non-destructive technique widely used to characterize crystalline materials in order to obtain information about their phase composition, phase purity, crystal structure, crystal orientation, and crystallite size. In this work, XRD analysis was used to investigate the phase composition and identify any impurities in the synthesized LLZO powder as well as in LLZO- and/or NMC-containing layers at various stages of the tape casting process.

XRD is based on the elastic scattering of monochromatic X-rays at the periodic atomic planes of a crystal (Figure 2.2a). When X-rays interact with a crystalline material, constructive interference occurs at specific angles, resulting in diffraction peaks that are characteristic of the material's atomic arrangement (Figure 2.2b)[132]. This behaviour is described by Bragg's Law:

$$n\lambda = 2d\sin\theta \qquad \text{Equation 2.1}$$

Where n is an integer, λ is the wavelength of the incident X-ray, d is the spacing between crystal planes, and θ is the incident angle. By scanning a range of θ angles, a diffraction pattern is obtained. Each phase exhibits a unique diffraction pattern, which enables the identification of the structure. X-rays are typically generated by the collision of accelerating electrons from a tungsten filament with a metal anode (e.g., Cu or Mo); the emitted characteristic X-ray lines are filtered to produce monochromatic lines such as Cu-Kα (λ = 1.54 Å) and Mo-Kα (λ = 0.71 Å), which are used for analysis.

In this work, XRD analysis was performed using D4 Endeavor (Bruker, Germany) with Cu-Kα radiation and a 1D LYNXEYE detector. For qualitative phase analysis, data were collected in a 2θ range of 10-80°**,** with a step size of 0.02° and a collection time of 0.75 s/step**.** For Rietveld refinement, an extended 2θ range of 10-140° was used to achieve higher accuracy. Powder samples were prepared on a silicon low-

background sample holder (Bruker AXS, Bruker Corporation, USA). For LLZO sintered tapes, a double-sided tape was used on the specimen holder to hold the sample during the measurement. Le Bail refinement was conducted using Jana2006 software.

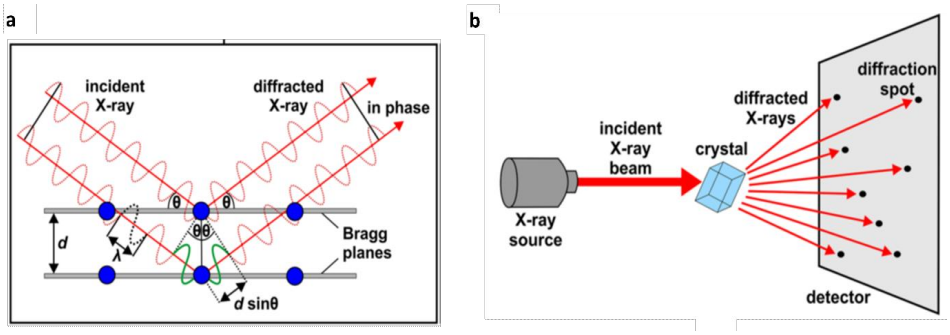


Figure 2.1| (a) Diffraction according to Bragg's Law; (b) basic scheme of an X-ray diffraction experiment[132].

2.2.2 Raman spectroscopy

Raman spectroscopy is a non-destructive technique that allows information about the chemical structure of materials by determining their vibrational modes. This technique is based on the interaction of monochromatic laser light with the chemical bonds in the material and relies on the inelastic scattering of photons (Figure 2.3a). Most scattered photons undergo elastic (Rayleigh) scattering, where their energy remains unchanged; however, a small fraction experience an energy shift corresponding to vibrational transitions, in which the scattered photons either lose energy (Stokes shift) or gain energy (anti-Stokes shift), depending on the vibrational state of the material[133]. Since most materials are in their ground vibrational state at room temperature, Stokes-Raman scattering is more intense and is commonly measured**.** The Raman shift corresponds to the energy difference between the ground and excited vibrational states, producing a characteristic spectral fingerprint that is unique to each material[134]. The scattering intensity follows a λ^{-4} dependence, meaning that shorter-wavelength lasers enhance the Raman signal but also increase the risk of autofluorescence, which can obscure the spectrum. Therefore, the laser selection depends on the electronic properties and fluorescence behaviour of the material. Figure 2.3b shows the basic setup of a Raman spectrometer. Raman spectroscopy provides additional insight into short-range order and vibrational properties, making it

valuable for confirming phase composition. Due to its sensitivity to short-range order and surface-near regions, Raman spectroscopy is particularly suitable for detecting amorphous phases, secondary phases, or surface-related species that may remain undetected by bulk-sensitive techniques such as XRD.

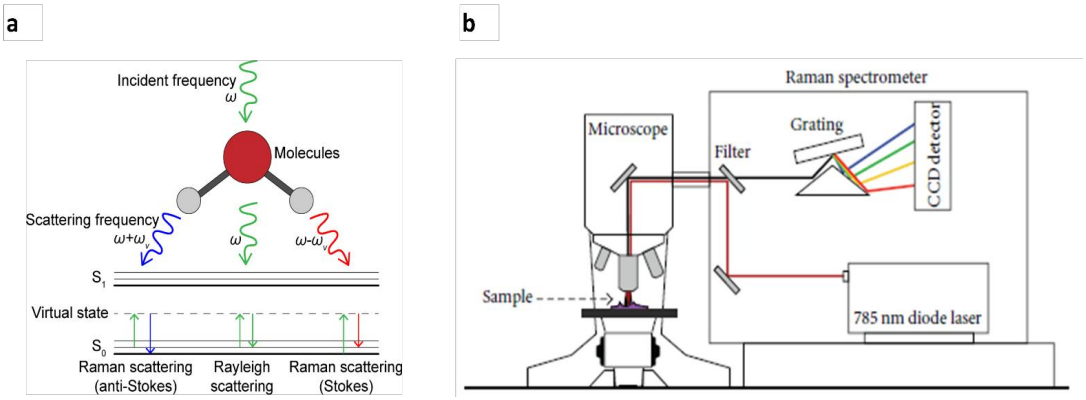


Figure 2.2|(a) scheme and Jablonski diagram illustrating Raman scattering and Rayleigh scattering. Reprinted from ref[232] with permission. Copyright Journal of enhanced Physics (2021); (b) setup for a Raman spectrometer with a near-infrared laser attached to a microscope[233] .

In this work, Raman spectroscopy was used to characterize phase composition of LLZO and NMC-based composite cathodes, track structural changes induced during fabrication, and assess phase homogeneity and material quality in multiphase and heterogeneous regions. The Raman spectroscopy measurements were performed using confocal Raman microscope (InVia Qontor, Renishaw, UK) equipped with a 532 nm laser laser (~2.5 mW) and a 2400 l·mm^{-1} grating. LLZO powders were analysed using single-point spectra at three different points each sample with 1 s integration time, 20 accumulations per point. Data post-processing included cosmic ray removal, baseline correction, and normalization. For the NMC composite cathodes, cross-sections of 100 × 40 µm^2 were mapped with a step size of 1 µm and an acquisition time of 1 s at 20 accumulations per point. In top-surface mapping, 2 µm step size 10 accumulations per point were used.

2.2.3 Solid-state neutron magnetic resonance spectroscopy (SS-NMR)

Solid-state nuclear magnetic resonance (SS-NMR) spectroscopy is an analytical technique used to investigate local atomic environments in solid materials, providing insights into structural and dynamic

properties. In this study, (SS-NMR) spectroscopy was employed to probe the local atomic environments and short-range structural changes in LLZO during the tape-casting process. Due to its sensitivity to local coordination and ion dynamics, SS-NMR enables the direct detection of subtle structural changes such as Li^+/H^+ exchange and local disorder, which are inaccessible with diffraction-based techniques.

The basic principle of SS-NMR involves aligning nuclear spins in a strong external magnetic field (B_0). Nuclei with a non-zero spin possess magnetic moments that align with B_0, resulting in a net magnetization along the field direction. This alignment leads to Larmor precession, in which the magnetic moments rotate around B_0 at a frequency (ω_0) defined by the Larmor equation[135]:

$$\omega_0 = \gamma B_0 \qquad \text{Equation 2.2}$$

Here, γ represents the gyromagnetic ratio specific to each nucleus. The net magnetization vector reaches thermal equilibrium through spin-lattice relaxation, characterized by the time constant T_1, which involves energy exchange between the nuclear spins and their surrounding lattice. The application of a radiofrequency (RF) pulse at the Larmor frequency perturbs this equilibrium, tipping the net magnetization into the transverse xy-plane. The subsequent precession of magnetization in this plane induces an oscillating voltage in the detection coil, producing the free induction decay (FID) signal. The decay of this signal is governed by spin-spin relaxation, with a time constant T_2, reflecting the loss of phase coherence among spins. By analysing the FID and its Fourier-transformed spectrum, NMR provides detailed information about the chemical environment, and dynamics of the sample under investigation (Figure 2.4). In solids, however, interactions such as dipolar couplings and chemical shift anisotropy can broaden the NMR signals. To improve spectral resolution, magic angle spinning (MAS) is employed[136], in which the sample is rapidly spun at an angle of 54.74° relative to B_0, effectively averaging out anisotropic interactions.

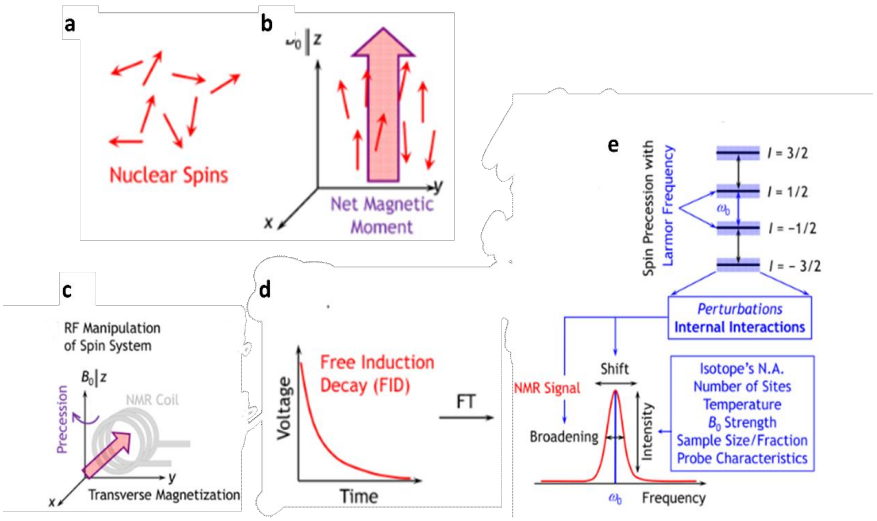


Figure 2.3| Illustration of the NMR working principle : (a) with the randomly orientated nuclear spins of the sample, there is no magnetization; (b) longitudinal magnetization along the Z-axis builds up as soon as a magnetic field B_0 is applied; (c) the spin system manipulated by RF pulses and the resulting transverse magnetization acts as a moving magnetic moment inside a coil; (d) the free induction decay (FID); (e) the Fourier Transformation (FT) of this voltage-time signal results in the NMR signal of frequency vs intensity (e) [135].

In our experiments, MAS SS-NMR measurements were conducted using a Bruker Ascend 500 MHz spectrometer (NEO console, Bruker BioSpin, Germany), operating at frequencies of 500.13 MHz for ^{1}H and 194.37 MHz for ^{7}Li. Samples were packed into 3.2 mm zirconia rotors and spun at 20 kHz. ^{1}H spectra were acquired using a background suppression pulse sequence with a 3 µs pulse length, while ^{7}Li spectra were obtained via a one-pulse experiment with a 4 µs pulse length. Recycle delays were set to three times the T_1 relaxation times, determined through saturation recovery experiments, to ensure quantitative signal acquisition. The ^{1}H MAS NMR spectra provided information on proton environments, indicative of protonation levels and the presence of hydroxyl groups within the LLZO structure. Variations in ^{7}Li chemical shifts and line shapes reflected changes in lithium coordination environments, influenced by protonation and structural modifications. By analysing these shifts, it was possible to infer the formation of specific protonation products and assess their impact on lithium-ion conduction pathways within the LLZO matrix.

2.2.4 Laser diffraction (LD)

Laser diffraction is a non-destructive technique widely used to quantify particle size distributions in powdered materials based on light scattering by dispersed particles. It provides statistically robust information over a broad size range, making it particularly suitable for assessing the effects of ball milling. In this work, LD was employed to determine the particle size distribution of LLZO and NMC powders before and after milling. The method is based on measuring the angular distribution of light scattered by a dispersed powder sample as it passes through a monochromatic laser beam (Figure 2.5). According to Mie theory, larger particles scatter light at smaller angles, while smaller particles scatter at wider angles. The resulting scattering pattern is used to calculate the PSD across a broad size range, typically from sub-micron to several hundred micrometres. Mie theory assumes spherical particles with known optical properties (refractive index and absorption coefficient). Therefore, SEM imaging was used to verify that the LLZO and NMC powders exhibit approximately spherical morphology, ensuring the validity of the model. The refractive index of the dispersant is selected from instrument libraries, while the sample's optical constants may be estimated iteratively to improve fitting accuracy.

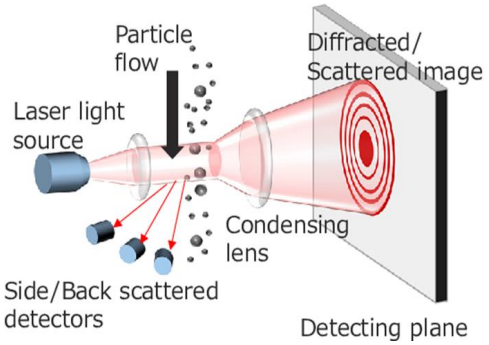


Figure 2.4| Schematic of laser diffraction particle size analysis method[234].

In this work, particle size distribution was analysed by laser diffraction (LA950, Horiba Scientific, Japan) with a 650 nm and a 405 nm laser source. Beforehand, the powders were dispersed in ethanol, and the PSD was recorded before and after 3 min sonication. The presented values for D10, D50 and D90 were determined after sonication. The data were the Mie-theory by using a refractive index of 1.2 and 1.833

for NCM and LLZO:Ta,Al respectively. In the case of Li_3BO_3, the Fraunhofer theory was applied to analyse the results.

2.2.5 Scanning electron microscopy (SEM)

Scanning electron microscopy (SEM) is a high-resolution technique for characterizing the surface morphology and microstructural features of solid materials. Due to its sensitivity to topography and compositional contrast, SEM is particularly well-suited for investigating particle morphology, microstructure evolution, and phase distribution in ceramic and composite systems. In this work, SEM was used to analyse LLZO and NMC powders, sintered tapes, and composite cathodes. In SEM, a focused electron beam is emitted from a thermionic, Schottky, or field emission gun and confined to a spot size of 0.4-5 nm using a system of condenser lenses. The beam is deflected across the sample surface by electromagnetic coils (Figure 2.6a). Upon interaction with the material, various signals are generated, including secondary electrons (SE), backscattered electrons (BSE), and characteristic X-rays[137]. SE are produced by inelastic scattering near the surface and provide detailed topographical contrast. BSE arises from elastic scattering and offers compositional contrast, with signal intensity increasing for heavier elements due to their higher atomic number. Characteristic X-rays result from the relaxation of excited atoms and allow for elemental identification using energy-dispersive X-ray spectroscopy (EDS)[137]. (Figure 2.6b,c). The SEM set-up is equipped with detectors to collect these X-rays, backscattered electrons, and secondary electrons and convert them into a signal that is sent to a screen. The X-ray lines are detected using Energy-Dispersive X-ray Spectroscopy (EDS), which identifies elements and maps their distribution. In this work, the EDS was employed in combination with scanning electron microscopy (SEM) to visualize spatial element distributions in the LLZO and NMC-based composite materials. EDS detects characteristic X-ray emissions in the energy range of approximately 0.1-30 keV, thereby enabling qualitative and semi-quantitative elemental analysis and elemental mapping. EDS complements phase identification techniques such as XRD and Raman spectroscopy by providing spatially resolved chemical information, thereby supporting the interpretation of microstructure, phase distribution, and morphology. It should be noted that the generation of characteristic X-ray lines requires the incident electron beam energy (E_o) to exceed the ionization energy of the corresponding atomic shell (E_a), commonly expressed by the overvoltage ratio.

$$U^0 = \frac{E^0}{E_a}$$ Equation 2.3

While this condition is readily fulfilled for most elements under standard SEM operating conditions, the detection of very light elements such as lithium remains challenging. Lithium emits extremely low-energy X-rays (Kα ≈ 0.052 keV), which are strongly absorbed by the detector window, the sample surface, and the surrounding medium and therefore lie beyond the detection capability of the used SEM-EDS setup.

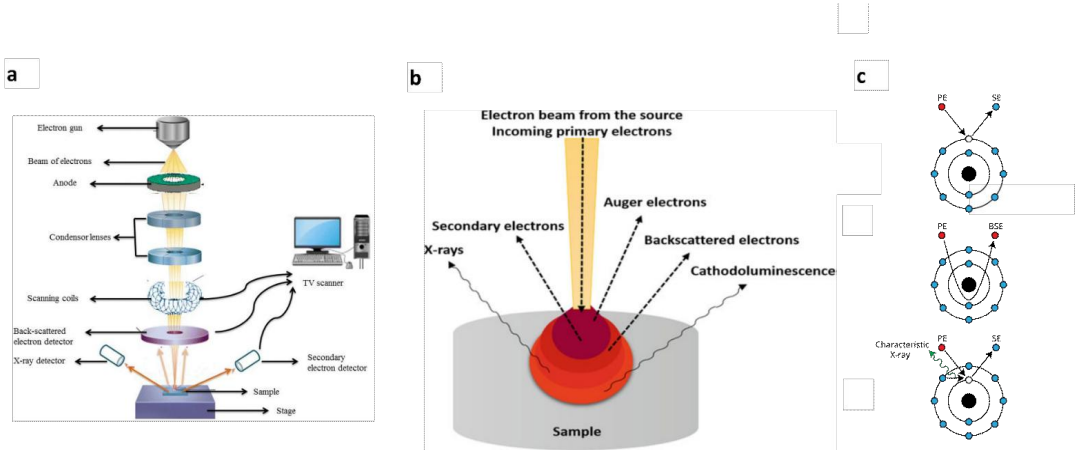


Figure 2.6| (a) Set-up of SEM unit. Reprinted from ref[236], with permission. Copyright Springer Nature (2021); (b) the interaction of electron beam with specimen and the signal emitted from the sample; (c) types of electrons emitted during beam-sample interaction. Reprinted from ref[137] . Copyright Springer, Cham (2018).

SEM imaging of powder samples was conducted using a scanning electron microscopy (Gemini 450, Carl Zeiss Microscopy, Germany) with a field emission source, operated at acceleration voltages between 3 kV and 15 kV. Sintered LLZO tapes and NMC-based composite cathodes were examined using EVO 15 (Carl Zeiss Microscopy, Germany) equipped with an energy-dispersive X-ray spectroscopy detector (Ultim Max 100, Oxford Instruments, UK), operated at voltages between 5 kV and 20 kV. Elemental analysis was performed using an EDS detector coupled with AZtec software (Oxford Instruments, UK). Sample preparation procedures were adapted to the type of material. Powder samples were mounted on carbon adhesive tape and coated with a thin platinum layer to prevent charging. For cross sectional

imaging of solid electrolyte tapes, the samples were embedded in EpoFix epoxy (Struers, Germany), mirror-polished, contacted with copper tape, and sputtered with a gold layer. Porous composite cathodes were analysed on fracture surfaces, mounted on a sample holder, and sputter-coated with a gold-platinum layer. Acceleration voltage and probe current (5-20 kV; 200-700 pA) were optimized based on material composition to ensure sufficient signal strength and spatial resolution. Beam energies between 8 kV and 20 kV were typically used to excite and detect characteristic X-ray lines of heavy elements such as La, Zr, Ni, Mn.

2.2.6 Confocal white light microscopy

Confocal white light microscopy is a non-contact optical profilometry technique used for the high-precision determination of surface topography and layer thickness. Broadband white light is focused through a lens onto the sample. Due to the confocal principle, only the light from the exact focal point is detected, enabling precise depth measurements. By moving the sample in x-y-z directions, the system generates 3D surface profiles or measures layer thicknesses with sub-micron resolution[138]. In this work, this technique was used to examine the topography and flatness of the sintered LLZO and NMC composite tapes. The topography was analyzed using a white light interferometry (CT350T, cyberTECHNOLOGIES GmbH, Germany) with P-CHR-10000 sensor. To ensure sample stability during scanning, specimens were affixed to the measurement stage using double-sided adhesive tape.

2.2.7 Thermo-analytical techniques

Thermogravimetric analysis (TGA) and differential scanning calorimetry (DSC) are thermal analysis techniques used to monitor changes in mass and heat flow as a function of temperature, providing insights into the thermal stability, decomposition processes, and phase transitions in solid materials. In TGA, changes in the material's mass are measured under controlled conditions as a function of temperature or time. The sample is placed on a microbalance inside a furnace, and its weight is continuously recorded while it is heated at a constant rate or held under isothermal conditions (Figure 2.7a). This allows for the detection of moisture loss, decomposition, oxidation, and gas release. Under oxidizing conditions, TGA can also detect mass increase due to oxygen uptake[139]. The resulting

thermogram plots the mass change versus temperature and provides quantitative information on thermal stability and mass loss. DSC detects differences in heat flow between a sample and a reference under identical temperature programs (Figure 2.7b). Endothermic transitions (e.g., melting or dehydration) and exothermic reactions (e.g., crystallization or oxidation) are detected, enabling the determination of thermal parameters such as glass transition temperature (Tg), crystallization temperature (Tc), and melting point (Tm)[140]. Combined TGA/DSC measurements provide a comprehensive thermal profile that correlates mass changes with heat flow events. In this work, TGA was used to determine the decomposition temperature of Li_2CO_3 on the LLZO powder surface and to identify decomposition of organic components in NMC composite tapes, which enabled the determination of suitable temperatures for calcination and heat treatments. DSC was used to determine the melting behaviour of the Li_3BO_3 (LBO) sintering aid, which served as a key parameter for designing the liquid-phase sintering protocol of NMC-based composite cathodes. Together, TGA/DSC data guided the selection of heat-treatment profiles to ensure controlled removal of organic components and effective densification without compromising phase integrity.

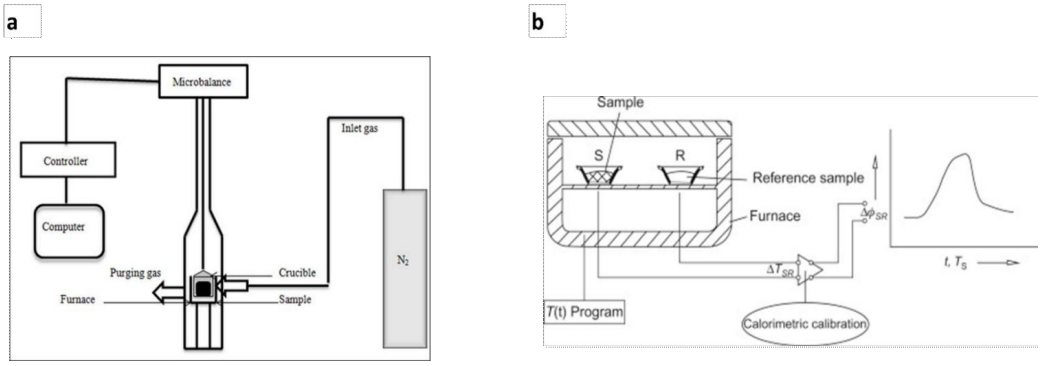


Figure 2.7| (a) Set-up of TGA. Reprinted from ref[237]. Copyright Elsevier (2014); (b) DSC instrument. Reprinted from ref[238]. Copyright Elsevier (2019).

Simultaneous TGA-DSC analysis was performed using a thermal analyser (STA 449C Jupiter, Netzsch, Germany) at a heating rate of 5 K min^{-1} in air from room temperature to 1000 °C, coupled with a QMS 403 C Aëolos Quadro mass spectrometer. The heat flow was 10°C per minutes from room temperature to 1000°C.

2.3 Electrochemical characterization techniques

The electrochemical characterization in this work was performed using coin cells and Swagelok cells (Figure 2.8a,b)

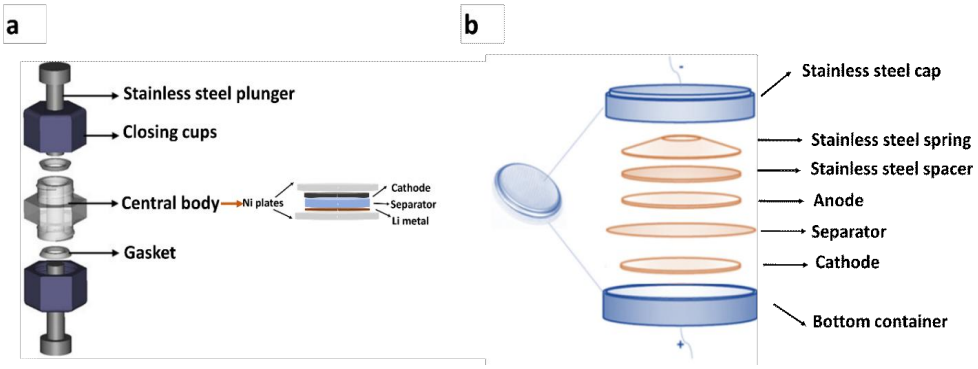


Figure 2.8|(a) illustration of the coin cell; (b) Swagelok set-ups used in this work

2.3.1 Galvanostatic cycling with potential limitation (GCPL)

Galvanostatic Cycling with Potential Limitation (GCPL) was used to evaluate the capacity retention, reversibility, and rate performance of NMC-based composite cathodes. In this method, a constant current is applied to a cell (Figure 2.9a) and the cell voltage is recorded as the electrochemical reactions proceed, resulting in charge/discharge curves (voltage profiles). During charge, the voltage changes continuously until the Faradaic (redox) reaction begins, during which the potential remains nearly constant until the reaction is complete. The redox processes are indicated by potential plateaus in the GCPL charge-discharge curves. The average potential value of the plateau corresponds to the standard potential of the respective oxidation or reduction reaction, while the length of the plateau corresponds to the charge consumed or released in this process and is proportional to the amount of reacting material. Discharge involves a polarity reversal with an immediate IR drop, followed by a continuous potential change and eventually a plateau corresponding to redox reactions (Figure 2.9b). The potential difference (potential hysteresis) between the charge and discharge plateaus results from polarization and internal resistance due kinetic limitations and resistive losses within the battery [141]. The cycling rate is expressed as a C-rate, corresponding to the time required to fully charge or discharge a cell. For

composite cathodes, the current was applied as a surface-normalized current density (µA cm^{-2}), which allows for a direct comparison of different samples.

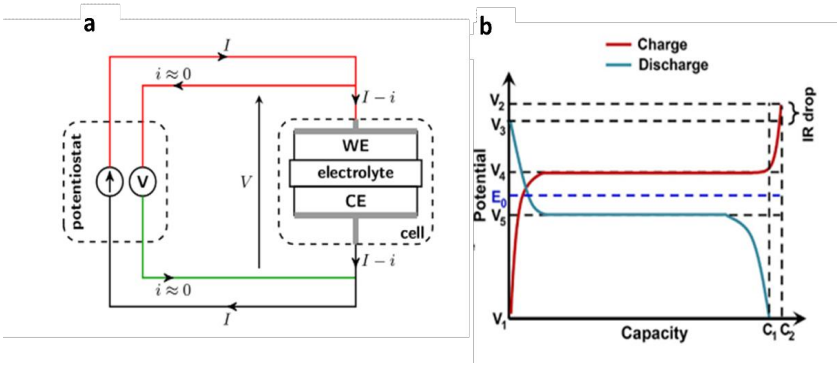


Figure 2.9| (a) Scheme of a potentiostat connected to a two-electrode cell. Adapted from ref [239]. Copyright American Chemical Society (2019); (b) representation of galvanostatic charge-discharge profile for a battery. Adapted from ref [141]. Copyright Elsevier (2023)

Measurements were performed using two cell configurations: coin cells with liquid electrolyte ($LiPF_6$ in EC: DMC: EMC) and Swagelok-type two-electrode cells employing LLZO as a solid-state electrolyte. In both setups, NMC composite cathodes were cycled against lithium metal between 3.0 V and 4.2 V vs. Li/Li^+ at a constant current density of 40 µA cm^{-2}, using a using a potentiostat (VMP-3, BioLogic Sciences Instruments Ltd, France) combined with a climate chamber (VT 4002EMC, Vötsch Industrietechnik VT 4002EMC, Germany) at 60 °C to enhance ionic conductivity and improve electrochemical kinetics.

2.3.2 Critical current density (CCD)

Critical current density (CCD) is a key parameter for evaluating the performance of lithium metal anodes in solid-state batteries. It defines the highest current density that a solid electrolyte can sustain in contact with Li metal anode without failure, such as a short circuit caused by the penetration of lithium dendrites. In this work, CCD measurements were used to assess the performance of optimized LLZO sintered tapes in symmetrical Li/LLZO/Li cells.

The CCD is determined by the processes at the interface between lithium metal and solid electrolyte separator during battery operation. The important processes are: (i) ion transfer and deposition/stripping kinetics, (ii) morphological evolution at the interface, and (iii) electrochemical and mechanical degradation leading to failure[142]. These processes begin with lithium nucleation, which occurs when the applied potential is sufficient to overcome the surface energy barrier, allowing the formation of Li nuclei on the solid electrolyte surface. During stripping, metallic lithium is oxidized to Li^+, leaving behind lithium vacancies (V_{Li}) as described by Equation 2.4[142]:

$$Li \rightarrow Li^+ + e^- + V_{Li} \qquad \text{Equation 2.4}$$

Over repeated cycles, these vacancies accumulate and form voids at the Li|electrolyte interface, thereby impairing interfacial contact. Without external pressure, such voids persist and lead to non-uniform lithium deposition during subsequent plating, which promotes localized current constriction and dendrite growth. CCD is typically measured using stepwise galvanostatic cycling, in which the current is gradually increased until voltage instability drop indicates a short-circuit. CCD measurements can be combined with electrochemical impedance spectroscopy (EIS) measurements after each individual cycle to monitor interfacial resistance. Further insight about the interfacial stability can also be obtained from the analysis of voltage profiles.

Dendrite-induced failures in lithium metal batteries are commonly classified into three types [142] (Figure 2.10). Hard short circuits occur when dendrites fully penetrate the electrolyte and connect both electrodes, leading to a sudden voltage drop and the appearance of a parallel leakage paths detected in impedance spectra. Partial short circuits involve lithium filaments that breach the interface without fully traversing the electrolyte, leading to moderate polarization losses. Soft short circuits result in minor voltage fluctuations and are often reversible by adjusting parameters such as current density, temperature, or pressure.

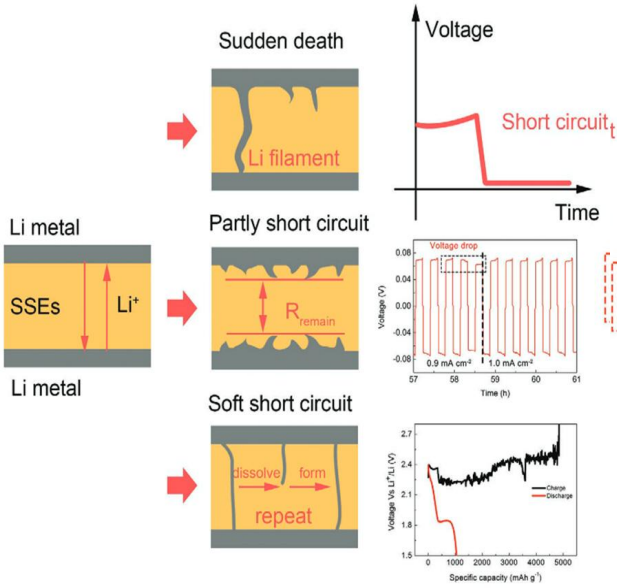


Figure 2.10| Types of dendrites formation and their corresponding charge profiles and fitting circuits. Adapted from ref [142] with permission. Copyright Wiley-VCH (2021).

To evaluate the electrochemical stability of the LLZO separator tapes, a ~30 nm gold interlayer was sputtered onto both surfaces using a Cressington 108auto coater to improve interfacial contact. Freshly calendared lithium metal was manually pressed onto each side of the coated LLZO tape. The assembly was sandwiched between two nickel current collectors and heated to 300 °C, then gradually cooled to 180 °C, 75 °C, and 40 °C, with 20-minute dwell times at each step to promote uniform mechanical and electrical contact. CCD measurements were performed in a Swagelok cell at 60 °C using the Biologic VMP-300 multipotentiostat. Cycling began at a current density of 50 µA cm^{-2} with a plating/stripping duration of 1 hour. In each subsequent cycle, the current was increased by 50 µA cm^{-2}, while the cycle time was proportionally reduced to maintain constant amount of transferred lithium (lithium capacity) in each cycle.

2.3.3 Electrochemical impedance spectroscopy (EIS)

Electrochemical impedance spectroscopy (EIS) is a non-destructive technique for analysing electrical behaviour over a wide frequency range, which makes it possible to deconvolute individual contributions to electrochemical performance. In this work, EIS was used to determine the ionic conductivity of sintered LLZO tapes and to monitor resistance evolution in a full cell during cycling. A small AC potential (typically a few millivolts) is applied across the sample over a frequency range from mHz to MHz. The resulting current response is used to calculate the complex impedance, defined by equation 2.5 [143]:

$$(t) = \frac{E(t)}{J(t)} = \frac{|\Delta E|\sin(\omega t)}{|\Delta j|\sin(\omega t + \Delta t} = |Z|\ (cos(\emptyset) + Isin\ (\emptyset) \qquad \text{Equation 2.5}$$

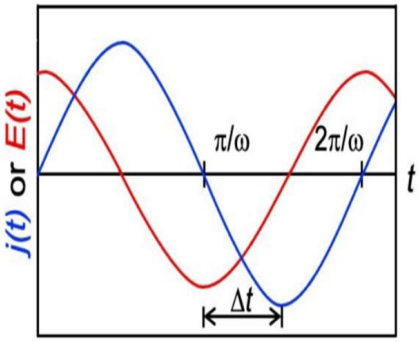


Figure 2.11|Plot describing the relationship between the input voltage, E(t) and output current, j(t) (or vice versa), the ratio of which results in impedance. Reprinted from ref [144] with permission. Copyright Wiley-VCH(2021)

where ω is the angular frequency and Δj represents the amplitude of the current density, Ø is the phase angle difference (phase shift), and |x| is the amplitude of sinusoidal signal x. Since impedance is a function of frequency, magnitude, and phase angle, three common plots are used to represent the data: Nyquist plots (real vs. imaginary impedance), Bode magnitude plots (|Z| vs. frequency), and Bode phase plots (phase angle vs. frequency) (Figure 2.11). Nyquist plot displays impedance data without explicitly showing the frequency, with high-frequency data located near the origin and low-frequency data extending outward. Bode magnitude plot displays the impedance magnitude (|Z|) as a function of frequency (f) but does not contain information about the phase angle. Bode phase plot displays the phase angle (Φ) of the impedance as a function of frequency (f) but does not show the evolution of the amplitude.

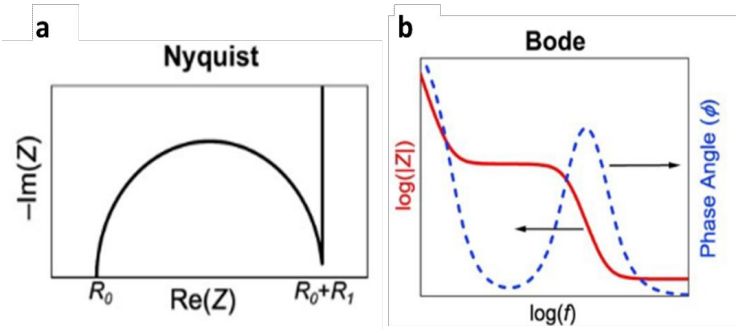


Figure 2.12|(a) Nyquist plot of the real impedance against the imaginary impedance showing the resistance for the electrolyte; (b) Bode plots of the magnitude of the impedance (red) and phase angle(blue) against frequency. Adapted from ref[144] with permission. Copyright Wiley-VCH (2021).

To evaluate the bulk resistance of the solid electrolyte, measurements were performed using an ion-blocking symmetric cell in which the LLZO pellet or LLZO tape was sandwiched between two inert metal electrodes. At high frequencies, the ion movement through the bulk electrolyte (bulk ionic conductivity) can be detected, whereas at lower frequencies, impedance associated with ion transfer through grain boundaries dominates the response, enabling to determine grain boundary resistance. In full cells, the EIS response includes additional contributions from the electrodes and their interfaces, with high-frequency features typically associated with bulk transport and low-frequency features associated with interfacial phenomena. The impedance spectra were modelled using equivalent circuit fitting. For symmetric ion-blocking configurations, a common model includes a series resistance (R_0) and double layer capacitance (C_2) and one or more parallel resistor-capacitor (RC) elements shown in Figure 2.13. The first high-frequency arc corresponds to the bulk and grain boundary resistance (R_1) and capacitance (C_1), while the appearance of second arc at lower frequencies may indicate the presence of even slower process, for example charge transfer at the interface.

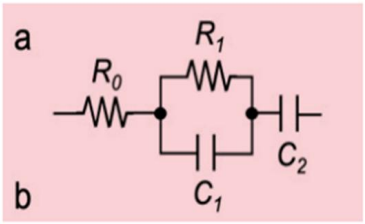


Figure 2.13|Equivalent circuit for single electron transfer and ion migration in the electrolyte. Adapted from ref[144] with permission. Copyright Wiley-VCH (2021)

The conductivity of the solid electrolyte is inversely proportional to the total resistance (R_{total}) given by Equation. 3.6[144], where l is the pellet thickness and S the electrode contact area:

$$\partial_{ionic} = \frac{I}{R_{total}\, S} \qquad \text{Equation 2.6}$$

Real solid electrolytes exhibit microstructural heterogeneities, such as grain size and grain boundary distributions, which lead to non-ideal behaviour typically visible as depressed semicircles in Nyquist plots. To model this, constant-phase elements (CPEs) are used instead of ideal capacitors. The effective capacitance associated with a CPE is given by Equation 2.7[145], where Q is the CPE parameter and α ($0 < \alpha \leq 1$) accounts for the distribution of time constants:

$$C = \frac{(QR)^{\frac{1}{\alpha}}}{R} \qquad \text{Equation 2.7}$$

Various electrochemical processes generally exhibit very different capacitance values (Table 2.2), which can be used to assign detected circuit elements to specific physical processes within the cell, such as bulk ionic conductivity, grain boundary resistance, or interfacial processes.

Table 2.2| Overview of capacities values related to electrochemical components. From ref [146]

Capacitance (F)	Responsible phenomenon
10^{-12}	Bulk
10^{-11}	Minor second phases
10^{-11}, 10^{-8}	Grain boundaries
10^{-8}, 10^{-9}	Bulk ferroelectric
10^{-9}, 10^{-7}	Surface layer
10^{-7}, 10^{-5}	Sample-electrode interface
10^{-4}	Electrochemical reactions

2.3.4 Galvanostatic Intermittent Titration Technique (GITT)

The Galvanostatic Intermittent Titration Technique (GITT) was used to investigate the transport properties of various NMC composite cathodes. In this method, a series of constant-current pulses is applied, each followed by a relaxation period at an open circuit. During the current pulse, lithium ions intercalate into or deintercalated from the electrode, resulting in a change in cell voltage. During the

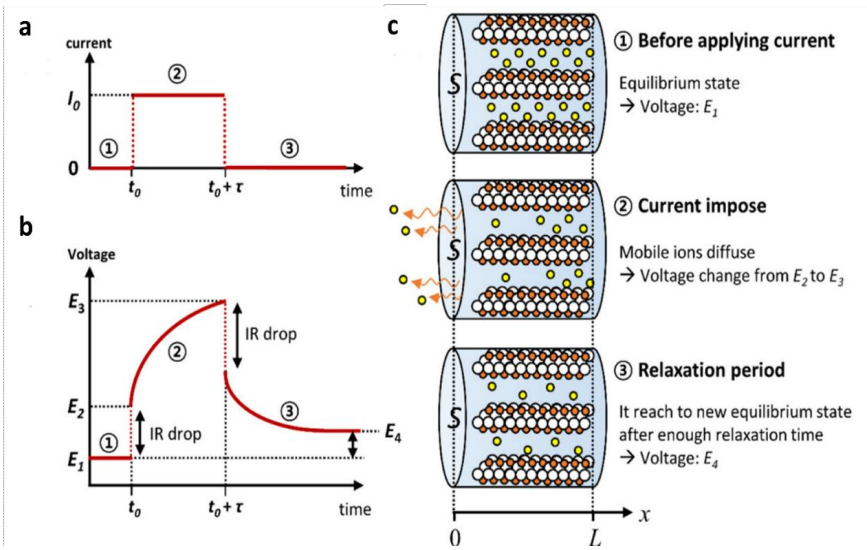


Figure 2.14| (a) Schematic diagram of a single galvanostatic titration step of GITT experiments. An imposed constant current pulse (Io) and (b) the resulting voltage changes; (c) schematic illustration of ion transport processes during galvanostatic titration steps.[147]

relaxation phase, the current is interrupted, allowing the cell to equilibrate and lithium ions to redistribute within the electrode. Figure 2.14 illustrates a galvanostatic titration step and the mobility of Li ions during the GITT step.

The voltage response during the GITT steps provides insights into the diffusion behaviour of lithium ions. The lithium-ion diffusion coefficient (D) can be determined using the Equation 2.8 [147], where t (s) is the current pulse time, mb (g) is the total mass loading, S (cm^2) is the cathode surface, Mb ($g\ mol^{-1}$) is the molecular weight, ΔE_s is the steady-state voltage change during the current pulse, and ΔE_t is the total voltage change during the current pulse.

$$D = \frac{4}{\pi t}\left(\frac{V_m m_b}{S\ M_b}\right)^2 \left(\frac{\Delta E_S}{\Delta E_t}\right)^2 \qquad \text{Equation 2.8}$$

In this study, GITT measurements were conducted on NMC composite cathodes. The cell was assembled by gluing the NMC cathode tape to a LLZO separator with a polymer. And attaching lithium metal anodes to the other side of the separator. In some cells, carbon black was incorporated into the polymer to improve electronic conductivity. The cells were subjected to current pulses of 40 µA cm^{-2} for 1 hour, followed by relaxation periods of 3 hours to establish equilibrium. The voltage range for the measurements was set between 3.0 V and 4.3 V vs. Li/Li^+. Electrochemical impedance spectroscopy (EIS) was performed at the end of each current pulse to monitor changes in cell resistance.

3 TAPE CASTING OF LLZO CERAMIC SEPARATORS: OVERVIEW OF THE CHALLENGES AND OPTIMIZATION STRATEGIES

This chapter provides a critical and systematic overview of the challenges associated with the tape casting of LLZO, with a particular focus on understanding the interrelationship between the individual processing steps throughout the entire fabrication chain. The review analyses current strategies described in the literature for overcoming key limitations in the individual steps of tape casting process and illustrates how they influence the microstructure and electrochemical performance of the final components.

This chapter is based on a review paper published in ChemSusChem with the title "*Tape Casting LLZO Ceramic Separators: An Overview of the Challenges, Optimization Strategies, and Paths to industrial implementation".* By Kaouther Touidjine, Ruijie Ye, Melanie Finsterbusch-Rosen, Artur Lang, Martin Finsterbusch, Dina Fattakhova-Rohlfing

The review was conceptualized and led by Kaouther Touidjine, who conducted the comprehensive literature review, critical evaluation, and manuscript preparation. Ruijie Ye, Melanie Finsterbusch-Rosen, Artur Lang, Martin Finsterbusch and Dina Fattakhova-Rohlfing contributed through scientific validation and revision of the manuscript.

Link to the published review paper: https://doi.org/10.1002/cssc.202502488

3.1 Background and chapter scope

Building on the discussion of LLZO as a solid electrolyte in Chapter 1, this chapter review the specific challenges encountered when processing LLZO into thin ceramic separator layers by tape casting. Despite several studies demonstrating the feasibility of tape casting LLZO[10,16,148,149], the process remains far from standardised, primarily due to a cascade of interdependent challenges encountered across the fabrication chain from powder pre-treatment and slurry formulation to casting, sintering, post-processing, and cell integration. At the core of these challenges, the precise control over multiple parameters to ensure the formation of defect-free, dense, and stable components is needed. First, slurry formulation requires careful optimisation of rheological properties to ensure stable, homogeneous casting, while simultaneously maintaining chemical compatibility between LLZO and the employed organic additives and solvents. Contact with protic solvents during slurry preparation initiates Li^+/H^+

exchange at the LLZO surface, modifies surface chemistry which first, destabilises the slurry, impairs green tape quality, possibly reduces sintering activity, and ultimately compromise the conductivity and integrity of the final separators[16,150,151]. During sintering, the high temperatures required for LLZO densification accelerate lithium volatilisation, further depleting the lithium content, which is especially severe in thin films due to their high surface-to-volume ratio. After sintering, post- treatments are still needed for surface optimisation to enable good interfaces with the other cell component during battery cell integration. Each of these challenges has been studied individually in the literature, where the mechanism of LLZO protonation, the effect of lithium loss on phase stability, and sintering optimisation strategies have all been reported as isolated problems. However, in the context of tape casting, these phenomena are not independent: degradation initiated at an early stage propagates and amplifies through subsequent steps, collectively determining the chemistry, microstructure, and electrochemical performance of the final separator. This interconnected nature of the tape-casting process chain has not been systematically addressed, and its recognition is essential for developing robust, scalable fabrication strategies.

This chapter addresses this gap by systematically analysing the challenges and degradation mechanisms at each stage of the LLZO tape-casting process through a critical review of the available literature. For each stage, the origins of degradation are identified, their propagation through the process chain is traced, and mitigation strategies are evaluated. The aim of this chapter is to establish the scientific framework that guides the experimental work presented in the following chapters, in which selected challenges are addressed experimentally and potential solutions for LLZO-based separators and composite cathodes are validated.

3.2 Manufacturing ceramic LLZO separators via tape casting

The fabrication of LLZO separators by tape casting comprises three main steps, as illustrated in Figure 3.1. The process begins with the formulation of a slurry (Step 1: Slurry optimisation), which is then cast onto a selected substrate (typically a polyethylene terephthalate (PET) or Mylar film) and dried to produce a “green” tape in Step 2. The flexible green tape is then removed from the substrate and cut or punched to obtain separators of the desired size and shape. The shaped green bodies are then transferred to a heat-resistant substrate and sintered in Step 3 (Tape sintering) to obtain the final rigid

thin ceramic layer. For battery manufacturing, the integration of such layers, e.g. as separator, must exhibit good mechanical robustness and flatness to ensure reliable cell assembly.

This section focuses mainly on the first two steps, in particular on the optimisation of the slurry formulation and its impact on the casting step. The key performance criteria (such as the ionic conductivity, microstructure, flatness, performance with Li anodes) of the final sintered separators are used throughout as quality benchmarks to evaluate the impact of processing decisions. The challenges specific to the sintering step are addressed later in this chapter.

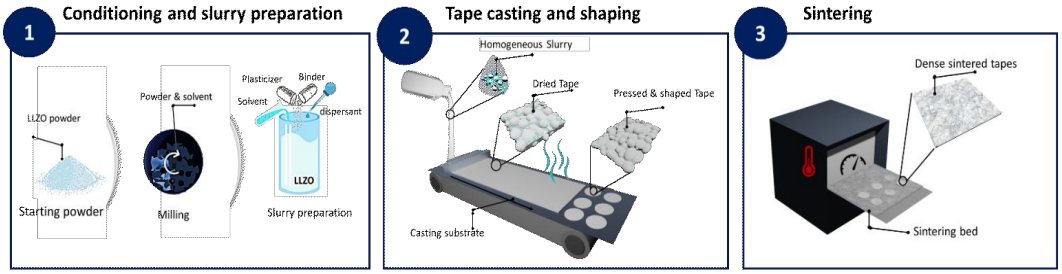


Figure 3.1| Illustration of a standard tape casting procedure for manufacturing LLZO separators.

The preparation of the slurry is a critical step, as it directly governs the properties of the green tapes as well as the properties of the final sintered separators. Factors such as density, porosity, and mechanical and electrochemical stability are closely related to the composition of the slurry and its processing. Before the LLZO powder is processed into a slurry, it is usually subjected to pre-treatment (conditioning) to reduce the particle size. This is typically achieved by milling the starting powders either in a dry or a wet milling in a suitable and compatible solvent to avoid protonation of the LLZO surface. Milled LLZO particles are then dispersed in a solvent with a carefully selected blend of organic additives, including binders, dispersants, and plasticisers. These additives stabilise particle-particle interactions within the suspension, preventing sedimentation, and optimizing rheology to ensure the production of flexible and defect-free green tapes. Table 3.1 provides an overview of various LLZO slurry formulations available in the literature, highlighting the different solvent-binder systems, dispersants, plasticizers, and additives that have been used to date for tape-cast LLZO separators.

Table 3.1| Overview of reported slurry recipes for tape casting LLZO separators and the important properties (ionic conductivity and relative density) of the sintered tapes

Solvent	Binder	Dispersant	Plasticizer	LLZO : structure dopant	Sinter aid	Relative density of tapes after sintering (%)	Conductivity of tapes after sintering (S cm^{-1})	Ref
Ethanol	PVB	Menhaden fish oil	Polyethylene glycol	LLZO: Al	ZnO		$0.8 \cdot 10^{-4}$	[152]
Ethanol, butanol	PVB	Alkylammonium salt of a copolymer	PEG	LLZO: Al, Ta		92.8	$3.9 \cdot 10^{-4}$	[16]
Ethanol, butanol	PVB	Alkylammonium salt of a copolymer	PEG	LLZO: Al, Ta	Li_2CO_3	95	$1.8 \cdot 10^{-4}$	[81]
Ethanol, Toluene	Ethyl-Cellulose	Menhaden fish oil	dibutyl phthalate, polyethylene glycol	LLZO: Nb	Li_3BO_3	90.8	$2.8 \cdot 10^{-4}$	[112]
Ethanol, Acetone	PVB		benzyl butyl phthalate	LLZO: Al	MgO	92.3	$2.25 \cdot 10^{-4}$	[128]
Ethanol, butyl acetate	Polyacrylic resin		Polyacrylic resin	LLZO: Ta	Li_2O	99	$5.2 \cdot 10^{-4}$	[95]
Ethanol, Acetone	PVB	PAA	benzyl butyl phthalate	LLZO: Al		94	$2 \cdot 10^{-4}$	[148]
Water	Methylcellulose		PEG, Glycole	LLZO: Al, Ta		90	$1.5 \cdot 10^{-4}$	[13]
Water	Acrylic-emulsion, xanthan gum	Ammonium polymethacrylate		LLZO: Al		95	$5 \cdot 10^{-4}$	[29]
Water, ethanol	Methylcellulose	Dispex Ultra PA4560	PEG, Glycerol	LLZO: Al	MgO	91	$2.3 \cdot 10^{-4}$	[128]
Toluene	MSB1-13	DS002 (phosphate ester)		LLZO: Al	MgO	87.9	$1.7 \cdot 10^{-4}$	[128]
Toluene, isopropanol	PVB	Menhaden fish oil	PAG	LLZO: Nb		Porous Bilayer	$5.35 \cdot 10^{-4}$	[153]
Toluene, isopropanol	PVB	Menhaden Fish oil	Benzyl butyl phthalate	LLZO: Ca, Nb		Porous Bilayer	$2.2 \cdot 10^{-4}$	[12,154]
Toluene, Isopropanol,	PVB	Menhaden fish oil	Benzyl butyl phthalate	LLZO: Nb,Ca		ca. 99 (Dense)		[155]
Ethylene glycol monomethyl ether	PVB		glycerol trioleate	LLZO: Ta		Porous		[156]

When selecting organic additives and solvents, chemical compatibility with LLZO must be ensured to avoid undesirable reactions that could compromise its stability. The solvent must effectively dissolve the binder and other organic components while maintaining an optimal balance between chemical stability with the LLZO, e.g., not triggering its protonation or corrosion. In addition, it must maintain its functionality within the suspension by minimizing potential interactions that could lead to polymerization, for example. Achieving this balance is important to ensure the desired flexibility of the green tapes for further processing. Sintering aids (introduced in Chapter 1) are often added to the slurry to improve densification during the heat treatment step. Therefore, their stability within the slurry mixture, particularly their tendency to react with solvents, binders, or LLZO, must also be carefully considered. After casting and drying the slurry, the green tapes must have sufficient cohesion and flexibility to withstand subsequent processing steps such as mechanical shaping and lamination. It is important that after the green tapes have been shaped, densification is achieved through heat treatment. Heat treatment removes the organic components (burning out the binder) and promotes the densification of the LLZO microstructure to form a mechanically stable, defect-free, dense body.

The selection of binders and solvents is particularly critical. Commonly used binders such as polyvinyl butyral (PVB) and ethyl cellulose are preferred due to their solubility in solvents like ethanol and toluene**,** which are generally compatible with LLZO, and can also burn at relatively low temperatures during sintering, facilitating the densification of ceramic tapes. Polyethylene glycol is typically used as a plasticiser, while the dispersants are either polymer-based (e.g., BYK-180) or surfactant-based (e.g., fish oil). While the choice of solvents and binders is primarily determined by technical factors such as slurry rheology, green tape flexibility, and final performance, safety and scalability considerations impose additional constraints. Water-based systems are particularly attractive for industrial applications owing to their safety, environmental compatibility, and ease of handling. However, water is not always ideal for tape LLZO casting, as it readily triggers LLZO protonation**,** leading potential degradation early in the slurry. In addition, aqueous slurries often suffer from poor wetting due to higher surface tension. Being polar, they can induce agglomeration through proton bonding (hydrogen bonding), thus impairing slurry flow. On the other hand, organic solvents such as toluene, ethanol, and acetone offer better rheological, though they raise concerns regarding flammability, toxicity, and environmental impact. Binder systems such as PVB, which require phthalate-based plasticisers, raise additional safety and regulatory concerns

due to the toxicity and restricted use of phthalates under REACH regulations. These trade-offs must be carefully weighed to optimise both the castability and performance of LLZO slurries while ensuring industrial viability**.** For example, Johnson et al. systematically screened binder and solvent combinations for LLZO slurries, highlighting the sensitivity of tape quality to formulation choices and the absence of a universally optimal system.[128]

Table 3.2| Guiding criteria for selecting possible slurry formulations for tape casting LLZO layers (adapted from ref[128])

Binder System	Solvent Health/Safety	LLZO Compatibility	Slurry Foaming	Ease of Carrier (support) Release	Green Mechanical Properties	Oxide-Only Density of Laminates (%)
PVA	Aqueous	Gels	–	–	–	–
PII – WB4101	Aqueous	Gels	–	–	–	–
Methylcellulose	Aqueous	Yes	Yes, Controllable	Controllable De-wetting	Good	40.2
PVB	Ethanol/Acetone	Yes	No	Poor	Brittle	44.3
Ethyl-Cellulose	Toluene/Ethanol	Yes	Minor	Good	Brittle	43.9
PII – MSB1-13	Toluene/Xylene	Yes	No	Good	Very Good	41.7

Defining a single "best" slurry formulation is inherently challenging, as the slurry formulation process involves trade-offs between technical feasibility, chemical compatibility, safety considerations, and a large scale reproductivity. While hazardous solvents and additives can be carefully handled under controlled conditions on a laboratory scale, industrial-scale production is subject to stricter safety regulations and requires consistent process stability. The transition from feasibility at laboratory scale to commercial viability requires balancing rheological performance, LLZO compatibility, environmental impact, and handling risks. To provide a clear, comparative perspective, we have created Table 3.3 that evaluates key slurry components based on their ability to meet the most important criteria for LLZO tape casting. This classification serves as a practical guide for researchers and engineers in selecting optimal binder-solvent-dispersant systems that meet both scientific requirements and industrial constraints.

Table 3.3| Estimation of the suitability of various binders, solvents and dispersants for formulating slurries for LLZO tape casting based on the rheological properties of the slurry, process safety, and performance of final LLZO separators in symmetrical Li/LLZO/LI cells

	Component	Good for Rheology	Toxicity	Safety for large-scale production	Good for performance of LLZO separators
Binder	PVA (Water-soluble, gel-forming)	No	No	Yes	**No**
	PVB (Solvent-based, flexible)	Yes	Yes	No	**Yes**
	Ethylcellulose (Thermoplastic, strong adhesion)	Yes	Yes	No	**Yes**
Solvent	Water	No	No	Yes	**No**
	Ethanol (Moderate evaporation, safe)	Yes	Moderate	Moderate	**Moderate**
	Isopropanol (Slower evaporation, safer)	Yes	Moderate	Moderate	**Moderate**
	Toluene (Low surface tension)	Yes	Yes	No	**Yes**
	Acetone (Fast evaporation)	Moderate	Yes	No	**Yes**
Dispersant	Menhaden Fish Oil	Moderate	No	Yes	**Yes**
	Dispex Ultra PA4560 (Polymeric, strong stabilization)	Yes	No	Yes	**Yes**
	Polyacrylic Acid (Electrostatic stabilization)	Moderate	No	Yes	**Moderate**
	Polyethylene Glycol	Yes	No	Yes	**Yes**

3.3 Main challenges during slurry fabrication

The surface of LLZO powders is sensitive to water[67] (including moisture[68–71]), carbon dioxode[73], and protic solvents[3]. This sensitivity is due to a lithium-proton exchange (protonation introduced in Chapter 1). The Protonation is particularly important in tape casting because the multi-stage workflow exposes LLZO to a greater variety of chemical environments including protic solvents, organic additives, and ambient atmosphere, than single-step processes.

The protonation of LLZO particles most probably occurs during the steps 1 and 2 (Figure 3.1) of tape casting including ball milling, slurry preparation, and drying. The formation of LiOH and Li_2CO_3 on the surface affect the wettability of LLZO particles with the binder solution, which in turn affects the rheology and viscosity of the slurry[157,158]. Depending on whether the LLZO surface is covered with Li_2CO_3, LiOH, or a combination of both, the interactions with the dispersant and binder in the slurry vary, leading to irregularities in the flow behaviour of the slurry. Furthermore, both Li_2CO_3 and LiOH can be dissolved to

a certain extent in solvents like water or ethanol. Although this interaction may not alter the particle surface as much, the increasing in slurry pH could significantly affect the properties of the binders and lead to different rheological behaviour. Such uncontrolled parameters often result in an inhomogeneous casting or, in severe cases, gelation of the slurry, rendering it uncastable. Fluctuations in environmental conditions such as temperature and humidity (especially seasonal fluctuations) further complicate the control of the protonation rate and the prediction of the nature and quantity of resulting Li-containing impurities on the LLZO surface. This variability complicates the reproducibility of slurry formulations and leads to batch-to-batch differences. Rosen et al. showed that storage duration and conditions of LLZO powders and slurry distinctly affect the viscosity profiles[16] (Figure 3.2a). It has also been demonstrated that the slurry properties, which are determined by the protonation state of the LLZO, have a direct influence on the properties of the sintered tapes, including morphology, porosity, and phase purity, which affect the ionic conductivity of the separator and its performance.[130,159] The use of different solvents for slurry preparation also influences the mechanical properties of the dried films. For example, Praejiya et al. demonstrated that green tapes prepared with ethanol compared to isopropanol often contain secondary phases, which is certainly due to the differences in protonation rates in these solvents[160] (Figure 3.2d,e). In addition, the use of strongly protic solvents such as acetonitrile (AcN) can induce structural decomposition of LLZO via the Thorpe reaction, in which LLZO acts as a base catalyst to capture protons from the AcN. The results of this reaction induce polymerization, which we expect to increase the viscosity of the slurry, and it has been shown to induce severe structural decomposition of LLZO into secondary phases such as $La_2O_2CO_3$ and $Al(OH)_3$ [77] . The presence of various protonation products, including Li_2CO_3, LiOH, protonated LLZO (LLZO: H), and any other possible degradation products in green tapes, complicates the sintering process, as each phase has distinct sintering temperatures and thermal shrinkage properties. As a result, non-uniform densification occurs, leading to the formation of insulating secondary phases such as $La_2Zr_2O_7$ and porous morphologies in the final tapes (Figure 3.2c,d). In many cases, the obtained separators after sintering cannot be tested in electrochemical cells due to their high porosity making them fragile to handle.

3.3.1 Treatment of LLZO powders for the fabrication of slurries

Although several methods have been developed to remove impurities from the surface of LLZO, preventing its continuous surface degradation remains a major challenge. Coatings have been proposed as potential barriers to inhibit such surface reactions for different materials, but their practical application for LLZO is limited since coatings must be applied in a dry or protonation-limiting environment, which makes the process significantly more complex and costly. Moreover, LLZO coatings must simultaneously exhibit lithium ionic conductivity and stability at high sintering temperatures required for LLZO densification, criteria that are difficult to meet simultaneously. To effectively control the protonation of LLZO during tape casting, it is necessary to control moisture and CO_2 exposure. Storage under inert atmosphere (typically in a glovebox or dry rooms) can prevent surface degradation during powder handling.

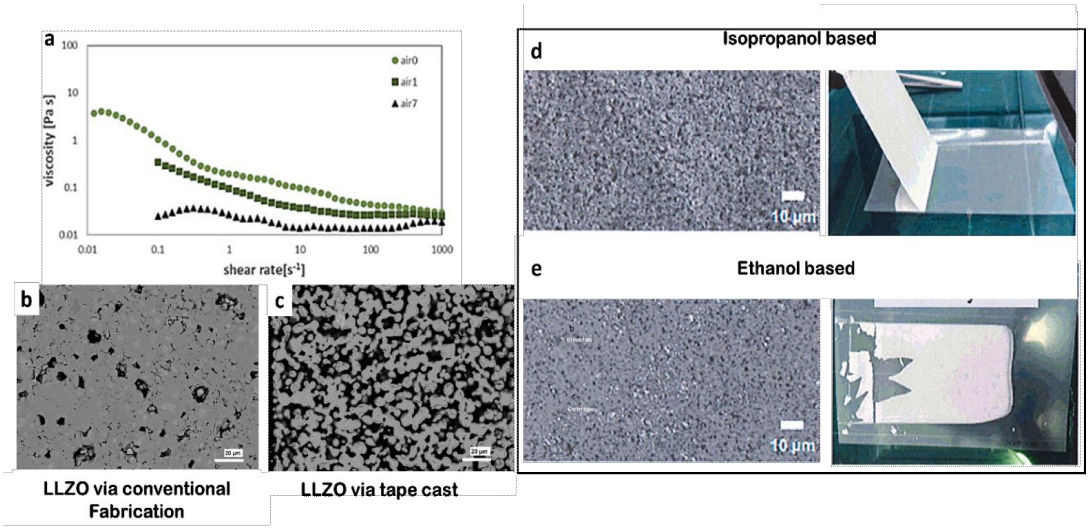


Figure 3.2| (a) Viscosity over shear rate of powders treated and stored in different atmospheres and periods (air0 = annealed in air, air1 = annealed in air and stored 1 day in air, air7 = annealed in air and stored 6 days). Reprinted from[16]; (b and c) SEM cross-section of sintered pellet and sintered tapes made of same starting powder[81]; (d and e) SEM (left) and photographs (right) of green tapes processed with different solvents (isopropanol and ethanol). Adapted from[155] with permission. Copyright Elsevier (2022).

However, maintaining such atmospheric control throughout the extended duration of the process, particularly during slurry preparation and casting, poses a significant technical and economical challenge. Several strategies have been proposed to reduce Li^+/H^+ exchange. One precautionary measure is to

introduce excess lithium during LLZO synthesis, typically between 7 and 50 wt%,[148,161] to compensate for losses during subsequent manufacturing steps. Another widely used strategy is to heat treat LLZO at around 750 °C in air. This process allows surface impurities such as Li_2CO_3 and LiOH to be efficiently removed from the LLZO before further processing according to the following reactions.[106,162]

$$Li_{7-x}H_xLa_3Zr_2O_{12}\cdot nH_2O \rightleftharpoons Li_{7-x}H_xLa_3Zr_2O_{12} + nH_2O \quad \text{Equation 3.1}$$

$$Li_{7-x}H_xLa_3Zr_2O_{12} \rightleftharpoons Li_{7-x}La_3Zr_2O_{12-x/2} + x/2H_2O \quad \text{Equation 3.2}$$

$$Li_{7-x}H_xLa_3Zr_2O_{12} + xLiOH \rightleftharpoons Li_7La_3Zr_2O_{12} + xH_2O \quad \text{Equation 3.3}$$

$$Li_{7-x}La_3Zr_2O_{12-x/2} + x/2Li_2CO_3 \rightleftharpoons Li_7La_3Zr_2O_{12} + x/2CO_2 \quad \text{Equation 3.4}$$

Rosen et al. demonstrated the effectiveness of heat treatment in increasing the reproducibility of the tape casting process. By removing surface contaminants such as Li_2CO_3, the fresh LLZO surface is better exposed to the dispersants in the slurry, promoting uniform coverage and stabilisation of the particles within the suspension,[16] as shown in Figure 3.3a. Subsequently, the better LLZO slurry suspension yielded a dense and mechanically stable separator (Figure 3.3b). To further reduce the formation of Li_2CO_3 during slurry preparation, our group has introduced a premixing step of the binder solution (consisting of binder, solvent, and additives) prior to the addition of LLZO. While dispersants are typically added before the binder to improve particle dispersion and break up agglomerates, this modified approach aims to reduce the direct contact time of the solvent with LLZO and has proven to be a helpful strategy.[130] We also showed that the incorporation of Li_2CO_3 during wet ball milling enables re-lithiation of LLZO by shifting the equilibrium of the protonation reaction to the left. This finding was supported by solid-state H-NMR analysis, which revealed a lower degree of protonation in samples milled with an add Li_2CO_3, resulting in a high-quality LLZO sintered separator[53], as shown in Figure 3.3d.

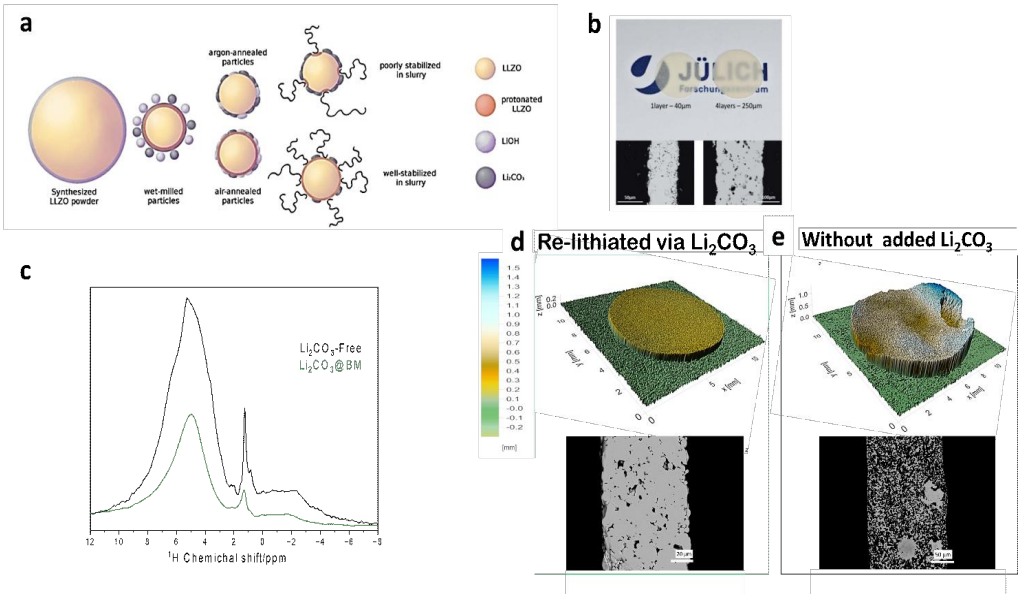


Figure 3.3| (a) illustration of LLZO surface coverage subjected to different heat treatments and their effect on slurry stabilization; (b) the SEM and photographs of sintered LLZO tapes obtained via air heat treated LLZO powder[16] ; (c) Comparison of proton SS-NMR of protonated LLZO powder (black) and relithiated powder by Li_2CO_3 (green). (d and e) comparison of 3D-light topography profiles (top) and SEM cross sections (bottom) of sintered tapes obtained from lithiated and non-lithiated LLZO[81].

3.4 Main problems during the sintering step

3.4.1 Li loss at high temperature

Sintering of LLZO requires high temperatures above 1100 °C and long dwelling times generally between 6-36 h[89,163,164] to achieve sufficient grain growth, neck formation, and pore elimination for dense ceramic tapes[102]. The precise sintering temperature depends on the LLZO dopant, as different dopant species and concentrations slightly modify the thermal behaviour of a material and onset of densification. Nevertheless, such high-temperature treatment inevitably induces “lithium loss” because of Li vitalisation according to Equation 3.5[165] or reactions with substrate sintering material[163]. Lithium in the LLZO can also react with atmospheric CO_2 at temperatures as low as 427 °C [73], which can cause Li depletion both during high-temperature sintering and the cooling stage. Thin LLZO tapes are particularly more susceptible to lithium loss due to their high surface-to-volume ratio, as demonstrated by Yi et

al.[148]. This enhanced Li depletion promotes the formation of Li-poor phases such as $La_2Zr_2O_7$, $La_2O_2CO_3$ as suggested by Equation 3.6[73], which are electronically, irreversible, insulating and significantly reduce the ionic conductivity of the separator[148].

$$Li_2O_{(s)} \rightarrow 2Li\ (g) + ½\ O_2 \qquad \text{Equation 3.5}$$

$$Li_7La_3Zr_2O_{12} + 4CO_2 \rightarrow 7/2Li_2CO_3 + ½\ La_2O_2CO_3 + La_2Zr_2O_7 \qquad \text{Equation 3.6}$$

Although LLZO densification can be achieved in ambient air, several studies have employed inert atmospheres (Ar or N_2) or oxygen-rich environments to suppress Li evaporation and reactions between lithium and atmospheric CO_2 during high-temperature sintering[148,153,161]. These controlled atmospheres have been shown to preserve the chemical composition and cubic structure of LLZO. Oxygen-rich atmosphere, in particular, often yields higher densities and ionic conductivities due to the high oxygen partial pressure, which inhibits reaction in Equation 3.6[165]. Often, sintering is performed using graphite sheets or carbon-based setters as sintering supports to prevent Li escape and to maintain the flatness of the sintered layers as will be discussed later. However, in these protocols, the inert atmosphere becomes necessary to prevent carbon oxidation that occurs in air and oxygen, and to prevent Li_2CO_3 formation.

In this regard, no single “best” sintering recipe exists for LLZO tapes, rather, a wide range of temperature-time-atmosphere combinations has been experimentally explored, as summarised in Table 3.4. The final performance of LLZO tapes cannot be attributed to sintering parameters alone. Variations in LLZO dopant chemistry, powder synthesis route (which determines crystallinity, particle size, and sintering reactivity), cell architecture, as well as differences in slurry formulation and tape-casting procedure, all critically affect densification and ionic conductivity. Even LLZO tapes fabricated from identical powders and sintered under the same conditions can exhibit markedly different properties, as differences in slurry formulation and tape-casting steps (dispersion quality, pretreatment, surface contamination) can affect sintering kinetics and final microstructure, leading to noticeable differences in density and ionic conductivity[81].

Table 3.4| Reported sintering conditions for LLZO tapes and their corresponding densities and ionic conductivities.

LLZO: structure dopant	Sintering steps	Temperature, dwelling time (°C,h)	Atmosphere,	Relative density of tapes after sintering (%)	Conductivity of tapes after sintering (S cm^{-1})	Ref
LLZO: Al (SSR: Solid state reaction**)**	2	(600°C, 1h) 1250°C, 5h)	Ambient	--	$0.8 \cdot 10^{-4}$	[152]
LLZO: Al, Ta (SSR)	1	(1175°C, 10h)	Ambient	92.8	$3.9 \cdot 10^{-4}$	[16]
LLZO: Al, Ta (SSR)	1	(1175°C, 10h)	Ambient	95	$1.8 \cdot 10^{-4}$	[81]
LLZO: Nb/ Li_3BO_3 (SSR)	2	(650°C, 1h) (1000°C, 10h)	Ambient Argon	90.8	$2.8 \cdot 10^{-4}$	[112]
LLZO: Al (SSR)	3	(600°C, 12h) (1100°C, 12h) (500°C, 2h)	Argon Air	>90	__	[155]
LLZO: Al:MgO (Commercial)	2	(700°C, 2h) (1115°C, 3h)	Air Argon	>90	$4.2 \cdot 10^{-4}$	[128]
LLZO: Ta (SSR)/ Li_2O	2	(650°C, 1h) (1100°C, 6h)	Air	99	$5.2 \cdot 10^{-4}$	[95]
LLZO: Al (LF-FSP: liquid-feed flame spray pyrolysis**)**	2	(1090°C, 1h) (800°C, 4h)	Nitrogen Oxygen	94	$2 \cdot 10^{-4}$	[148]
LLZO: Al, Ta (SSR)	1	(1175°C, 4h)	Air	90	$1.5 \cdot 10^{-4}$	[13]
LLZO: Al	__	__	__	95	$5 \cdot 10^{-4}$	[29]
LLZO: Nb,Ca	1	(1050°C, __h)	Oxygen	Porous Bilayer	$5.35 \cdot 10^{-4}$	[153]
LLZO: Ca, Nb (SSR)	2	(700°C, 4h) (1100°C, __h)	__	Porous Bilayer	$2.2 \cdot 10^{-4}$	[12,154]
LLZO: Ta/Al_2O_3(SSR)	3	(350°C, 4h) (700°C, 2h)	__	Al_2O_3 pellet-supported porous layer	__	[156]

In practice, sintering under inert atmosphere is less economically attractive for large-scale production, which is why the majority of published studies shifted to employing air sintering . As a technical measure to mitigate the risk of Li loss during sintering, sealed crucibles and a sacrificial LLZO powder bed are commonly employed to maintain a Li-rich sintering environment. The Li volatilisation at high sintering temperature induce lithium-deficient secondary phases formation, mainly pyrochlore ($La_2Zr_2O_7$) as evidenced by XRD pattern of sintered tapes when sintered with and without Li excess (Figure 3.4b). Another widely used strategy is to decrease the sintering temperature, time or both by utilizing sintering aids. Al_2O_3[89], whether added intentionally as a sintering aid or incorporated unintentionally from alumina crucibles, promotes densification in LLZO through eutectic phases formation (e.g., $LiAlO_2$), which can trap mobile lithium in grain boundaries, improving densification and reducing Li loss[166]. Although these mechanisms have been primarily evidenced in pelletised LLZO, analogous behaviour is anticipated in tape-cast systems given the same underlying chemistry. Other sintering aids such as Li_3BO_3[161], MgO[128] Li_2O [14], and ZnO[152] ,have been explored in tape-cast systems, each influencing densification through different mechanisms. Li_3BO_3 and Li_2O enhance densification through low-temperature liquid-phase formation which improved particle rearrangement and reducing residual porosity, thereby increasing conductivity. However, higher Li_3BO_3 concentrations lead to borate-rich intergranular phases (Figure 3.4c) which has shown to increase impedance at dosage higher than 1.5 wt% (Figure 3.4d). ZnO operates through a similar liquid-phase mechanism, which reduces porosity, presumably through increasing capillary forces and aiding grain relocation. Hanc et al.[167] reports that 0.05 wt% ZnO also improves sinterability and lowers the temperature of garnet formation. However, at higher ZnO loadings, Zn becomes reactive toward the Al-containing support substrates used during sintering. The Zn reaction toward Al-substrate foster secondary phases such as $LiAlO_2$, $LaAlO_3$, and $La_2Li_{0.5}Al_{0.5}O_4$ which, reduce both density and conductivity, demonstrating the narrow optimal window for ZnO dosage. MgO reduces Li loss through a mechanism that operates on the microstructural evolution during sintering. MgO has a very high melting point (~2852 °C)[168] and does not form eutectic or liquid phases with LLZO and instead remains chemically inert. During the initial and intermediate sintering stages, MgO distributes at LLZO grain surfaces and gradually segregates toward triple grain junctions. This redistribution suppresses abnormal grain growth and increases the tortuosity of grain-boundary pathways. As a result, the outward flux of Li^+ toward the surface is reduced, indirectly hindering long-range Li diffusion along the grain-boundary network and mitigating lithium volatilisation during high-temperature sintering[169]. As

demonstrated by Johnson et al.[157], MgO promotes uniform microstructures with minimal secondary-phase formation, while excessive MgO and extended sintering dwelling times leads to grain boundary segregation as shown in Figure 3.4e[157]. Notably, high relative density does not necessarily translate to high ionic conductivity, as densification may be accompanied by the formation of resistive secondary phases or grain boundary segregates. These secondary phases reduce effective Li-ion transport and introduce local variations in ionic conductivity and act as electronic blocking regions[170]. Nonetheless, these resistive regions create non-uniform current density distributions during cycling, manifesting as sites of localised current constriction that significantly reduce the critical current density and promote lithium filament nucleation even when LLZO has dense structures[171,172]. Direct comparison of sintering aid effectiveness across studies remains difficult owing to differences in LLZO dopant chemistry, sintering temperature, and dwell time all of which significantly influence microstructure development and ionic transport properties.

Table 3.5| Summary of reported sintering additives for LLZO and their influence on densification and ionic conductivity under different sintering conditions.

Additive	LLZO: dopant	Sintering temperature (°C)	Dosage (Wt%)	Density (%)	Ionic conductivity (S cm^{-1})	Ref
Li_3BO_3	LLZO: Nb	1000 (6h)	0	92.3	$1.28.10^{-4}$	[161]
			0.5	90.8	$2.82.10^{-4}$	
			1.5	83.0	$9.08.10^{-5}$	
			3	85.9	$7.21.10^{-5}$	
Li_2O	LLZO:Ta	1100 (6h)	__	99	$5.2.10^{-4}$	[95]
MgO	LLZO:Al	1115(3h)	0	89.3	$2.9.10^{-4}$	
			3	87.8	$4.2.10^{-4}$	
			5	91.0	$2.3.10^{-4}$	
			7	91	$0.3.10^{-4}$	
ZnO	**LLZO:Al**	1250 (5h)	0.05	__	$0.8.10^{-4}$	[167]

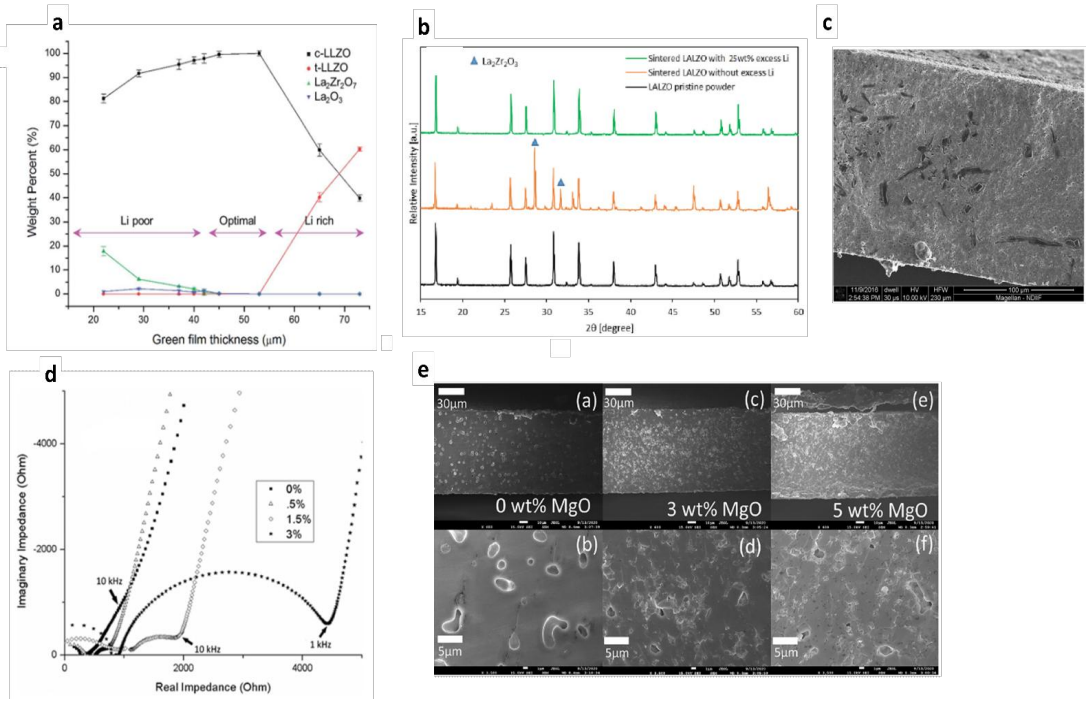


Figure 3.4| (a) Diagram of LLZO phase composition with thickness of the films heated in the same conditions[148]; (b) XRD patterns of sintered films with and without Li excess. Adapted from [155] with permission. Elsevier (2022); (c) SEM image of sintered LLZO showing the segregation of Li_3BO_3 sintering aid; (d) EIS plots showing the effect of the amount of Li_3BO_3 as sintering aid on the resistance of sintered tapes. Adapted from[161] with permission. Copyright Elsevier (2018); (e) SEM images of sintered tapes showing impact of the MgO addition to the microstructure. Adapted from[128] with permission. Copyright ACS Publications (2021).

3.4.2 Deformation of tapes during sintering and the influence of the sintering substrate

Beyond lithium loss and secondary phase formation, the high-temperature sintering of tape-cast LLZO separators introduces additional interrelated challenges that directly affect structural integrity, manufacturing yield, and separator reproducibility. These include adhesion to the crucible or sintering substrate, tape bending and warpage, and elemental interdiffusion between LLZO and substrate. One of the most persistent problems is crucible adhesion due to formation of sintering neck between the LLZO tapes and the sintering substrate at high temperature[173].This results in tapes adhering (sticking) to the crucible surface after sintering,[130] often resulting in mechanical damage and separator fracture during demoulding. While this may appear to be a minor handling issue on a laboratory scale, such defects on an industrial scale result in significant production losses and increased material waste, posing a major

obstacle to commercialization. Sheet deformation (warping, bending, curling) is another critical defect particularly observed in LLZO films sintering. Its primary cause is non-uniform particle size distribution in the green tape, where finer LLZO particles sinter and densify earlier than coarser particles, generating internal shrinkage gradients. As demonstrated by Rosen et al.[130], LLZO layers with particle-size gradients roll up completely during sintering (Figure 3.5a), rendering the separator unusable for cell integration. The non-uniform distribution or incomplete binder burnout can also induce asymmetric porosity and differential mass transport during sintering. Furthermore, secondary phases that form during earlier processing stages, such as slurry preparation (discussed above) and are retained within the green tape body introduce chemical and structural heterogeneity that directly impacts sintering behaviour. Since these phases densify at different temperatures from the LLZO matrix, sintering proceeds unevenly across the tape, generating localised differential shrinkage and asymmetric internal stresses. Upon cooling, these stresses manifest as macroscopic warping or curvature of the sintered separator[81,173]. An additional source of residual stress arises from the lamination of multiple green tapes prior to sintering which, is needed to achieve the desired separator thickness. The mechanical stresses introduced during pressing can be heterogeneously distributed across the laminated stack, producing non-uniform stress fields that persist at sintering temperatures and result in differential densification behaviour across the assembly.

Another critical challenge is elemental interdiffusion at elevated sintering temperatures. It is documented that elements from the sintering support or the crucible material, can diffuse into LLZO during sintering, resulting in various material transformations[71]. In some cases, the diffused elements can act as a sintering aid[174], improving densification. More commonly, however; such interdiffusion leads to undesired phase transformations and deterioration of properties of the final product[76]. For example, Al^{3+} from alumina sintering substrates can substitute for Li-ions in the LLZO structure particularly under conditions of lithium deficiency induced by prior volatilisation. The Al^{3+} diffusion into LLZO promotes the formation of Li-deficient secondary phases such as $La_2Zr_2O_7$ and $LaAlO_3$ at elevated temperatures. This behaviour was demonstrated by Johnson et al.[161] , who observed the emergence of these phases in XRD patterns when LLZO green tapes were sintered directly on Al_2O_3 plates (Figure 3.5d).

The above-mentioned problems are interconnected, and different lab-based strategies have been implemented, to mitigate them. To avoid element cross-diffusion and to support tape flatness during

sintering, LLZO films are commonly sintered on a sacrificial bed of “mother powder”, or on a pre-sintered LLZO pellet. Figure 3.5e schematically illustrates these protocols. The mother-powder or pellet layer act as both a physical and chemical barrier, preventing direct contact with the crucible and thereby reducing undesirable reactions with the support material[81,130,159]. It also provides a mechanically compatible substrate that helps preserve tape flatness during shrinkage. The improvement in tape flatness is evident when comparing LLZO films sintered on a mother-powder layer to those sintered directly on a bare substrate, as shown in the 3D topography images (Figure 3.5b,c). However, the LLZO powder bed or pellets degrade after repeated use and loses its ability to act as a barrier over several sintering cycles and must be replaced frequently with fresh material. This approach therefore presents significant scalability limitations, as the large quantities of mother powder required increases both material and operating costs. A similar strategy involves placing green tapes between graphite setter plates[158], this technique also prevents element diffusion and provides structural support but need inner atmosphere sintering to inhibit carbon oxidation. Parejiya et al.[160] reported that graphite “sandwich” assemblies yield flatter LLZO tapes compared to those sintered on mother powder alone (Figure 3.5g). However, peaks corresponding to residual graphite are clearly observed in LLZO XRD pattern after sintering (Figure 3.5d), indicating carbon contamination, which necessitates an additional high-temperature annealing step in air to remove residual carbon. These additional steps increase manufacturing complexity, operating costs, and processing time, making the method less attractive for large-scale applications[130]. These challenges highlight the urgent need for scalable, reproducible sintering strategies that satisfy the requirements of high densification, phase stability, and cost efficiency.

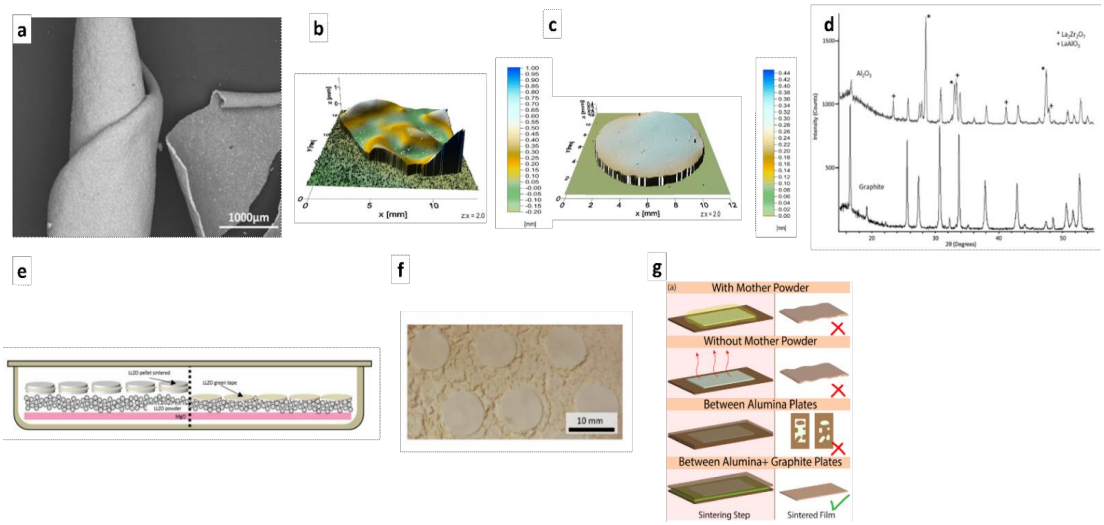


Figure 3.5| (a) SEM of sintered LLZO tape made of gradient particle size; (b and c) 3D light topography of sintered tapes with and without support. Reprinted from[130] with permission from M. Rosen-Finsterbusch; (d) XRD patterns of LLZO-Li_3BO_3 tapes sintered between graphite sheets in argon (bottom) and Al_2O_3 plates (top). Reprinted from[161] with permission. Copyright Elsevier (2018); (e) scheme representing possible sintering protocols for LLZO tapes (left) between LLZO pre-sintered pellets and (right) by using sintering bed of LLZO mother powder; (f) photographs of LLZO sintered tapes using a mother bed protocol[173]; (g) diagram of different sintering supports during sintering green LLZO films. Reprinted from[155] with permission. Copyright Elsevier (2022).

3.4.3 Integration of advanced sintering techniques

While conventional sintering processes for LLZO face significant challenges in terms of lithium loss and densification, advanced sintering techniques that combine high temperatures with external driving forces such as pressure or electric fields could offer an alternative. Processes such as spark plasma sintering (SPS), flash sintering (FS) employ Joule heating from electric fields to achieve rapid sintering temperatures (within seconds/ minutes) densification[102], significantly reducing lithium volatilisation and overall processing time compared to conventional sintering. Although these processes have been extensively researched for thick LLZO pellets[175,176] , their application to tape-cast thin separator layers remains at an early stage of development. A key challenge specific to tape-cast films is the presence of the organic binders in the green tapes, which must be removed by controlled binder burnout (de-binding process) prior to sintering. This step significantly compromises mechanical integrity complicating handling and increasing the risk of fracture. Additionally, those sintering techniques (such as SPS) use carbon moulds or foils can introduce carbon contamination or cause partial reduction of LLZO, necessitating an additional annealing step in air to oxidise residual carbon and restore LLZO stoichiometry[92]. Despite these challenges, these processes show promise for the rapid fabrication of

LLZO thin films. Initial publications in this field report phase stability at current densities exceeding 1 $mA \cdot cm^{-2}$[177] , though reproducibility and processing yield have not yet been systematically reported.

3.5 Post-Processing of Sintered Tapes

After successful sintering, post-processing steps of the LLZO-based components are needed for the integration in battery cells. These treatments involve modification of surface properties to improve compatibility with electrode materials[73,178] and establish good interfaces with lithium metal anodes[179], thus ensure optimal performance in solid-state batteries. The following sections discuss key post-processing techniques, their impact on the properties of LLZO separators, and the challenges associated with scaling them for industrial production.

3.5.1 Optimization of the surface

After sintering, LLZO separators remain highly susceptible to surface degradation and aging due to protonation. In dense separators, contact with air reportedly leads to rapid formation of Li_2CO_3 on the surface, with prolonged exposure extending this contamination also along the grain boundaries.[180] Even under controlled glovebox conditions (<0.5 ppm H_2O, <5 ppm CO_2), thin surface layers of LiOH and Li_2CO_3 has been confirmed to form within minutes.[181] These resistive layers significantly increase interfacial impedance in full cells and lead to inhomogeneous current distribution between the LLZO separator and the electrodes[68]. Consequently, they create uneven contact with the Li metal and localised current density which results in dendrite initiation and propagation.[182] Therefore, Li_2CO_3 must be removed before cell assembly. For thick pellets (500 nm- 1 mm), mechanical polishing is a standard method for removing surface contaminants; however, this approach is unsuitable for thin films due to their mechanical fragility. Alternatively, only force-free methods such as heat treatment can be used, as this effectively decomposes Li_2CO_3. This technique was used for tape-cast LLZO separator as demonstrated by Ye et al.[13]. In their work, SEM images (Figure 3.6a,b) of the as-sintered tapes showed dark surface regions indicative of low contrast Li_2CO_3 accumulation, which was confirmed by XRD (Figure 3.6c). The as-sintered tapes also exhibited a yellowish appearance consistent with carbonate contamination. After annealing in argon, the tapes became more transparent, the SEM surface contrast brightened (Figure 3.6a), and the Li_2CO_3 peaks disappeared from the XRD patterns, confirming successful carbonate removal. The heat-treated tapes enabled stable cycling for over 100 h in symmetric Li/LLZO/Li cells at 10

μA cm^{-2} (Figure 3.6d). A similar improvement in interface quality was reported following argon annealing was reported by Rosen et al[130], where removing the surface carbonate layer led to a pronounced decrease in interfacial resistance in Li/LLZO/Li cell from approximately 20 kΩ before annealing to about 0.5 kΩ after bakeout (Figure 3.6e). The authors reported that before heat treatment, the poor adhesion between molten lithium and the LLZO surface resulted in limited effective contact area; the lithium layer could be easily peeled off the separator, and the lithium surface in contact with LLZO exhibited a dark discolouration, consistent with reactions between lithium and surface-adsorbed species. After argon annealing, the LLZO surface was restored to a chemically clean state, and lithium-wetting was significantly improved. The molten Li adhered uniformly to the LLZO and could no longer be removed without damaging the interface, indicating a substantial increase in the effective contact area. The electrochemical response of the symmetric cell reflected this improvement. LLZO tapes annealed under argon exhibited flat and symmetric voltage plateaus during lithium plating and stripping at current densities up to 50 μA cm^{-2}, consistent with homogeneous lithium dissolution and deposition. Only above approximately 60 μA cm^{-2} did noticeable voltage asymmetry appear, signalling the onset of interfacial limitations (Figure 3.6f,g). This technique has subsequently been employed across multiple reported studies, where Li/LLZO/Li cells demonstrated critical current density (CCD) values in the range of 0.05 to 1 mA cm^{-2}[13,16,81]. The cost-effectiveness of argon annealing for large-scale production, however, remains limited by the requirement for controlled atmosphere equipment and additional processing time. Acid treatment represents an alternative method for removing surface contaminants from sintered thin LLZO separators. Acids such as HF, HCl, lactic citric or acid dissolve Li_2CO_3 and LiOH to form soluble salts (e.g., LiCl and LiF)[183]. Lactic acid ($C_3H_6O_3$)[184] has been shown to effectively remove Li_2CO_3 from LLZO pellets within 30 seconds according to Equation 3.7.

$$Li_2CO_3 + 2C_3H_6O_3 \rightarrow 2C_3H_5LiO_3 + CO_2 + H_2O \qquad \text{Equation 3.7}$$

Raman spectroscopy (Figure 3.6h), confirms the removal of the Li_2CO_3 by using acid treatments yielding a clean LLZO surface with significantly improved lithium wettability seen in Figure 3.6i,j. The acid-treated pellets demonstrated stable cycling for over 240 h in symmetric Li/LLZO/Li cells. Although this approach has not yet been demonstrated for tape-cast LLZO, the same chemical principle is anticipated to apply, and the reaction time required for Li_2CO_3 removal may be reduced owing to the smaller thickness and higher surface-to-volume ratio of tape-cast layers. The advantage of this process is inexpensive cost making it an attractive candidate for scalable industrial surface preparation. However, it poses significant challenges, such as the risk of LLZO corrosion and protonation during prolonged treatment[185].

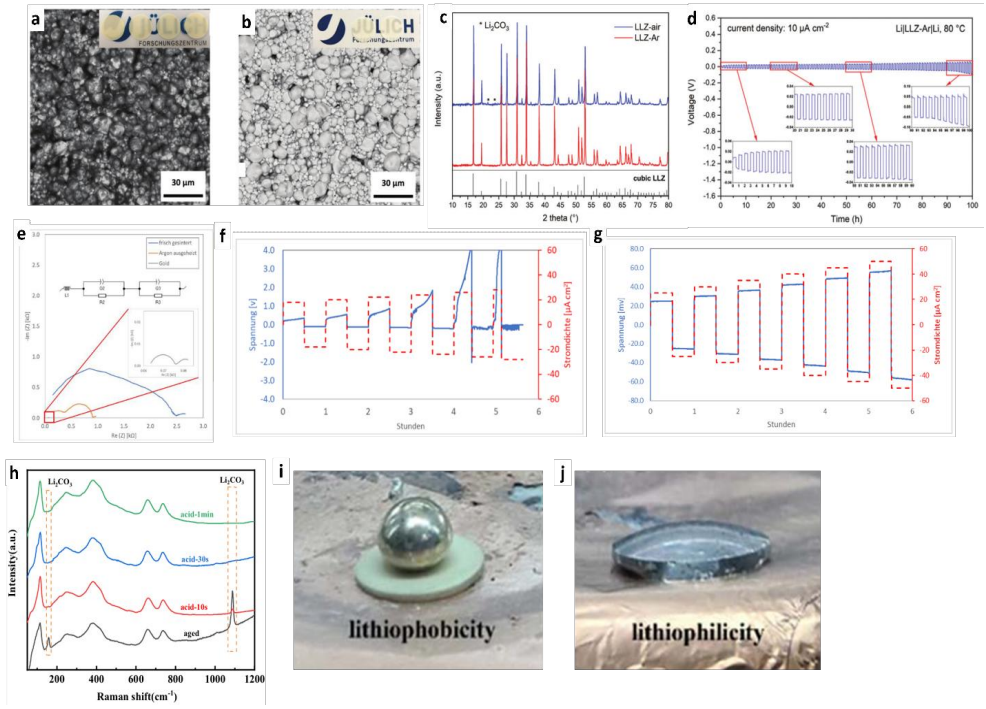


Figure 3.6| (a) surficial SEM image of LLZ-air (inset: photograph of LLZ-air); (b) surficial SEM image LLZ-Ar (inset: photograph of LLZ-air); (c) XRD patterns of LLZ-air and LLZ-Ar; d) galvanostatic cycling of a Li|LLZ-Ar|Li symmetric cell at 10 µA cm^{-2} at 80 °C. Adapted from[13] with permission. Copyright Royal Society of Chemistry (2020); (e) EIS spectrum of symmetric Li|LLZO|Li cells of the freshly sintered LLZO films and argon baked films at room temperature; f) critical current density by DC cycling of freshly sintered LLZO samples; (g) critical current density by DC cycling of argon-sintered LLZO samples. Reprinted from[130] with permission from M. Rosen-Finsterbusch; (h) Raman spectra of LLZTO-aged and LLZTO with different acid treatment times from 10 s and 1 minute on the solid electrolytes; (i and j) photograph of the wettability of molten lithium and LLZTO of aged pellet and after 30s acid treatment[184].

Unlike heat treatment, in which lithium can be reincorporated into the LLZO structure, acid treatment results in an irreversible loss of lithium[185]. Therefore, the storage and handling of LLZO thin films must be further optimised from an industrial perspective to ensure reliable cell integration.

3.5.2 Integration of tape-cast LLZO separators into the cells

Due to the inherent brittleness of thin LLZO ceramic separators, they are susceptible to fracture during battery assembly. Therefore, strategies to integrate LLZO separators into cells and maintain adequate interfacial contact with electrode components both during assembly and throughout operation are therefore essential. Despite the relevance of this challenge, it remains less evaluated in the LLZO tape-casting literature, and relatively few published results provide complete proof-of-concept demonstrations in symmetric or full-cell configurations. Early demonstrations employed melting lithium directly onto both surfaces of tape-cast LLZO to fabricate Li/LLZO/Li symmetric cells[13,16]. For full cells, a similar approach involves melting Li on one side while coating the opposing surface with a cathode slurry. Using this configuration, Li/LLZTO/$LiFePO_4$ solid-state cell has demonstrated stable cycling at 60 °C and 0.1C, delivering an initial capacity of 125.8 mAh g^{-1} and retaining 92.3% after 50 cycles[99] (Figure 3.7a). In symmetric Li/LLZTO/Li cells, the same tape-cast LLZO has also demonstrated stable plating-stripping for more than 300 h at 0.05 mA cm^{-2} at 60 °C (Figure 3.7b). Using the same technique, the CCD of Li/LLZO:Ta,Al /Li cell in other study reached critical current densities of 1 mA cm^{-2} without short circuit[119] (Figure 3.7c), further confirming the viability of tape-cast separators in Li-metal systems. In other full cell configurations, the thin LLZO was laminated with a ceramic LCO-LLZO composite cathode tape using a poly (ethylene oxide) (PEO) polymer interlayer as a catholyte to improve adhesion and ensure ionic conductivity at the cathode-separator interface [105] (Figure 3.7e). While the use of polymer interlayer provides a facile method of cell assembly, the cells using this protocol suffer from severe degradation[9] at current densities as low as 25 µA cm^{-2} (Figure 3.7d). The capacity fade was accompanied by a progressive increase in resistance, which has been attributed to microcrack formation and loss of electrical contact. Additionally, polymer interlayers introduce other disadvantages such as lower ionic conductivity, limited thermal stability, and chemical incompatibility with high-voltage cathodes (>4 V vs. Li^+/Li)[186]. more architecturally advanced approach employs trilayer LLZO design featuring porous-dense-porous structures (Figure 3.7f), in which the porous outer layer serves as three-dimensional ionic scaffolds that can be infiltrated with electrode active material. Such designs have been demonstrated in

particular by the Wachsman group[10]. Trilayer LLZO separators exhibit mechanical strength up to nine times higher than monolithic dense film separators as demonstrated by the breaking force measurement[12] (Figure 3.7g). The improved mechanical properties bring significant advantages for industrial handling and assembly. When combined with conventional NMC622 cathodes, hybrid cells incorporating trilayer LLZO demonstrated long-term cycling stability reaching 500 cycles at 2.3 mA cm^{-2} or 350 cycles at 1.15 mA cm^{-2} at room temperature and demonstrated operation across a range of current densities, albeit with decreasing delivered capacity at higher rates [10] (Figure 3.7h). In symmetric cells, CCD of 100 mA cm^{-2} was achieved at room temperature, and galvanostatic cycling in Li symmetric cells was demonstrated at current densities of 10, 20, 30, 50 or 60 mA cm^{-2}over 560 h without overpotential increase (Figure 3.7i). Nevertheless, in these advanced cell concepts, achieving uniform lithium wetting and stable interface formation often requires the deposition of thin metal-oxide coatings such as ZnO to improve Li wettability and interfacial stability. These coatings are typically applied using chemical vapour deposition (CVD) or atomic layer deposition (ALD), which provide excellent conformality but introduce substantial cost and scalability constraints from an industrial perspective. As an alternative, polymer interlayers can also be infiltrated into the porous LLZO prior to lithium application[154,187] to homogenise the surface by filling the pores and suppress localised current density hotspots that promote dendrite nucleation (Figure 3.7j). Symmetric cells assembled following this design exhibited stable cycling for 180 h at 0.3 mA cm^{-2} (Figure 3.7k)[46]

Despite this progress to integrate LLZO tapes into full solid-state cells, it is important to note that the demonstrated results have been achieved in hybrid cell configurations that include polymers either in the cathode or as interlayer. The hybrid solid-state configurations are constrained to moderate operating temperatures owing to the limited thermal stability of the polymer components employed [25]. To achieve all-solid-state batteries, LLZO separators must interface directly with an inorganic electrode. This concept can be realised by co-sintering LLZO with a ceramic cathode tape, or co-synthesising active cathode material directly into a porous LLZO framework. Nevertheless, co-sintering LLZO with cathode active materials requires careful management of chemical compatibility at elevated temperatures. Problems such as elemental interdiffusion, cation segregation, formation of electrochemically inactive secondary phases, and high interfacial resistance have all been reported at LLZO-CAM interfaces [24,91,92,96,113,115,117,118,188–191]. Those issues are further exacerbated in thin-film geometries owing to the

higher surface-to-volume ratio and increased susceptibility to lithium loss. These effects could significantly impair electrochemical performance and long-term stability, making co-sintering of LLZO with cathode materials one of the central fabrication challenges in the field.

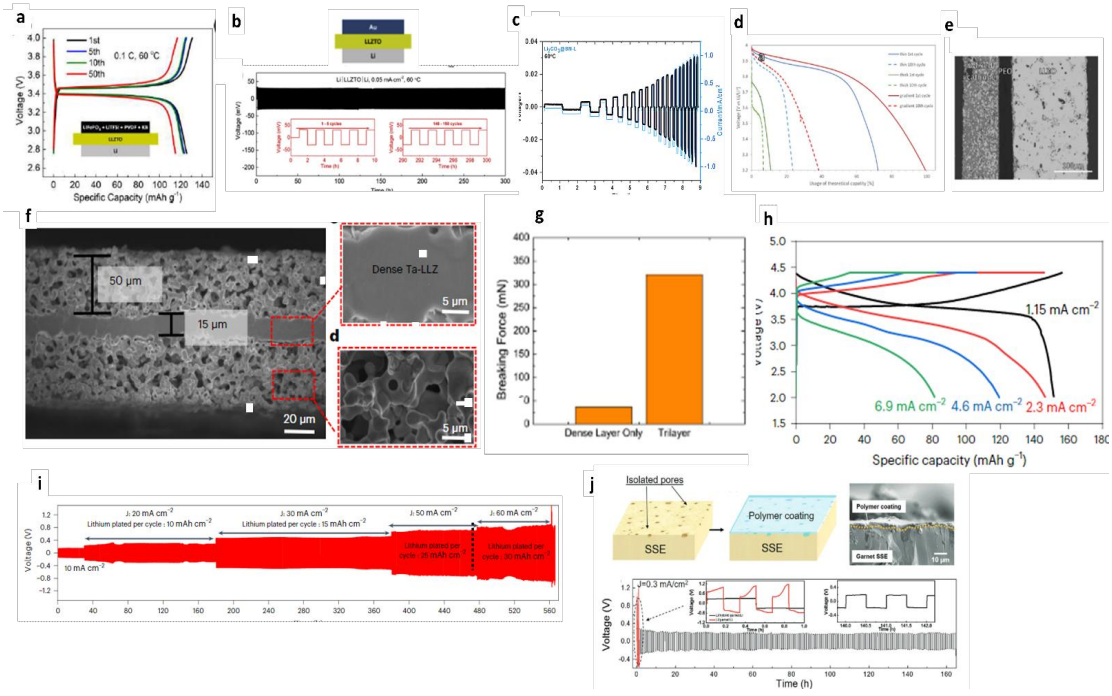


Figure 3.7| (a) charge-discharge curves for the solid-state Li/LLZTO/LiFePO4 battery at 0.1C; (b) voltage profiles of Li/LLZO/Au plating and striping. Adapted from[95] with permission. Copyright Elsevier (2019); (c) CCD of Li/LLZO/Li reaching 1mA cm^{-2} without breakage[81]; (d) discharge curves for Li/LLZO/PEO/LCO-LLZO semi-solid-state battery; (e) SEM cross-section of the Li/LLZO/PEO/LCO-LLZO semi-solid-state battery[9]; (f) SEM cross section of a porous-dense-porous LLZO separator. Reprinted from[10] with permission. Copyright Springer Nature (2023); (g) bar chart comparing the breaking force of porous/dense/porous (50µm/20 µm /50 µm) separator to the dense layer only (20 µm). Adapted from[12] with permission. Copyright Elsevier (2019); (h) charge-discharge curves of porous/dense/porous LLZO with a Li anode and a conventional cathode (NMC622) at RT; (i) galvanostatic cycling of a symmetric Li cell at a current density at different current densities reaching 60 mA cm^{-2}. Reprinted from[10] with permission. Copyright Springer Nature (2023); (j) illustration of Polymer infiltrated in porous LLZO with SEM image, (k); Voltage profile of the Li plating/stripping cycling with at 0.3 mA cm^2. Adapted from[154] with permission. Copyright Royal Society of Chemistry (2017).

3.6 Chapter summary

This chapter reviewed the challenges of fabricating LLZO ceramic separators by tape casting from a process-chain perspective, analysing each stage, from powder conditioning and slurry preparation to sintering, post-treatment, and cell integration. In this chapter , we comprehend that these challenges are not independent. Protonation-induced lithium loss during slurry preparation destabilises the slurry castability and reduces sintering activity; incomplete densification compromises phase purity and surface chemistry; and surface re-contamination after sintering impairs interfacial quality during cell integration. This cascade of interdependent effects collectively determines the electrochemical performance of the final separator. Yet in the literature, these challenges have largely been studied and addressed in isolation, without a systematic understanding of their cumulative impact across the production chain.

4 Minimising Lithium Loss in the Production of LLZO Separators Via the Tape-casting Process

Building on the systematic analysis of the challenges in LLZO tape casting presented in Chapter 3, this chapter investigates the protonation of LLZO throughout the entire tape casting fabrication chain, as well as its direct influence on the morphology and electrochemical performance of the resulting separators. The chapter is based on the research article published in Energy Storage Materials titled "*The Impact of Lithium Carbonate on Tape Cast LLZO Battery Separators: A Balanced Interplay between Lithium Loss and Relithiation"* by Kaouther Touidjine, Melanie Finsterbusch-Rosen, Vivien Kiyek, Swapna Ganapathy, Martin Finsterbusch, Olivier Guillon, Mark Huijben, Erik Kelder, Marnix Wagemaker, Dina Fattakhova-Rohlfing

Kaouther Touidjine conducted the experimental work, data analysis, and the first draft of the manuscript. The solid-state NMR measurements and their evaluation were performed by Dr. Swapna Ganapathy.

The link to the published research article: https://doi.org/10.1016/j.ensm.2024.103487

4.1 Background and chapter scope

Tape casting exposes LLZO powder to various chemical environments across sequential processing stages of varying degrees of Li^+/H^+ exchange that progressively depletes the LLZO structure of lithium, with consequent surface modification, as detailed in Chapter 3. A conventional approach to compensating for the lithium loss in LLZO fabrication is the incorporation of excess lithium during powder synthesis or at the sintering stage. Depending on the powder synthesis method and processing conditions, this excess Lithium can vary between 10 wt %[192,193] up to 50 wt %,[148] which increases the synthesis and manufacturing cost. The type of the employed Li source can affect the separator properties by changing the composition of the grain boundaries, introducing additional phases, and sometimes leading to additional porosity as explained in chapter 3. Table 4.1, gives an overview of the state of the art for tape-casting of LLZO separators, correlating the employed lithium-excess amount with the resulting electrochemical property. The lithium-excess concentration used across the published data reveal no convergence toward an optimal value, a scatter that reflects the absence of systematic understanding of lithium loss across processing, and it remains unclear which specific process stage of

the tape-casting chain contributes most critically to lithium depletion, and how this translates into separator microstructure and electrochemical performance degradation.

This chapter addresses this gap by systematically tracking the evolution of LLZO surface chemistry and phase composition at each stage of the tape-casting process chain and correlating these changes with separator microstructure and electrochemical performance. By identifying the critical processing step responsible for the highest degree of protonation and lithium loss, a targeted compensation strategy based on Li_2CO_3 addition is developed and evaluated with the aim of relithiating the LLZO and producing dense, flat, free-standing LLZO separators with competitive electrochemical performance through a simplified process with reduced lithium excess.

Table 4.2| Examples of lithium excess used in fabrication of thin LLZO separators

Composition	Li excess (mol %)	Ionic conductivity (mS cm^{-1})	CCD (mA cm^{-2})	Reference
$Li_{6.25}Al_{0.25}La_3Zr_2O_{12}$	50	0.2	n.d.	[148]
$Li_{6.5}Al_{0.25}La_3Zr_2O_{12}$	10,15,20	0.3	n.d.	[193]
$Li_{6.4}La_3Zr_{1.4}Ta_{0.6}O_{12}$	16	0.5	0.05 at 60°C	[95]
$Li_{6.4}5Al_{0.05}La_3Zr_{1.6}Ta_{0.4}O_{12}$	20	0.15	0.02 at 60°C	[13]
$Li_{6.45}Al_{0.05}La_3Zr_{1.6}Ta_{0.4}O_{12}$	20	0.39	0.3 at 60°C	[16]
$Li_{6.75}La_{2.75}Ca_{0.25}Zr_{1.5}Nb_{0.5}O_{12}$	10	n.d.	10 in 3D design	[12]

4.2 Processing Route as a Determinant of LLZO Separator Quality

To isolate the specific contribution of the tape-casting route to lithium depletion, the tape-casting process chain is benchmarked in this section against a conventional pressing-sintering route using identical starting powder. This direct comparison allows the lithium loss and phase degradation specifically introduced by the tape-casting to be estimated independently of powder-related variability, providing a process-specific baseline. Thus, LLZO separators were produced from a single batch of $Li_{6.45}Al_{0.05}La_3Zr_{1.6}Ta_{0.4}O_{12}$ (LLZO:Al,Ta) powder synthesised with 10 wt% excess lithium via three distinct routes: (i) conventional uniaxial pressing and sintering, serving as a reference baseline with minimal protonation exposure, (ii) tape casting with dry-milled powder, and (iii) tape casting with wet-milled powder. Routes (ii) and (iii) allow the specific contribution of wet milling and the associated solvent-

induced protonation risk to be isolated from other processing variables. The complete process flow and key differences between the three fabrication routes are illustrated schematically in Figure 4.1.

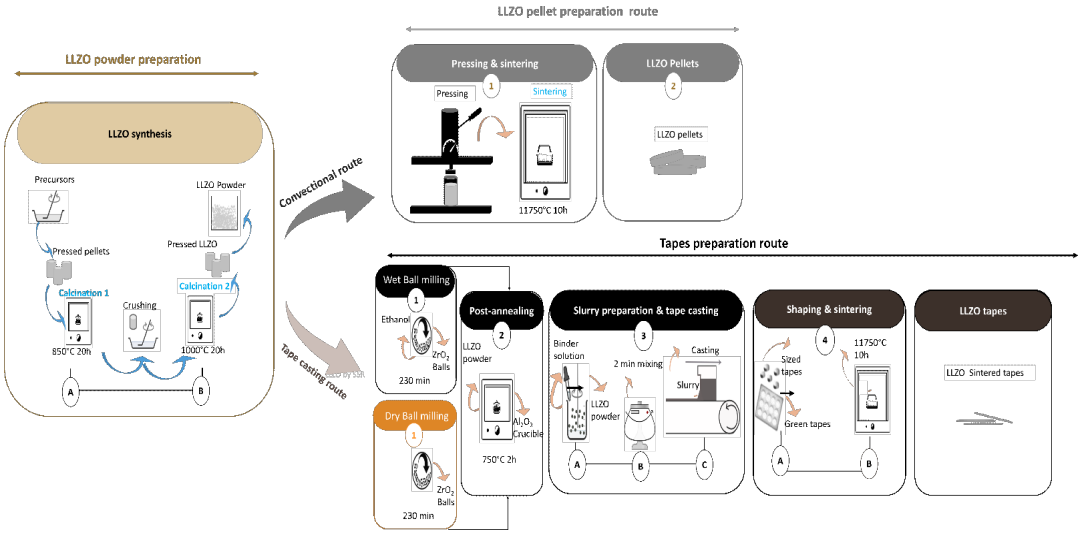


Figure 4.1| Schematic comparison of the conventional pressing-sintering route and the tape casting process chain for LLZO separator fabrication, illustrating the additional wet processing steps in tape casting that increase the risk of lithium loss and degradation

For the pressed-sintered reference samples, the as-synthesised LLZO powder, with a particle size of D50 ≈ 8.6 µm, was directly uniaxially pressed into pellets and sintered at 1175 °C for 10 h. In contrast, to enable tape casting, the same powder required an additional particle size reduction step, as the as-synthesised particle size was unsuitable for preparing homogeneous slurry. To achieve the necessary fine particle size and to investigate the influence of the milling environment on LLZO stability, both dry and wet milling (in ethanol) were performed under identical parameters (time and speed). The wet and the dry milled powders exhibited particle size distributions in the range of D50 ≈ 2.4 and 4.6 µm, respectively (Figure 4.2), adequate for slurry preparation and tape casting.

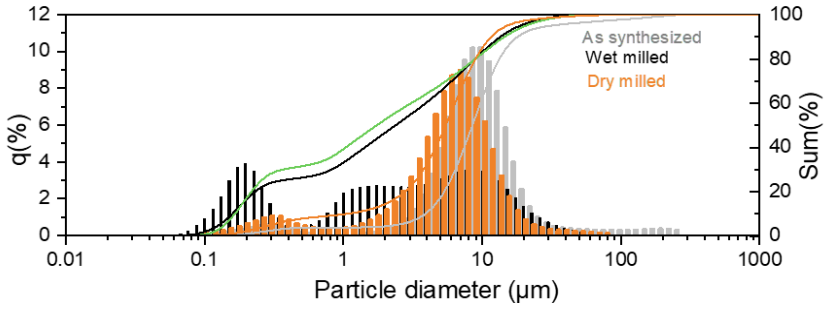


Figure 4.2| Particle size distribution of the LLZO powder: As synthesized (grey), wet milled (black), dry milled (orange)

Both powders could be successfully formulated into homogeneous slurries (Figure 4.3) which were subsequently cast and sintered in identical sintering conditions of the pressed pellets, including the same furnace, crucible, and sintering profile, thereby ensuring that any differences in phase stability, surface chemistry, and electrochemical performance between the two sample sets are exclusively attributable to the processing route, independent of sintering-related variables.

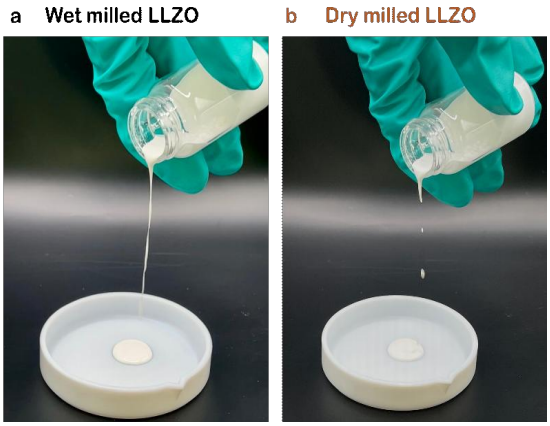


Figure 4.3|Photographs of the LLZO slurries obtained from the (a) wet-milled LLZO powder; (b) dry-milled powders.

The phase purity and electrochemical behaviour of the samples fabricated by pressing sintering and tape casting were first evaluated by XRD and electrochemical impedance spectroscopy (Figure 4.4). The pellets produced from the as-synthesised powder exhibit a dominant cubic LLZO phase with only minor

secondary phases of $LiAlO_2$, attributed to unintentional aluminium uptake from the alumina crucibles during sintering [194,195] (Figure 4.4a). The Nyquist plot of the impedance spectra (Figure 4.4 b) shows a single semicircle corresponding to the contribution of bulk and grain boundary conductivity, which could not be deconvoluted at room temperature owing to the overlapping time constants of bulk and grain boundary processes. The total ionic conductivity, derived from the low-frequency intercept, is 0.6 mS cm^{-1}. In contrast, the tapes prepared from both dry-milled and wet-milled powders exhibit a markedly lower phase purity. XRD analysis of the sintered tapes (Figure 4.4a) reveals the formation of secondary phases, notably Li_2CO_3 and $La_2Zr_2O_7$, indicating extensive Li^+/H^+ exchange reactions and lithium loss in tape casting route. This is reflected in the electrochemical behaviour, where the impedance spectra of both tape-cast samples (Figure 4.4b) display two distinct semicircles. The high-frequency semicircle corresponds to bulk resistance, with capacitances of 3.46×10^{-10} F and 1.03×10^{-10} F for the dry-milled and wet-milled samples, respectively. The low-frequency semicircle corresponds to grain boundary resistance, with capacitances of 5.49×10^{-8} F and 4.15×10^{-8} F, respectively. The total ionic conductivity is markedly reduced to 0.08 mS cm^{-1} for the dry-milled tape and 0.05 mS cm^{-1} for the wet-milled tape. The slightly lower conductivity of the wet-milled tape than the dry-milled tape, is potentially due to the greater protonation risk associated with solvent exposure during wet milling. Nonetheless, these results confirming the detrimental effect of processing route on both phase composition and electrochemical performance.

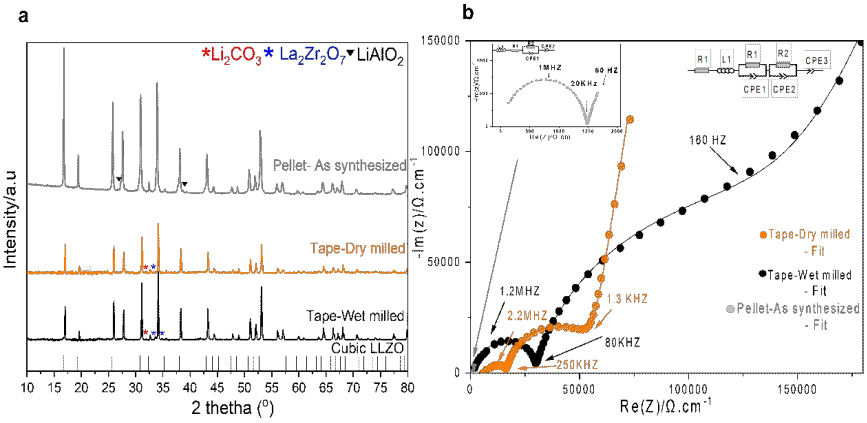


Figure 4.4|(a) XRD pattern; (b) Nyquist plots of the impedance spectra of the pressed pellet and tape cast LLZO separators sintered at 1175 °C for 10 h from dry and wet milled powders[81].

The microstructural analysis (Figure 4.5) further supports the observed electrochemical and structural degradation. The pressed-sintered pellets (Figure 4.5a) exhibit a dense microstructure with only 6% residual porosity, consistent with their high phase purity and ionic conductivity. In contrast, both dry-milled and wet-milled tape-cast samples (Figure 4.5b,c) show poor densification, with porosities up to 34%, indicating severely impaired densification. This inferior sintering behaviour is attributed to the formation of Li_2CO_3 and $La_2Zr_2O_7$ secondary phases (Figure 4.4a), which lower the sintering activity of LLZO by disrupting grain boundary migration and inhibit neck formation between LLZO particles, while the associated lithium depletion reduces the availability of lithium-rich transient phases that would otherwise promote densification during sintering[196]. The resulting porous microstructure and the second phases directly account for the elevated grain boundary resistance observed in the EIS measurements.

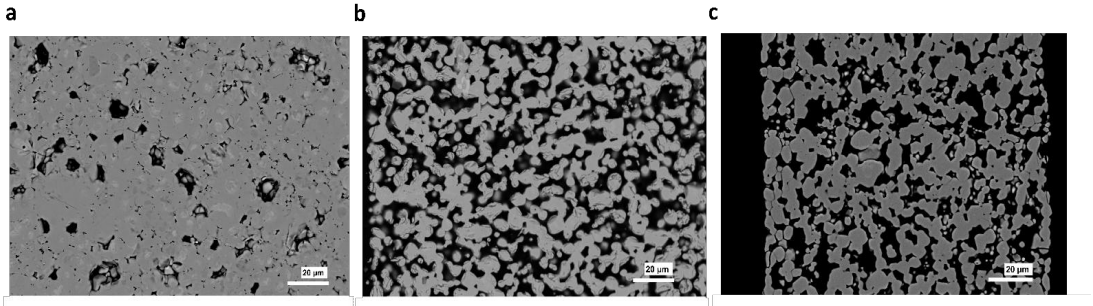


Figure 4.5| Cross-sectional SEM images of LLZO separators sintered 1175 °C for 10 h: (a) pressed-sintered pellet; (b) tape from wet-milled powder; (c) tape from dry-milled powder[81].

4.3 Optimization of Lithium Compensation Strategy via Li_2CO_3 Addition

4.3.1 Effect of Li_2CO_3 Addition Timing on LLZO Morphology and Phase Stability

The pronounced degradation of tape-cast LLZO separators necessitates targeted lithium compensation along the process chain. To address this, Li_2CO_3 was selected as the relithiation agent due to its favourable characteristics for LLZO processing. Li_2CO_3 naturally forms on LLZO surfaces upon air exposure and can reintegrate into the LLZO lattice without introducing impurities or promoting the formation of unwanted phases. Additionally, its chemical neutrality prevents pH alterations in the tape-casting slurry, unlike LiOH, and does not require modifications to the established tape casting parameters.

To systematically evaluate the effect of lithium compensation timing, Li_2CO_3 was introduced at distinct process steps, namely during ball milling, annealing, slurry preparation, and sintering (Figure 4.6). The amount of Li_2CO_3 was fixed at 2.6 wt% relative to the LLZO powder, corresponding to an additional 10 mol% lithium excess with respect to LLZO stoichiometry. This concentration was selected based on prior works and preliminary experiments[6,7], as a representative value for effective lithium loss mitigation without introducing processing complexity. The tapes obtained in the processes in which Li_2CO_3 was added either during ball milling, annealing, slurry preparation, or sintering steps are assigned further as Li_2CO_3@BM, Li_2CO_3@annealing, Li_2CO_3@slurry, Li_2CO_3@sintering, respectively.

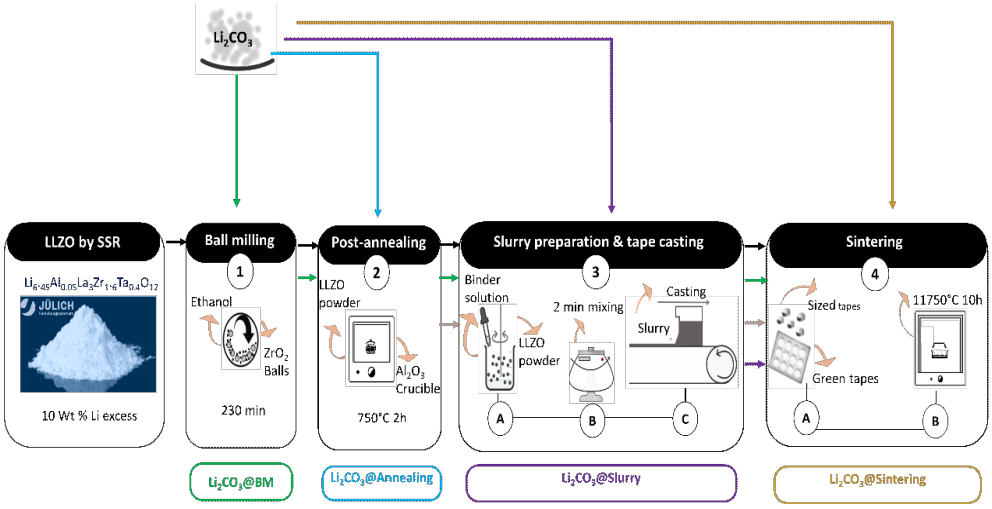


Figure 4.6| schematic overview of the main process steps in the studied tape-casting process and labelling of samples for different insertion points of Li_2CO_3[81]

XRD analysis of the sintered samples (Figure 4.7) revealed that the phase composition of the sintered tapes resulting from all variants of the process route corresponds to cubic LLZO, indicating that Li_2CO_3 as an excess lithium source and the chosen concentration are suitable to produce phase-pure LLZO separators.

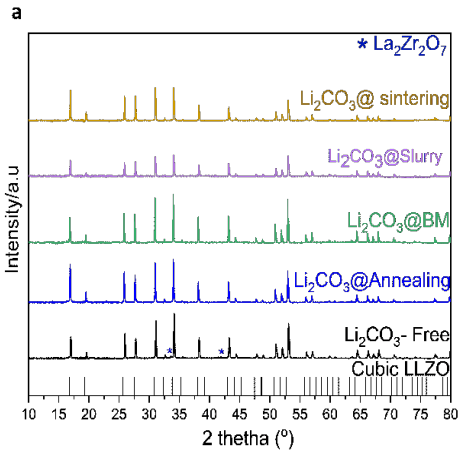


Figure 4.7| XRD patterns of sintered LLZO tapes at 1175 °C for 10 h: Li_2CO_3 was added to ball-milling (Li_2CO_3@BM,green), Li_2CO_3 was added annealing (Li_2CO_3@Annealing,blue), Li_2CO_3 was added to slurry (Li_2CO_3@Slurry, purple), Li_2CO_3 was added to sintering (Li_2CO_3@Annealing,yellow). All compared to tape prepared in the same condition without Li_2CO_3 addition (Li_2CO_3-Free, black)[81].

However, white light topography and cross-sectional SEM images of sintered separators images (Figure 4.8), reveal notable differences in morphology and topography. Only the tapes prepared via the Li_2CO_3@BM route (where Li_2CO_3 was added during wet ball milling) are flat and exhibit sufficient densification to serve as functional separators. The Li_2CO_3@BM samples have a relative porosity of 5.8%, similar to the porosity achieved with conventionally pressed samples (Figure 4.5a). The separators prepared by other routes show a pronounced warpage and edge curling caused by inhomogeneous shrinkage, (Figure 4.8a-e) and low relative densities (Figure 4.8f-j) with porosities above 35%, although all samples were sintered under the same conditions and showed high phase purity in the XRD analysis. The mechanically damage separators preclude cell assembly and electrochemical characterisation. This observation demonstrates that the stage of Li_2CO_3 introduction governs its efficacy as a relithiation agent and this stage-dependent behaviour implies that Li_2CO_3 interacts differently with the LLZO surface chemistry and phase composition at the intermediate process steps.

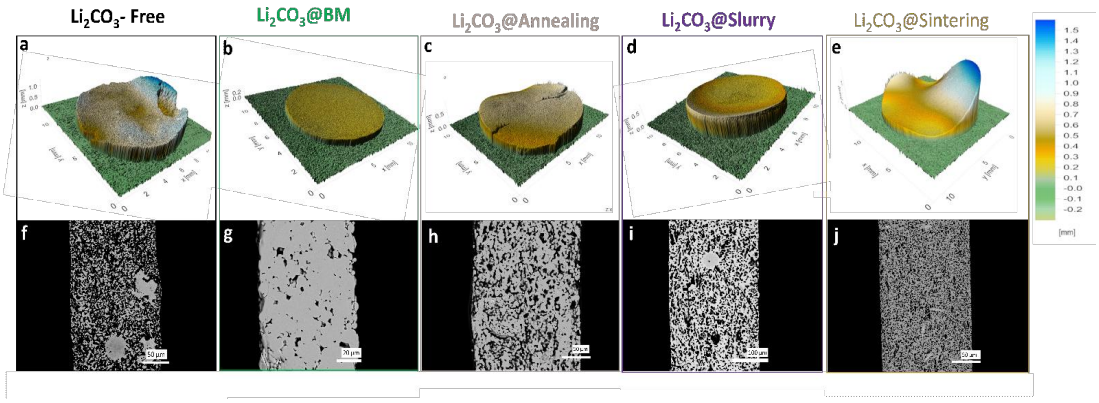


Figure 4.8| White light topography images of sintered tapes: (a) wet-milled starting powder; (b) Li_2CO_3@BM; (c) Li_2CO_3@ Annealing; (d) Li_2CO_3@Slurry; (e) Li_2CO_3@Sintering. Cross-sectional SEM images of sintered separators: (f) wet-milled starting powder; (g) Li_2CO_3@BM; (h) Li_2CO_3@ Annealing; (i) Li_2CO_3@ Slurry; (j) Li_2CO_3@ sintering[81].

The XRD analysis of the powders collected at intermediate stages of the process chain (Figure 4.9) further elucidates the effect of Li_2CO_3 addition timing on phase evolution. In the Li_2CO_3-free powders (Li_2CO_3-Free), $La_2Zr_2O_7$ formation was detected after the ball milling step, confirming that lithium loss and structural destabilisation are already initiated at this early stage (Figure 4.9a). In contrast, when Li_2CO_3 was introduced during ball milling, the cubic LLZO phase was retained with significantly suppressed $La_2Zr_2O_7$ formation (Figure 4.9a). This means that the Li_2CO_3 addition at the ball milling significantly hinders the protonation of LLZO and the associated formation of $La_2Zr_2O_7$. It can be assumed that adding Li_2CO_3 in this step shifts the equilibrium of the protonation reaction in ethanol towards LLZO stoichiometry, reducing the amount of protonated phase and thus minimizing the undesirable changes in the LLZO crystal structure.

The addition of Li_2CO_3 at the annealing stage (Li_2CO_3@annealing) resulted in the formation of $LiAlO_2$ as an unintended secondary phase (Figure 4.9b), attributed to the poor dispersion of the solid Li_2CO_3 at this stage, leading to localized reactions with the alumina crucible. The consumption of lithium by this parasitic reaction reduces the amount available for relithiation of the protonated LLZO, thereby indirectly promoting the persistence of $La_2Zr_2O_7$.

The XRD patterns of the green tapes showed no significant phase changes relative to the annealed powders (Figure 4.9c), consistent with the minimal LLZO exposure time to solvent during slurry preparation and tape casting. Accordingly, the Li_2CO_3@slurry sample exhibited a phase composition comparable to the Li_2CO_3-free reference, confirming the Li_2CO_3 addition at the slurry stage is therefore

insufficient to counterbalance the structural degradation and protonation already accumulated in the preceding processing steps, as evidenced by the persistent $La_2Zr_2O_7$ phase fraction comparable to that of the Li_2CO_3-free reference. Notably, the Li_2CO_3@BM sample exhibited only a weak $La_2Zr_2O_7$ reflection at the green tape stage, which was absent after annealing, demonstrating that Li_2CO_3 addition during ball milling effectively delays the onset of protonation, confining the residual Li^+/H^+ exchange to the later and shorter solvent exposure steps rather than allowing it to propagate from the earliest stage. Given the clear superiority of ball milling as the critical intervention point for Li_2CO_3 addition, the following section investigates the mechanistic origin of this protective effect through complementary Raman and solid-state NMR spectroscopy.

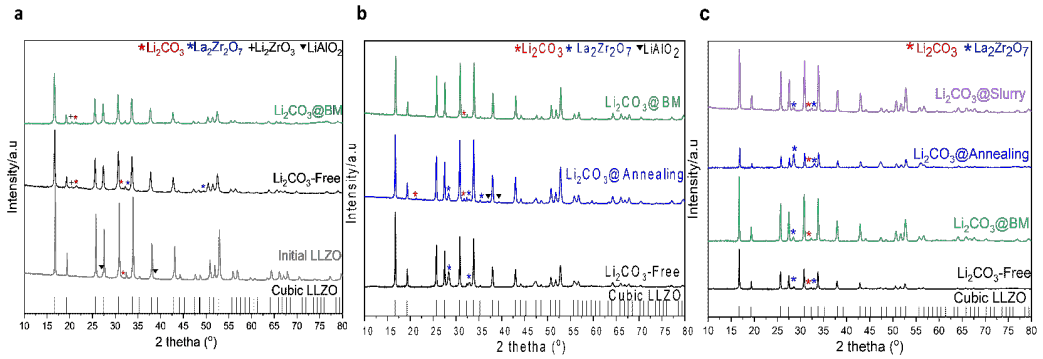


Figure 4.9 | XRD patterns of LLZO powder and tape samples at intermediate processing stages: (a) dried powder after ball-milling; (b) powder after annealing; (c) green tapes. Li_2CO_3 was added during ball milling (Li_2CO_3@BM, green), annealing (Li_2CO_3@annealing, blue), slurry preparation (Li_2CO_3@slurry, purple)[81].

4.3.2 Raman and NMR Investigation of Li_2CO_3-Mediated Protonation Suppression during Ball Milling

To elucidate the mechanistic origin of the improved phase stability conferred by Li_2CO_3 addition during ball milling, LLZO powders were processed under two conditions: ball-milled with Li_2CO_3 (Li_2CO_3@BM) and ball-milled without Li_2CO_3 addition (Li_2CO_3-free), followed by drying and annealing at 750 °C for 2 h. The annealed powders were analysed by Raman spectroscopy (Figure 4.10a) and solid-state NMR spectroscopy (Figure 4.10b,c). The Raman spectra of the annealed powders confirmed that the Li_2CO_3@BM sample retained the cubic LLZO phase as the dominant component, while the Li_2CO_3-free sample showed significant $La_2Zr_2O_7$ formation, consistent with the XRD results (Figure 4.9b). A Raman peak at 326 cm^{-1}, characteristic of the low-temperature cubic LLZO phase (LT-LLZO)[197–199], is detected

in both samples, but to a much lesser extent in the powder_Li_2CO_3@BM sample. To confirm the attribution of this peak to Li^+/H^+ exchange, a validation experiment was conducted in which protonation severity was intentionally increased by adding 5 wt% water during milling (H_2O@BM). The resulting pronounced enhancement of the 326 cm^{-1} peak unambiguously supports its assignment to protonation-induced structural modification, consistent with the stronger proton donor character of water relative to ethanol (Chapter 3). furthermore, a broad peak at 289 cm^{-1} characteristics of the $La_2Zr_2O_7$ phase[200] was detected exclusively in the powder processed without additional Li_2CO_3 (Li_2CO_3-Fee), confirming the profound Li loss in this sample. It can be therefore safely concluded that the addition of Li_2CO_3 during ball milling can significantly reduce the Li^+/H^+ exchange during processing. The characteristic Raman peaks of Li_2CO_3 t at 156 cm^{-1}, 194 cm^{-1}, and 1090 cm^{-1} [201] in the Raman spectra indicate the presence of Li_2CO_3 on the surface of the particles. This is due to the handling of the powders, and since the Raman spectroscopy measurement is performed after annealing in ambient air, some Li^+/H^+ exchange is to be expected.

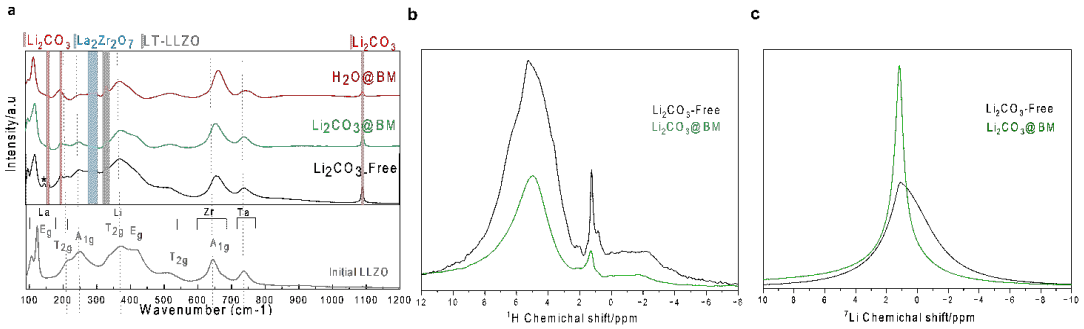


Figure 4.10| (a) Raman spectra of annealed LLZO powders: wet-milled without the addition of Li_2CO_3 (powder_Li_2CO_3-free, black), with addition of Li_2CO_3 (powder_ Li_2CO_3@BM, green) , and without addition of Li_2CO_3, but with additional water (powder_H_2O@BM red); (b) 1H-NMR spectra of annealed LLZO powders: wet-milled without addition of Li_2CO_3 (powder_Li_2CO_3-free, black) and with addition of Li_2CO_3 (powder_Li_2CO_3@BM, green); (c) 7Li-NMR spectra of annealed LLZO powders: wet-milled without addition (powder_Li_2CO_3-free, black) and with addition of Li_2CO_3 (powder_ Li_2CO_3@BM, green)[81].

^{1}H-NMR spectroscopy (Figure 4.10b) of the Li_2CO_3-free sample exhibited a broad main peak at 5.29 ppm assigned to lattice-incorporated protons in the LLZO lattice[202], with two shoulders at 3.65 ppm and 6.35 ppm. The presence of multiple resonances indicate that protons occupy multiple distinct crystallographic sites, which is a direct signature of extensive Li^+/H^+ exchange and progressive substitution of lithium

across both tetrahedral and octahedral lattice positions. Narrow peaks at 1.2 ppm and 0.9 ppm, present in both samples, are assigned to surface-adsorbed water[106], while an additional resonance at −2 ppm is attributed to LiOH[202]. The Li_2CO_3@BM sample exhibit a single, narrow resonance at 5.29 ppm, indicating that that protons occupy a single site in the LLZO lattice, consistent with a higher lithium content (as confirmed from Li-NMR). Importantly, the overall peak intensities in the Li_2CO_3@BM spectrum were significantly reduced relative to the Li_2CO_3-free reference, providing direct evidence that Li_2CO_3 addition during ball milling effectively attenuates Li^+/H^+ exchange during solvent exposure and limits proton incorporation into the LLZO framework.

^{7}Li-NMR spectrum of the Li_2CO_3@BM sample (Figure 4.10c) shows a singular peak at 0.5 ppm, characteristic of well-defined Li^+ occupancy within a single crystallographic environment of the LLZO lattice. The Li_2CO_3-free sample, by contrast, displayed a markedly broad signal encompassing multiple overlapping resonances, consistent with the coexistence of several distinct lithium environments. This confirms the formation of Li-containing impurity phases such as Li_2CO_3 or LiOH during heat treatment in the absence of a lithium-source, and the redistribution of Li in tetrahedral and octahedral LLZO sites, which generally occurs in proton-exchanged LLZO[202]. The ^{1}H and ^{7}Li NMR results are consistent with the Raman and XRD findings, providing direct spectroscopic evidence that Li_2CO_3 addition during wet ball milling effectively suppresses Li^+/H^+ exchange, reduces proton incorporation into the LLZO lattice, and preserves lithium site occupancy.

4.3.3 Process Refinement: Lowering Li_2CO_3 Addition during Ball Milling

Having established the timing of Li_2CO_3 addition as critical, further process optimisation was pursued by reducing the concentration of lithium excess added during ball milling. The Li_2CO_3 content was decreased by 50% relative to the previously used concentration, corresponding to an additional lithium excess of only 5 mol% relative to the LLZO stoichiometry. XRD analysis conducted after each processing step (Figure 4.11a) confirmed that even at the lower lithium excess, high phase purity was maintained throughout the process chain. Minimal traces of $La_2Zr_2O_7$ were observed only in the green tape, consistent with previous results obtained at higher Li_2CO_3 content (Li_2CO_3@BM). SEM cross-sectional analysis (Figure 4.11b) revealed a homogeneous microstructure with a closed porosity of 4.7% and minor secondary phase inclusions (1.1%) exhibiting bright contrast. Achieving equivalent microstructural quality with only 5 mol% excess lithium compared to the 10-50 mol% typically reported in the literature. This represents a significant improvement in process efficiency and material utilisation.

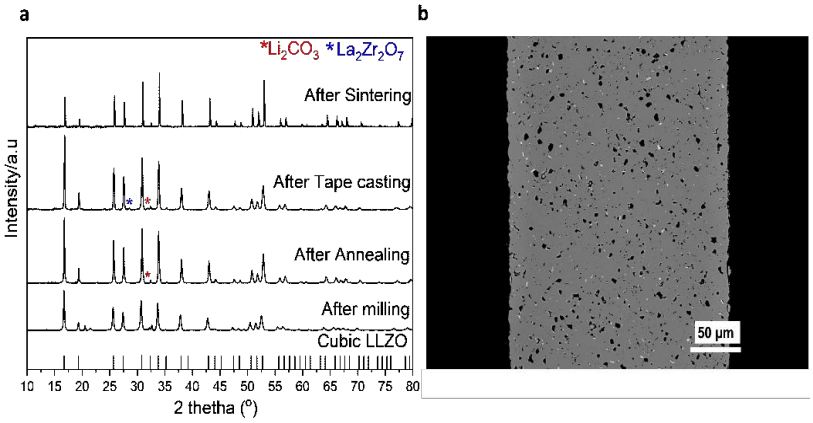


Figure 4.11| (a) XRD analysis of the primary process steps with lowered addition of Li_2CO_3; (b) cross-sectional SEM images of sintered BM-L separator[81].

Energy-dispersive X-ray spectroscopy (EDX) analysis of the bright-contrast inclusions (Figure 4.12) revealed a higher concentration of lanthanum and oxygen, suggesting residual La_2O_3 from the initial powder synthesis, rather than degradation-induced phases. These findings demonstrate that, by targeting the ball milling step for lithium compensation, it is possible to significantly reduce the required lithium excess while preserving phase purity and microstructural quality (density, flatness, mechanical

stability). This reduction directly lowers material cost and processing complexity without compromising separator quality.

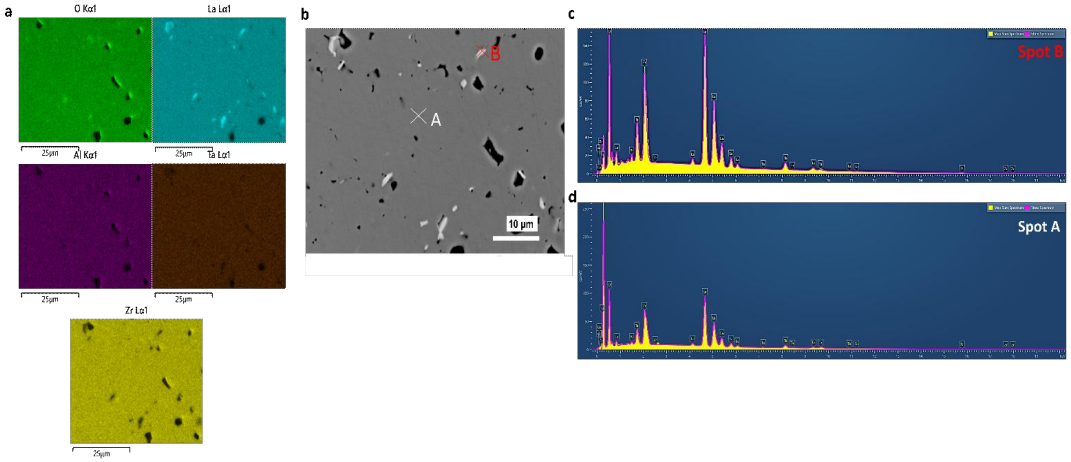


Figure 4.12|(a) EDX measurements of Oxygen; Lanthanum, Aluminium, Zirconium, and Tantalum; (b) magnified SEM picture of Li_2CO_2@BM-L; (c) point analyses of spot A and B, respectively.

4.4 Electrochemical Evaluation of Optimized LLZO Tape-Cast Separators

The electrochemical performance of LLZO separators fabricated with optimised lithium compensation strategies was evaluated through impedance spectroscopy (EIS), critical current density (CCD) measurements (Figure 4.13), and long-term cycling in symmetric Li/LLZO/Li cells (Figure 4.14). Separators prepared with 10 mol% excess lithium (Li_2CO_3@BM-H) and a reduced 5 mol% excess (Li_2CO_3@BM-L) were compared to assess the influence of Li_2CO_3 electrochemical performance. EIS revealed Nyquist plots characterised by a single semicircle for both samples (Figure 4.13a), representing overlapping contributions from bulk and grain boundary resistances. The extracted capacitances (3.57×10^{-10} F for BM-H and 3.46×10^{-10} F for BM-L) were comparable, confirming comparable charge transport characteristics for both samples. The total ionic conductivities at room temperature were 0.16 mS·cm^{-1} for Li_2CO_3@BM-H and 0.18 mS cm^{-1} for Li_2CO_3@BM-L, indicating that reducing the lithium excess by half does not compromise ionic conductivity, consistent with the phase purity and densification observed in previous structural analyses.

The suitability of the optimized separators for lithium-metal battery applications was further validated through lithium plating and stripping tests. Symmetrical Li|LLZO|Li cells were assembled with gold adhesive layers to ensure uniform contact with lithium electrodes. capacitive CCD measurements at 60 °C demonstrated that both Li_2CO_3@BM-H and Li_2CO_3@BM-L samples withstood current densities up to 1 mA cm^{-2} without dendrite formation, which is a competitive result for tape-cast separators produced by a cost-efficient processing route and without external stack pressure during cell testing (Figure 4.13b,c). Interestingly, the Li_2CO_3@BM-L separator exhibited flatter potential steps and lower polarization compared to its higher lithium excess counterpart, despite the slightly lower ionic conductivity. This suggests enhanced interfacial stability and reduced defect concentration, aligning with the observed density improvements.

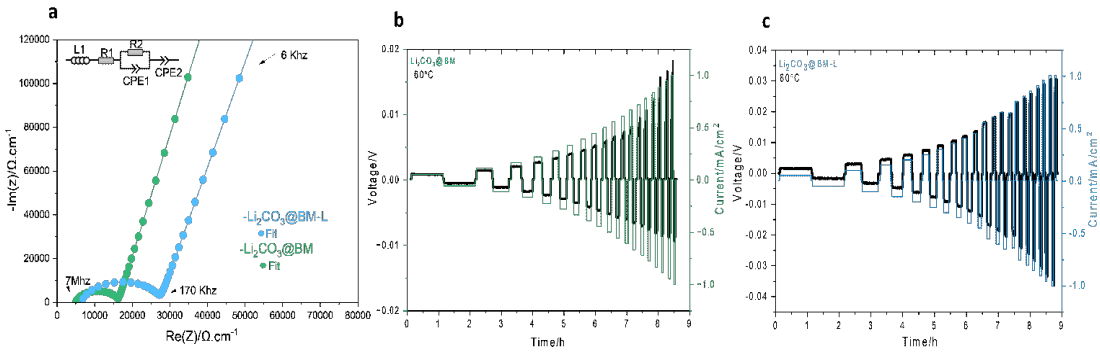


Figure 4.13|(a) Impedance spectra of optimized and sintered Li_2CO_3@BM-H and Li_2CO_3@BM-L samples, normalized for sample thickness; (b) CCD measurement of Li_2CO_3@BM-H; (c) CCD measurement of Li_2CO_3@BM-L[81].

Long-term cycling tests at current densities of 0.05, 0.1, 0.25, and 0.5 mA cm^{-2} confirmed stable operation over 225 h (Figure 4.14), with minor polarization effects attributed to surface roughness and contact imperfections rather than intrinsic material limitations as evidenced by the absence of significant resistance growth in intermediate-EIS measurements (Figure S1, appendix). These results demonstrate that the optimized tape casting process with targeted lithium compensation enables the fabrication of LLZO separators with high electrochemical performance while significantly reducing lithium excess. This process refinement not only improves separator quality but also enhances economic viability, supporting the development of scalable and cost-effective solid-state battery technologies.

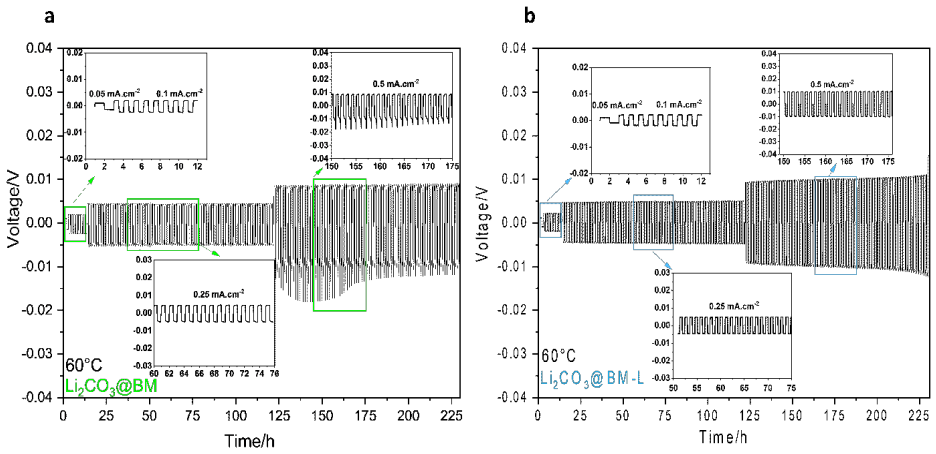


Figure 4.14| Galvanostatic cycling of Li|LLZO|Li cells at 0.05 mA cm^{-2},0.1mA cm^{-2}, 0.25 mAcm^{-2}, 0.5 mA cm^{-2} at 60° C : (a) Li_2CO_3@BM; (b) Li_2CO_3@BM-L[81].

4.5 Chapter summary

This chapter systematically investigated the evolution of LLZO protonation and lithium loss across the tape-casting process chain and their impact on separator quality. Benchmarking the tape-casting route against a conventional pressing–sintering route using identical starting powder demonstrated that tape casting induces significantly greater lithium loss, leading to insulating secondary phase formation and high residual porosities. This establishes that the poor mechanical stability and low ionic conductivity of tape-cast separators originate primarily from protonation-induced porosity rather than from intrinsic powder limitations.

To counteract protonation, Li_2CO_3 was introduced as a relithiation agent at four distinct stages of the tape-casting workflow. Wet ball milling was identified as the most critical intervention point. Raman spectroscopy, XRD, and solid-state ^1H and ^7Li NMR confirmed that Li_2CO_3 addition during milling effectively suppresses Li^+/H^+ exchange and limits secondary phase formation, enabling good sintering activity and the obtention of functional dense, flat LLZO separators by economically feasible approach.

The Li_2CO_3 excess was further reduced to 5 mol% relative to LLZO stoichiometry, which was shown to be sufficient to fully preserve the garnet phase and achieve dense separators with a residual porosity of ~4.7% . The obtained dense, flat, and phase-pure tape-cast separator achieved an ionic conductivity of

0.16 and 0.18 mS cm^{-1}, a critical current density of 1 mA cm^{-2} at 60 °C, and stable galvanostatic cycling (pressure-less) over 225 h in symmetric Li|LLZO|Li cells.

5 TAPE-CAST NMC-BASED COMPOSITE CATHODES FOR SOLID-STATE BATTERIES

Building on the tape-casting process developed for LLZO separators in the previous Chapter 4, this chapter extends the tape casting methodology to the fabrication of thick, free-standing Ni-rich NMC-based composite cathode layers for LLZO-based solid-state batteries and critically evaluates the role of LLZO as a catholyte under realistic processing conditions. By correlating cathode chemistry, secondary phase formation and electrochemical response, this work demonstrates how the balance between ionic and electronic percolation determines capacity utilization and ionic resistance of hybrid polymer–ceramic SSBs.

This chapter is adapted from an article published in *Batteries & Supercaps* with the title "*Tape Casting LLZO Ceramic Separators: An Overview of the Challenges, Optimization Strategies, and Paths to industrial implementation".* By Kaouther Touidjine, Christoph Roitzheim, Xiaochen Liu, Walter Sebastian Scheld, Andreas Paulus, Muhammad Zubair, Mark Huijben, Erik Kelder, Marnix Wagemaker, Martin Finsterbusch, Dina Fattakhova-Rohlfing

Kaouther Touidjune conceived and led the work by developing and optimizing the tape-casting process, performing the experimental work, conducting structural and electrochemical analyses, interpreting the results, and drafting the manuscript. Xiaochen Liu optimized polymer interlayers for full-cell assembly. Andreas Paulus performed the Rietveld refinement of the XRD data.

Link to the published article: https://doi.org/10.1002/batt.202500959

5.1 Chapter background and scope

Unlocking the full energy density potential of LLZO-based solid-state batteries with lithium metal anodes requires the use of high-capacity CAMs incorporated into thick, three-dimensionally (3D) percolating composite cathode layers, where intimate contact between the CAM and the solid electrolyte ensures both ionic and electronic continuity throughout the cathode volume[203,204], as discussed in Chapter 1. Tape casting is particularly well-suited for this purpose, offering precise control over layer thickness and CAM loading while enabling the scalable fabrication of large-area, free-standing composite cathode tapes. However, tape-cast of 3D ceramic composite cathodes for LLZO-based cells have to date been

limited to $LiCoO_2$ (LCO), owing to its comparatively high thermal stability against LLZO during co-sintering[9,205].

High-capacity Ni-rich $LiNi_xMn_yCoz O_2$ (NMC) offers a compelling alternative, but its chemical reactivity with LLZO already at temperatures near 600 °C[96,115,118], and its sensitivity to protonation in protic processing environments have prevented its integration into tape-cast composite cathode architectures prior to this work.

To overcome the limited thermal compatibility between NMC and LLZO, liquid-phase sintering strategies using additives with low melting points were explored. In particular, Li_3BO_3 (LBO) was used as a sintering aid to enable the consolidation of NMC-LLZO composite cathode at reduced temperatures of 750 °C [161,206,207]. Using this approach, fully inorganic NMC-based SSBs were successfully fabricated by screen printing thin composite cathode layers onto dense LLZO thick substrates and then sintered at low temperatures[24,96,119]. Although this approach allows sufficient densification of cathode layers, chemical interactions between NMC and LLZO cannot be completely suppressed[96,208]. Reported $LiNi_{0.8}Mn_{0.1}Co_{0.1}O_2$ (NMC811) screen-printed cell designs exhibit limited capacity utilisation, with reported discharge capacities for NMC811-LLZO composite cathodes not exceeding 120 mAh g^{-1}[96], which is well below the theoretical capacity. An alternative strategy for eliminating thermal incompatibility issues is to completely exclude LLZO from the cathode and use LBO as a catholyte. In the NMC-LBO configuration, LBO enables low-temperature sintering, serves as catholyte, and suppresses the LLZO-related secondary phase formation. However, it should be taken into account that LBO has significantly lower (by almost three orders of magnitude) ionic conductivity compared to LLZO and is therefore generally applicable only to thin cathode layers[161]. Using screen-printing techniques, the NMC111-LBO composite cathodes have delivered a discharge capacity of up to 140 $mAh \cdot g^{-1}$ without detectable secondary phase formation after co-sintering[209]. It is noteworthy that the reported performance of LLZO-free cathodes has only been demonstrated for thin layers when extended to thick cathodes with high CAM loading, it remains unclear whether these composite cathode configurations can be implemented successfully. It can be expected that in an LLZO-free configuration, the low ionic conductivity of LBO would lead to pronounced polarization in thicker layers, while in the LLZO-containing cathodes, the formation of detrimental secondary phases can increase the interfacial resistance and most likely further impede the ion and electron transport across the electrode thickness.

In this chapter, we have developed a tape-casting route to produce thick oxide ceramic Ni-rich NMC-based composite cathodes for solid-state batteries. We developed a slurry formulation that enables stable dispersion of NMC, LLZO, and LBO and allows reproducible fabrication of free-standing cathode tapes with controlled thickness and high active material loading. Two cathode configurations were investigated: (i) NMC-LLZO-LBO composite cathodes, in which LLZO with high ionic conductivity acts as catholyte and LBO serves as the sintering aid, and (ii) LLZO-free NMC-LBO cathodes, in which LBO, with its significantly lower ionic conductivity, is the only ionic conductor and thus performs both the function of a sintering aid and that of a catholyte. After co-sintering, the residual porosity of the ceramic cathode tapes is infiltrated with a polymer electrolyte with and without conductive carbon additives to form hybrid polymer-ceramic solid-state batteries. By systematically comparing the structural and chemical properties of the resulting NMC cathode configurations with their electrochemical performance in full cells with and without carbon, we elucidate how the cathode chemistry, the secondary phase formation, and the balance between ionic and electronic transport pathways govern the capacity utilization and cycling stability of tape cast Ni-rich NMC based composite cathodes.

5.2 NMC composite cathode fabrication:

5.2.1 Tape casting process optimization

To produce free-standing NMC-based composite cathode tapes, the established tape-casting process developed in Chapter 4 for LLZO separator fabrication was adopted. The slurry for casting composite cathodes contained LLZO as the catholyte, NMC as cathode active material and Li_3BO_3 (LBO) as sintering aid[210]. While the overall workflow was retained, significant modifications were required to the slurry formulation to account for the differences in the chemical composition and reactivity of the additional components NMC and LBO. The binder polyvinyl butyral (PVB) had to be changed due to its incompatibility with LBO. Li_3BO_3 can undergo partial dissociation in aqueous and polar solutions, leading to the formation of borate species such as $B(OH)_4^-$ and $B_2O_4^{2-}$ through reactions similar to the hydrolysis of B_2O_3[211]. These borate species readily coordinate with hydroxyl-rich polymers such as in PVB, promoting uncontrolled crosslinking and gelation. In this case, this resulted in severe slurry thickening and polymer-like behaviour, rendering the slurry uncastable (Figure 5.1).

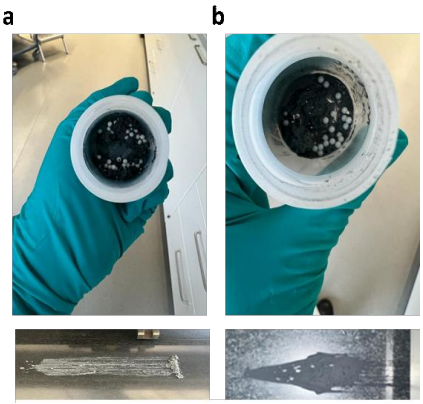


Figure 5.1| Photographs of the first slurries trial using polyvinyl butyral (PVB) as binder : (a) NMC-LLZO-LBO; (b) NMC-LBO.

To resolve this incompatibility, the binder system was re-evaluated, and PVB was replaced with carboxymethyl cellulose (CMC), a polysaccharide-based binder with a more chemically tolerant structure. Despite also containing hydroxyl groups, CMC exhibited significantly lower reactivity with borate species under the same solvent conditions, likely due to its linear, anionic backbone and weaker coordination affinity. At the same time, the concentration of the ammonium-based dispersant (BYK-180) in the slurry was reduced to avoid excessive basicity, which could otherwise promote further borate dissociation and destabilise the slurry rheology. Prior to slurry preparation and tape casting, the LLZO and NMC powders were ball milled to reduce particle size and achieve a more uniform distribution suitable for tape casting. Particle size distribution (PSD) analysis confirms that the milling significantly shifted particle size distributions of both LLZO and NMC powders toward the submicron and low-micron range (Figure 5.2), improving the homogeneity and dispersion of the slurry. The LLZO powder was annealed in air at 750 °C after ball milling to remove Li_2CO_3 formed on the particle surface due to protonation, established in Chapter 4. The LBO powder was manually ground to avoid any structural or compositional changes associated with high-energy solvent-based milling.

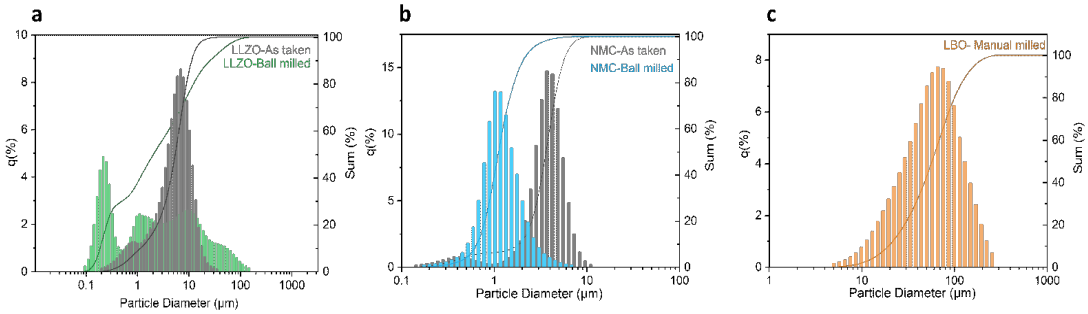


Figure 5.2 |Particle size distribution of the composite cathode powders before and after milling: (a) LLZO; (b) NMC; (c) LBO

The optimised binder system and controlled particle size distribution enabled the preparation of stable, homogeneous composite cathode slurries suitable for tape casting. The process comprises four separate steps, namely (i) powder conditioning (pre-treatment), (ii) slurry preparation, (iii) slurry casting, (iv) shaping, pressing and sintering (Figure 5.3)

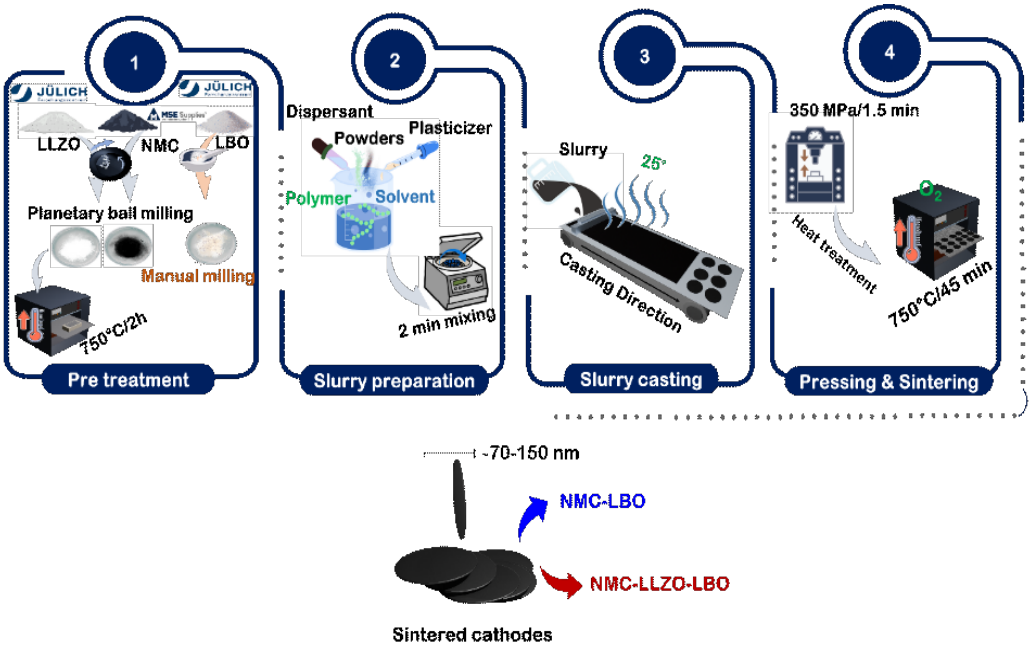


Figure 5.3| Schematic of the composite cathode fabrication process, including powder pre-treatment, slurry preparation, tape casting, and pressing/sintering.

Following this optimised protocol, two different composite cathode variants were prepared, namely NMC-LLZO-LBO (46:46:8 wt%) and NMC-LBO (92:8 wt%). The LBO content was set at 8 wt% in both configurations to minimize the effect of LBO on electrochemical performance, as LBO possesses a significantly lower lithium-ion conductivity (~2×10^{-6} S cm^{-1})[161] than LLZO (1×10^{-3} S cm^{-1})[212] and fluctuations in its concentration could otherwise lead to uncontrolled differences in ionic transport within the composite cathode. After tape casting and drying, uniform green tapes were obtained for both composite cathode compositions (NMC-LBO and NMC-LLZO-LBO). The green tapes exhibited good flexibility and mechanical integrity. The dried green tapes could be handled and punched into discs of 10 mm without cracking and showed uniform thickness across the entire cast area, as shown in Figure 5.4



Figure 5.4| Photographs of modified NMC composite slurry and tapes: (a) fresh NMC-LBO cast slurry; (b) dried NMC-LBO tape; (c) disc-shaped NMC-LLZO-LBO tape

5.2.2 Sintering composite cathode

The sintering temperature and atmosphere were selected with consideration for the thermal sensitivity of Ni-rich NMC material ($LiNi_{0.8}Mn_{0.1}Co_{0.1}O_2$), which is prone to oxygen loss and structural degradation at elevated temperatures and in reducing atmospheres[118,213]. To mitigate this, sintering was performed at 750 °C for 45 min in a pure oxygen atmosphere. The temperature choice was supported by TGA/DTA measurements of LBO (Figure 5.5a), which confirmed a melting onset at approximately 750 °C. The sintering duration of 45 min was determined experimentally as the minimum time required to achieve sufficient densification and mechanical stability (shorter durations such as 30 min resulted in mechanically fragile cathode layers). The pure oxygen atmosphere was necessary to preserve Ni in the oxidation state Ni^{3+} and suppress the formation of oxygen-deficient reduced phases that could impair the electrochemical performance[118,214]. The temperature ramped from room temperature to 600 °C at

a rate of 2 °C min^{-1}, with intermediate dwell steps of 15 min at 200 °C and 600 °C. to ensure complete solvent evaporation and binder decomposition, respectively, before the onset of ceramic densification. This controlled burnout minimises gas pressure build-up, reduces internal stress gradients, and thus suppresses warping or deformation of the tapes during subsequent high-temperature sintering. The full sintering profile, including heating rate, dwell time, and cooling ramp, is presented in Figure 5.5b.

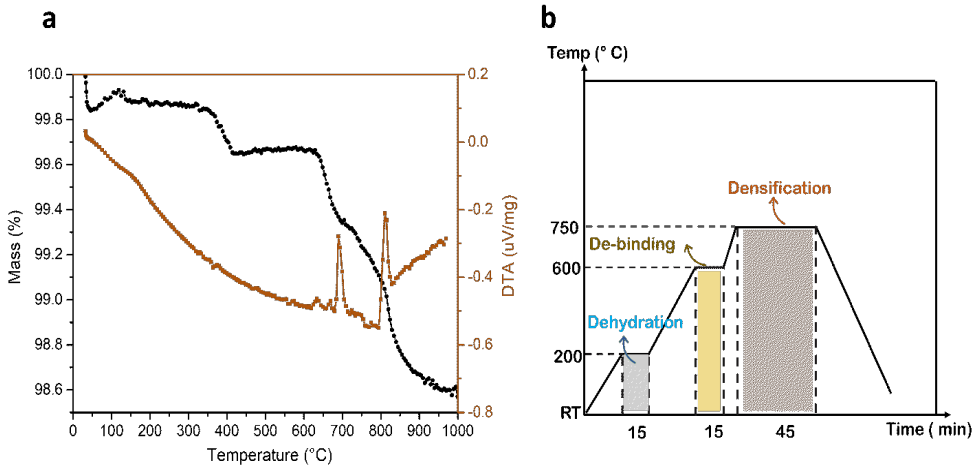


Figure 5.5 | (a) TGA/DTA analysis of LBO showing endothermic events near 750-810 °C; (b) schematic illustration of key temperature stages during sintering, highlighting dehydration, de-binding, and densification.

After sintering, free-standing, fully ceramic composite cathodes with a diameter of 9.4 mm were obtained. Both composite cathode tapes (NMC-LBO and NMC-LLZO-LBO) exhibited sufficient mechanical integrity and remained visibly flat, as shown in the photographs (Figure 5.6a,d). Optical profilometry further confirms a uniform surface topography at the microscale (Figure 5.6b,e) and shows uniform, flat surfaces without significant warping or delamination. The successful retention of tape geometry confirms the effectiveness of the optimised slurry formulation and controlled sintering conditions.

Cross-sectional SEM images showed comparable final thicknesses of approximately 90 µm for both tapes (Figure 5.6c,f). This dimensional consistency is particularly important to ensure uniform current distribution and minimising cell-to-cell variability during electrochemical characterisation.

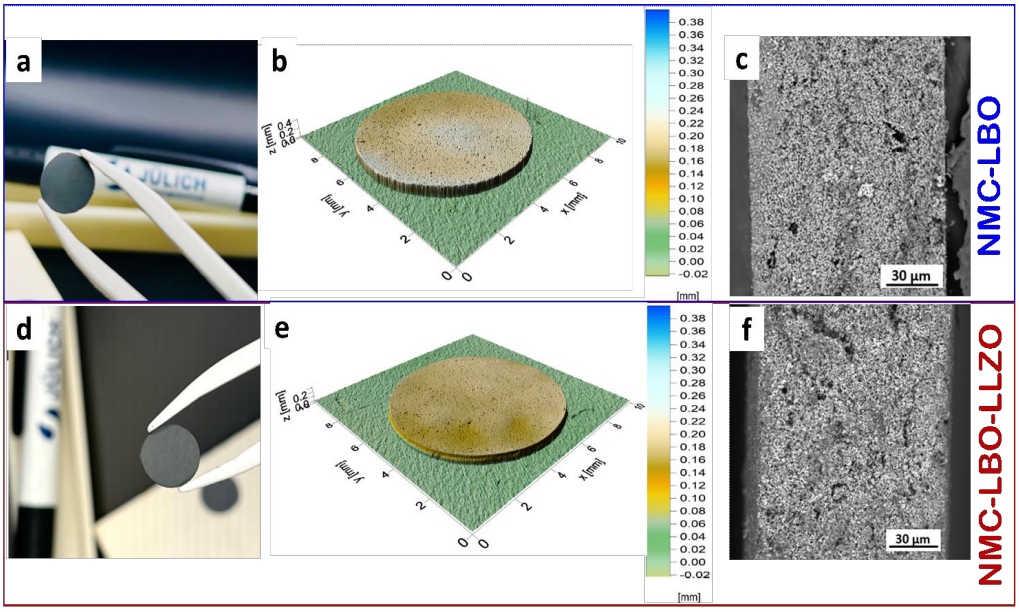


Figure 5.6| Morphological comparison of sintered composite cathodes. NMC-LBO (top, blue frame) and NMC-LLZO-LBO (below, red frame): (a and d) photographs of the sintered tapes at 750 °C in pure oxygen; (b and e) white light topography showing flatness and thickness uniformity of sintered tapes; (c and f) SEM images of cross-sections of cathode tapes after sintering at 750°C for 45 min.

5.3 Structural analysis of composite cathode:

SEM analysis of fracture surfaces reveals a densely packed granular microstructure for both NMC-LBO and NMC-LLZO-LBO composite cathodes (Figure 5.7a,b)**.** The backscattered electron (BSE) images distinguish the constituent phases based on their atomic number (Z) contrast. LLZO (containing heavy La and Zr) appears as very bright particles, while the NMC particles are light grey. Due to its low average atomic number, the LBO phase appears as dark grey regions surrounding the LLZO and NMC particles, which is confirmed by EDX analysis (Figure S4, appendix). The spatial distribution and morphology of these LBO-rich regions suggest liquid phase-assisted densification during sintering. Moreover, they appear similar in both composites, confirming that LBO does not undergo any detectable reactions with the other components under the processing conditions applied. SEM/EDX does not detect any additional secondary phases with distinct morphology or material contrast at the magnifications investigated. This suggests that all secondary phases identified by XRD are either present in low volume fractions or below the spatial resolution of SEM/EDX.

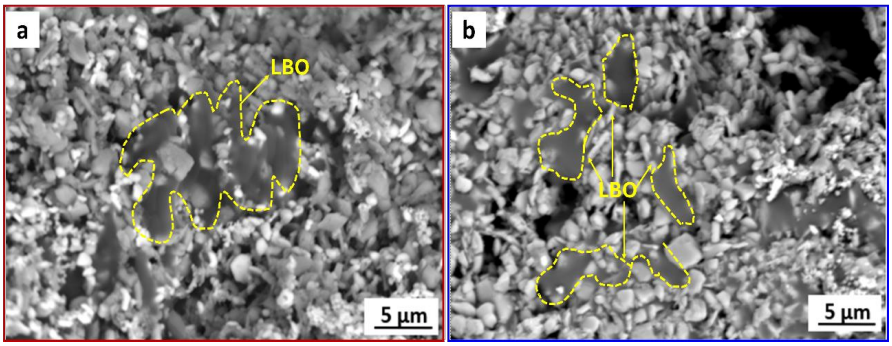


Figure 5.7| Backscattered electron SEM images of: (a) fracture surfaces of the NMC-LLZO-LBO and (b) NMC-LBO composite cathodes sintered at 750°C for 45 min.

X-ray diffraction (XRD) and Raman spectroscopy mapping were performed on the sintered samples (Figure 5.8). The XRD pattern of the NMC-LBO composite shows only reflections associated with the layered NMC phase. No reflections associated with crystalline LBO are detected, which is probably due to its low weight ratio (8 wt%) and amorphous nature after sintering. In contrast, the XRD pattern of the NMC-LLZO-LBO composite shows beyond those of cubic LLZO and layered NMC, additional peaks indexed to the $La_2Li_{0.5}Ni_{0.5}O_4$ phase, consistent with previous published work[115,177]. However, cubic LLZO and NMC remains the main phases after co-sintering (Figure 5.8a). Importantly, in both composite cathodes, the characteristic diffraction features of the hexagonal layered NMC structure are preserved after tape casting and sintering. The layered NMC structure remains intact in both composites, as evidenced by the characteristic splitting of the (006)/(012) and (108)/(110) reflections, confirming a well-ordered hexagonal layered structure[215,216]. A quantitative evaluation of the (003)/(104) intensity ratio is not reliable for the LLZO-containing composite due to the overlap of the NMC (104) reflection with a diffraction peak of LLZO. Therefore, the structural changes were instead evaluated based on the lattice parameters. Le Bail refinement of the powder XRD patterns reveals a slight decrease in the c/a lattice parameter ratio for both NMC-LBO and NMC-LLZO-LBO (4.94) compared to the initial NMC (4.95) (Figure S3, appendix), indicating only a minor increase in cation disorder (antisite defects, Ni^{2+} occupying Li sites) after tape casting and sintering. No influence of LLZO addition in the composite cathode on the cation mixture was observed by XRD.

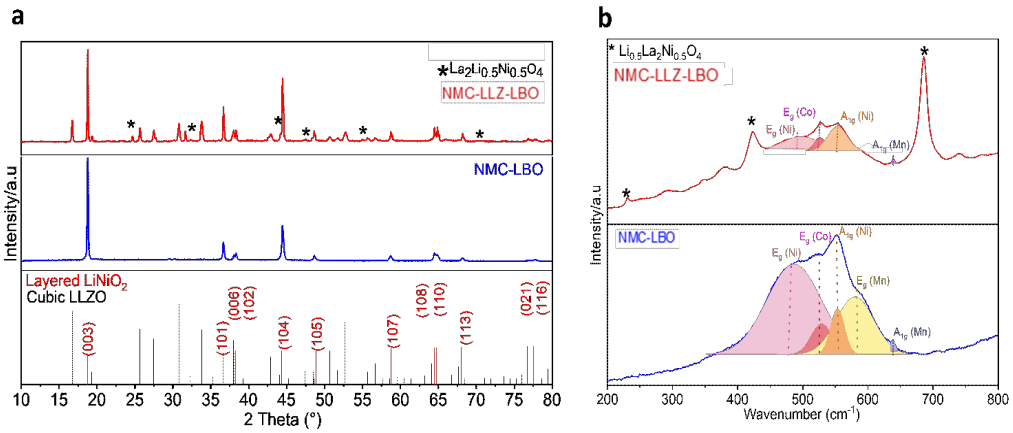


Figure 5.8| (a) XRD patterns and (b) Raman spectra of the composite cathodes: NMC-LBO (blue) and NMC-LLZO-LBO (red) of tapes after sintering at 750°C for 45 min.

Raman mapping spectroscopy (Figure 5.8b) provides further insights into the structure evolution after co-sintering. In the NMC-LBO cathode, characteristic Raman bands of the layered structure are clearly visible in the range of 400-600 cm^{-1} [217], including well-resolved peaks corresponding to E_g(Ni), E_g(Co), A_{1g}(Ni), and E_g(Mn)[217,218]. The presence of a relatively strong A_{1g}(Ni) mode could indicate a minor degree of cation mixing, which is consistent with Le Bail refinement. On the other hand, the Raman spectrum of the NMC-LLZO-LBO composite exhibits a broad and significantly attenuated NMC signals. It is noteworthy that the A_{1g}(Ni) mode shows a significant reduction in intensity, and the A_{1g}(Ni)/E_g(Co) intensity ratio is relatively reduced. This is indicative of increased cation disorder within the NMC structure, likely caused by the abovementioned antisite defects or Ni leaching from the layered structure, which disrupts the layered symmetry and attenuates the vibrational modes. The NMC spectral distortions are also accompanied by the formation of a secondary phase, as evidenced by the appearance of sharp peaks around 220, 410, and 689 cm^{-1} which correspond to the vibrational modes reported for $La_2Li_{0.5}Ni_{0.5}O_4$ [115,208] and are consistent with the XRD results. We can therefore confirm that a La-Ni-O secondary phase is formed at the expense of Ni leaching from the NMC structure, which probably reacts with LLZO during co-sintering at 750 °C.

To better understand the structural evolution leading to secondary phase formation in NMC-LLZO-LBO variant, temperature-resolved XRD and Raman spectroscopy (Figure 5.9) were performed on the NMC-LLZO-LBO tapes at selected intermediate temperatures (200, 400, 600, and 750 °C). XRD (Figure 5.9a) confirm that up to 600 °C, the composite maintains the characteristic reflections of NMC and LLZO with no evidence of new phase formation. However, at 750 °C, additional reflections assigned to $La_2Li_{0.5}Ni_{0.5}O_4$ emerged, indicating the onset of a solid-state reaction between LLZO and NMC at temperature higher than 600 °C. The corresponding Raman spectra (Figure 5.9b) provides complementary localized insight into the chemical and structural transformations. From 200 to 400 °C, The NMC vibrational modes (400-600 cm^{-1}) remain clearly visible, a shoulder near ~690 cm^{-1}, attributed to the Zr-O stretching mode in LLZO[219], is still present, confirming partial retention of the cubic phase. Meanwhile, additional broad bands observed in the low-wavenumber region (~250-350 cm^{-1}) are not typical of pristine LLZO[219] and may indicate the formation of intermediate phases such as low-temperature cubic LLZO (LT-cLLZO)[197–199] or $La_2Zr_2O_7$ phase[200], both of which are known to form upon Li depletion in LLZO. This transformation has been widely reported in the literature to occur at moderate temperatures (400-600 °C), particularly under carbon-rich or CO_2-containing environments[220], such as those generated during binder decomposition in our system. At 600 °C, the LLZO Raman modes weakens progressively, and by 750 °C, only weak residual LLZO features remains with emergence of new peaks near 220 and 410 cm^{-1}, consistent with the formation of $La_2Li_{0.5}Ni_{0.5}O_4$[115] in agreement with the XRD results. The weakening of LLZO-related bands at this stage, at least on the surface depth of the Raman detection, supports the hypothesis that intermediate LLZO degradation products such as LT-cLLZO or $La_2Zr_2O_7$ may act as reactive precursors that facilitate the incorporation of Ni^{2+} cations leached from NMC. These degraded phases, being Li-deficient and structurally disordered, are more prone to cation absorption, making them likely intermediary phases in the formation of the La-Ni-O secondary phase during sintering.

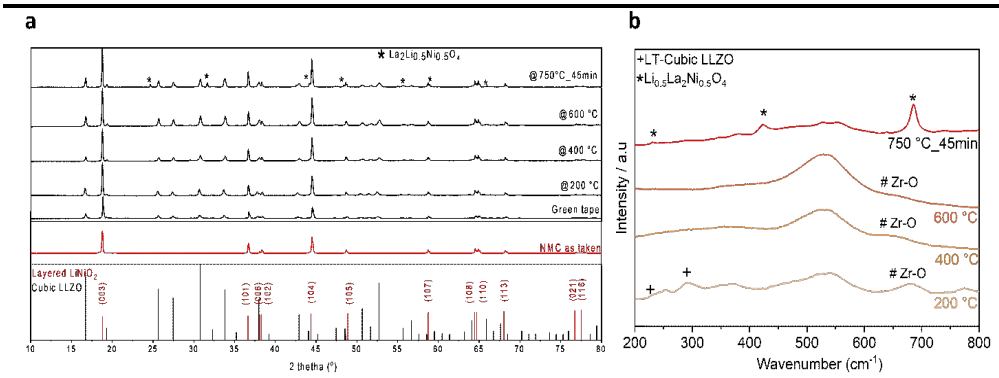


Figure 5.9 | (a) Temperature-resolved XRD; (b) Raman spectra of the NMC-LLZO-LBO composite cathode at 200 °C, 400 °C, 600 °C, and 750 °C.

5.4 Electrochemical Evaluation of Composite Cathodes

To evaluate the electrochemical performance of the NMC-LBO and NMC-LLZO-LBO cathodes, the composite cathode tapes were incorporated into hybrid polymer-ceramic solid-state batteries with lithium anodes. A solution of poly(ε-caprolactone) grafted cyclodextrin (GCD-PCL) polymer and lithium bis(trifluoromethanesulfonyl)imide (LiTFSI) in tetrahydrofuran THF was infiltrated into the composite cathode tapes and used as a bridging layer between the composite cathode tape and the dense, pre-sintered LLZO:Ta separator. GCD-PCL was selected due to its low interfacial charge transfer resistance and stability at high voltages up to 4.3 V, ensuring compatibility with Ni-rich NMC during electrochemical cycling[221]. To obtain a full cell, a Li metal anode was attached to the other side of the dense LLZO:Ta separator.

Four composite cathode configurations were tested to systematically decouple the contributions of ionic and electronic transport to electrochemical performance. The NMC-LBO cathode, which has low total ionic conductivity but high phase purity, is compared with the NMC-LLZO-LBO variant, which should have significantly higher ionic conductivity due to the presence of LLZO, but also contains a secondary phase whose effects on electrochemical performance have not yet been explored. In addition, given the inherently low electronic conductivity of the NMC811 (10^{-8} S cm^{-1})[101], 5 wt% carbon black was added to the GCD-PCL electrolyte to improve the electron conduction pathways within the composite cathode in two other configurations . In total, four cathode configurations: NMC-LBO, NMC-LBO+C, NMC-LLZO-

LBO, and NMC-LLZO-LBO+C, A schematic representation of the four full-cell configurations is provided in Figure 5.10.

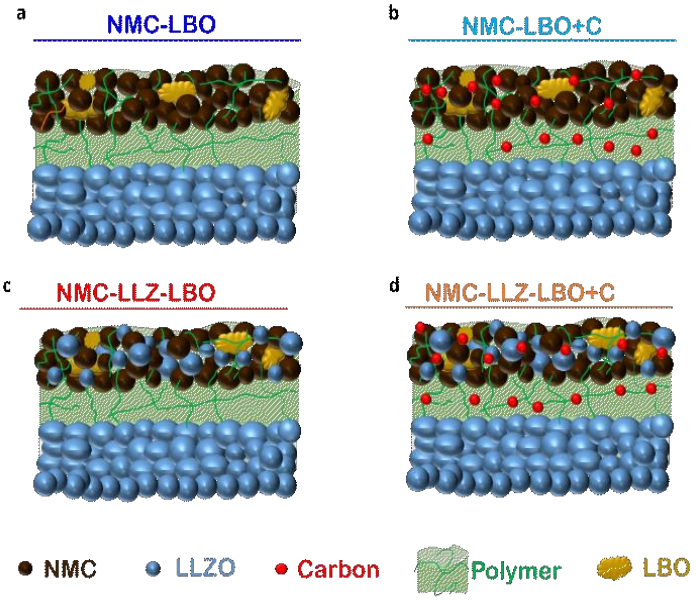


Figure 5.10| Schematic illustration of the four cell configurations investigated in this work: (a) NMC-LBO based cell; (b) NMC-LLZO-LBO based cell; (c) NMC-LBO+C based cell; (d) NMC-LLZO-LBO+C based cell.

The designed cell configurations enable the evaluation of different transport contributions: (I) The comparison of NMC-LBO with NMC-LLZO-LBO isolates the contribution of LLZO ionic conductivity to cathode performance. (II) Comparing NMC-LBO with and without carbon isolates the effect of enhanced electronic conductivity introduced by carbon addition. (III) Comparing the two carbon-containing composites helps to assess whether the addition of carbon can compensate for the performance limitations caused by the secondary phase in the LLZO-containing cathode or the low ionic conductivity of LLZO-free counterparts.

The backscattered electron SEM images of the fractured half-cell (Figure 5.11) reveal a continuous polymer interlayer that conformally bridges the composite cathode and the LLZO separator. The polymer infiltrates the porous cathode and fills the residual porosity, indicating good adhesion and intimate interfacial contact. Similar infiltration behaviour is observed in both cathode configurations, which is

consistent with their comparable relative densities of 79% for NMC-LBO and 81% for NMC-LLZO-LBO, suggesting a similar degree of infiltration.

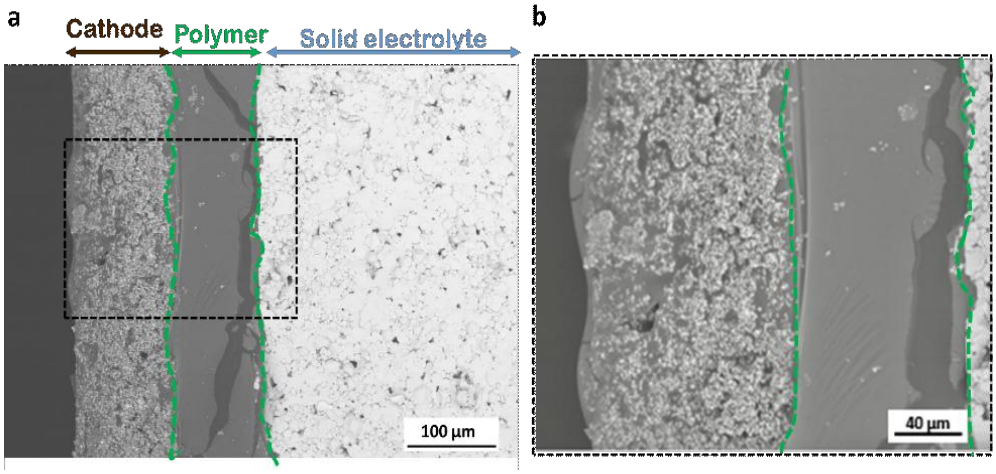


Figure 5.11| (a) Backscattered electron SEM images of fractured half cell (NMC-LLZO-LBO), showing the polymer interlayer between the composite cathode and the solid LLZO separator; (b) Magnified image of the boxed region, highlighting the polymer infiltrated composite cathode.

The hybrid polymer-ceramic SSBs were characterized by galvanostatic charge-discharge experiments at a constant current density of 40 µA cm^{-2} at 60 °C. When comparing the first charge-discharge profiles (Figure 5.12), all cells exhibit defined voltage plateaus within the expected voltage range of Ni-rich NMC, indicating that the optimised slurry preparation and co-sintering do not impair the electrochemical activity of the CAM. This is further supported by the differential capacity analysis (Figure S6, appendix), which shows distinct redox peaks at potentials typically associated with Ni-rich NMC, confirming reversible lithium extraction and insertion. The NMC-LLZO-LBO cell delivered a higher initial discharge capacity of 134 mAh g^{-1} (~63% utilization) and lower polarisation compared to NMC-LBO (Figure 5.12a,b), which delivered only 46 mAh g^{-1} (~21% utilization), accompanied by higher polarization and significant voltage hysteresis, indicating higher total resistance of the electrode layer. With carbon addition, the NMC-LBO+C configuration showed the best performance (Figure 5.12c), achieving an initial areal discharge capacity of 6.1 mAh cm^{-2} and a gravimetric discharge capacity of 205 mAh g^{-1} corresponding to ~97% capacity utilisation relative to the expected practical capacity of Ni-rich NMC811 (~210 mAh g^{-1})[222]. This is accompanied by reduced polarization and improved electrochemical reversibility, attributed primarily to the improved electronic percolation provided by the carbon

network. We assume that the carbon network improves total electronic conductivity of the composite cathodes so that previously isolated regions in the NMC-LBO cathode with an extremely high NMC loading of around 26 mg cm^{-2} become accessible to participate in the electrochemical reaction. The NMC-LLZO-LBO+C (Figure 5.12d) cell also showed improved performance compared to its carbon-free counterpart, achieving 169 mAh g^{-1} (80% utilisation) at slightly lower polarisation. However, despite this improvement, its overall performance remained lower compared to the NMC-LBO+C composite cathode. It is noteworthy that the electrochemical performance and both the areal and gravimetric discharge capacities of the NMC-LBO+C cell exceed the values typically reported for NMC-based composite cathodes produced by co-sintering at elevated temperatures[96,117,119,209], where capacity utilisation is often limited to comparable or lower loadings due to interfacial degradation and transport limitations. This performance advantage is further highlighted by comparison with pure polymer-based cell configurations. In a recent study[53] on conventional NMC622 electrodes infiltrated with the same GCD-PCL polymer electrolyte, also cycled at 60 °C, reported a gravimetric discharge capacity of only 94 mAh g^{-1} at 0.05C for an electrode loading of 6 mg cm^{-2}, while their highest-loading cathodes (12 mg cm^{-2}, approximately half the areal loading of our NMC-LBO+C cathode) achieved only ~80% of the theoretical discharge capacity at the same rate. These results confirm that the operating temperature of 60 °C is not the key performance enabler of the ceramic system and demonstrate that the hybrid ceramic-assisted design enables substantially higher active material utilization at high areal loading than a pure polymer-based cell designs. The markedly different effect of carbon in the two systems suggests that electron transport is the main limiting factor in the NMC-LBO cathode, while in LLZO-containing cathodes, the electrochemical performance is likely governed by more complex interfacial and chemical constraints. In the latter case, multiple ceramic-ceramic interfaces and secondary phases ($La_2Li_{0.5}Ni_{0.5}O_4$) formed during co-sintering, restricts the effective interaction between carbon and the NMC particles, diminishing the benefit of improved electronic percolation. These results suggest that while LLZO may facilitate the initial electrochemical activation of NMC thick composite cathode by providing ion conducting pathways, its presence does not necessarily lead to higher capacity utilisation when interfacial resistances dominate. Instead, improved electronic percolation alone is sufficient to achieve near-complete capacity utilisation of NMC, even when LLZO is not present in the composite cathode.

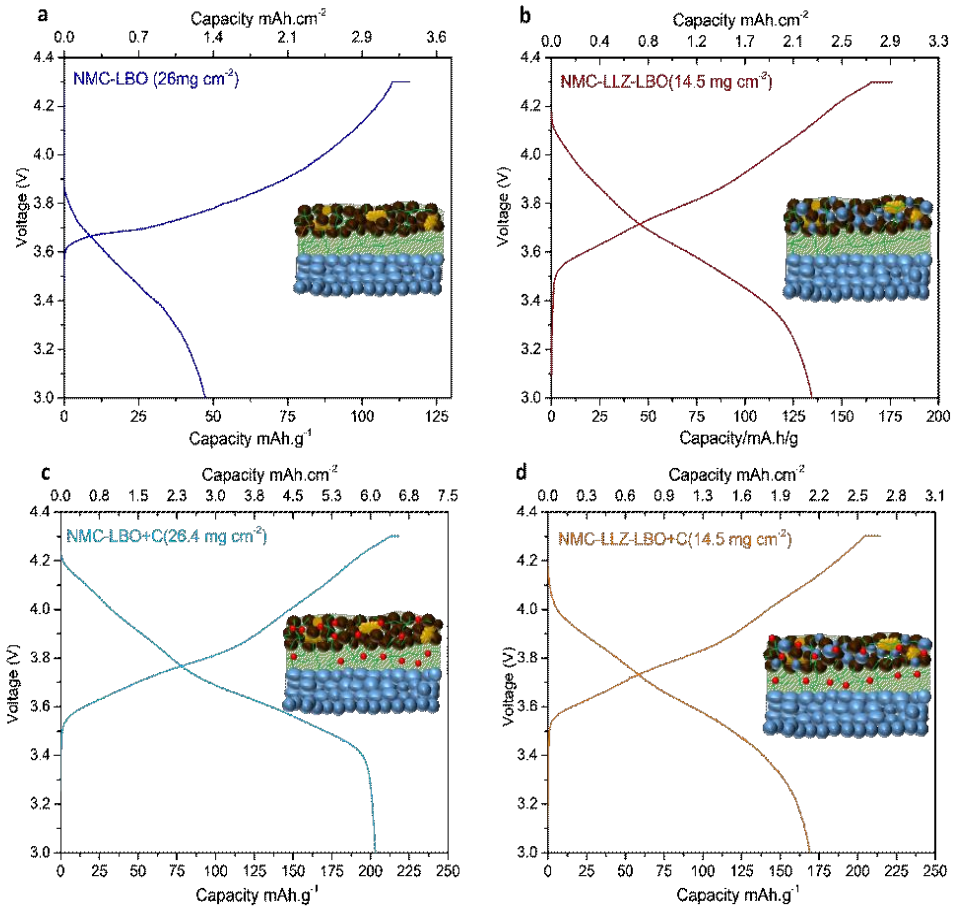


Figure 5.12| Charge-discharge voltage profiles (first cycle) of the hybrid, polymer-ceramic SSBs with the four different composite cathode configurations at 60°C and 0.01C: (a) NMC-LBO based cell (dark blue); (b) NMC-LLZO-LBO based cell (red); (c) NMC-LBO+C based cell (light blue), and (d) NMC-LLZO-LBO+C based cell (orange).

Electrochemical impedance spectroscopy (EIS) (Figure 5.13) corroborates the trends observed during galvanostatic cycling. The impedance spectra were fitted using equivalent circuits, as shown in Figure 5.13a,b. The NMC-LLZO-LBO cathodes, both with and without carbon, exhibit three overlapping semicircles distributed across the high, mid, and low-frequency ranges (Figure 5.13a). The high-frequency feature ($C_1 \approx 10^{-10}$ F) is consistent with contributions from the bulk and grain boundaries impedance of LLZO[9,16], while the mid-frequency and low-frequency semicircles ($C_2 \approx 10^{-4}$-10^{-5} F) most likely reflect interfacial processes involving the interfaces of the polymer-NMC, polymer-LLZO, and

secondary phase interfaces[9]. The NMC-LBO cell without carbon also exhibits three strongly overlapping semicircles, but with markedly different effective capacitances. The high and mid-frequency semicircles have larger capacitances (C_1 and $C_2 \approx 10^{-7}$ F), suggesting contributions from the CAM[205], while the low-frequency semicircle ($C_3 \approx 10^{-5}$ F) is related to slow Li^+ transport across the polymer interface[9]. The different capacitance ranges indicate that the NMC-LLZO-LBO and NMC-LBO cathodes are likely governed by different rate-determining mechanisms. Owing inherent complexity of hybrid polymer-ceramic composite cathodes with multiple interfaces, a detailed deconvolution of individual impedance contributions is not readily possible. Therefore, the comparison here is based on the total cell resistance extracted from the fitting of the equivalent circuit model (Table S3, appendix).The total cell resistance of the NMC-LLZO-LBO cell is 654 Ω cm², which is significantly lower than that of the NMC-LBO cell (2182 Ω cm²), consistent with a reduced overall ionic transport limitation when LLZO is present as a catholyte. This also confirms that the NMC-LLZO-LBO cathode remains more conductive overall than the NMC-LBO cathode when assembled in an identical cell configuration, despite the secondary phases observed previously. The poor capacity utilisation of the NMC-LBO cathode is likely related to impeded electrochemical exchange caused by the low ionic and electronic conductivity in the cathode. The addition of carbon reduces the total resistance of the NMC-LLZO-LBO+C composite to 541 Ω cm², while NMC-LBO+C exhibits the lowest total resistance among the four cathode configurations investigated within this work (308 Ω cm²). The total cell resistance is one order of magnitude lower than that of the NMC-LBO cathode without carbon. The reduced resistance in the NMC-LBO+C configuration is accompanied by a single depressed semicircle indicating a more homogeneous impedance response, possibly dominated by improved electronic percolation. The greatly reduced resistance is consistent with the high initial capacities and low polarization observed during the first cycle. The EIS results confirm that improved electronic conductivity can compensate for the limited ionic conductivity in the absence of LLZO. In contrast, the addition of carbon to LLZO-containing cathodes affected by secondary phase formation has a more limited effect on reducing interfacial resistance and improving overall electrochemical performance.

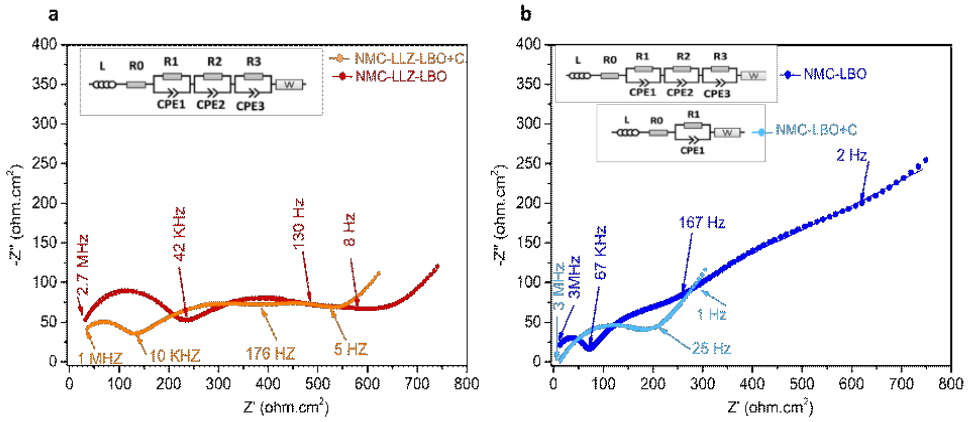


Figure 5.13 | Nyquist plots of the EIS spectra of the of the hybrid polymer-ceramic SSBs before cycling measured at 60°C and the equivalent circuits used for fitting: (a) NMC-LLZO-LBO and NMC-LLZO-LBO+C based cells ; (b) NMC-LBO and NMC-LBO+C based cells.

All composite cathode configurations examined show a significant capacity fade during prolonged cycling (Figure 5.14a). Among all systems, the NMC-LBO+C cathode exhibits the most stable early cycling behaviour, retaining 95% of its initial capacity with a Coulombic efficiency exceeding 90% in the first five cycles. This performance exceeds the capacity retention reported for comparable NMC-based composite cathodes in similar hybrid solid-state configurations and surpassing the cycling stability of thinner cathode layers[96,119]. Nevertheless, further cycling leads to a continuous capacity decline, and all systems suffer from severe capacity degradation to only 20 mAh g^{-1} within fewer than ten cycles, which is comparable to the degradation rate typically reported for oxide-based composite cathodes[9,205]. To gain further insights into the degradation process, EIS was performed again after the third cycle (Figure 5.14c,d). All cells show a significant increase in total resistance after three cycles. In particular, the carbon-free NMC-LBO cell exhibits a sharp increase in the low-frequency impedance contribution, indicating a rapid build-up in the effective charge transfer resistance at the interfaces already in the first cycles. This behaviour is consistent with the intrinsically limited ion and electron transport in this cathode configuration, leading to a rapid decay in electrochemical activity. It is evident that the presence of LLZO in the NMC-LLZO-LBO cathodes mitigates such early failure. LLZO-containing cells exhibit a monotonic capacity decay accompanied by a comparable increase in impedance, dominated by contributions in the mid-to-low frequency range, suggesting that their electrochemical performance is determined by the

progressive build-up of interfacial resistances that cannot be significantly mitigated by improved electronic percolation alone. Similar correlations between monotonic capacity fading and the build-up of interfacial impedance during cycling have been reported for LLZO-based composite cathodes with comparable composition, suggesting an interface-dominated degradation process[96,119]. The addition of carbon has only a limited influence on the short-term cycling stability of the NMC-LBO+C cathode. It is noteworthy that this cell exhibits a non-monotonic capacity evolution during the initial cycles (Figure 5.14a), suggesting that the observed capacity fluctuations cannot be attributed solely to purely progressive build-up of interfacial resistances or a continuous loss of electrochemical activity. Rather, the resistance increase after the third cycle indicates changes in the electrochemically accessible fraction of the CAM. A plausible mechanism is a mechanically induced loss of contact within the composite cathode, in which chemo-mechanical volume changes during cycling locally damage interfaces or isolate parts of the NMC from the percolating transport network. Similar capacity decay trends have been observed in LCO-LLZO composite cathodes fabricated by tape casting, where the loss of capacity during cycling was mainly attributed to electro-chemo-mechanical degradation caused by volume changes in LCO particles during lithiation and delithiation.[9,205] A comparable mechanism could also contribute to the performance degradation observed here, which can be exacerbated by additional degradation processes of Ni-rich NMC,[37,223,224] including greater lattice strain, volume change, and potential interfacial reactivity. Raman of the carbon free cells after cycling (Figure S8, appendix), show that the NMC-LBO remains largely preserved. The characteristic layered-structure modes are still clearly distinguishable. The Ni-O vibrational modes Eg (Ni) and A1g(Ni) are still present, exhibiting only minor peak broadening. Importantly, the A1g(Ni)/Eg intensity ratio does not show a significant additional decrease compared to as prepared cathodes. This indicates that, in the absence of LLZO, the layered NMC framework remains structurally stable during cycling. The observed degradation is therefore more likely associated with mechanical or electrochemical effects rather than chemically driven interfacial reactions. In contrast, the cycled NMC-LLZO-LBO composite exhibits further attenuation and broadening of the NMC-related Raman bands, with a diminish of the Eg(Ni) mode intensity at the end of cycling. The characteristic secondary-phase peaks assigned to $La_2Li_{0.5}Ni_{0.5}O_4$ remain clearly visible and stable in position, indicating the persistence of the La-Li-Ni-O phase formed during co-sintering. The progressive suppression of layered NMC vibrational modes suggests ongoing structural degradation, likely associated with transition-metal redistribution and local symmetry distortion at the NMC-LLZO interface. The

stability of the $La_2Li_{0.5}Ni_{0.5}O_4$ phase further supports that this interfacial reaction product remains electrochemically inactive and contributes to impedance growth during cycling. Nonetheless, electrochemical and mechanical instability of the polymer interlayer upon repeated cycling can contribute to the capacity decay. Therefore, further targeted studies are needed in the future to examine the cycling stability of thick NMC composite cathode in such hybrid-ceramic cells.

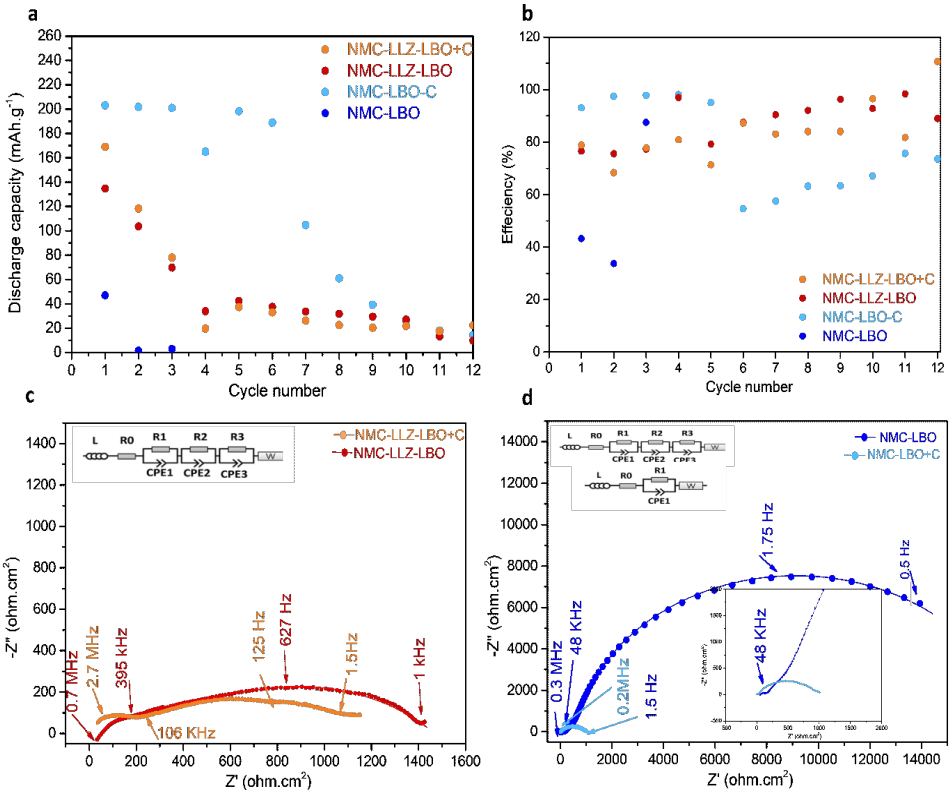


Figure 5.14| (a) Discharge capacity of the hybrid, polymer-ceramic SSBs with the four different composite cathode configurations for the first 12 cycles at 60°C and 0.01C; (b) Coulombic efficiency for the cycles shown in (a); (c) EIS spectra of the NMC-LLZ-LBO and NMC-LLZ-LBO+C configurations after the third cycle, and (d) EIS spectra of the NMC-LBO and NMC-LBO+C configuration after the third cycle.

The EIS characterisation was also supported by galvanostatic intermittent titration technique (GITT) measurements. GITT measurements were conducted at 60 °C with a current density of 40 µA cm^{-2}, consisting of 3 h current steps followed by 1 h relaxation intervals. EIS was performed after each titration step. The apparent diffusion coefficient D was calculated using Equation 5.1[147], where t (s) is the dwell

time, mb (g) is the total mass loading, S (cm^2) is the cathode surface, Mb (g mol^{-1}) is the molecular weight, ΔE_s is the steady-state voltage change during the current step, and ΔE_t is the total voltage change during the current pulse.

$$D = \frac{4}{\pi t}\left(\frac{V_m m_b}{S\, M_b}\right)^2 \left(\frac{\Delta E_S}{\Delta E_t}\right)^2 \qquad \text{Equation 5.3}$$

Despite the relatively long relaxation times applied during the GITT measurements, the voltage response in the GITT profiles is dominated by abrupt IR drops and only limited diffusion-controlled relaxation (Figure 5.15a). This behaviour indicates that the GITT profiles primarily reflect instantaneous polarisation and transport effects at the electrode level rather than diffusion-controlled processes. Accordingly, the diffusion coefficients derived from these measurements are treated as apparent parameters that describe effective transport kinetics in the entire cathode and not the intrinsic solid-state lithium diffusion in the active materials.

The amplitude of the instantaneous IR drop after current shutdown is largest for the NMC-LBO electrode, consistent with the high electrode resistance arising from the low ionic conductivity of LBO and the limited electronic conductivity of the carbon-free composite. The incorporation of LLZO into the composite cathode (NMC-LLZO-LBO) moderately reduces the IR drop amplitudes compared to NMC-LBO, suggesting that LLZO provides higher ionic conductivity and thus lower overall resistance of the electrode. In LLZO-containing cathodes, the addition of carbon leads to a further (albeit slight) reduction in the IR-drop amplitude and marginally higher apparent diffusion coefficients. This observation is consistent with the EIS results and suggests that electrode kinetics are primarily determined by high interfacial resistances that cannot be significantly reduced by improved electronic percolation alone. In contrast, the addition of carbon to the LLZO-free NMC-LBO+C cathode results in a significant reduction in the IR-drop amplitude and yields the highest apparent lithium diffusion coefficients over the entire state of charge (SOC) range (Figure 5.15b). This strong correlation suggests that, in the absence of LLZO, electrode resistance is dominated by electronic contribution, which can be effectively improved by adding carbon. We therefore conclude that the incorporation of LLZO primarily improves ion transport, but at the same time introduces interfacial limitations that restrict further kinetic gains. In contrast, the addition of carbon reduces electronic resistance and improves exchange kinetics in NMC-LBO+C

cathodes, making it the most effective strategy for improving NMC capacity utilisation in thick composite cathodes without LLZO incorporation.

Analysis of distribution of relaxation times (DRT) (Figure S7,appendix) confirms the trends observed in the GITT measurements. The main difference between the cathode systems studied is reflected in the evolution of the mid-frequency relaxation process P3 (10^4-10^2 Hz), which is sensitive to cathode chemistry and interfacial transport within the cathode[189]. In LLZO-containing cathodes (NMC-LLZO-LBO), the P3 process broadens with increasing state of charge, probably due to the continuously increasing interfacial resistance. Although the addition of carbon partially suppresses this contribution, a residual broadening persisted, confirming that transport in LLZO-containing cathodes was predominantly governed by chemically and structurally induced interfacial effects.

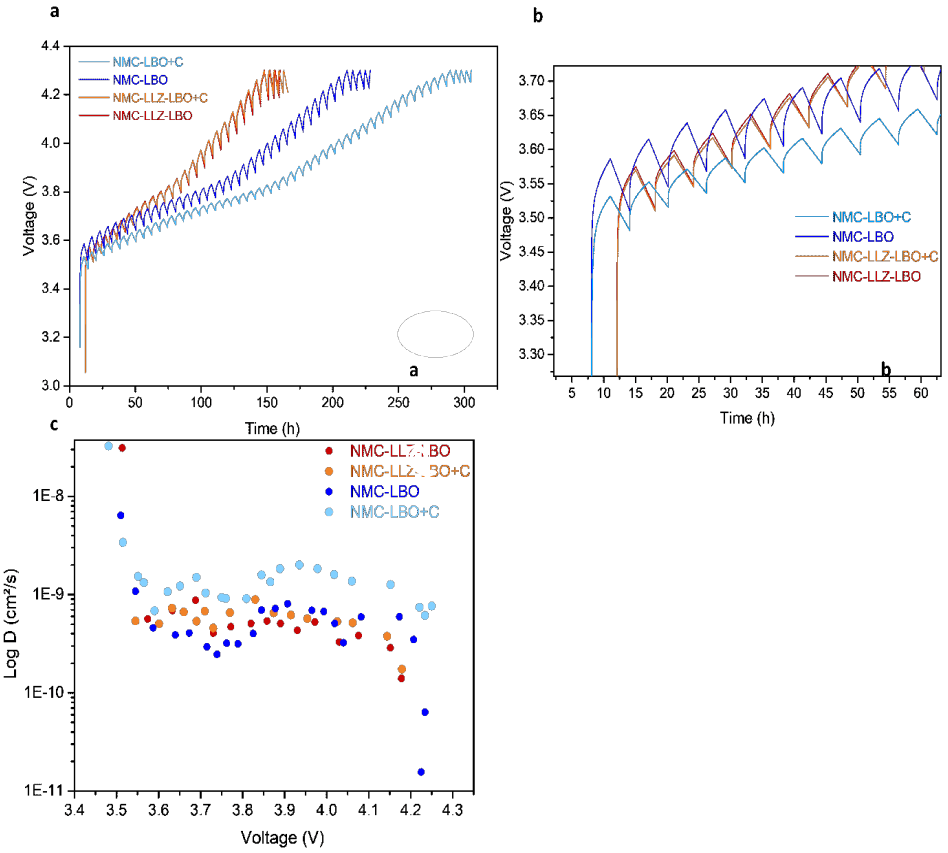


Figure 5.15| (a) GITT voltage profiles for NMC-LBO, NMC-LBO+C, NMC-LLZO-LBO, and NMC-LLZOLBO+C at 60 °C; (b) magnified GITT voltage profiles for NMC-LBO, NMC-LBO+C, NMC-LLZO-LBO, and NMC-LLZOLBO+C at 60 °C between 3.3 and 3.7 V; (c) Li^+ diffusion coefficients calculated from the GITT profiles

5.5 Chapter summary

This chapter reported for the first time the fabrication of thick, high loading, free-standing, Ni-rich NMC-ceramic composite cathode by tape-casting and sintering. The incompatibility challenge of the conventional PVB binder with the Li_3BO_3 sintering aid required for low-temperature co-sintering was resolved by replacing PVB with carboxymethyl cellulose (CMC), enabling reproducible flat, mechanically stable composite cathode tapes in two chemistries NMC-LLZO-LBO and NMC-LBO.

Structural and spectroscopic analyses confirm that the hexagonal layer structure of NMC and the cubic LLZO phase are largely retained after processing, however, co-sintering of LLZO, NMC and LBO as a sintering aid leads to the formation of $La_2Li_{0.5}Ni_{0.5}O_4$ as secondary phase even at a reduced temperature of only 750 °C. Electrochemical testing in hybrid polymer-ceramic full cells demonstrated that electronic conductivity is as critical as ionic conductivity for capacity utilisation in thick composite cathodes. The NMC-LBO+C configuration delivered the highest performance of 205 mAh g^{-1} (~97% utilisation) and 6.1 mAh cm^{-2} areal capacity. This value exceeds values reported for NMC-based composite cathodes produced by co-sintering as well as cathodes employed in full polymer cell designs. EIS, GITT, and DRT analysis confirmed that electronic transport governs performance in LLZO-free cathodes, while secondary phase formation and interfacial resistance limit LLZO-containing systems. All configurations exhibited rapid capacity fade within fewer than ten cycles. EIS and post-cycling Raman indicating mechanical origin in NMC-LBO and progressive interfacial degradation with persistent electrochemically inactive $La_2Li_{0.5}Ni_{0.5}O_4$ in NMC-LLZO-LBO. The long-term cycling stability of thick NMC composite cathodes in hybrid polymer-ceramic cells represents an important direction for future investigation.

CONCLUSION AND OUTLOOK

This thesis investigated the fabrication of LLZO-based solid-state battery components by tape casting, focusing on the controlled processing of LLZO ceramic separators and free-standing Ni-rich NMC composite cathodes.

Chapter 3 provided a systematic analysis of the process chain in LLZO tape casting, critically examining the specific challenges of each processing step and relating them to the structural evolution of LLZO as well as electrochemical performance of the final separators. Analysis of the existing literature from a process chain perspective revealed that protonation and lithium loss are interrelated degradation phenomena that occur as early as the initial stages of the tape casting process and influence all subsequent process steps as well as the properties of the final components. For instance, the protonation of LLZO during slurry preparation alters the surface chemistry of LLZO, which destabilizes the slurry and promotes the formation of secondary phases in the green tape. The presence of secondary phases leads to inhomogeneous densification of the tapes during sintering, while lithium loss at high temperatures results in the formation of lithium-poor phases, residual porosity, mechanical deformation (manifested as bending and warping), and impaired lithium wettability at the separator surface. The accumulation of these structural changes throughout the entire process chain directly impairs both the cell assembly process and the electrochemical performance of the final cells. Our analysis demonstrates that the isolated optimization of individual processing steps is insufficient; rather, a coherent strategy is required that accounts for the interrelated degradation phenomena across the entire tape-casting process chain.

Building on the conclusions from Chapter 3, we experimentally investigated the protonation mechanisms within the tape-casting process in Chapter 4. It was found that an intense Li^+/H^+ exchange already occurs during wet ball-milling step, leading to the formation of a lithium-depleted protonated LLZO phase (H:LLZO) and to the enrichment of Li_2CO_3 at the surface and continue to propagate along the fabrication chain. The decomposition of H:LLZO during sintering, results in the formation of Li-poor impurity phases such as $La_2Zr_2O_7$, that lead to porous, poorly densified separators. The direct addition of excess Li_2CO_3 during ball milling counteracted this protonation through in-situ relithiation, preserved the cubic LLZO structure throughout the entire process chain, and enabled the reproducible fabrication of dense and flat free-standing separators with a competitive ionic conductivity of 0.18 mS cm^{-1}, a critical current

density of 1 mA cm^{-2} at 60 °C in symmetric cells with Li electrodes, and stable cycling over 220 h. Optimization of the process chain enabled to reduce a lithium excess to only 5 mol%, which is significantly lower than 10-50 mol% typically reported in the literature.

Subsequently, in Chapter 5, we extended the optimised tape-casting process developed in Chapter 4 to the fabrication of free-standing Ni-rich NMC composite cathodes with high NMC loading. We succeeded in optimizing the slurry composition such that reproducible casting of 90 µm thick composite cathodes composed of either NMC, LLZO and LBO (NMC-LLZO-LBO configuration) or NMC and LBO only (NMC-LBO configuration) was possible. The use of LBO enabled co-sintering at 750 °C .The hexagonal NMC layered structure was largely preserved in both configurations after co-sintering; however, co-sintering with LLZO led to the formation of $La_2Li_{0.5}Ni_{0.5}O_4$ as a secondary phase, introducing additional interfacial resistance in the cathode layer. The composite cathodes exhibited electrochemical activity tested in hybrid polymer-ceramic solid-state batteries with a Li metal anode and a dense LLZO separator. A systematic comparison between LLZO-containing and LLZO-free composite cathode configurations shows that the incorporation of LLZO improves electrochemical performance by providing ion transport pathways in the thick composite cathodes, however, it simultaneously leads to higher interfacial resistance due to the secondary phases formed during co-sintering, which limits effective capacity utilization. When carbon was added to the cathodes, the NMC-LBO+C configuration delivered an initial discharge capacity of 205 mAh g^{-1} (~97% utilisation) and an areal capacity of 6.1 mAh cm^{-2}, surpassing the values obtained for the LLZO-containing counterpart with carbon (NMC–LLZO-LBO+C). These results confirmed that improved electronic percolation can effectively compensate for the absence of LLZO as an ionic conductor in thick cathode architectures.

Despite high initial capacities, all cathode configurations exhibited a rapid capacity decline during cycling. Based on the results of post-mortem Raman spectroscopy and electrochemical analysis, we suggested that electro-chemo-mechanical degradation is the primary cause of capacity fading in composite cathodes, both with and without LLZO; therefore, improving the mechanical cohesion of the electrodes under cycling-induced strain should be the main objective. This can be achieved, for example, by reducing the CAM particle size or by using NMC particles with concentration gradients to reduce intergranular cracking and minimize the cumulative stress caused by the CAM volume change. Another possibility is also to optimize the protocol for polymer infiltration, for example using heating or curing

techniques that ensure a conformal CAM/catholyte interface and better compensate for cycling-induced volumetric stresses. In addition to chemo-mechanical degradation, LLZO-containing cathodes exhibit another degradation pathway related to reactions at the CAM/LLZO interface. For these systems, it is therefore expected that suppressing the formation of $La_2Li_{0.5}Ni_{0.5}O_4$ during sintering would improve electrode performance. To prevent the formation of secondary phases, the use of protective surface coatings on LLZO and NMC particles (e.g., $LiNbO_3$ or Li_3PO_4), as well as fast and low-temperature sintering methods such as field assisted sintering (FAST/SPS) should be investigated.

This work established clear process-structure-performance relationships for tape-cast LLZO separators and Ni-rich NMC composite cathodes and provided experimentally grounded guidelines for the development of oxide-based solid-state battery components in a scalable process. However, further efforts are needed to make the fabrication of LLZO solid-state batteries via tape casting more effective and to improve the electrochemical performance of the components .

The necessary efforts to further optimized the processing and performance of tape cast LLZO separators should focus on the following:

- Reviewing the entire tape-casting workflow for time efficiency and stability: Rapid drying technologies and fast-evaporating solvent systems would limit exposure to ambient air and improve the quality of green tape, throughput, as well as decrease production cost and time.
- Rapid low-temperature sintering methods should be implemented and optimised to reduce lithium evaporation, production cost, and time.
- Dry tape-casting processes represent a transformative long-term direction: This approach can drastically reduce exposure to moisture and CO_2, shorten fabrication time, lower costs, and on significantly suppress protonation and Li loss. The next research direction should focus on the feasibility of adapting the dry process for LLZO. This requires the identification of conditions under which the LLZO powder can form cohesive, defect-free green tapes without the rheological control typically provided by solvent-based slurries. Future research in this direction should therefore investigate the properties of the LLZO powder (particle size distribution, surface chemistry, morphology) and identify suitable green binders that provide sufficient plasticity and mechanical integrity without solvents.

- From an industrial perspective: The successful implementation of LLZO tape casting depends on minimizing time- and atmosphere-sensitive steps through workflow automation and integrating inline monitoring to reduce batch-to-batch variation. The slurry formulation should adopt non-toxic or flammable solvents as much as possible, and the number of additives could be minimized to improve safety and reproducibility in large-scale production.

For high loading NMC composite cathodes, further investigations are needed:

- Increasing the cycling stability is the decisive challenge. The practical qualification threshold of ≥80% capacity retention after 100 cycles remains far off for both architectures developed in this work. Therefore, further efforts are needs to investigate the degradation mechanisms in such high-loading Ni-rich NMC cathodes and to implement strategies to mitigate rapid capacity decay.
- For NMC-LLZO-LBO cathodes, the formation of $La_2Li_{0.5}Ni_{0.5}O_4$ must be suppressed. Possible strategies include implementation of fast-low sintering techniques that limits the degradation reaction .
- For NMC-LBO+C cathodes, single-crystal or concentration-gradient NMC particles, which exhibit lower volume change and less intergranular cracking, could significantly extend cycle life. Optimizing the polymer infiltration process to better accommodate cycling-induced volumetric expansion stress represents another short-term direction.

For ceramic batteries, cell architecture and design must be further optimization by co-sintering the LLZO separator and composite cathode layers to eliminate the polymer interlayer entirely. This remains the ultimate fabrication goal and the most important direction for future work toward the realisation of high-energy, fully ceramic oxide-based solid-state batteries.

REFERENCES

[1] IEA, "Batteries and Secure Energy Transitions," IEA, Paris, 2023. Available at: https://www.iea.org/reports/batteries-and-secure-energy-transitions (accessed 25 October 2025).

[2] M. Winter, B. Barnett, K. Xu, "Before Li Ion Batteries" *Chem. Rev.* 2018, *118*, 11433–11456. DOI: 10.1021/acs.chemrev.8b00422.

[3] Y. Horowitz, C. Schmidt, D.-H. Yoon, L. M. Riegger, L. Katzenmeier, G. M. Bosch, M. Noked, Y. Ein-Eli, J. Janek, W. G. Zeier, C. E. Diesendruck, D. Golodnitsky, "Between Liquid and All Solid: A Prospect on Electrolyte Future in Lithium-Ion Batteries for Electric Vehicles" *Energy Technol.* 2020, *8*, 2000580. DOI: 10.1002/ente.202000580.

[4] T. Hettesheimer, C. Neef, I. Rosellón Inclán, S. Link, T. Schmaltz, F. Schuckert, A. Stephan, M. Stephan, A. Thielmann, L. Weymann, T. Wicke, *Lithium-Ion Battery Roadmap – Industrialization Perspectives Toward 2030*, Fraunhofer ISI, Karlsruhe, 2023.

[5] P. Sun, R. Bisschop, H. Niu, X. Huang, "A Review of Battery Fires in Electric Vehicles" *Fire Technol.* 2020, *56*, 1361–1410. DOI: 10.1007/s10694-019-00944-3.

[6] X. B. Cheng, R. Zhang, C. Z. Zhao, Q. Zhang, "Toward Safe Lithium Metal Anode in Rechargeable Batteries: A Review" *Chem. Rev.* 2017, *117*, 10403–10473. DOI: 10.1021/acs.chemrev.7b00115.

[7] R. Murugan, W. Weppner, Eds., *Solid Electrolytes for Advanced Applications: Garnets and Competitors*, Springer, Cham, 2019.

[8] R. K. Nishihora, P. L. Rachadel, M. G. N. Quadri, D. Hotza, "Manufacturing porous ceramic materials by tape casting — A review" *J. Eur. Ceram. Soc.* 2018, *38*, 988–1001. DOI: 10.1016/j.jeurceramsoc.2017.11.047.

[9] M. Rosen, M. Finsterbusch, O. Guillon, D. Fattakhova-Rohlfing, "Free standing dual phase cathode tapes – scalable fabrication and microstructure optimization of garnet-based ceramic cathodes" *J. Mater. Chem. A* 2022, *10*, 2320–2326.

[10] G. V. Alexander, C. Shi, J. O'Neill, E. D. Wachsman, "Extreme lithium-metal cycling enabled by a mixed ion- and electron-conducting garnet three-dimensional architecture" *Nat. Mater.* 2023, *22*, 1136–1143.

[11] Z. Fu, L. Zhang, J. E. Gritton, G. Godbey, T. Hamann, Y. Gong, D. McOwen, E. Wachsman, "Probing the Mechanical Properties of a Doped Li7La3Zr2O12 Garnet Thin Electrolyte for Solid-State Batteries" *ACS Appl. Mater. Interfaces* 2020, *12*, 24693–24700.

[12] G. T. Hitz, D. W. McOwen, L. Zhang, Z. Ma, Z. Fu, Y. Wen, Y. Gong, J. Dai, T. R. Hamann, L. Hu, E. D. Wachsman, "High-rate lithium cycling in a scalable trilayer Li-garnet-electrolyte architecture" *Materials Today* 2019, *22*, 50–57.

[13] R. Ye, C. L. Tsai, M. Ihrig, S. Sevinc, M. Rosen, E. Dashjav, Y. J. Sohn, E. Figgemeier, M. Finsterbusch, "Water-based fabrication of garnet-based solid electrolyte separators for solid-state lithium batteries" *Green Chem.* 2020, *22*, 4952–4961.

[14] R. Grissa, S. Payandeh, M. Heinz, C. Battaglia, "Impact of Protonation on the Electrochemical Performance of Li7La3Zr2O12 Garnets" *ACS Appl. Mater. Interfaces* 2021, *13*, 14700–14709.

[15] X. Huang, Y. Lu, Y. Niu, J. Tang, Y. Zhou, Y. Yang, B. Tian, "From protonation and Li-rich contamination to grain-boundary segregation: Evaluations of solvent-free vs. wet routes on preparing Li7La3Zr2O12 solid electrolyte" *J. Energy Chem.* 2022, *73*, 223–239.

[16] M. Rosen, R. Ye, M. Mann, S. Lobe, M. Finsterbusch, O. Guillon, D. Fattakhova-Rohlfing, "Controlling the lithium proton exchange of LLZO to enable reproducible processing and performance optimization" *J. Mater. Chem. A* 2021, *9*, 4831–4840.

[17] S. A. Arote in *Lithium-Ion and Lithium–Sulfur Batteries*, IOP Publishing, Bristol, 2022, pp. 1-1–1-26.

[18] Y. Liang, C. Z. Zhao, H. Yuan, Y. Chen, W. Zhang, J. Q. Huang, D. Yu, Y. Liu, M. M. Titirici, Y. L. Chueh, H. Yu, Q. Zhang, "A review of rechargeable batteries for portable electronic devices" *InfoMat* 2019, *1*, 6–32. DOI: 10.1002/inf2.12000.

[19] M. S. Whittingham, "Electrical Energy Storage and Intercalation Chemistry" *Science* 1976, *192*, 1126–1127.

[20] J.-M. Tarascon, M. Armand, "Issues and challenges facing rechargeable lithium batteries" *Nature* 2001, *414*, 359–367.

[21] K. Mizushima, P. C. Jones, P. J. Wiseman, J. B. Goodenough, "LixCoO2 (0<x≤1): A new cathode material for batteries of high energy density" *Mater. Res. Bull.* 1980, *15*, 783–789.

[22] S. Megahed, B. Scrosati, "Lithium-ion rechargeable batteries" *J. Power Sources* 1994, *51*, 79–104.

[23] W. Van Gool, Ed., *Fast Ion Transport in Solids*, Elsevier, New York, 1973.

[24] W. S. Scheld, *Photonic Sintering of Garnet-Based Solid-State Batteries*, Forschungszentrum Jülich GmbH, Jülich, 2024.

[25] D. Baril, C. Michot, M. Armand, "Electrochemistry of liquids vs. solids: polymer electrolytes" *Solid State Ion.* 1997, *94*, 35–47.

[26] J. Schnell, F. Tietz, C. Singer, A. Hofer, N. Billot, G. Reinhart, "Prospects of production technologies and manufacturing costs of oxide-based all-solid-state lithium batteries" *Energy Environ. Sci.* 2019, *12*, 1818–1833.

[27] C. Julien, G.-A. Nazri, *Solid State Batteries: Materials Design and Optimization*, Springer US, Boston, MA, 1994.

[28] S. Ohno, A. Banik, G. F. Dewald, M. A. Kraft, T. Krauskopf, N. Minafra, P. Till, M. Weiss, W. G. Zeier, "Materials design of ionic conductors for solid state batteries" *Prog. Energy* 2020, *2*, 022001. DOI: 10.1088/2516-1083/ab73dd.

[29] E. Yi, H. Shen, S. Heywood, J. Alvarado, D. Y. Parkinson, G. Chen, S. W. Sofie, M. M. Doeff, "All-Solid-State Batteries Using Rationally Designed Garnet Electrolyte Frameworks" *ACS Appl. Energy Mater.* 2020, *3*, 170–175.

[30] J. B. Goodenough, K. S. Park, "The Li-Ion Rechargeable Battery: A Perspective" *J. Am. Chem. Soc.* 2013, *135*, 1167–1176. DOI: 10.1021/ja3091438.

[31] B. Nykvist, M. Nilsson, "Rapidly falling costs of battery packs for electric vehicles" *Nat. Clim. Chang.* 2015, *5*, 329–332.

[32] D. Linden, T. B. Reddy, *Handbook of Batteries*, 3rd ed., McGraw-Hill, New York, 2002.

[33] P. U. Nzereogu, A. D. Omah, F. I. Ezema, E. I. Iwuoha, A. C. Nwanya, "Anode materials for lithium-ion batteries: A review" *Appl. Surf. Sci. Adv.* 2022, *9*, 100233. DOI: 10.1016/j.apsadv.2022.100233.

[34] Y. Zhao, Y. Fu, Y. Meng, Z. Wang, J. Liu, X. Gong, "Recent progress on cathode materials for lithium-ion batteries" *Chem. Eng. J.* 2024, *479*, 148047. DOI: 10.1016/j.cej.2023.148047.

[35] M. S. Whittingham, "Lithium batteries and cathode materials" *Chem. Rev.* 2004, *104*, 4271–4301.

[36] C. Liu, Z. G. Neale, G. Cao, "Understanding electrochemical potentials of cathode materials in rechargeable batteries" *Materials Today* 2016, *19*, 109–123. DOI: 10.1016/j.mattod.2015.10.009.

[37] C. M. Julien, A. Mauger, K. Zaghib, H. Groult, "Comparative Issues of Cathode Materials for Li-Ion Batteries" *Inorganics* 2014, *2*, 132–154.

[38] D. Deng, "Li-ion batteries: basics, progress, and challenges" *Energy Sci. Eng.* 2015, *3*, 385–418. DOI: 10.1002/ese3.95.

[39] H. Yang, N. Wu, "Ionic conductivity and ion transport mechanisms of solid-state lithium-ion battery electrolytes: A review" *Energy Sci. Eng.* 2022, *10*, 1645–1663. DOI: 10.1002/ese3.1163.

[40] B. Flamme, G. Rodriguez Garcia, M. Weil, M. Haddad, P. Phansavath, V. Ratovelomanana-Vidal, A. Chagnes, "Guidelines to design organic electrolytes for lithium-ion batteries: environmental impact, physicochemical and electrochemical properties" *Green Chem.* 2017, *19*, 1828–1849.

[41] M. M. Kabir, D. E. Demirocak, "Degradation mechanisms in Li-ion batteries: a state-of-the-art review" *Int. J. Energy Res.* 2017, *41*, 1963–1986. DOI: 10.1002/er.3762.

[42] H. Gao, J. Cai, G. L. Xu, L. Li, Y. Ren, X. Meng, K. Amine, Z. Chen, "Surface Modification for Suppressing Interfacial Parasitic Reactions of a Nickel-Rich Lithium-Ion Cathode" *Chem. Mater.* 2019, *31*, 2723–2730.

[43] J. Henschel, F. Horsthemke, Y. P. Stenzel, M. Evertz, S. Girod, C. Lürenbaum, K. Kösters, S. Wiemers-Meyer, M. Winter, S. Nowak, "Lithium-ion battery electrolyte degradation of field-tested electric vehicle battery cells – A comprehensive analytical study" *J. Power Sources* 2020, *447*, 227370. DOI: 10.1016/j.jpowsour.2019.227370.

[44] W. Xu, J. Wang, F. Ding, X. Chen, E. Nasybulin, Y. Zhang, J. G. Zhang, "Lithium metal anodes for rechargeable batteries" *Energy Environ. Sci.* 2014, *7*, 513–537.

[45] J. Janek, W. G. Zeier, "A solid future for battery development" *Nat. Energy* 2016, *1*, 16141.

[46] Y. Zhang, W. Lu, L. Cong, J. Liu, L. Sun, A. Mauger, C. M. Julien, H. Xie, J. Liu, "Cross-linking network based on Poly(ethylene oxide): Solid polymer electrolyte for room temperature lithium battery" *J. Power Sources* 2019, *420*, 63–72.

[47] P. Sedlak, A. Gajdos, R. Macku, J. Majzner, V. Holcman, V. Sedlakova, P. Kubersky, "The effect of thermal treatment on ac/dc conductivity and current fluctuations of PVDF/NMP/[EMIM][TFSI] solid polymer electrolyte" *Sci. Rep.* 2020, *10*, 20635. DOI: 10.1038/s41598-020-78363-6.

[48] S. Ram Prasanth, V. Prasannavenkadesan, V. Katiyar, A. S. Achalkumar, "Polymer electrolytes: evolution, challenges, and future directions for lithium-ion batteries" *RSC Appl. Polym.* 2025, *3*, 499–531. DOI: 10.1039/D4LP00325J.

[49] Z. Zhang, X. Wang, X. Li, J. Zhao, G. Liu, W. Yu, X. Dong, J. Wang, "Review on composite solid electrolytes for solid-state lithium-ion batteries" *Mater. Today Sustain.* 2023, *21*, 100316. DOI: 10.1016/j.mtsust.2023.100316.

[50] A. M. Abakumov, S. S. Fedotov, E. V. Antipov, J. M. Tarascon, "Compositionally complex doping for bridging disordered and ordered electrode materials" *Nat. Commun.* 2020, *11*, 4976. DOI: 10.1038/s41467-020-18736-7.

[51] J. Kincs, S. W. Martin, "Non-Arrhenius Conductivity in Glass: Mobility and Conductivity Saturation Effects" *Phys. Rev. Lett.* 1996, *76*, 70–73.

[52] C. Wang, K. Fu, S. P. Kammampata, D. W. McOwen, A. J. Samson, L. Zhang, G. T. Hitz, A. M. Nolan, E. D. Wachsman, Y. Mo, V. Thangadurai, L. Hu, "Garnet-Type Solid-State Electrolytes: Materials, Interfaces, and Batteries" *Chem. Rev.* 2020, *120*, 4257–4300. DOI: 10.1021/acs.chemrev.9b00427.

[53] M. V. Reddy, C. M. Julien, A. Mauger, K. Zaghib, "Sulfide and Oxide Inorganic Solid Electrolytes for All-Solid-State Li Batteries: A Review" *Nanomaterials* 2020, *10*, 1606. DOI: 10.3390/nano10081606.

[54] A. Manthiram, X. Yu, S. Wang, "Lithium battery chemistries enabled by solid-state electrolytes" *Nat. Rev. Mater.* 2017, *2*, 16103.

[55] W. Zhao, J. Yi, P. He, H. Zhou, "Solid-State Electrolytes for Lithium-Ion Batteries: Fundamentals, Challenges and Prospects" *Electrochem. Energy Rev.* 2019, *2*, 574–605. DOI: 10.1007/s41918-019-00048-0.

[56] L. Buannic, B. Orayech, J. M. López Del Amo, J. Carrasco, N. A. Katcho, F. Aguesse, W. Manalastas, W. Zhang, J. Kilner, A. Llordés, "Dual Substitution Strategy to Enhance Li+ Ionic Conductivity in Li7La3Zr2O12 Solid Electrolyte" *Chem. Mater.* 2017, *29*, 1769–1778.

[57] R. Murugan, V. Thangadurai, W. Weppner, "Fast lithium ion conduction in garnet-type Li7La3Zr2O12" *Angew. Chem. Int. Ed.* 2007, *46*, 7778–7781.

[58] J. Awaka, N. Kijima, H. Hayakawa, J. Akimoto, "Synthesis and structure analysis of tetragonal Li7La3Zr2O12 with the garnet-related type structure" *J. Solid State Chem.* 2009, *182*, 2046–2052.

[59] M. M. Raju, F. Altayran, M. Johnson, D. Wang, Q. Zhang, "Crystal Structure and Preparation of Li7La3Zr2O12 (LLZO) Solid-State Electrolyte and Doping Impacts on the Conductivity: An Overview" *Electrochem* 2021, *2*, 390–414.

[60] T. Thompson, J. Wolfenstine, J. L. Allen, M. Johannes, A. Huq, I. N. David, J. Sakamoto, "Tetragonal vs. cubic phase stability in Al-free Ta doped Li7La3Zr2O12 (LLZO)" *J. Mater. Chem. A* 2014, *2*, 13431–13436.

[61] S. Guo, Y. Sun, A. Cao, "Sintering Behavior of Li7La3Zr2O12 Ceramics" *Chem. Res. Chin. Univ.* 2020, *36*, 342–349. DOI: 10.1007/s40242-020-0116-0.

[62] C. Liu, K. Rui, C. Shen, M. E. Badding, G. Zhang, Z. Wen, "Reversible ion exchange and structural stability of garnet-type Nb-doped Li7La3Zr2O12 in water for applications in lithium batteries" *J. Power Sources* 2015, *282*, 286–293.

[63] S. Song, B. Yan, F. Zheng, H. M. Duong, L. Lu, "Crystal structure, migration mechanism and electrochemical performance of Cr-stabilized garnet" *Solid State Ion.* 2014, *268*, 135–139.

[64] S. Ohta, T. Kobayashi, T. Asaoka, "High lithium ionic conductivity in the garnet-type oxide Li7−XLa3(Zr2−X, NbX)O12 (X = 0–2)" *J. Power Sources* 2011, *196*, 3342–3345.

[65] F. Han, Y. Zhu, X. He, Y. Mo, C. Wang, "Electrochemical Stability of Li10GeP2S12 and Li7La3Zr2O12 Solid Electrolytes" *Adv. Energy Mater.* 2016, *6*, 1501590. DOI: 10.1002/aenm.201501590.

[66] Y. Zhu, X. He, Y. Mo, "Origin of Outstanding Stability in the Lithium Solid Electrolyte Materials: Insights from Thermodynamic Analyses Based on First-Principles Calculations" *ACS Appl. Mater. Interfaces* 2015, *7*, 23685–23693.

[67] S. Uhlenbruck, C. Dellen, S. Möller, S. Lobe, C. L. Tsai, M. Finsterbusch, M. Bram, O. Guillon, "Reactions of garnet-based solid-state lithium electrolytes with water — A depth-resolved study" *Solid State Ion.* 2018, *320*, 259–265.

[68] L. Cheng, E. J. Crumlin, W. Chen, R. Qiao, H. Hou, S. Franz Lux, V. Zorba, R. Russo, R. Kostecki, Z. Liu, K. Persson, W. Yang, J. Cabana, T. Richardson, G. Chen, M. Doeff, "The origin of high electrolyte-electrode interfacial resistances in lithium cells containing garnet type solid electrolytes" *Phys. Chem. Chem. Phys.* 2014, *16*, 18294–18300.

[69] Y. Jin, P. J. McGinn, "Li7La3Zr2O12 electrolyte stability in air and fabrication of a Li/Li7La3Zr2O12/Cu0.1V2O5 solid-state battery" *J. Power Sources* 2013, *239*, 326–331.

[70] W. Xia, B. Xu, H. Duan, X. Tang, Y. Guo, H. Kang, H. Li, H. Liu, "Reaction mechanisms of lithium garnet pellets in ambient air: The effect of humidity and CO2" *J. Am. Ceram. Soc.* 2017, *100*, 2832–2839.

[71] W. Xia, B. Xu, H. Duan, Y. Guo, H. Kang, H. Li, H. Liu, "Ionic Conductivity and Air Stability of Al-Doped Li7La3Zr2O12 Sintered in Alumina and Pt Crucibles" *ACS Appl. Mater. Interfaces* 2016, *8*, 5335–5342.

[72] A. Sharafi, S. Yu, M. Naguib, M. Lee, C. Ma, H. M. Meyer, J. Nanda, M. Chi, D. J. Siegel, J. Sakamoto, "Impact of air exposure and surface chemistry on Li–Li7La3Zr2O12 interfacial resistance" *J. Mater. Chem. A* 2017, *5*, 13475–13487.

[73] M. Nakayama, T. Horie, R. Natsume, S. Hashimura, N. Tanibata, H. Takeda, H. Maeda, M. Kotobuki, "Reaction Kinetics of Carbonation at the Surface of Garnet-Type Li7La3Zr2O12 as Solid Electrolytes for All-Solid-State Li Ion Batteries" *J. Phys. Chem. C* 2023, *127*, 7595–7601.

[74] L. Cheng, C. H. Wu, A. Jarry, W. Chen, Y. Ye, J. Zhu, R. Kostecki, K. Persson, J. Guo, M. Salmeron, G. Chen, M. Doeff, "Interrelationships among Grain Size, Surface Composition, Air Stability, and Interfacial

Resistance of Al-Substituted Li7La3Zr2O12 Solid Electrolytes" *ACS Appl. Mater. Interfaces* 2015, *7*, 17649–17655.

[75] R. Kun, F. Langer, M. Delle Piane, S. Ohno, W. G. Zeier, M. Gockeln, L. Colombi Ciacchi, M. Busse, I. Fekete, "Structural and Computational Assessment of the Influence of Wet-Chemical Post-Processing of the Al-Substituted Cubic Li7La3Zr2O12" *ACS Appl. Mater. Interfaces* 2018, *10*, 37188–37197.

[76] R. Grissa, S. Payandeh, M. Heinz, C. Battaglia, "Impact of Protonation on the Electrochemical Performance of Li7La3Zr2O12 Garnets" *ACS Appl. Mater. Interfaces* 2021, *13*, 14700–14709.

[77] K. Nie, S. Wu, J. Wang, X. Sun, Z. Yan, J. Qiu, Q. Yang, R. Xiao, X. Yu, H. Li, L. Chen, X. Huang, "Reaction Mechanisms of Ta-Substituted Cubic Li7La3Zr2O12 with Solvents during Storage" *ACS Appl. Mater. Interfaces* 2021, *13*, 38384–38393.

[78] Y. Arinicheva, X. Guo, M. T. Gerhards, F. Tietz, D. Fattakhova-Rohlfing, M. Finsterbusch, A. Navrotsky, O. Guillon, "Competing Effects in the Hydration Mechanism of a Garnet-Type Li7La3Zr2O12 Electrolyte" *Chem. Mater.* 2022, *34*, 1473–1480.

[79] R. Ye, M. Ihrig, N. Imanishi, M. Finsterbusch, E. Figgemeier, "A Review on Li+/H+ Exchange in Garnet Solid Electrolytes: From Instability against Humidity to Sustainable Processing in Water" *ChemSusChem* 2021, *14*, 4397–4407.

[80] A. Ishii, D. Kume, S. Nakayasu, I. Oikawa, H. Matsumoto, H. Kato, H. Takamura, "Proton conductivity of Li+–H+ exchanged Li7La3Zr2O12 dense membranes prepared by molten long-chain saturated fatty acids" *Mater. Adv.* 2024, *5*, 1531–1539.

[81] K. Touidjine, M. Finsterbusch-Rosen, V. M. Kiyek, S. Ganapathy, M. Finsterbusch, O. Guillon, M. Huijben, E. M. Kelder, M. Wagemaker, D. Fattakhova-Rohlfing, "The impact of lithium carbonate on tape cast LLZO battery separators: A balanced interplay between lithium loss and relithiation" *Energy Storage Mater.* 2024, *71*, 103487. DOI: 10.1016/j.ensm.2024.103487.

[82] R. Ye, *Sustainable Fabrication of Ceramic Solid Electrolytes for Solid-State Lithium Batteries*, PhD thesis, RWTH Aachen University, Forschungszentrum Jülich GmbH, Jülich, 2023. DOI: 10.18154/RWTH-2023-05660.

[83] C. Fritsch, T. Zinkevich, S. Indris, M. Etter, V. Baran, T. Bergfeldt, M. Knapp, H. Ehrenberg, A.-L. Hansen, "Garnet to hydrogarnet: effect of post synthesis treatment on cation substituted LLZO solid electrolyte and its effect on Li ion conductivity" *RSC Adv.* 2021, *11*, 30283. DOI: 10.1039/d1ra05961k.

[84] C. Galven, J. Dittmer, E. Suard, F. Le Berre, M. P. Crosnier-Lopez, "Instability of lithium garnets against moisture. Structural characterization and dynamics of Li7−xHxLa3Sn2O12 and Li5−xHxLa3Nb2O12" *Chem. Mater.* 2012, *24*, 3335–3345.

[85] L. Cheng, M. Liu, A. Mehta, H. Xin, F. Lin, K. Persson, G. Chen, E. J. Crumlin, M. Doeff, "Garnet Electrolyte Surface Degradation and Recovery" *ACS Appl. Energy Mater.* 2018, *1*, 7244–7252.

[86] L. Porz, T. Swamy, B. W. Sheldon, D. Rettenwander, T. Frömling, H. L. Thaman, S. Berendts, R. Uecker, W. C. Carter, Y. M. Chiang, "Mechanism of Lithium Metal Penetration through Inorganic Solid Electrolytes" *Adv. Energy Mater.* 2017, *7*, 1701003. DOI: 10.1002/aenm.201701003.

[87] N. Zhang, X. Long, Z. Wang, P. Yu, F. Han, J. Fu, G. Ren, Y. Wu, S. Zheng, W. Huang, C. Wang, H. Li, X. Liu, "Mechanism Study on the Interfacial Stability of a Lithium Garnet-Type Oxide Electrolyte against Cathode Materials" *ACS Appl. Energy Mater.* 2018, *1*, 5968–5976.

[88] C. L. Tsai, V. Roddatis, C. V. Chandran, Q. Ma, S. Uhlenbruck, M. Bram, P. Heitjans, O. Guillon, "Li7La3Zr2O12 Interface Modification for Li Dendrite Prevention" *ACS Appl. Mater. Interfaces* 2016, *8*, 10617–10626.

[89] N. Janani, C. Deviannapoorani, L. Dhivya, R. Murugan, "Influence of sintering additives on densification and Li+ conductivity of Al doped Li7La3Zr2O12 lithium garnet" *RSC Adv.* 2014, *4*, 51228–51238.

[90] W. Xue, Y. Yang, Q. Yang, Y. Liu, L. Wang, C. Chen, R. Cheng, "The effect of sintering process on lithium ionic conductivity of Li6.4Al0.2La3Zr2O12 garnet produced by solid-state synthesis" *RSC Adv.* 2018, *8*, 13083–13088.

[91] W. S. Scheld, S. Lobe, C. Dellen, M. Ihrig, G. Häuschen, L. C. Hoff, M. Finsterbusch, S. Uhlenbruck, O. Guillon, D. Fattakhova-Rohlfing, "Rapid thermal processing of garnet-based composite cathodes" *J. Power Sources* 2022, *545*, 231872. DOI: 10.1016/j.jpowsour.2022.231872.

[92] M. Ihrig, *Advanced Sintering of Garnet-Based Ceramic Composite Cathodes for All-Solid-State Lithium Batteries*, PhD thesis, RWTH Aachen University, Forschungszentrum Jülich GmbH, Jülich, 2022. (Schriften des Forschungszentrums Jülich, Reihe Energie & Umwelt, Vol. 571).

[93] Y. Ren, T. Danner, A. Moy, M. Finsterbusch, T. Hamann, J. Dippell, T. Fuchs, M. Müller, R. Hoft, A. Weber, L. A. Curtiss, P. Zapol, M. Klenk, A. T. Ngo, P. Barai, B. C. Wood, R. Shi, L. F. Wan, T. W. Heo, M. Engels, J. Nanda, F. H. Richter, A. Latz, V. Srinivasan, J. Janek, J. Sakamoto, E. D. Wachsman, D. Fattakhova-Rohlfing, "Oxide-Based Solid-State Batteries: A Perspective on Composite Cathode Architecture" *Adv. Energy Mater.* 2022, *12*, 2201939. DOI: 10.1002/aenm.202201939.

[94] K. J. Kim, J. L. M. Rupp, "All ceramic cathode composite design and manufacturing towards low interfacial resistance for garnet-based solid-state lithium batteries" *Energy Environ. Sci.* 2020, *13*, 4930–4945.

[95] K. Gao, M. He, Y. Li, Y. Zhang, J. Gao, X. Li, Z. Cui, Z. Zhan, T. Zhang, "Preparation of high-density garnet thin sheet electrolytes for all-solid-state Li-Metal batteries by tape-casting technique" *J. Alloys Compd.* 2019, *791*, 923–928.

[96] C. Roitzheim, Y. J. Sohn, L. Y. Kuo, G. Häuschen, M. Mann, D. Sebold, M. Finsterbusch, P. Kaghazchi, O. Guillon, D. Fattakhova-Rohlfing, "All-Solid-State Li Batteries with NCM–Garnet-Based Composite Cathodes: The Impact of NCM Composition on Material Compatibility" *ACS Appl. Energy Mater.* 2022, *5*, 6913–6926.

[97] J. Wang, G. Huang, X. B. Zhang, "Rechargeable Lithium–Oxygen Batteries" *Batteries Supercaps* 2020, *3*, 886–898. DOI: 10.1002/batt.202000082.

[98] K. K. Fu, Y. Gong, B. Liu, Y. Zhu, S. Xu, Y. Yao, W. Luo, C. Wang, S. D. Lacey, J. Dai, Y. Chen, Y. Mo, E. Wachsman, L. Hu, "Toward garnet electrolyte–based Li metal batteries: An ultrathin, highly effective, artificial solid-state electrolyte/metallic Li interface" *Sci. Adv.* 2017, *3*, e1601659. DOI: 10.1126/SCIADV.1601659.

[99] B. Liu, L. Zhang, S. Xu, D. W. McOwen, Y. Gong, C. Yang, G. R. Pastel, H. Xie, K. Fu, J. Dai, C. Chen, E. D. Wachsman, L. Hu, "3D Lithium Metal Anodes Hosted in Asymmetric Garnet Frameworks toward High Energy Density Batteries" *Joule* 2018, *2*, 1903–1916.

[100] M. Wang, J. B. Wolfenstine, J. Sakamoto, "Temperature dependent flux balance of the Li/Li7La3Zr2O12 interface" *Electrochim. Acta* 2019, *296*, 842–847.

[101] H. J. Noh, S. Youn, C. S. Yoon, Y. K. Sun, "Comparison of the structural and electrochemical properties of layered Li[NixCoyMnz]O2 (x = 1/3, 0.5, 0.6, 0.7, 0.8 and 0.85) cathode material for lithium-ion batteries" *J. Power Sources* 2013, *233*, 121–130.

[102] R. Castro, K. van Benthem, Eds., *Sintering*, Springer Berlin Heidelberg, Berlin, Heidelberg, 2013.

[103] M. Sopicka-Lizer, *High-Energy Ball Milling: Mechanochemical Processing of Nanopowders*, CRC Press, Boca Raton, 2010.

[104] A. M. Laptev, H. Zheng, M. Bram, M. Finsterbusch, O. Guillon, "High-pressure field assisted sintering of half-cell for all-solid-state battery" *Mater. Lett.* 2019, *247*, 155–158. DOI: 10.1016/j.matlet.2019.03.109.

[105] F. Okur, H. Zhang, J. F. Baumgärtner, J. Sivavec, M. Klimpel, G. P. Wasser, R. Dubey, L. P. H. Jeurgens, D. Chernyshov, W. van Beek, K. V. Kravchyk, M. V. Kovalenko, "Ultrafast Sintering of Dense Li7La3Zr2O12 Membranes for Li Metal All-Solid-State Batteries" *Adv. Sci.* 2024, *11*, 2412370. DOI: 10.1002/advs.202412370.

[106] P. Ghorbanzade, A. Pesce, K. Gómez, G. Accardo, S. Devaraj, P. López-Aranguren, J. M. López del Amo, "Impact of thermal treatment on the Li-ion transport, interfacial properties, and composite preparation of LLZO garnets for solid-state electrolytes" *J. Mater. Chem. A* 2023, *11*, 11675–11683.

[107] Z. Huang, K. Liu, L. Chen, Y. Lu, Y. Li, C. A. Wang, "Sintering behavior of garnet-type Li6.4La3Zr1.4Ta0.6O12 in Li2CO3 atmosphere and its electrochemical property" *Int. J. Appl. Ceram. Technol.* 2017, *14*, 921–927.

[108] X. Huang, T. Xiu, M. E. Badding, Z. Wen, "Two-step sintering strategy to prepare dense Li-garnet electrolyte ceramics with high Li+ conductivity" *Ceram. Int.* 2018, *44*, 5660–5667.

[109] N. Janani, S. Ramakumar, S. Kannan, R. Murugan, "Optimization of Lithium Content and Sintering Aid for Maximized Li+ Conductivity and Density in Ta-Doped Li7La3Zr2O12" *J. Am. Ceram. Soc.* 2015, *98*, 2039–2046.

[110] P. Barai, T. Fister, Y. Liang, J. Libera, M. Wolfman, X. Wang, J. Garcia, H. Iddir, V. Srinivasan, "Investigating the Calcination and Sintering of Li7La3Zr2O12 (LLZO) Solid Electrolytes Using Operando Synchrotron X-ray Characterization and Mesoscale Modeling" *Chem. Mater.* 2021, *33*, 4337–4352.

[111] X. Huang, Y. Lu, Z. Song, K. Rui, Q. Wang, T. Xiu, M. E. Badding, Z. Wen, "Manipulating Li2O atmosphere for sintering dense Li7La3Zr2O12 solid electrolyte" *Energy Storage Mater.* 2019, *22*, 207–217.

[112] R. A. Jonson, P. J. McGinn, "Tape casting and sintering of Li7La3Zr1.75Nb0.25Al0.1O12 with Li3BO3 additions" *Solid State Ion.* 2018, *323*, 49–55.

[113] W. S. Scheld, K. Kim, C. Schwab, A. C. Moy, S. Jiang, M. Mann, C. Dellen, Y. J. Sohn, S. Lobe, M. Ihrig, M. G. Danner, C. Chang, S. Uhlenbruck, E. D. Wachsman, B. J. Hwang, J. Sakamoto, L. F. Wan, B. C. Wood, M. Finsterbusch, D. Fattakhova-Rohlfing, "The Riddle of Dark LLZO: Cobalt Diffusion in Garnet Separators of Solid-State Lithium Batteries" *Adv. Funct. Mater.* 2023, *33*, 2302939. DOI: 10.1002/adfm.202302939.

[114] E. Kurian, J. Pitchai, S. Neelanarayanan, K. Ramesha, "In pursuit of all solid state batteries (ASSB): advances at the cathode–electrolyte interface for garnet-based ASSB" *RSC Appl. Interfaces* 2024, *1*, 868–895.

[115] A. Bauer, C. Roitzheim, S. Lobe, Y. J. Sohn, D. Sebold, W. S. Scheld, M. Finsterbusch, O. Guillon, D. Fattakhova-Rohlfing, S. Uhlenbruck, "Impact of Ni–Mn–Co–Al-Based Cathode Material Composition on the Sintering with Garnet Solid Electrolytes for All-Solid-State Batteries" *Chem. Mater.* 2023, *35*, 8958–8968.

[116] M. Ihrig, M. Finsterbusch, C. L. Tsai, A. M. Laptev, C. H. Tu, M. Bram, Y. J. Sohn, R. Ye, S. Sevinc, S. K. Lin, D. Fattakhova-Rohlfing, O. Guillon, "Low temperature sintering of fully inorganic all-solid-state batteries – Impact of interfaces on full cell performance" *J. Power Sources* 2021, *482*, 228905.

[117] D. Wang, Q. Sun, J. Luo, J. Liang, Y. Sun, R. Li, K. Adair, L. Zhang, R. Yang, S. Lu, H. Huang, X. Sun, "Mitigating the Interfacial Degradation in Cathodes for High-Performance Oxide-Based Solid-State Lithium Batteries" *ACS Appl. Mater. Interfaces* 2019, *11*, 4954–4961.

[118] Y. Ren, T. Liu, Y. Shen, Y. Lin, C. W. Nan, "Chemical compatibility between garnet-like solid state electrolyte Li6.75La3Zr1.75Ta0.25O12 and major commercial lithium battery cathode materials" *J. Materiomics* 2016, *2*, 256–264.

[119] W. S. Scheld, Y. Collette, K. Touidjine, C. Roitzheim, Y. J. Sohn, D. Fattakhova-Rohlfing, "Increasing the cycling stability of LLZO-based solid-state batteries with Li3BO3 as catholyte" *J. Power Sources* 2025, *652*, 237322. DOI: 10.1016/j.jpowsour.2025.237322.

[120] M. Balaish, J. C. Gonzalez-Rosillo, K. J. Kim, Y. Zhu, Z. D. Hood, J. L. M. Rupp, "Processing thin but robust electrolytes for solid-state batteries" *Nat. Energy* 2021, *6*, 227–239. DOI: 10.1038/s41560-020-00759-5.

[121] J. Tan, A. Tiwari, "Fabrication and characterization of Li7La3Zr2O12 thin films for lithium ion battery" *ECS Solid State Lett.* 2012, *1*, M31–M33. DOI: 10.1149/2.013206ssl.

[122] J. Reinacher, S. Berendts, J. Janek, "Preparation and electrical properties of garnet-type Li6BaLa2Ta2O12 lithium solid electrolyte thin films prepared by pulsed laser deposition" *Solid State Ion.* 2014, *258*, 1–7.

[123] Y. Yu, M. Gong, C. Dong, X. Xu, "Thin-film deposition techniques in surface and interface engineering of solid-state lithium batteries" *Next Nanotechnol.* 2023, *3–4*, 100028.

[124] H. Katsui, T. Goto, "Preparation of cubic and tetragonal Li7La3Zr2O12 film by chemical vapor deposition" *Thin Solid Films* 2015, *584*, 130–134.

[125] S. Lobe, C. Dellen, M. Finsterbusch, H. G. Gehrke, D. Sebold, C. L. Tsai, S. Uhlenbruck, O. Guillon, "Radio frequency magnetron sputtering of Li7La3Zr2O12 thin films for solid-state batteries" *J. Power Sources* 2016, *307*, 684–689.

[126] G. Vardar, W. J. Bowman, Q. Lu, J. Wang, R. J. Chater, A. Aguadero, R. Seibert, J. Terry, A. Hunt, I. Waluyo, D. D. Fong, A. Jarry, E. J. Crumlin, S. L. Hellstrom, Y. M. Chiang, B. Yildiz, "Structure, Chemistry, and Charge Transfer Resistance of the Interface between Li7La3Zr2O12 Electrolyte and LiCoO2 Cathode" *Chem. Mater.* 2018, *30*, 6259–6276.

[127] S. Ohta, T. Kobayashi, J. Seki, T. Asaoka, "Electrochemical performance of an all-solid-state lithium ion battery with garnet-type oxide electrolyte" *J. Power Sources* 2012, *202*, 332–335.

[128] R. A. Jonson, E. Yi, F. Shen, M. C. Tucker, "Optimization of Tape Casting for Fabrication of Li6.25Al0.25La3Zr2O12 Sheets" *Energy Fuels* 2021, *35*, 8982–8990.

[129] M. Mann, M. Küpers, G. Häuschen, M. Finsterbusch, D. Fattakhova-Rohlfing, O. Guillon, "Evaluation of scalable synthesis methods for aluminum-substituted Li7La3Zr2O12 solid electrolytes" *Materials* 2021, *14*, 6809. DOI: 10.3390/ma14226809.

[130] M. Finsterbusch-Rosen, *Herstellung von Freitragenden Oxid-Keramischen Batteriekomponenten für Festkörperbatterien per Folienguss*, PhD thesis, University of Duisburg–Essen, 2022.

[131] M. Broseghini, L. Gelisio, M. D'Incau, C. L. Azanza Ricardo, N. M. Pugno, P. Scardi, "Modeling of the planetary ball-milling process: The case study of ceramic powders" *J. Eur. Ceram. Soc.* 2016, *36*, 2205–2212.

[132] A. Bijelic, A. Rompel, "Polyoxometalates: more than a phasing tool in protein crystallography" *ChemTexts* 2018, *4*, 10. DOI: 10.1007/s40828-018-0064-1.

[133] L. Lin, X. Bi, Y. Gu, F. Wang, J. Ye, "Surface-enhanced Raman scattering nanotags for bioimaging" *J. Appl. Phys.* 2021, *129*, 191101. DOI: 10.1063/5.0047578.

[134] E. Smith, G. Dent, *Modern Raman Spectroscopy: A Practical Approach*, 2nd ed., Wiley, Chichester, 2019.

[135] O. Pecher, J. Carretero-Gonzalez, K. J. Griffith, C. P. Grey, "Materials' Methods: NMR in Battery Research" *Chem. Mater.* 2017, *29*, 213–242. DOI: 10.1021/acs.chemmater.6b03183.

[136] A. R. Haworth, C. W. Cook, J. M. Griffin, "Solid-state NMR studies of coatings and interfaces in batteries" *Curr. Opin. Colloid Interface Sci.* 2022, *62*, 101638. DOI: 10.1016/j.cocis.2022.101638.

[137] K. Akhtar, S. A. Khan, S. B. Khan, A. M. Asiri, "Scanning Electron Microscopy: Principle and Applications in Nanomaterials Characterization" in *Handbook of Materials Characterization*, Springer International Publishing, Cham, 2018, pp. 113–145.

[138] B. Amos, G. McConnell, T. Wilson, "Confocal Microscopy" in *Comprehensive Biophysics*, Elsevier Inc., Amsterdam, 2012, vol. 2, pp. 3–23.

[139] N. Saadatkhah, A. Carillo Garcia, S. Ackermann, P. Leclerc, M. Latifi, S. Samih, G. S. Patience, J. Chaouki, "Experimental methods in chemical engineering: Thermogravimetric analysis — TGA" *Can. J. Chem. Eng.* 2020, *98*, 34–43. DOI: 10.1002/cjce.23673.

[140] R. Machado, V. Sencadas, "Advanced Techniques for Characterizing Bioinspired Materials" in *Bioinspired Materials for Medical Applications*, Elsevier, Amsterdam, 2017, pp. 177–214.

[141] S. Sarkar, T. K. Dutta, A. Sah, A. Patra, "Fundamental Mechanisms and Requirements of Energy Storage Materials" in *Polymer Blend Nanocomposites for Energy Storage Applications*, Elsevier, Amsterdam, 2023, pp. 35–87.

[142] Y. Lu, C. Z. Zhao, H. Yuan, X. B. Cheng, J. Q. Huang, Q. Zhang, "Critical Current Density in Solid-State Lithium Metal Batteries: Mechanism, Influences, and Strategies" *Adv. Funct. Mater.* 2021, *31*, 2009925. DOI: 10.1002/adfm.202009925.

[143] B. Y. Chang, S. M. Park, "Electrochemical impedance spectroscopy" *Annu. Rev. Anal. Chem.* 2010, *3*, 207–229.

[144] P. Vadhva, J. Hu, M. J. Johnson, R. Stocker, M. Braglia, D. J. L. Brett, A. J. E. Rettie, "Electrochemical Impedance Spectroscopy for All-Solid-State Batteries: Theory, Methods and Future Outlook" *ChemElectroChem* 2021, *8*, 1930–1947. DOI: 10.1002/celc.202100108.

[145] M. E. Orazem, I. Frateur, B. Tribollet, V. Vivier, S. Marcelin, N. Pébère, A. L. Bunge, E. A. White, D. P. Riemer, M. Musiani, "Dielectric Properties of Materials Showing Constant-Phase-Element (CPE) Impedance Response" *J. Electrochem. Soc.* 2013, *160*, C215–C225.

[146] J. T. S. Irvine, D. C. Sinclair, A. R. West, "Electroceramics: Characterization by Impedance Spectroscopy" *Adv. Mater.* 1990, *2*, 132–138. DOI: 10.1002/adma.19900020304.

[147] J. Kim, S. Park, S. Hwang, W. S. Yoon, "Principles and Applications of Galvanostatic Intermittent Titration Technique for Lithium-Ion Batteries" *J. Electrochem. Sci. Technol.* 2022, *13*, 19–31. DOI: 10.33961/jecst.2021.00836.

[148] E. Yi, W. Wang, J. Kieffer, R. M. Laine, "Flame made nanoparticles permit processing of dense, flexible, Li+ conducting ceramic electrolyte thin films of cubic-Li7La3Zr2O12 (c-LLZO)" *J. Mater. Chem. A* 2016, *4*, 12947–12954.

[149] H. Zhang, R. Dubey, M. Inniger, F. Okur, R. Wullich, A. Parrilli, D. T. Karabay, A. Neels, K. V. Kravchyk, M. V. Kovalenko, "Ultrafast-sintered self-standing LLZO membranes for high energy density lithium-garnet solid-state batteries" *Cell Rep. Phys. Sci.* 2023, *4*, 101473. DOI: 10.1016/j.xcrp.2023.101473.

[150] H. Huo, J. Luo, V. Thangadurai, X. Guo, C. W. Nan, X. Sun, "Li2CO3: A Critical Issue for Developing Solid Garnet Batteries" *ACS Energy Lett.* 2020, *5*, 252–262.

[151] A. Boulant, J. F. Bardeau, A. Jouanneaux, J. Emery, J.-Y. Buzaré, O. Bohnke, "Reaction mechanism of Li0.3La0.57TiO3 powder with ambient air: H+/Li+ exchange with water and Li2CO3 formation" *Dalton Trans.* 2010, *39*, 3968–3975.

[152] E. Hanc, W. Zając, L. Lu, B. Yan, M. Kotobuki, M. Ziąbka, J. Molenda, "On fabrication procedures of Li-ion conducting garnets" *J. Solid State Chem.* 2017, *248*, 51–60.

[153] T. Hamann, L. Zhang, Y. Gong, G. Godbey, J. Gritton, D. McOwen, G. Hitz, E. Wachsman, "The Effects of Constriction Factor and Geometric Tortuosity on Li-Ion Transport in Porous Solid-State Li-Ion Electrolytes" *Adv. Funct. Mater.* 2020, *30*, 1910362. DOI: 10.1002/adfm.201910362.

[154] K. Fu, Y. Gong, G. T. Hitz, D. W. McOwen, Y. Li, S. Xu, Y. Wen, L. Zhang, C. Wang, G. Pastel, J. Dai, B. Liu, H. Xie, Y. Yao, E. D. Wachsman, L. Hu, "Three-dimensional bilayer garnet solid electrolyte based high energy density lithium metal–sulfur batteries" *Energy Environ. Sci.* 2017, *10*, 1568–1575.

[155] A. Parejiya, M. B. Dixit, D. Parikh, R. Amin, R. Essehli, J. Li, D. L. Wood, I. Belharouak, "Understanding slurry formulations to guide solution-processing of solid electrolytes" *J. Power Sources* 2022, *544*, 231894. DOI: 10.1016/j.jpowsour.2022.231894.

[156] K. Liu, C. A. Wang, "Honeycomb-alumina supported garnet membrane: Composite electrolyte with low resistance and high strength for lithium metal batteries" *J. Power Sources* 2015, *281*, 399–403.

[157] G. J. Redhammer, G. Tippelt, A. Portenkirchner, D. Rettenwander, "Aging Behavior of Al- and Ga-Stabilized Li7La3Zr2O12 Garnet-Type, Solid-State Electrolyte Based on Powder and Single Crystal X-ray Diffraction" *Crystals* 2021, *11*, 644. DOI: 10.3390/cryst11060644.

[158] A. Parejiya, M. B. Dixit, D. Parikh, R. Amin, R. Essehli, J. Li, D. L. Wood, I. Belharouak, "Understanding slurry formulations to guide solution-processing of solid electrolytes" *J. Power Sources* 2022, *544*, 231894. DOI: 10.1016/j.jpowsour.2022.231894.

[159] V. Kiyek, M. Hilger, M. Rosen, J. P. Gross, M. Mann, D. Fattakhova-Rohlfing, R. Schwaiger, M. Finsterbusch, O. Guillon, "Waste minimization in all-solid-state battery production via re-lithiation of the garnet solid electrolyte LLZO" *J. Power Sources* 2024, *609*, 234709. DOI: 10.1016/j.jpowsour.2024.234709.

[160] A. Parejiya, M. B. Dixit, D. Parikh, R. Amin, R. Essehli, J. Li, D. L. Wood, I. Belharouak, "Understanding slurry formulations to guide solution-processing of solid electrolytes" *J. Power Sources* 2022, *544*, 231894. DOI: 10.1016/j.jpowsour.2022.231894.

[161] R. A. Jonson, P. J. McGinn, "Tape casting and sintering of Li7La3Zr1.75Nb0.25Al0.1O12 with Li3BO3 additions" *Solid State Ion.* 2018, *323*, 49–55.

[162] G. Larraz, A. Orera, M. L. Sanjuán, "Cubic phases of garnet-type Li7La3Zr2O12: The role of hydration" *J. Mater. Chem. A* 2013, *1*, 11419–11428.

[163] X. Huang, Y. Lu, Z. Song, K. Rui, Q. Wang, T. Xiu, M. E. Badding, Z. Wen, "Manipulating Li2O atmosphere for sintering dense Li7La3Zr2O12 solid electrolyte" *Energy Storage Mater.* 2019, *22*, 207–217.

[164] Z. Huang, K. Liu, L. Chen, Y. Lu, Y. Li, C. A. Wang, "Sintering behavior of garnet-type Li6.4La3Zr1.4Ta0.6O12 in Li2CO3 atmosphere and its electrochemical property" *Int. J. Appl. Ceram. Technol.* 2017, *14*, 921–927.

[165] X. Ping, Q. Zheng, B. Meng, W. Lin, Y. Chen, C. Fang, H. Zhang, W. Liang, "Influence of sintering atmosphere on the phase, microstructure, and lithium-ion conductivity of the Al-doped Li7La3Zr2O12 solid electrolyte" *Ceram. Int.* 2022, *48*, 25689–25695.

[166] K. Liu, J. T. Ma, C. A. Wang, "Excess lithium salt functions more than compensating for lithium loss when synthesizing Li6.5La3Ta0.5Zr1.5O12 in alumina crucible" *J. Power Sources* 2014, *260*, 109–114.

[167] E. Hanc, W. Zając, L. Lu, B. Yan, M. Kotobuki, M. Ziąbka, J. Molenda, "On fabrication procedures of Li-ion conducting garnets" *J. Solid State Chem.* 2017, *248*, 51–60.

[168] S. Li, C. Song, X. Qin, Z. Zeng, "Densification and grain growth behavior of highly dense MgO ceramics in pressureless sintering" *Ceram. Int.* 2015, *41*, 10148–10151.

[169] X. Huang, Y. Lu, Z. Song, T. Xiu, M. E. Badding, Z. Wen, "Preparation of dense Ta-LLZO/MgO composite Li-ion solid electrolyte: Sintering, microstructure, performance and the role of MgO" *J. Energy Chem.* 2019, *39*, 8–16.

[170] T. Dussart, N. Rividi, M. Fialin, G. Toussaint, P. Stevens, C. Laberty-Robert, "Critical Current Density Limitation of LLZO Solid Electrolyte: Microstructure vs Interface" *J. Electrochem. Soc.* 2021, *168*, 120550.

[171] B. Hao, W. Chen, J. Wu, Z. J. Jiang, X. Chen, Z. Jiang, "Long-Term Cycling Stability and Dendrite Suppression in Garnet-Type Solid-State Lithium Batteries via Plasma-Induced Artificial SEI Layer Formation" *Adv. Funct. Mater.* 2025, *35*, 2502429. DOI: 10.1002/adfm.202502429.

[172] M. Siniscalchi, Y. Shi, G. Li, J. S. Gibson, R. S. Weatherup, R. S. Bonilla, S. C. Speller, C. R. M. Grovenor, "Initiation of dendritic failure of LLZTO via sub-surface lithium deposition" *Energy Environ. Sci.* 2024, *17*, 2431–2440.

[173] V. M. Kiyek, *Oxide-Based All-Solid-State Batteries for and from Recycling Processes*, PhD thesis, RWTH Aachen University, Forschungszentrum Jülich GmbH, Jülich, 2024. (Schriften des Forschungszentrums Jülich, Reihe Energie & Umwelt, Vol. 656). ISBN: 978-3-95806-806-3.

[174] M. Kotobuki, K. Kanamura, Y. Sato, T. Yoshida, "Fabrication of all-solid-state lithium battery with lithium metal anode using Al2O3-added Li7La3Zr2O12 solid electrolyte" *J. Power Sources* 2011, *196*, 7750–7754.

[175] M. Abdulai, K. B. Dermenci, S. Turan, "SPS sintering and characterization of Li7La3Zr2O12 solid electrolytes" *MRS Energy Sustain.* 2023, *10*, 94–99.

[176] M. Ihrig, T. P. Mishra, W. S. Scheld, G. Häuschen, W. Rheinheimer, M. Bram, M. Finsterbusch, O. Guillon, "Li7La3Zr2O12 solid electrolyte sintered by the ultrafast high-temperature method" *J. Eur. Ceram. Soc.* 2021, *41*, 6075–6079.

[177] H. Zhang, R. Dubey, M. Inniger, F. Okur, R. Wullich, A. Parrilli, D. T. Karabay, A. Neels, K. V. Kravchyk, M. V. Kovalenko, "Ultrafast-sintered self-standing LLZO membranes for high energy density lithium-garnet solid-state batteries" *Cell Rep. Phys. Sci.* 2023, *4*, 101473. DOI: 10.1016/j.xcrp.2023.101473.

[178] Y. N. Yang, Y. X. Li, Y. Q. Li, T. Zhang, "On-surface lithium donor reaction enables decarbonated lithium garnets and compatible interfaces within cathodes" *Nat. Commun.* 2020, *11*, 5519. DOI: 10.1038/s41467-020-19417-1.

[179] J. van den Broek, S. Afyon, J. L. M. Rupp, "Interface-Engineered All-Solid-State Li-Ion Batteries Based on Garnet-Type Fast Li+ Conductors" *Adv. Energy Mater.* 2016, *6*, 1600736. DOI: 10.1002/aenm.201600736.

[180] L. Cheng, C. H. Wu, A. Jarry, W. Chen, Y. Ye, J. Zhu, R. Kostecki, K. Persson, J. Guo, M. Salmeron, G. Chen, M. Doeff, "Interrelationships among Grain Size, Surface Composition, Air Stability, and Interfacial Resistance of Al-Substituted Li7La3Zr2O12 Solid Electrolytes" *ACS Appl. Mater. Interfaces* 2015, *7*, 17649–17655.

[181] H. Yamada, T. Ito, S. P. Kammampata, V. Thangadurai, "Toward Understanding the Reactivity of Garnet-Type Solid Electrolytes with H2O/CO2 in a Glovebox Using X-ray Photoelectron Spectroscopy and Electrochemical Methods" *ACS Appl. Mater. Interfaces* 2020, *12*, 36119–36127.

[182] J. Wu, Y. Wang, W. Chen, Z. Xu, Z. J. Jiang, T. Maiyalagan, Z. Jiang, "Key challenges and recent advances in advanced characterization techniques for LLZO-based solid-state lithium metal batteries" *Energy Storage Mater.* 2025, *82*, 104672. DOI: 10.1016/j.ensm.2025.104672.

[183] W. M. Seong, Y. Kim, A. Manthiram, "Impact of Short-Range Ordering on the Properties of Ni-Rich Layered Oxide Cathodes for Lithium-Ion Batteries" *Chem. Mater.* 2020, *32*, 9305–9313. DOI: 10.1021/acs.chemmater.0c02808.

[184] X. Liu, Z. Huang, "Rapid treatment of LLZTO solid electrolyte surface impurities by lactic acid solution" *J. Phys.: Conf. Ser.* 2024, *2840*, 012018. DOI: 10.1088/1742-6596/2840/1/012018.

[185] H. Huo, Y. Chen, N. Zhao, X. Lin, J. Luo, X. Yang, Y. Liu, X. Guo, X. Sun, "In-situ formed Li2CO3-free garnet/Li interface by rapid acid treatment for dendrite-free solid-state batteries" *Nano Energy* 2019, *61*, 119–125.

[186] Z. Song, F. Chen, M. Martinez-Ibañez, W. Feng, M. Forsyth, Z. Zhou, M. Armand, H. Zhang, "A reflection on polymer electrolytes for solid-state lithium metal batteries" *Nat. Commun.* 2023, *14*, 4884. DOI: 10.1038/s41467-023-40609-y.

[187] B. R. Chen, A. G. Monson, P. L. Barnes, C. M. Efaw, W. C. Chuirazzi, M. E. Woods, H. W. Rollins, J. F. Rufner, A. S. Preston, D. P. Guillen, E. J. Dufek, "Digital light processing of porous LLZTO scaffolds for Li-garnet solid-state batteries" *Cell Rep. Phys. Sci.* 2025, *6*, 102918. DOI: 10.1016/j.xcrp.2025.102918.

[188] E. Kurian, J. Pitchai, S. Neelanarayanan, K. Ramesha, "In pursuit of all solid state batteries (ASSB): advances at the cathode–electrolyte interface for garnet-based ASSB" *RSC Appl. Interfaces* 2024, *1*, 868–895.

[189] G. Vardar, W. J. Bowman, Q. Lu, J. Wang, R. J. Chater, A. Aguadero, R. Seibert, J. Terry, A. Hunt, I. Waluyo, D. D. Fong, A. Jarry, E. J. Crumlin, S. L. Hellstrom, Y. M. Chiang, B. Yildiz, "Structure, Chemistry, and Charge Transfer Resistance of the Interface between Li7La3Zr2O12 Electrolyte and LiCoO2 Cathode" *Chem. Mater.* 2018, *30*, 6259–6276.

[190] K. Yao, W. S. Scheld, Q. Ma, Y. Zeng, S. Ganapathy, M. Ihrig, R. Ye, M. Ma, V. Kiyek, O. Guillon, M. Huijben, J. E. ten Elshof, M. Finsterbusch, D. Fattakhova-Rohlfing, "Holistic view on cation interdiffusion during processing and operation of garnet all-solid-state batteries" *Energy Storage Mater.* 2024, *71*, 103662. DOI: 10.1016/j.ensm.2024.103662.

[191] W. S. Scheld, Y. Collette, K. Touidjine, C. Roitzheim, Y. J. Sohn, D. Fattakhova-Rohlfing, "Increasing the cycling stability of LLZO-based solid-state batteries with Li3BO3 as catholyte" *J. Power Sources* 2025, *652*, 237322. DOI: 10.1016/j.jpowsour.2025.237322.

[192] X. Xiang, F. Chen, Q. Shen, L. Zhang, C. Chen, "Effect of the lithium ion concentration on the lithium ion conductivity of Ga-doped LLZO" *Mater. Res. Express* 2019, *6*, 085539. DOI: 10.1088/2053-1591/ab2799.

[193] S. Heywood, M. Lessneier, D. Driscoll, S. Sofie, "Tailoring solid-state synthesis routes for high confidence production of phase pure, low impedance Al-LLZO" *J. Am. Ceram. Soc.* 2023. DOI: 10.1111/jace.18994.

[194] X. Xiang, F. Chen, Q. Shen, L. Zhang, C. Chen, "Effect of the lithium ion concentration on the lithium ion conductivity of Ga-doped LLZO" *Mater. Res. Express* 2019, *6*, 085539. DOI: 10.1088/2053-1591/ab2799.

[195] Y. Li, J. T. Han, C. A. Wang, H. Xie, J. B. Goodenough, "Optimizing Li+ conductivity in a garnet framework" *J. Mater. Chem.* 2012, *22*, 15357–15361.

[196] R. Grissa, L. Seidl, W. Dachraoui, U. Sauter, C. Battaglia, "Li7La3Zr2O12 Protonation as a Means to Generate Porous/Dense/Porous-Structured Electrolytes for All-Solid-State Lithium-Metal Batteries" *ACS Appl. Mater. Interfaces* 2022, *14*, 46001–46009.

[197] L. Dhivya, R. Murugan, "Effect of simultaneous substitution of Y and Ta on the stabilization of cubic phase, microstructure, and Li+ conductivity of Li7La3Zr2O12 lithium garnet" *ACS Appl. Mater. Interfaces* 2014, *6*, 17606–17615.

[198] C. Deviannapoorani, S. Ramakumar, N. Janani, R. Murugan, "Synthesis of lithium garnets from La2Zr2O7 pyrochlore" *Solid State Ion.* 2015, *283*, 123–130.

[199] L. Dhivya, K. Karthik, S. Ramakumar, R. Murugan, "Facile synthesis of high lithium ion conductive cubic phase lithium garnets for electrochemical energy storage devices" *RSC Adv.* 2015, *5*, 96042–96051.

[200] L. Kong, I. Karatchevtseva, D. J. Gregg, M. G. Blackford, R. Holmes, G. Triani, "A Novel Chemical Route to Prepare La2Zr2O7 Pyrochlore" *J. Am. Ceram. Soc.* 2013, *96*, 935–941.

[201] G. Larraz, A. Orera, M. L. Sanjuán, "Cubic phases of garnet-type Li7La3Zr2O12: The role of hydration" *J. Mater. Chem. A* 2013, *1*, 11419–11428.

[202] G. Larraz, A. Orera, J. Sanz, I. Sobrados, V. Diez-Gómez, M. L. Sanjuán, "NMR study of Li distribution in Li7−xHxLa3Zr2O12 garnets" *J. Mater. Chem. A* 2015, *3*, 5683–5691.

[203] A. Banerjee, X. Wang, C. Fang, E. A. Wu, Y. S. Meng, "Interfaces and Interphases in All-Solid-State Batteries with Inorganic Solid Electrolytes" *Chem. Rev.* 2020, *120*, 6878–6933. DOI: 10.1021/acs.chemrev.0c00101.

[204] M. M. U. Din, L. Ladenstein, J. Ring, D. Knez, S. Smetaczek, M. Kubicek, M. Sadeqi-Moqadam, S. Ganschow, E. Salagre, E. G. Michel, S. Lode, G. Kothleitner, I. Dugulan, J. G. Smith, A. Limbeck, J. Fleig, D. J. Siegel, G. J. Redhammer, D. Rettenwander, "A Guideline to Mitigate Interfacial Degradation Processes in Solid-State Batteries Caused by Cross Diffusion" *Adv. Funct. Mater.* 2023, *33*, 2303680. DOI: 10.1002/adfm.202303680.

[205] V. Kiyek, C. Schwab, W. S. Scheld, C. Roitzheim, A. Lindner, W. Menesklou, M. Finsterbusch, D. Fattakhova-Rohlfing, O. Guillon, "Direct Precursor Route for the Fabrication of LLZO Composite Cathodes for Solid-State Batteries" *Adv. Sci.* 2024, *11*, 2404682. DOI: 10.1002/advs.202404682.

[206] S. Ohta, S. Komagata, J. Seki, T. Saeki, S. Morishita, T. Asaoka, "All-solid-state lithium ion battery using garnet-type oxide and Li3BO3 solid electrolytes fabricated by screen-printing" *J. Power Sources* 2013, *238*, 53–56.

[207] K. Tadanaga, R. Takano, T. Ichinose, S. Mori, A. Hayashi, M. Tatsumisago, "Low temperature synthesis of highly ion conductive Li7La3Zr2O12–Li3BO3 composites" *Electrochem. Commun.* 2013, *33*, 51–54.

[208] K. Heo, Y. W. Song, D. Hwang, M. Y. Kim, J. Y. Hwang, J. Kim, J. Lim, "Effect of a self-assembling La2(Ni0.5Li0.5)O4 and amorphous garnet-type solid electrolyte composite on a layered cathode material in all-solid-state batteries" *RSC Adv.* 2022, *12*, 14209–14222.

[209] S. Ohta, Y. Kihira, T. Asaoka, "Spontaneous formation of a core–shell structure by a lithium ion conductive garnet-type oxide electrolyte for co-sintering with the cathode" *J. Mater. Chem. A* 2021, *9*, 3353–3359.

[210] V. Montouillout, H. Fan, L. del Campo, S. Ory, A. Rakhmatullin, F. Fayon, M. Malki, "Ionic conductivity of lithium borate glasses and local structure probed by high resolution solid-state NMR" *J. Non-Cryst. Solids* 2018, *484*, 57–64.

[211] C. C. Li, J. H. Jean, "Interactions of organic additives with boric oxide in aqueous barium titanate suspensions" *J. Am. Ceram. Soc.* 2002, *85*, 1441–1448.

[212] S. W. Baek, J. M. Lee, T. Y. Kim, M. S. Song, Y. Park, "Garnet related lithium ion conductor processed by spark plasma sintering for all solid state batteries" *J. Power Sources* 2014, *249*, 197–206.

[213] Y. Ren, T. Liu, Y. Shen, Y. Lin, C. W. Nan, "Chemical compatibility between garnet-like solid state electrolyte Li6.75La3Zr1.75Ta0.25O12 and major commercial lithium battery cathode materials" *J. Materiomics* 2016, *2*, 256–264.

[214] J. Kim, H. Lee, H. Cha, M. Yoon, M. Park, J. Cho, "Prospect and Reality of Ni-Rich Cathode for Commercialization" *Adv. Energy Mater.* 2018, *8*, 1702028. DOI: 10.1002/aenm.201702028.

[215] M. Fakhrudin, E. Kartini, "Synthesis of LLZO by solid-state method" *AIP Conf. Proc.* 2022, *2454*, 020022.

[216] J. Ji, B. J. Lee, "Analyzing the effect of Li/Ni intermixing on Ni-rich layered cathode structures using atomistic simulation of the Li–Ni–Mn–Co–O quinary system" *J. Power Sources* 2023, *556*, 232535. DOI: 10.1016/j.jpowsour.2022.232535.

[217] K. Ben-Kamel, N. Amdouni, A. Mauger, C. M. Julien, "Study of the local structure of LiNi0.33+δMn0.33+δCo0.33−2δO2 (0.025 ≤ δ ≤ 0.075) oxides" *J. Alloys Compd.* 2012, *528*, 91–98.

[218] C. M. Julien, A. Mauger, "Review of 5-V Electrodes for Li-Ion Batteries: Status and Trends" *AIMS Mater. Sci.* 2018, *5*, 650–665. DOI: 10.3934/matersci.2018.4.650.

[219] F. Tietz, T. Wegener, M. T. Gerhards, M. Giarola, G. Mariotto, "Synthesis and Raman micro-spectroscopy investigation of Li7La3Zr2O12" *Solid State Ion.* 2013, *230*, 77–82.

[220] S. Toda, K. Ishiguro, Y. Shimonishi, A. Hirano, Y. Takeda, O. Yamamoto, N. Imanishi, "Low temperature cubic garnet-type CO2-doped Li7La3Zr2O12" *Solid State Ion.* 2013, *233*, 102–106.

[221] F. Scharf, A. Krude, P. Lennartz, M. Clausnitzer, G. Shukla, A. Buchheit, F. Kempe, D. Diddens, P. Glomb, M. M. Mitchell, T. Danner, A. Heuer, A. Latz, M. Winter, G. Brunklaus, "Synergistic Enhancement of Mechanical and Electrochemical Properties in Grafted Polymer/Oxide Hybrid Electrolytes" *Small* 2024, *20*, 2404537. DOI: 10.1002/smll.202404537.

[222] A. Butt, G. Ali, K. T. Kubra, R. Sharif, A. Salman, M. Bashir, S. Jamil, "Recent Advances in NMC-Based Cathodes for Sodium-Ion Batteries" *Energy Technol.* 2022, *10*, 2100775. DOI: 10.1002/ente.202100775.

[223] M. Leal de Souza, M. Morcrette, "Coupling differential voltage analysis and distribution of relaxation times I: Evaluating the impact of NMC811 coating in the degradation of NMC811/Gr cells" *J. Power Sources* 2025, *645*, 237184. DOI: 10.1016/j.jpowsour.2025.237184.

[224] W. S. Yoon, K. Y. Chung, J. McBreen, X. Q. Yang, "A comparative study on structural changes of LiCo1/3Ni1/3Mn1/3O2 and LiNi0.8Co0.15Al0.05O2 during first charge using in situ XRD" *Electrochem. Commun.* 2006, *8*, 1257–1262.

[225] Y. Qiu, F. Jiang, "A review of heat transfer mechanisms and thermal management of vehicle lithium-ion batteries" *Int. J. Heat Mass Transfer* 2022, *182*, 122288. DOI: 10.1016/j.ijheatmasstransfer.2021.122288.

[226] Y. Merla, B. Wu, V. Yufit, N. P. Brandon, R. F. Martinez-Botas, G. J. Offer, "Novel application of differential thermal voltammetry as an in-depth state-of-health diagnosis method for lithium-ion batteries" *J. Power Sources* 2016, *307*, 308–319.

[227] Y. Zhu, X. He, Y. Mo, "Origin of Outstanding Stability in the Lithium Solid Electrolyte Materials: Insights from Thermodynamic Analyses Based on First-Principles Calculations" *ACS Appl. Mater. Interfaces* 2015, *7*, 23685–23693.

[228] T. Famprikis, *Studies on Inorganic Solid Electrolytes for Batteries: Focus on Na3PS4*, PhD thesis, Université de Picardie Jules Verne, Amiens, 2020. Available at: https://theses.fr/2020AMIE0056.

[229] Y. Li, A. M. Prabhu, T. S. Choksi, P. Canepa, "H2O and CO2 surface contamination of the lithium garnet Li7La3Zr2O12 solid electrolyte" *J. Mater. Chem. A* 2022, *10*, 4960–4973.

[230] R. M. Salgado, F. Danzi, J. E. Oliveira, A. El-Azab, P. P. Camanho, M. H. Braga, "The Latest Trends in Electric Vehicles Batteries" *Molecules* 2021, *26*, 3188.

[231] S. Somiya, Ed., *Handbook of Advanced Ceramics*, Elsevier, Amsterdam, 2003.

[232] L. Lin, X. Bi, Y. Gu, F. Wang, J. Ye, "Surface-enhanced Raman scattering nanotags for bioimaging" *J. Appl. Phys.* 2021, *129*, 191101. DOI: 10.1063/5.0047578.

[233] M. B. Fenn, P. Xanthopoulos, G. Pyrgiotakis, S. R. Grobmyer, P. M. Pardalos, L. L. Hench, "Raman Spectroscopy for Clinical Oncology" *Adv. Opt. Technol.* 2011. DOI: 10.1155/2011/213783.

[234] S. Yamada, "Manufacturing Processes and Powder Property of Metal Powders for Additive Manufacturing" *J. Jpn. Soc. Powder Powder Metall.* 2024, *71*, 610–618. DOI: 10.2497/jjspm.24-00053.

[235] M. Wedd, "Particle Size Analysis" in *Encyclopedia of Analytical Science*, 2nd ed., Elsevier, Amsterdam, 2005, pp. 18–29.

[236] N. Munir, M. Hanif, D. A. Dias, Z. Abideen, "The role of halophytic nanoparticles towards the remediation of degraded and saline agricultural lands" *Environ. Sci. Pollut. Res.* 2021, *28*, 60383–60405.

[237] M. U. H. Joardder, A. Karim, C. Kumar, R. J. Brown, "Determination of Effective Moisture Diffusivity of Banana Using Thermogravimetric Analysis" *Procedia Eng.* 2014, *90*, 538–543.

[238] M. Kodal, N. Karakaya, A. A. Wis, G. Ozkoc, "Thermal Properties (DSC, TMA, TGA, DTA) of Rubber Nanocomposites Containing Carbon Nanofillers" in *Carbon-Based Nanofillers and Their Rubber Nanocomposites: Fundamentals and Applications*, Elsevier, Amsterdam, 2019, pp. 325–366.

[239] R. Dugas, J. D. Forero-Saboya, A. Ponrouch, "Methods and Protocols for Reliable Electrochemical Testing in Post-Li Batteries (Na, K, Mg, and Ca)" *Chem. Mater.* 2019, *31*, 8613–8628.

APPENDIX

EIS of optimized LLZO separators during long-term cycling (Chapter 4)

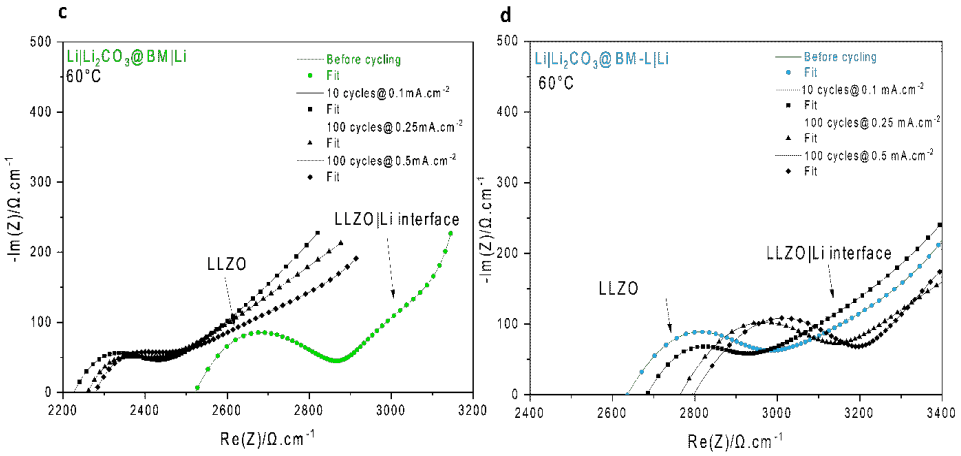


Figure S1| Impedance spectra of optimized and sintered Li_2CO_3@BM-H (left) and Li_2CO_3@BM-L (right) tapes before and across the cycling at different current densities (10,100,200 cycles at 0.1, 0.25, 0.5 mA cm^{-2})

PSD of powders before and after milling

The SEM images and the PSD confirm the particle size reduction of the powder after milling. The particles reserve the spheres like shape after the milling

Table S1| Particle size distribution powders before and after milling

Sample	Distribution model	D10 (µm)	D50 (µm)	D90 (µm)
NMC-as taken	Bi-model	1.87	3.75	5.77
NMC-BM	Mono-model	0.61	1.05	1.69
LLZO- as taken	Bi model	1.07	5.12	10.69
LLZO-BM	Tri-model	0.18	2.05	26.04
LBO-manual milled	Mono-model	18.60	52.5	120.7

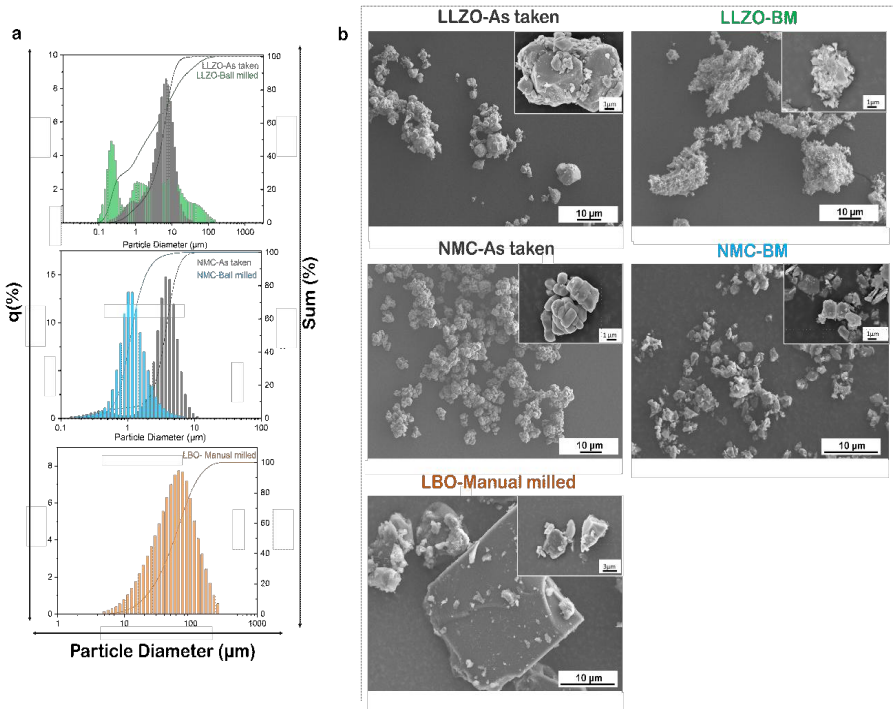
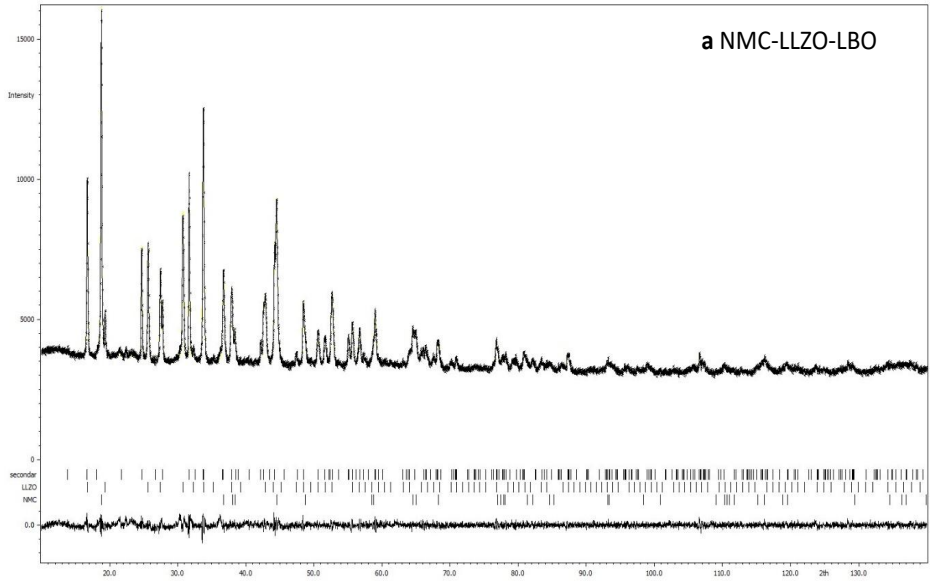


Figure S2|. Particle size distribution of the composite cathode powders before and after milling (a), SEM images of the composite cathode powders before and after milling: LLZO (green) NMC (blue); LBO (orange)

XRD Le bail refinement

Table S2| Refined a- and c-lattice parameter for NMC for NMC-LLZO-LBO, NMC-LBO and reference NMC

	NMC-LLZO-LBO	**NMC-LBO**	**reference NMC**
***a*-lattice parameter (Å)**	2.868(8)	2.872(6)	2.869(1)
***c*-lattice parameter (Å)**	14.189(9)	14.186(3)	14.202(4)
c/a	4.94	4.94	4.95



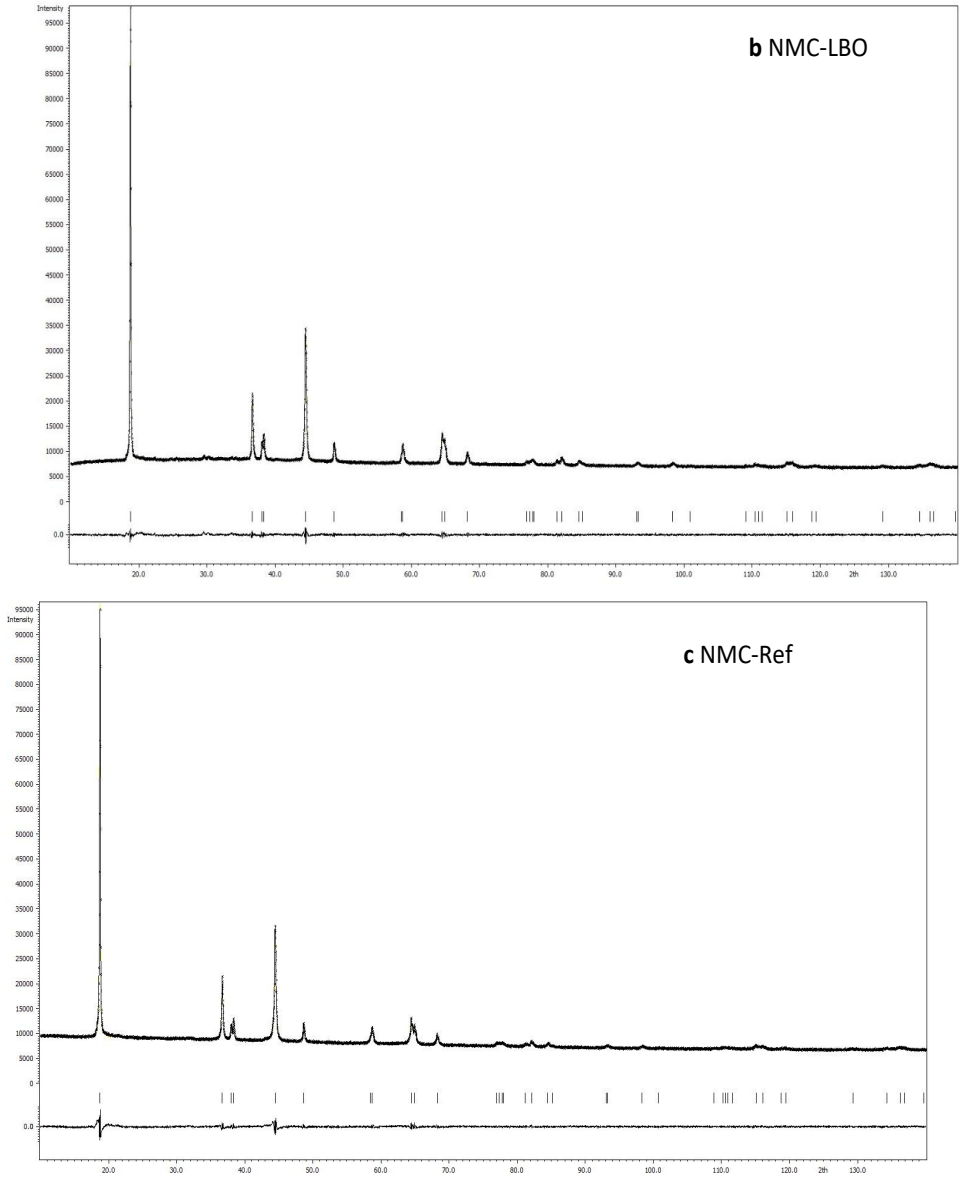
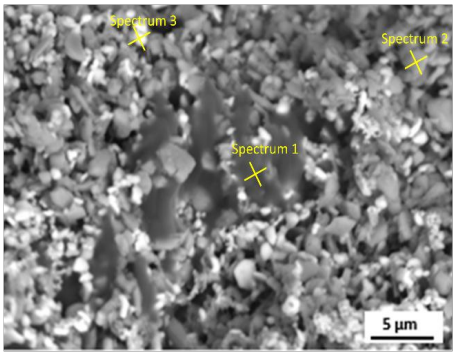


Figure S3 | PXRD patterns of (a) NMC-LLZO-LBO; (b)NMC-LBO, and (c) reference NMC, after refinement with the Le Bail method, the vertical bars mark the reflection positions

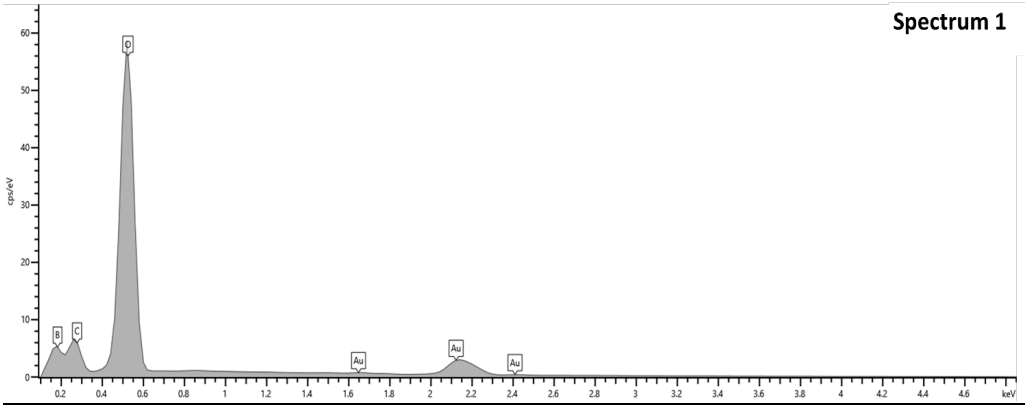
SEM and point EDS of surface fracture of cathode

a



Surface fracture (NMC-LLZ-LBO)

b



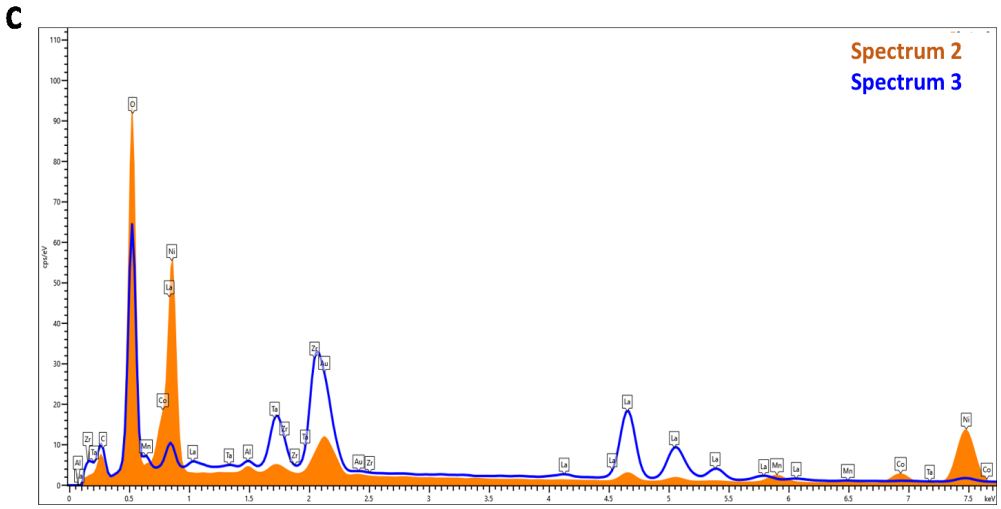


Figure S4| (a) Magnified SEM image of NMC-LLZ-LBO surface fracture;(B and c) Point EDS of different spots

Raman of powders before tape casting

The Raman spectroscopy confirms that no major changes occur after milling the powder, except LLZO after milling features a characteristic peak of Li_2CO_3 which likely emerged during the exposure to air during Raman measurements.

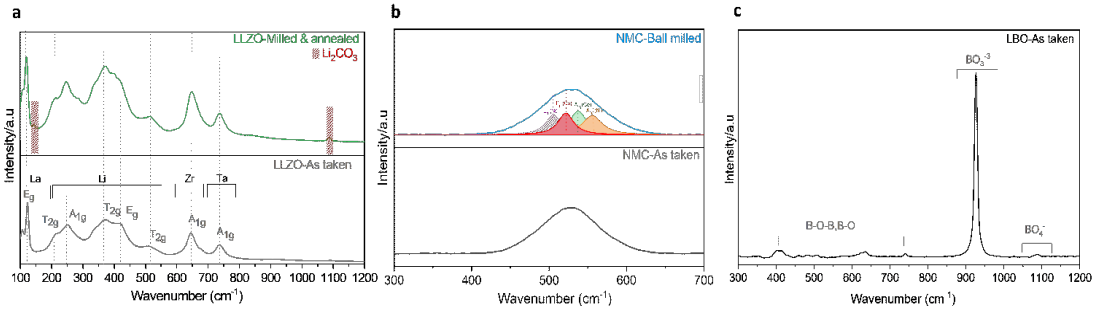


Figure S5| Raman spectra of the powders before and after milling: (a) LLZO; (b) NMC; (c) LBO after manual milling

Calculated resistance and capacitance from the EIS data of composite cathodes

TableS3| Resistance and capacitance measurement from the EIS spectra

Cell system	R1 (Ω.cm²)	C1 (F)	R2 (Ω.cm²)	C2 (F)	R3 (Ω.cm²)	C3 (F)
NMC-LBO-LLZ	207	7.69 10^{-10}	267	6.45 10^{-5}	180	1.85 10^{-5}
	0.5 MHz		1.5 KHz		32 HZ	
NMC-LBO-LLZ+C	107	9.34 10^{-10}	364	1.87 10^{-4}	70	8.5 10^{-5}
	0.8 MHz		1.1 KHz		28 HZ	
NMC-LBO	210	3.48 10^{-7}	172	1.56 10^{-7}	1820	1.5 10^{-5}
	0.8 MHz		1.1 KHz		8 HZ	
NMC-LBO+C	308		6.2 10^{-7}			
	0.8 KHz					

The resistance is calculates using the formula $\sigma = \frac{dR}{A}$,

And the capacitance is calculated using the formula $C = \frac{(QR)^{1/\alpha}}{R}$

The incremental capacity (dQ/dV) profiles of composite cathodes

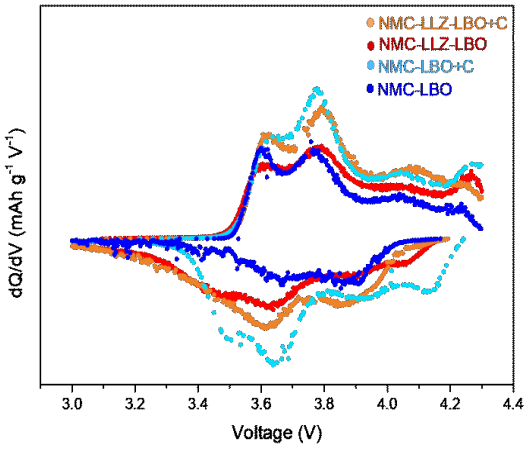


Figure S6| Incremental capacity (dQ/dV) profiles of the four composite cathodes (NMC–LBO, NMC–LBO+C, NMC–LLZO–LBO, and NMC–LLZO–LBO+C) during the first charge–discharge cycle at 60 °C.

The incremental capacity (dQ/dV) profiles reveal pronounced differences in peak sharpness, intensity, and number. The NMC–LBO+C sample exhibits the most distinct and well-resolved peaks, corresponding to the sequential $Ni^{2+}/Ni^{3+}/Ni^{4+}$ redox transitions, which indicates good structural integrity, low polarization, and efficient lithiation/delithiation. In contrast, the NMC–LBO sample shows weaker and less defined peaks, highlighting the incomplete activation of NMC probably due to the absence of electronic percolation pathways. The LLZO-containing composites (NMC–LLZO–LBO and NMC–LLZO–LBO+C) display broader and partially merged peaks compared to NMC–LBO+C, suggesting increased polarization and structural disorder, likely induced by Li^{+}/Ni^{2+} antisite defects and the presence of secondary La-Ni-O phases. While the addition of carbon in NMC-LLZO-LBO+C slightly sharpens the redox peaks and improves activity

Table 4S| Values of calculated Diffusion coefficient as function of charging potential

NMC-LLZ-LBO		NMC-LLZ-LBO+C		NMC-LBO		NMC-LBO+C	
Potential (V)	D (cm^2/s)	Potential (	D (cm^2/s)	Potential (	D (cm^2/s)	Potential (	D (cm^2/s)
3.5136	3.10E-08	3.05	8.27E-09	3.51	6.40E-09	3.481	3.24E-08
3.574	5.67E-10	3.545	5.39E-10	3.545	1.08E-09	3.515	3.40E-09
3.633	6.88E-10	3.601	5.06E-10	3.587	4.59E-10	3.551	1.53E-09
3.688	8.77E-10	3.632	7.27E-10	3.6226	6.34E-12	3.565	1.32E-09
3.73	4.06E-10	3.66	6.65E-10	3.6399	3.88E-10	3.59	6.86E-10
3.772	4.70E-10	3.69	5.36E-10	3.673	4.07E-10	3.6215	1.07E-09
3.82	5.09E-10	3.71	6.77E-10	3.715	2.94E-10	3.6507	1.22E-09
3.858	5.39E-10	3.73	4.57E-10	3.739	2.47E-10	3.69	1.50E-09
3.89	5.09E-10	3.77	6.55E-10	3.762	3.20E-10	3.7119	1.04E-09
3.93	4.34E-10	3.83	8.91E-10	3.789	3.16E-10	3.75	9.37E-10
3.9718	5.24E-10	3.874	6.51E-10	3.825	4.02E-10	3.76	9.18E-10
4.03	3.29E-10	3.915	6.19E-10	3.845	6.95E-10	3.8089	9.11E-10
4.076	3.83E-10	3.954	5.70E-10	3.878	7.22E-10	3.845	1.59E-09
4.1517	2.87E-10	4.025	5.32E-10	3.907	8.07E-10	3.866	1.35E-09
4.178	1.40E-10	4.062	5.18E-10	3.965	6.91E-10	3.889	1.84E-09
4.183	7.70E-12	4.144	3.77E-10	3.993	6.73E-10	3.935	2.01E-09
4.199	2.87E-12	4.179	1.74E-10	4.019	5.09E-10	3.978	1.84E-09
4.206	1.55E-12	4.2	2.72E-12	4.04	3.24E-10	4.018	1.60E-09
4.2077	3.90E-13	4.205	2.50E-12	4.082	5.92E-10	4.06	1.37E-09
4.211	2.97E-12	4.208	1.14E-12	4.173	5.95E-10	4.152	1.27E-09
4.213	7.96E-12	4.21	3.91E-12	4.207	3.49E-10	4.221	7.43E-10
4.2167	3.65E-13	4.2147	1.65E-13	4.218	1.45E-12	4.234	6.13E-10
4.2203	0	4.2212	1.42E-13	4.225	1.56E-11	4.25	7.64E-10
	--	4.2219	3.91E-14	4.234	6.35E-11	4.251	8.16E-12

DRT profiles of composite cathodes during first charge

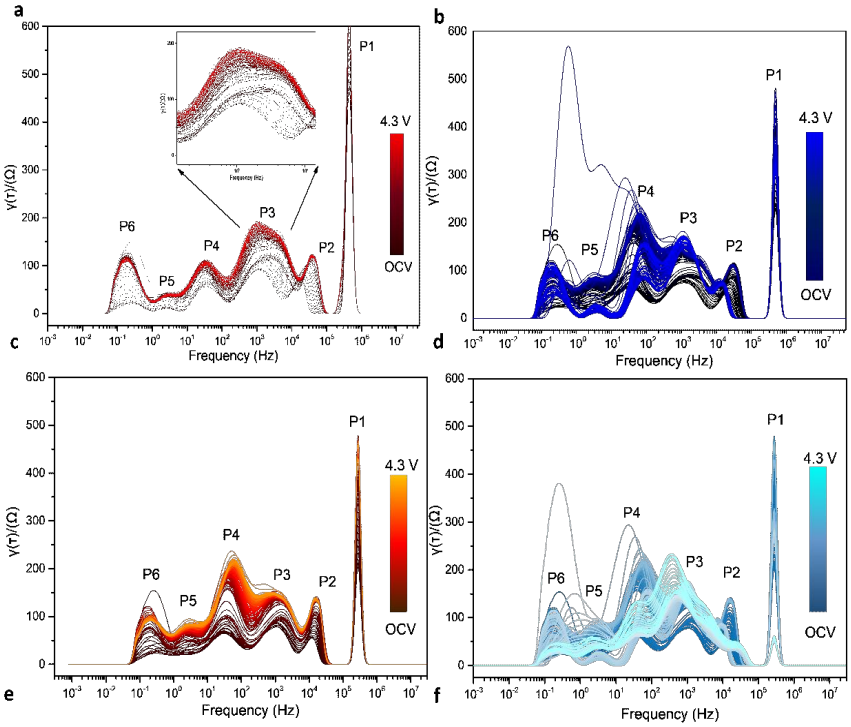


Figure S7| Evolution of the DRT spectra for the four composite cathodes during the first charge: (a)NMC-LLZO-LBO; (b) NMC-LBO; (c) NMC-LLZO-LBO+C, and (f) NMC–LBO+C; Each colour gradient reflects increasing state of charge from OCV to 4.3 V

Postmortem RAMAN of composite cathodes

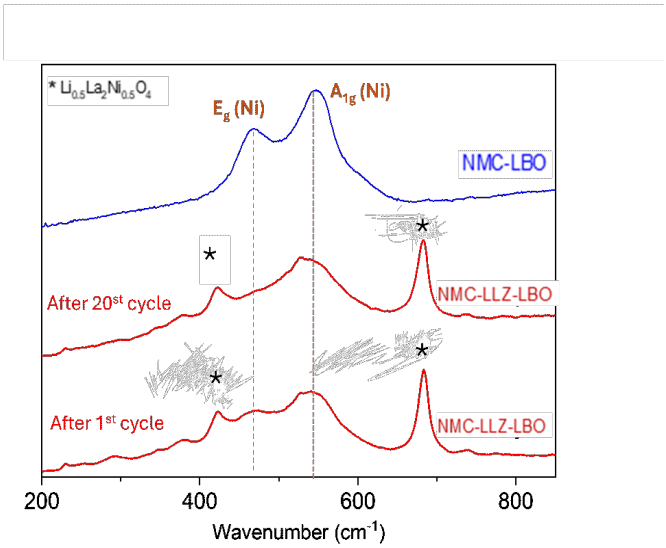


Figure S8| Evolution of Raman spectra for the composite cathodes after cycling

PUBLICATIONS AND PRESENTATIONS

- Publications

This doctoral thesis was conducted as part of the DESTINY doctoral programme, funded by the European Union's Horizon 2020 research and innovation programme under the Marie Skłodowska-Curie Actions COFUND scheme (Grant Agreement No. 945357).

1.The impact of lithium carbonate on tape cast LLZO battery separators: A balanced interplay between lithium loss and lithiation": Research paper

Kaouther Touidjine, Melanie Finsterbusch-Rosen, Vivien Kiyek, Swapna Ganapathy, Martin Finsterbusch, Olivier Guillon, Mark Huijben, Erik Kelder, Marnix Wagemaker, Dina Fattakhova-Rohlfing

Published: https://doi.org/10.1016/j.ensm.2024.103487

2.Is there any benefit of coating Si particles for a negative electrode material for lithium-ion batteries with metal-organic frameworks? The case of aluminum fumarate

Nassima Kana, Kaouther Touidjine, Sarah Olivier-Archambaud, Effrosyni Gkaniatsou, Michael Paris, Nicolas Dupré, Nicolas Gautier, Philippe Moreau, Clémence Sicard, Bernard Lestriez, Thomas Devic

Published: https://doi.org/10.1021/acsaem.3c00658

3.Advancing LLZO Ceramic Separators by Tape Casting: A Review of Challenges, Strategies, and Pathways to Industrial Implementation: Review paper

Kaouther Touidjine, Ruijie Ye, Melanie Finsterbusch-Rosen, Artur Lang, Martin Finsterbusch, Dina Fattakhova-Rohlfing

Submitted: cssc.202502488 for ChemSusChem

4.NMC Tape-Cast NMC-LLZO-LBO based Composite Cathodes for Solid-State Lithium Batteries

Kaouther Touidjine, Christoph Roitzheima, Xiaochen Liu, Walter Sebastian Scheld, Andreas Paulus, Muhammad Zubair, Mark Huijben, Erik Kelder, Marnix Wagemaker, Martin Finsterbusch, Dina Fattakhova-Rohlfing

Submitted: batt.202500959 for Batteries & Supercapacitors

5.Increasing the cycling stability of LLZO-based solid-state batteries with Li3BO3 as catholyte

Walter Sebastian Scheld, Yannic Collette, Kaouther Touidjine, Christoph Roitzheim, Yoo Jung Sohn, Dina Fattakhova-Rohlfing
Published: https://doi.org/10.1016/j.jpowsour.2025.237322

6.High-rate performance solid-state lithium batteries achieved by infiltrating a single-layer LLZO scaffold

Muhammad Zubair, Ruijie Ye, Xiaochen Liu, Kaouther Touidjine, Frank Tietz, Dina Fattakhova-Rohlfing, Olivier Guillon
published: https://doi.org/10.1016/j.jpowsour.2025.239065

7.Improved interphase Li+ transport via surface modification for stable Solid-State Lithium Metal Batteries:

Xiaochen Lui, Kaouther Touidjine, Ruijie Ye, Christian Schwab, *Martin Finsterbusch, Olivier Guillon*, Dina Fattakhova-Rohlfing
To be submitted

- Poster and presentation

1.Development of High-Performance LLZO Separators for Solid-State Batteries: Balancing Li Loss, Stability, and Morphology in a Tape Casting Process

Kaouther Touidjine, Melanie Finsterbusch Rosen, Vivien Kiyek, Swapna Ganapathy, Martin Finsterbusch, Olivier Guillon, Mark Huijben, Erik Kelder, Marnix Wagemaker, Dina Fattakhova-Rohlfing
Electrochemical Society Meeting Abstracts 245. Sab Francisco, USA.

2. Controlling the LLZO ceramic composition for high-quality thin ceramic separators obtained by tape casting

Kaouther Touidjine, Melanie Finsterbusch Rosen, Vivien Kiyek, Martin Finsterbusch, Olivier Guillon, Mark Huijben, Erik Kelder, Marnix Wagemaker, Dina Fattakhova-Rohlfing
98th DKG Annual Meeting. Ernst-Abbe-Hochschule Jena, Germany

- Awards

1.Recipient of a $500 travel grant for the ECS Annual Conference, San Francisco, USA, 26−30 May 2024

2.Recipient of a full sponsorship for a PANACEA summer school, Venice, Italy, 16−21 June 2024

- Workshops

1.NMR school, Venice (Italy). 16-21.06.2024.

2. Destiny Training School on XRD refinements tool, CICEnergiGUNE (Spain). 15-19.01.2024

3. Destiny Training School on Market intelligence, Umicore,(Belgium). 11-2023-03-2024

4.Hitec Graduate School training, Forschungszentrum Jülich, (Germany). 2021-2024

ACKNOWLEDGEMENT

This work would not have come to pass without the generosity, guidance, and good humour of a great many peoples, to whom I owe my sincerest thanks.

I am profoundly grateful to the DESTINY programme (funded by the European Union's Horizon 2020 research and innovation programme under the Marie Skłodowska-Curie Actions COFUND scheme, Grant Agreement No. 945357). and its coordinators, for affording me such an excellent fellowship, and for the high calibre of training I was privileged to receive throughout. It has shaped not only this thesis, but the researcher I have become.

My deepest thanks go to my main supervisor, Prof. Dr. Dina Fattakhova-Rohlfing, for her guidance, trust, and steady support throughout this journey, and to my co-supervisors, Prof. Dr. Mark Huijben, Prof. Dr. Marnix Wagemaker, and Dr. Erik Kelder, whose insight and encouragement were invaluable at every turn. I owe particular thanks to Martin Finsterbusch, for his day-to-day supervision and the many thoughtful discussions that so often set me on the right path.

My thanks also go to the members of my examination committee, for their time, careful examination of my thesis, and valuable questions during my defence, and to the University of Duisburg-Essen, for hosting and guarantying my defence and degree.

I wish to thank Dr.Swapna Ganapathy, of the SEE group at TU Delft, for the NMR measurements and for her generous help in discussion, Dr. Christoph Roitzheim, Dr. Walter Sebastian Scheld, Dr. Andreas Paulus, and Dr. Muhammed Zubair, for their pleasant collaboration and for so willingly sharing their knowledge of composite cathode materials for LLZO batteries, and Dr. Ruijie Ye for the insight so generously offered on LLZO tape casting. I am also grateful for Dr. Vivien Kiyek and Dr. Melanie Finsterbusch-Rosen for the shared work and collaboration on LLZO tape cast work. My thanks also go to my co-authors, for so sharing their expertise and for their careful proofreading of the articles published from this work. To the colleagues who made this journey thoughtful, joyful, and often very funny: Liu Xiaochen, Yannic Collette, Artur Lang, Ernesto Claure Ramirez, and Kai Yao.

I am equally thankful to my colleagues at the SEE group in TU Delft: Dr. Theodosios Famprikis, Biffo Abdulkadir, Dr. Pierfrancesco Ombrini, Dr. Pedro Groszewicz, and Xavier Kauoi who gave me the warmest and kindest welcome during my time there.

My warmest thanks too, to the technicians whose skill made this work possible: Grit Häuschen and Tobias Lammert, for providing the LLZO used throughout this work, and Volker Bader, for performing the sintering treatments of the components built in this thesis, and Philipp Hecker for the overall technical support.

And to my dear friends: Catalina Pineda Heresi, Fatemeh Azhdari, Deema Abubaker, Sana Aslam, and Asma Aouamri, who, come what may, made my years of PhD and time in Jülich a genuinely happy chapter of my life. For your unwavering support, and for every memory we wove together along the way, I am, and shall always remain, sincerely grateful. Many thanks extend, too, to those who stayed close throughout this long journey, and to those who joined only near its end, yet left their mark all the same. And to one who arrived *à pas de lechat* , creatively and quietly, thank you, whatever comes next.

To my family, my gratitude runs deeper than words allow. To my mother, Zouzou, who has been my pillar, my support, my joy, and my fun, in equal and constant measure. To my father, for his easy, good-humoured spirit, which has a rare way of making life's burdens feel lighter and its pleasures nearer, and for his rather heroic efforts in diagnosing my car troubles over video call, a skill for which no doctoral training could have prepared him. To my brother Aymen, for accommodating my every IT panic and, without fail, solving it, and to my brother Haithem, for his steadfast support and for so bigheartedly spreading love. And to my one and only sister, who is nothing like me, who has never once approved of my red shoes, and who is, in all the ways that matter, entirely too similar to me, thank you!

There are women, too, whose influence reaches back to my youth, who shaped not only my skills but the person I became. To my primary school teacher, Mrs. Noura Haichour, and Mrs. Cherfaoui Naziha, who taught me English during the U.S. Embassy's Access Leadership Programme: your mark upon me has proved lasting, and I carry a part of each of you into everything I do.

Finally, my thanks extend to all those who have shaped this journey, and the road that led me to it, including my professors at the University of Badji Mokhtar, Annaba, and the free education I received in Algeria, which formed and equipped me for everything that followed.

CURRICULUM VITAE

Personal Details

Kaouther Nahr El Khouloud Touidjine

Born 6 July 1997,Sétif, Algeria

Email: kaouthertouidjinedz@gmail.com

Education

Oct 2021-March 2025 PhD in Solid-State Batteries

- Fellowship: Marie Skłodowska-Curie Research Fellowship (DESTINY)
- Conducted at Institute IMD-2 (Microstructure and Properties of Materials), Forschungszentrum Jülich GmbH with Secondment: TU Delft (SEE Group) & University of Twente, Netherlands
- Graduated from University of Duisburg-Essen, Germany
- Supervisor: Prof. Dr. Dina Fattakhova-Rohlfing
- Grade: 1.0 (Sehr gut)

Sep 2019 – Sep 2021 MSc in Materials for Energy Storage and Conversion (MESC+)

- Fellowship: Erasmus Mundus Excellence Scholarship
- University of Picardie Jules Verne, France.
- Mobility program: Semester 1 at Warsaw University of Technology, Poland. Semester 2 at University of Paul Sabatier in Toulouse, France. Semester 3 at University of Ljubljana, Slovenia. Semester 4, internship at Jean Rouxel Institute (IMN), Nantes, France.
- Master's Thesis on Silicon anode coating under the supervision of Dr.Bernard Lestriez
- Grade: 15.6/20 (Très bien)

Sep 2015 – Sep 2019 BSc in Metallurgy and Materials Engineering

- University of Badji Mokhtar, Annaba, Algeria
- Bachelor's Thesis on Thermal fatigue of stainless steels under the supervision of Prof. Boudebane Azzedine
- Grade: 18/20 (Excellent)

Language Skills

English :C1

French: C1

Arabic: C1

German: B1

Volunteering & Leadership

2025 – Ongoing Community and Social Media Manager at DAAS (Deutsch-Algerischer Akademiker und Studierender Verein e.V)

2023 – 2025 MESC Program Representative, Erasmus Mundus Alumni Association, Brussels, Belgium

2020 Ambassador, GO Platform, Doha, Qatar

2016 – 2017 Education Program Manager, U.S. Embassy, Algiers, Algeria

2016 – 2017 Head, UGEL Student Organization, Annaba, Al

Band / Volume 730
Land-Atmosphere Coupling in a Changing Climate: Understanding Variability, Extremes, and Human Influence through Regional Climate Modeling
Y. Zhang (2026), 135 pp
ISBN: 978-3-95806-980-0 (Print)
ISBN: 978-3-95806-981-7 (E-Book)

Band / Volume 731
Abbildung gekoppelter Infrastrukturen in Energiesystemmodellen
P. Freitag (2026), XIX, 322 pp
ISBN: 978-3-95806-984-8 (Print)
ISBN: 978-3-95806-985-5 (E-Book)

Band / Volume 732
Cost-reduced and Sustainable Interconnects and their Coatings for Solid Oxide Cells
M. Hilger (2026), viii, 185 pp
ISBN: 978-3-95806-988-6 (Print)
ISBN: 978-3-95806-989-3 (E-Book)

Band / Volume 733
Liquid-Phase Synthesis of Silicon and Silicon Carbide Thin-Films via Atmospheric Pressure Chemical Vapor Deposition
B. Fischer (2026), xxii, 211, A15 pp
ISBN: 978-3-95806-990-9 (Print)
ISBN: 978-3-95806-991-6 (E-Book)

Band / Volume 734
Modellgestützte Transformationspfade des deutschen Energiesystems
R. Maier (2026), xxvii, 331 pp
ISBN 978-3-95806-994-7 (Print)
ISBN 978-3-95806-995-4 (E-Book)

Band / Volume 735
Dynamical drivers of deep and shallow branches in the stratospheric circulation and transport
R.- A. Baikhadzhaev (2026), 120 pp
ISBN 978-3-95806-996-1 (Print)
ISBN 978-3-95806-997-8 (E-Book)

Band / Volume 736
Silicon heterojunction solar cells on thin wafers – prospects in different utilization scenarios
U. K. Chime (2026), 151 pp
ISBN 978-3-95806-998-5 (Print)
ISBN 978-3-95806-999-2 (E-Book)

Band / Volume 737
Advancing the understanding of actual evapotranspiration and critical soil moisture thresholds using lysimeter networks
X. Lu (2026), XXX, 159 pp
ISBN 978-3-69367-000-2 (Print)
ISBN 978-3-69367-001-9 (E-Book)

Band / Volume 738
Einfluss des automatisierten Fahrens auf die technoökonomische Performance von Verkehrssystemen
E. Jungblut (2026), VIII, 304 pp
ISBN 978-3-69367-006-4 (Print)
ISBN 978-3-69367-007-1 (E-Book)

Band / Volume 739
Photon-assisted Degradation and Recovery of Transparent Passivating Contact Silicon Solar Cells
B. Xu (2026), xii, 189 pp
ISBN 978-3-69367-008-8 (Print)
ISBN 978-3-69367-009-5 (E-Book)

Band / Volume 740
Effects of Microplastics on Carbon and Nitrogen Turnover Processes in the Rhizosphere of Crops
K. J. Neubert (2026), xxii, 193 pp
ISBN 978-3-69367-010-1 (Print)
ISBN 978-3-69367-011-8 (E-Book)

Band / Volume 741
Comprehensive Understanding and Optimization of the Tape Casting Process for the Fabrication of LLZO-Based Solid-State Battery Components
K. N. El K. Touidjine (2026), XV, 170 pp
ISBN 978-3-69367-016-3 (Print)
ISBN 978-3-69367-017-0 (E-Book)

Weitere ***Schriften des Verlags im Forschungszentrum Jülich*** unter
http://wwwzb1.fz-juelich.de/verlagextern1/index.asp

Energie & Umwelt / Energy & Environment
Band / Volume 741
ISBN 978-3-69367-017-0

Mitglied der Helmholtz-Gemeinschaft

JÜLICH
Forschungszentrum